Modelling of the Blood-Brain Barrier Endothelium and Analysis of the Impacts of Shear Stress

By

Koji L Foreman

A dissertation submitted in partial fulfillment of

the requirements for a degree of

Doctor of Philosophy

(Chemical and Biological Engineering)

at the

UNIVERSITY OF WISCONSIN – MADISON

2023

Date of final oral examination: 7/25/2023

This dissertation is approved by the following members of the Final Oral Committee:

Eric V. Shusta, Chemical and Biological Engineering

Sean P. Palecek, Chemical and Biological Engineering

John Yin, Chemical and Biological Engineering

Brian F. Pfleger, Chemical and Biological Engineering

Krishanu Saha, Biomedical Engineering

Abstract

The human brain vasculature uniquely regulates the influx of nutrients into the brain while restricting the penetration of toxins and blood constituents. Blood-brain barrier (BBB) properties include efflux transporter activity and other passive resistances which limit brain uptake of pharmaceuticals, creating a roadblock for neurotherapeutic development. Through this document we sought to expand knowledge of both the *in vivo* BBB, and of *in vitro* models to provide an understanding of the biology and models of the BBB. Analysis of laser extracted microvessels from human and mouse brains revealed key species specific differences including lack of human expression of a key mouse brain pericyte marker. Additionally, this dataset provides a valuable supplemental tool to current efforts to assess the human brain transcriptome via single cell sequencing by providing greater depth and limited inflammatory and temperature shock gene expression associated with disassociation of brain tissue. Utilizing *in vitro* models we explored the dynamic response of the BBB to increased shear stress. Previous research demonstrated regional neuronal activation in a mouse model drives a local increase in BBB permeability. We hypothesized that this increase in permeability may be partly driven by the transient increase in blood flow that accompanies neuronal activation. We observed shear stress was sufficient to reduce efflux transport of the Rhodamine123 fluorescent efflux substrate in primary rat BMECs. In addition, we observed pharmacological activation of Piezo1, a recently discovered mechanosensitive ion channel thought to be involved in vascular pathfinding and development, led to a reduction in P-gp activity. Overall, we believe this work suggests a potential shear mediated mechanism to reduce efflux activity, and that this effect could potentially be mediated by Piezo1. We further assessed the effect of long term shear stress on the transcriptome of four BBB *in vitro* models which drove upregulation of BBB relevant genes, but

did not reverse a loss of phenotype due to extended *in vitro* culture. Together this work provides several transcriptional datasets with value to literature, compares multiple commonly utilized models with relevance to drug design, and provides several insights into potential BBB biology.

Acknowledgements

The author would like to thank Benjamin D. Gastfriend and Moriah E. Katt for their camaraderie and extensive assistance in experimental design, experimental operation, writing, and data analysis. Further, the author would like to acknowledge Jacob L. Veire, Maritza Cruz Hernandez, Catarina Profaci and Bill Ding for assistance with technical expertise and data analysis. This work was funded in part by the National Institutes of Health (NS103844, NS107461, HL154254, AA020476, NS103844) and the National Science Foundation (1703219).

Table of Contents

List of Tables

List of Figures

Chapter 1 – A Review of Human *in vitro* Blood-Brain Barrier Models Derived from Stem Cells[1]

[1] The following chapter is adapted from [1]:

Foreman KL, Palecek SP, Shusta EV. Chapter 9: Human in vitro Blood-Brain Barrier Models Derived from Stem Cells. In: De Lange ECM, Hammarlund-Udenaes M, Thorne RG, editors. Drug Delivery to the Brain: Physiological Concepts, Methodologies and Approaches [Internet]. Cham: Springer International Publishing; 2022

1.1 Summary

In vitro blood-brain barrier (BBB) models have significant utility in understanding the BBB in health and disease. While human BBB models using primary and immortalized brain endothelial cells have been described, issues regarding retention of BBB properties and scalability have hampered their use for certain applications cells exhibiting BBB properties offers advantages including high barrier, human relevance, and ease of scaling. In this chapter we will introduce stem cells and how they are being used to model the blood-brain barrier (BBB). We will focus predominantly on the characteristics of models differentiated from human pluripotent stem cells (hPSCs), which express some BBB markers and exhibit barrier and transporter activities. We will also discuss incorporation of co-culture with other stem cell-derived or primary cells of the neurovascular unit (NVU) into stem cell-derived BBB models, as well as microfluidic and suspension culture models. These stem cell-derived BBB models have applications in modeling human BBB development, studying the roles of disease on BBB function, drug discovery, and development of strategies for neurotherapeutic delivery.

1.2 Introduction

The blood-brain barrier (BBB) is a major roadblock in the development of new therapeutics targeting central nervous system diseases such as brain tumors and neurodegenerative diseases [2]. Human *in vitro* BBB models offer platforms for systematic study of BBB development and its role in disease, as well as for drug discovery. However, primary and immortalized human brain microvascular endothelial cells (BMECs), which typically are the basis for these models, often possess significantly diminished BBB characteristics. For example, transendothelial electrical resistance (TEER), a commonly used metric of paracellular permeability, is frequently abnormally low. TEER of these models typically falls below 100 Ω-cm^2 [3,4]; however, it is estimated that the true physiologic TEER can be above 5000 Ω-cm^2 *in vivo* [5,6]. Human BBB models with low TEER values (~100-200 Ω-cm^2) allow aberrant paracellular passage of larger proteins and increased penetration of small molecules [7], making these models insufficient for predictive *in vitro* drug permeability studies. Primary human BMECs are a finite resource that cannot be easily scaled for scientific or drug development studies. The use of primary animal BMECs can alleviate scaling and availability pressures; however, animal models possess numerous key differences compared to human BBB performance, particularly with respect to efflux transporter expression, a key component of BBB resistance [8–11]. To address issues such as human relevance, scalability, and model fidelity, researchers have recently begun to build BBB models using human stem cell sources. These models are comprised of stem cell-derived brain microvascular cell-like (BMEC-like) cells possessing BBB properties which can be combined with supporting cells of the NVU such as stem cell-derived astrocytes, pericytes, neurons and microglia. Below we will outline the stem

cell sources, cellular differentiation strategies and multicellular constructs that can be used to investigate the BBB in health and disease.

1.3 Stem Cell Sources for BBB Modeling

With the development of stem cell isolation, culture, and differentiation technologies, scalable human BBB models with physiological properties have become possible. A stem cell is defined as a cell that is capable of self-renewing and differentiating into more specialized cell types [12]. This self-renewal capacity means that the stem cells can be expanded in the undifferentiated state and serve as a source for large quantities of the various cell types, enabling large scale studies and screens. Having a single self-renewing precursor can also help limit the batch-to-batch variability intrinsic to human primary cells. Moreover, stem cells can be isolated from individual patients, allowing the study of disease conditions with a genetic basis. Finally, the transition from an undifferentiated stem cell to one possessing BBB properties could offer insights regarding the mechanisms of human BBB induction and maintenance.

There are many different types of stem and progenitor cells found throughout development, only some of which reside in the adult. Here, we will largely focus on human pluripotent stem cells (hPSCs), which include human embryonic stem cells (hESCs) and induced pluripotent stem cells (iPSCs). hPSCs possess the theoretical capacity for infinite self-renewal (although in practice, they are limited by eventual acquisition of genetic mutations) and can differentiate into any cell type in the adult [13]. hESCs, are derived from the inner cell mass of human blastocysts, as first demonstrated in 1998 by the Thomson lab [14]. iPSCs are generated by reprogramming somatic cell types, such as fibroblasts or lymphocytes, by inducing expression of core transcription factors that regulate pluripotency to produce an hESC-like cell [15,16]. As

will be discussed below, iPSCs enable a whole new spectrum of patient-specific BBB modeling, with particular application in studying how human genetic diseases influence the BBB.

Umbilical cord blood-derived stem cells have also been used to generate human BMEC-like cells. While these cord blood-derived adult stem cells are substantially more fate restricted than hPSCs, they have the capacity to differentiate to endothelial cells [17] and some attempts have been made to induce BBB properties in these endothelial cells [18,19].

It is important to note that while stem cell-derived BBB models recapitulate some aspects of BBB protein expression and phenotypes, they are not perfect facsimiles of the *in vivo* BBB. They differentiate under conditions inspired by human BBB development, but do not receive all cues found in the developing brain. Moreover, the culture conditions *in vitro* differ from the *in vivo* microenvironment. Thus, in matching a model to a specific application, it is important to consider particular attributes the model lacks or possesses relative to the *in vivo* BBB. Below, we will discuss the various routes that researchers have employed for the differentiation of BMEC-like cells and the use of these cells in modeling the BBB.

1.4 Differentiation of Stem Cells to BMEC-like Cells

The incorporation of stem cell-derived BMEC-like cells into BBB models has been enabled by the development of several differentiation protocols, as discussed in detail below. From here forward, we will refer to all the different forms of stem cell-derived BMEC-like cells simply as BMECs. This is not meant to imply, however, that they are perfect facsimiles of *in vivo* or *in vitro* human BMECs. In fact, it has been well established that many lack key components of BMEC

1.4.1 hPSC-Derived BMECs

1.4.1.1 Co-differentiation with Neural Progenitors

As the endothelial cells of the perineural vascular plexus invade the developing neural tube during development, they acquire a BBB phenotype in part by interactions with developing neural cells [20]. A stem cell co-differentiation technique was developed to attempt to mimic this interaction to generate hPSC derived BMEC-like cells [21]. Initially, hPSCs are seeded and allowed to expand for three days prior to inducing differentiation. Next, the hPSCs are exposed to basal medium supplemented with amino acids, a serum replacement cocktail, and β-mercaptoethanol that drives differentiation to a mixed population containing neural and endothelial cells, among other cell types. This co-differentiation results in colonies of PECAM-1 positive endothelial cells surrounded by βIII tubulin and nestin expressing neural tracts that somewhat resemble the *in vivo* cellular environment [21,22]. During this phase, cells gain GLUT-1 expression in concert with nuclear β-catenin localization, likely a consequence of Wnt signaling from the co-differentiating neural cells [21]. These data suggested the importance of Wnt signaling in induction of BBB properties during the differentiation process, in agreement with BBB development in mice [23–26].The co-differentiating cell mixture is then switched to endothelial medium [21].

At the end of this growth phase, the endothelial cells exhibited expression of BBB markers including tight junction associated proteins ZO-1, occludin, and claudin-5; and efflux transporters MRP1, BCRP, and P-gp (Table 1.1). Extremely weak signaling of endothelial markers were observed. Passaging and subculture of the cell mixtures onto a matrix of collagen IV and fibronectin yields a monolayer of BMEC-like cells [21]. This model demonstrates strong tight junction formation with TEER values up to 500 Ω-cm^2 [27], which is below *in vivo* levels

[5,6], but equivalent to or greater than most other models [3]. The cells also possess polarized P-gp, MRP1, and BCRP efflux transporter activities [21,27–29]. The barrier quality can vary greatly depending on initial stem cell seeding density and stem cell line, so careful optimization is required to generate cells that express BMEC markers and exhibit BBB phenotypes [28,30,31]. BMEC-like cells at both the subculture stage and post-differentiation can be cryopreserved, though addition of a ROCK inhibitor post-thaw is necessary to restore barrier function and increase cell attachment and survival [31,32].

Addition of retinoic acid (RA) during the endothelial expansion and subculture phases of BMEC differentiation improved expression of endothelial markers and increased barrier tightness [33]. RA is critical for the patterning of the central nervous system along the anterior-posterior axis [34], and has been implicated in BBB specification *in vivo*, possibly through regulation of Wnt signaling [35–38]. RA addition during the endothelial expansion phase of BMEC differentiation was shown to improve multiple BBB phenotypes [33]. Supplementation significantly increased TEER, peaking between 1000-3000 Ω-cm^2 for monocultured BMECs, corresponding with increased continuity of tight junction proteins occludin and claudin-5. Efflux transporter transcripts were also upregulated, but this did not translate to improved efflux transport activity as assessed by substrate accumulation assays [33].

1.4.1.2 Accelerated Co-differentiation

The accelerated co-differentiation protocol is a variant of the previously described method that reduces differentiation duration from thirteen to seven days. The stem cell expansion period is reduced from three days to one. The co-differentiation occurs in the same basal medium, but rather than use a serum replacement mixture, a combination of L-ascorbic acid 2 phosphate sesquimagnesium salt, sodium selenite, sodium bicarbonate, human insulin, and

human holotransferin is used instead [39]. This modified medium is applied for four days in the compared with six days in the co-differentiation protocol. The following endothelial expansion and subculture phases, including media compositions, remained the same. The resulting cells require four fewer days to generate, but display similar barrier properties as assessed by TEER, efflux substrate accumulation assays, and immunocytochemistry (Table 1.1).

Further modifications of this accelerated protocol demonstrated that B-27 and N-2 media supplements, originally designed for neural differentiations [40,41], can be applied in place of the platelet poor plasma-derived serum in the endothelial expansion phase [42]. The B-27 supplement performed as well or better than supplementation with serum with respect to efflux transporter activity and TEER. In addition, reducing the supplement to only insulin, transferrin, and selenium was sufficient to differentiate cells having similar barrier properties. Taken together, these approaches provide a rapid, and chemically-defined-serum free method to differentiate hPSCs to BMEC-like cells.

1.4.1.3 Differentiation in Low Osmolarity Medium

Control of osmolarity during the differentiation has also been suspected to affect the quality of the differentiation. Therefore, during the induction phase, the basal medium was replaced with a low osmolarity alternative [43]. The differentiation continues in medium supplemented with platelet poor plasma-derived serum and bFGF. The authors claim that unlike the aforementioned protocols, the extended low osmolarity protocol generated BMEC-like cells without coculture, though neural cell presence was not explored. There is no selective matrix used for purification and the method can take up to twenty-one days before an optimal barrier forms. The resulting BMEC-like cells demonstrate TEER up to 1500 Ω-cm^2 and could be used to discriminate BBB passage of antibodies for targeted drug delivery. The cells express the vascular

markers von Willebrand factor and CD31, tight junction associated proteins occludin, claudin-5, and ZO-1, as well as the transporters P-gp and GLUT1 (Table 1.1). An RNA microarray for transport and BBB-related transcripts showed good transcriptional alignment with primary human BMECs. As of this writing, this method has only been applied to a single iPSC line.

1.4.1.4 Induction of BMEC Properties in Endothelial Progenitors

Two approaches for BMEC differentiation have been reported which first generate endothelial progenitors from hPSCs using general endothelial cell differentiation protocols and subsequently induce BMEC phenotypes by factor addition and co-culture with NVU cells [44,45]. The first demonstration of this approach treated hPSCs with a proprietary mesoderm induction medium with additional VEGF, Activin A, BMP4, and CHIR99021 for three days [45]. Cells were then driven to a vascular fate using proprietary vascular specification medium supplemented with VEGF and SB431542, a TGFβ signaling inhibitor, for eight days. The resulting endothelial progenitors were then sorted via magnetic activated cell sorting for CD31 expression and added to transwells containing hPSC-derived pericytes and primary human astrocytes and neurons. Compared to monoculture, co-culture improved TEER to a peak near 100 Ω-cm^2, increased expression of GLUT1 and occludin, and decreased caveolin 1 expression, demonstrating some acquisition of BBB character (Table 1.1). There was no observable increase in P-gp activity or resistance to small molecule transfer and TEER remained substantially below other BBB models, indicating less robust BBB functions.

In the second approach, immature endothelial progenitors were differentiated from hPSCs using medium containing BMP4, FGF-β, and VEGF to generate a mixed population of endothelial progenitors and non-endothelial cells. The population was sorted for PECAM-1 positive cells via magnetic activated cell sorting. The purified endothelial progenitor population

was then treated with endothelial growth medium that contained VEGF for one passage, followed by treatment with VEGF, Wnt3a, and RA over four passages [44]. This combination is similar to previously described protocols which combined Wnt and retinoic acid signaling. *In vivo,* VEGF and RA are released by or present in the neural tube during the invasion of nascent endothelial cells [38]. Wnt7a, but not Wnt3a, is suspected in BMEC specification *in vivo* [24,26], although any Wnt activation may be sufficient to elicit the transition *in vitro*. The resultant cells demonstrate expression of tight junction and endothelial cell markers including claudin-5, occludin, VE-cadherin, CD31, von Willebrand factor, and GLUT-1. However, TEER does not exceed 60 Ω-cm^2, similar to non-tissue specific endothelial cells [46]. In addition, the cells demonstrated P-gp activity through substrate accumulation assays, but this required the presence of pericyte co-culture. Taken together, the findings from these endothelial progenitor-based protocols indicate the difficulty in inducing BBB barrier properties onto immature endothelial cells as well as the value of pericytes in barrier induction. However, the similarity to *in vivo* developmental processes and high endothelial nature could make this a useful model for studying BBB development and identifying cues that can induce more robust BBB properties.

1.4.2 Comparison of BMEC-like Cells Using the Various Protocols

Above, and in Table 1.2, we have compared some of the phenotypes of the hPSC-derived BBB models arising from various differentiation protocols. hPSC-derived endothelial progenitors co-cultured with astrocytes, neurons, and hPSC-pericytes saw induction of barrier related protein transcripts, but at a lower level than those observed in co-differentiated hPSC-BMEC-like cells in coculture (Delsing et al. 2018). However, the BMECs derived from endothelial progenitors had much higher expression of endothelial transcripts, such as CD31 and VE-cadherin, than those generated from alternate routes. Instead, the co-differentiated BMEC-

like cells had a much higher expression of epithelial-associated transcripts (Delsing et al. 2018). Similarly, a recent study also noted the expression of epithelial associated transcripts in co-differentiated BMECs [47]. Given the epithelial signatures of BMECs derived through co-differentiation or directed differentiation routes, BMECs derived from induction of endothelial progenitors may prove more effective at modeling endothelial attributes such as inflammatory response or studying cues involved in endothelial development, despite their subpar barrier and transport properties [48,49]. Identifying routes to an hPSC derived BBB model with both barrier and endothelial properties is still an area of active research.

1.4.3 Cord Blood Progenitor Cell Models

In addition to the numerous hPSC derived models described above, others have used umbilical cord-derived progenitor cells to produce BMEC-like cells. A population of CD34+ mononuclear cells was isolated from cord blood, and when exposed to an endothelial cell growth medium, these expanding colonies progressed into endothelial cell progenitors that expressed CD31, VE-cadherin, and von Willebrand factor [19]. To induce BBB properties in these endothelial progenitors, they were exposed to co-culture with bovine brain pericytes [19]. The resulting endothelial cells displayed membrane polarization and P-gp activity, tight junction associated proteins occludin, claudin-5, and ZO-1 were expressed, and TEER was ~100-200 Ω-cm^2 (Table 1.1). Application of selective agonists or ligands once again implicated Wnt signaling in development of BBB characteristics due to pericyte co-culture, which aligns with *in vitro* [21] and *in vivo* [24,26] studies.

A similar protocol employed outgrowth of cord blood mononuclear cells in endothelial growth medium to generate cord blood endothelial progenitors [18]. In an effort to induce BBB properties, these endothelial progenitors were co-cultured with primary rat astrocytes. Compared

to monoculture endothelial progenitors, resultant BMEC-like cells possessed increased occludin, GLUT-1, and P-gp expression, and improved resistance to small molecule transport [18] (Table 1.1). Since these models are derived from donor umbilical cord blood, they are less amenable to the modeling of genetic disease than BMECs differentiated from patient-sourced iPSCs. However, this model has been used to measure the rates of transmigration of different CD4+ T helper cell subpopulations across the BBB, and comparison with transmigration across a model of the choroid plexus allowed the authors to conclude that different T helper cell populations may enter the CNS through different routes [50].

1.5 Co-culture Models

Thus far, we have described sourcing for stem cell-derived models. Monocultures are the simplest models and are oftentimes well suited for experimental goals. However, monoculture BMEC models lack several cellular components of the NVU. Therefore, there are situations where BMECs are combined with other NVU cell types in various co-culture architectures, particularly if the addition of NVU cells is required to induce a specialized property in the BMECs or if one wishes to examine intercellular communication between cell types of the NVU. In the CNS, various cells of the NVU induce and maintain BBB phenotypes in BMECs [38,51–53] (Figure 1.1).

Co-culture is often performed in a Transwell setting with some combination of neurons, pericytes, and astrocytes in the basolateral chamber and a BMEC model on the porous filter (Figure 1.2). These models are simple, scalable and allow paracrine signaling via release of soluble factors, but the cells are not able to form cell-cell contacts even when co-cultured cells are plated on the opposite side of a BMEC-containing filter [54]. There are many variations of models using the Transwell configuration with stem cell-derived BMECs and different

combinations of NVU cell types and sources. We will examine each co-cultured cell type in more detail below.

1.5.1 Neurons

Neurons are frequently added to the lower chamber of transwell-based BBB models (Table 1.2). Most approaches to date have employed hPSC-derived neurons that are generated from the EZ-sphere neuron differentiation method [55]. Using this approach, hPSCs are placed in a neural progenitor growth medium with additional bFGF, epidermal growth factor, and heparin. To generate the EZ-spheres that are reminiscent of primary human neurospheres, the cells are maintained in low attachment conditions, resulting in spheres of nestin expressing neural progenitors. These cells can be disassociated and treated with basal medium supplemented with B-27 without vitamin A to induce differentiation to neurons [56]. Co-culture of neurons with hPSC-BMECs has been shown to improve TEER above monoculture, and the impacts were additive with astrocyte co-culture [56] (Table 1.2).

1.5.2 Astrocytes

Astrocytes are also often used for co-culture because of their important roles in BBB induction and maintenance [38]. Since astrocyte end feet contact the vasculature *in vivo*, there have been some attempts to keep astrocytes in close proximity and encourage both paracrine and juxtacrine signaling [47]. Astrocytes, like neurons, have been generated in multiple ways, however most co-cultures have employed EZ-spheres to generate hPSC-astrocytes. The EZ-spheres can be treated with medium with RA and N-2 supplement [57], resulting in a cell population that, when disassociated and maintained in basal medium with N-2, forms astrocytes [56]. Though astrocytes are not present during the initial stages of development when invasion and BBB patterning occurs [38], primary rat astrocytes have been used to induce BMEC

phenotypes in cord blood-derived stem cells [18]. Co-culture of BMECs with hPSC-derived or primary astrocytes, often in addition to other NVU cell types, has been shown to result in increased TEER, resistance to small molecule permeability, and improved tight junction continuity [21,39,56] (Table 1.2). A recent study has also shown that brain region specific hPSC-astrocytes demonstrate different barrier inductive properties as assessed by TEER and small molecule permeability [58]. However, co-culture of hPSC-derived BMECs with a mixture of astrocytes and neurons does not appear to affect efflux transporter expression and activity [56].

1.5.3 Pericytes

Pericytes are found throughout the body in close association with capillaries. In the brain, pericytes have been shown to be indispensable to BBB function. Mouse experiments have indicated a marked increase in BBB permeability that correlates with a loss in pericyte number [59,60]. In addition, as described above, bovine brain pericytes have been used to induce BBB phenotypes in endothelial progenitors *in vitro* [19]. Moreover, co-culture of pericytes with hPSC-derived endothelial progenitors prior to endothelial maturation was necessary for acquisition of efflux transport activity [44] (Table 1.2).

When mesoderm-derived pericytes were directly plated on hPSC-BMECs to simulate the close proximity of pericytes to the vasculature, there were not significant changes in the barrier properties. However, the pericytes were found to self-organize to the basolateral side of the hPSC-derived BMEC-like cells [61]. While most pericytes in the body are derived from mesodermal lineages, forebrain pericytes derive from the neural crest, a multipotent ectodermal cell population [62]. Until recently, there were no established differentiation protocols for brain-specific pericyte-like cells. Two techniques have recently been reported to generate neural crest-derived hPSC-pericyte-like cells. Both approaches begin by generating neural crest stem cells.

One neural crest protocol accomplishes this through application of CHIR99021, B-27 supplement, and bovine serum albumin over five days [63]. The second neural crest protocol employs fifteen days of basal medium supplemented with L-ascorbic acid 2-phosphate magnesium, bFGF, heparin, sodium selenium, insulin, transferrin, CHIR99021, sodium bicarbonate, and TGFβ and BMP pathway inhibitors to generate neural crest stem cells [64]. The resulting neural crest stem cells can then be further differentiated to brain pericyte-like cells using a proprietary pericyte medium [65] or basal medium supplemented L-ascorbic acid 2-phosphate magnesium, sodium selenium, insulin, sodium bicarbonate, transferrin, heparin, and fetal bovine serum [64]. Neural crest-derived pericyte-like cells express many of the "pericyte-specific" transcripts identified by single cell RNA sequencing of *in vivo* brain pericytes [64,66]; however, there are differences between *in vivo* pericytes and neural crest-derived pericytes, as expected [64,65]. Neural crest-derived brain pericyte-like cells increased resistance to paracellular transport, as assessed by TEER and small molecule permeability, and decreased non-specific transcytosis in co-cultured hPSC-derived BMEC-like cells [64]. Also, despite the transcriptional differences between neural crest and mesoderm derived pericytes, both improved TEER compared to monoculture in a side by side comparison [65]. While TEER increases and reduction of permeability are seen with co-culture with other NVU cell types such as neurons and astrocytes, reduction in non-specific transcytosis was observed only with pericyte co-culture [54,64], indicating the importance of including pericytes in modelling applications where the mechanisms of transcellular transport are important. This reduction in transcytosis persisted for 24 hours after removal of pericytes from co-culture [54] (Table 1.2).

1.5.4 Multiple Cell Co-culture

To better mimic the *in vivo* NVU and account for crosstalk between the multiple cell types of the NVU, researchers have performed multi-cellular co-cultures with various models. These combined models often yield additive improvements in tight junction continuity and TEER [39,54,56], as well as retention of the unique nonspecific transcytosis phenotype induced by hPSC-brain pericytes [54] (Table 1.2). Other studies have reported more minimal impact of co-cultured NVU cells [67]. The application of pericytes, astrocytes, and neurons have also been used to induce modest BBB phenotypes in hPSC-derived endothelial progenitor cells [45]. In choosing the cell types to include in a BBB model, the added complexity of obtaining and organizing these cells should be balanced by improvements in model performance resulting from each cell type.

1.6 Application of Physiologically Relevant Structures and Forces to Stem Cell-Derived BBB Models

It is challenging to generate *in vitro* BBB models that capture all of the crucial elements of the *in vivo* niche. Although co-culture approaches described above allow paracrine signaling amongst NVU cells, there are other components missing, such as direct cell contact and shear flow forces. As microfluidics and organ-on-a-chip technologies have developed, more realistic models can now be developed. Microfluidic devices have been seeded with the stem cell-derived NVU cells to model human brain microvessels in a more physiologic environment. Moreover, stacked flow channels allow precise spatial and temporal regulation of the fluidic environment, maintaining optimal conditions on the vascular and parenchymal sides of the chips (Figure 1.2). These models certainly offer improved fidelity at the expense of increased complexity and cost.

BBB organ-on-a-chip models typically consist of two overlaid channels, separated by a non-cell permeable membrane which allows soluble factor exchange. Different NVU cell types are seeded in each channel to simulate the vasculature and parenchyma, much like the transwell co-cultures described above. Brain parenchyma is simulated by a combination of astrocytes, neurons, and pericytes [47,67,68] (Table 1.2). Some models have successfully demonstrated extension of astrocyte end feet through the membrane, more closely representing astrocyte-BMEC interactions *in vivo* [47]. These models have also been shown to successfully localize blood proteins to the apical side and restrict passage of small molecules [32,47,68].

In efforts to improve performance of BBB fluidic chips, design elements have been added to simulate other *in vivo* conditions. For instance, hPSC-pericytes have been embedded inside the gel to mimic the position of pericytes *in vivo* [61]. In addition, to more accurately mimic the environment in the developing brain, hypoxia was applied to differentiating BMEC-like cells followed by shear stress after differentiation. These conditions increased TEER and expression of endothelial markers and transporters in the resulting BMECs [69]. Hydrogel scaffolds have been constructed to create small capillaries lined with BMEC-like cells and NVU cells embedded in the surrounding hydrogel. Such constructs can capture the size of microvessels, flow shear stress, and physical positioning of BMECs relative to NVU cells [32,61,70,71]. Other work has focused on replacing the commonly used transwell membrane with more biologically relevant collagen I hydrogels [72]. In addition, iPSC-BMECs, iPSC-mural cells, and iPSC-astrocytes have been combined in a Matrigel scaffold and the combination allowed to mature for up to a month in an effort to better mimic the three dimensional structure of the NVU [70]. These models are useful when trying to mimic the behavior of cells within the *in vivo* BBB, understanding the mechanisms by which environmental cues regulate BBB behavior, as well as

potentially providing a more accurate model for drug penetration. Of course, complexity of these models will impact cost, throughput, and robustness. Thus, the experimental questions must warrant the added complexity of creating these advanced models.

1.7 Stem Cell-Derived Aggregate BBB Models

Several recent reports have described efforts toward the development of 3D cell aggregate models of the brain and NVU. In these models, cell types of interest are formed into small free-floating aggregates, reminiscent of an organ or tissue (Figure 1.2). A spheroid is assembled from somatic cells post-differentiation while an organoid is a co-differentiated 3D structure that spontaneously self-organizes [73]. These models provide direct cell-cell contact and 3D structures similar to those observed *in vivo* which fluidic and transwell models struggle to generate. In addition, organoid models most closely recapitulate BBB developmental stages, allowing us to study human CNS development *in vitro* and elucidate critical pathways regulating BBB induction.

Some neurovascular spheroids have been created entirely from primary cells [74]. Frequently these spheroids are constructed from primary astrocytes, pericytes, and endothelial cells [74–76] though more complicated combinations utilizing neurons and microglia have also been developed [77]. These spheroids spontaneously organize with a layer of endothelial cells surrounding the brain parenchymal cells. With endothelial cells on the exterior, the spheroids can be exposed to a compound of interest and accumulation within the brain “parenchyma” can be measured [74,75]. Recently, neurovascular spheroids have been assembled from stem cell-derived cells [78], including human bone marrow-derived mesenchymal stromal cells (MSCs), hPSC-derived neural progenitor cells, and hPSC-derived endothelial cells. The neurovascular spheroids were formed by fusion of neural, endothelial, and MSC aggregates. The neural

progenitors differentiate into astrocytes and neurons during spheroid maturation, demonstrated by the presence of mature neuron and astrocyte markers such as βIII-tubulin, S100β, GFAP, and vimentin. Imaging post-aggregation showed CD31 expressing endothelial cells were dispersed throughout the spheroids but did not form a perfusable vasculature. A similar approach to form neurovascular spheroids first seeded human neural progenitors in a polyethylene glycol-based scaffold [79]. Following spontaneous neuronal and glial formation and organization, hPSC-derived endothelial cells were added, followed three days later by hPSC-derived microglial precursors. The constructs contained a mixed population of astrocytes, neurons, as well as a capillary network identified by CD31 expressing cells. It is not clear whether these capillaries exhibited BBB barrier phenotypes. Another study integrated hPSC-derived endothelial cells into hPSC-derived neural organoids before implantation into mouse brains to perfuse and enlarge the organoid [80]. Despite the presence of mouse vasculature, the organoids contained capillary-like networks composed of cells expressing human-specific CD31. It is not clear whether these vessels exhibit BBB phenotypes.

Organoids are derived from a single source that proliferates and undergoes morphogenesis to generate tissue-like structures. While unvascularized brain organoids derived from hPSCs were among the first organoid systems developed [81], assembly of a brain organoid with an integrated NVU may be especially difficult because the cells of vascularized brain tissue originate from multiple germ layers [82]. Thus, it may be necessary to assemble the organoids from multiple progenitors to mimic the invasion of the vascular plexus into the developing neural tube. A recent report attempted to generate an NVU organoid [83]. hPSCs were gene edited to express ETV2, a transcription factor that regulates vascular development, under control of a doxycycline-inducible promoter. These cells were aggregated with unmodified hPSCs and then

treated with neural induction medium. Next, doxycyclin was applied *in situ* to reprogram the ETV2-inducible cells to an endothelial fate. The BBB phenotype of the integrated endothelial cells was examined to a limited extent, but further work is needed to better understand their properties. Generation of vascularized organoids is still in its infancy, but these models offer the ability to understand mechanisms of BBB morphogenesis during brain development and to model the roles of disease on NVU structure.

1.8 Applications of Stem Cell-derived BBB Models

1.8.1 Drug Permeability

Many of the stem cell-derived BBB models described in this chapter possess well developed tight junctions and exhibit substantial barrier properties. TEER is the standard metric for measuring tight junction quality *in vitro* and through systematic study, it was found that ~1000 Ω-cm^2 is sufficiently high to prevent aberrant paracellular leakage of both small and large molecules [7]. Thus, these models have been used to examine correlation between a drug permeability measured *in vitro* to the drug uptake *in vivo*, thereby demonstrating their potential utility in drug permeability estimation and screening [7,21,68,84]. For example, candidate drugs have been screened in an hPSC model to quickly eliminate those that may be unable to cross the BBB at therapeutically relevant rates [85]. Also, fluorescently-conjugated cancer targeting molecules, which could be potentially used for intraoperative brain cancer imaging, were evaluated for their permeabilities across hPSC models. The data indicated that the fluorophore conjugated molecules, unlike the parent molecule, had lower BBB permeability because of selective MRP and BCRP efflux [86]. Such information can help guide further drug development.

1.8.2 Studying Human BBB Development

One of the major benefits of stem cell-derived BBB models is the ability to elucidate the molecular and cellular mechanisms of human BBB development and maintenance of human BBB properties. For example, the co-culture of BMEC-like cells with hPSC-derived or primary brain pericytes resulted in a reduction of nonspecific transcytosis [54,64] while astrocyte or neuron co-culture did not have the same effect [54,56]. Also, hPSC-BMEC differentiations can be used to explore human BBB development in a tractable *in vitro* setting. As discussed in section 1.5.1.1, induction of GLUT1 expression in differentiating BMECs correlated with nuclear localization of β-catenin [21]. Conversely, Wnt inhibition during endothelial progenitor induction increased permeability compared to vehicle controls [19]. These data suggest that, like in mouse, Wnt signaling is important to the development of the human BBB. In addition, RA has been shown to improve the quality of the BMEC barrier [33,44], consistent with findings in mouse models [37]. Subsequent analysis of specific retinoic acid receptor agonists and antagonists revealed that RARα, RARγ, and RXRα activation mimicked the effects of RA application [87].

Stem cell derived *in vitro* BBB models also permit investigation of factors that induce and regulate BMEC phenotype. In many types of endothelial cells, shear stress from blood flow is well known to cause a change in morphology and orientation with direction to the flow [88–91]. However, it has been observed that BMEC-like cells do not undergo any substantial alignment or morphological change with respect to shear stress [92]. This is consistent with immortalized BMECs [93] and seems to indicate that BMECs respond uniquely to shear stress, although the physiologic significance of this difference is not yet understood.

1.8.3 Modeling BBB Disease

Another major benefit of stem cell-derived models over other *in vitro* BBB models is the ability to model genetically-linked human diseases by employing patient-sourced or gene-edited iPSCs. While many CNS diseases are thought to be associated with BBB dysfunction, it has been difficult to mechanistically investigate this dysfunction *in vitro*. Since iPSC lines can be generated from patients with disease-related genotypes, subsequent differentiation into iPSC-BMECs and other NVU cells can allow *in vitro* analysis of human cells carrying disease-causing mutations, which often result in cells that exhibit disease-associated phenotypes [94]. Genome editing tools can also be used to either introduce or correct mutations to an iPSC line, allowing direct exploration of the impacts of a single mutation on the BBB without the confounding factors of patient-to-patient variability or line-to-line iPSC variability.

As an example, psychomotor retardation, a disease caused by inactivating mutations of thyroid hormone transporter MCT8 [95] results in a thyroid hormone deficit in the brain, leading to serious developmental deficits. A clear genetic link to molecular transport, which can readily be quantified *in vitro*, made this disease an ideal test case for patient-sourced iPSC-derived BBB models. While MCT8-deficient iPSC-derived neural cells demonstrated thyroid hormone responsiveness, transport across the iPSC-BMECs was impaired [85], suggesting that access to thyroid hormone in the developing brain was restricted due to a dysfunctional BBB. In another study, analysis of different neurodegenerative disease state derived iPSC lines (Alzheimer's disease, Huntington's disease, Parkinson's disease, and amyotrophic lateral sclerosis) consistently showed that disease iPSC-BMECs exhibited impaired efflux transport activity when compared to healthy controls. Reductions in tight junction quality were also observed in the disease models [96], and these data suggest that a weakened BBB could contribute to disease

progression [96,97]. To explore childhood cerebral adrenoleukodystrophy, characterized by BBB breakdown through a well-known mutation in *ABCD1*, hPSC-BMECs from patient and healthy iPSC lines were used and demonstrated a reduction in tight junction quality as measured by increased frayed tight junctions and a reduction in TEER [98]. Patient-sourced iPSCs were also used to investigate BBB function in Huntington's Disease (HD), a debilitating neurodegenerative disease caused by a mutation in the HTT gene [99]. HD BMECs exhibited discontinuous tight junctions as well as dysregulation in angiogenesis and activation of TGFβ1, Wnt3a, GLI2, ANGPT2 signaling cascades suggesting significant BBB dysfunction [97]. As mentioned previously, model complexity should be justified by the experimental question. For example, BBB dysfunction in Alzheimer's disease (AD) is thought to be a result of interactions between several cells of the NVU, warranting a multicellular three-dimensional BMEC model. The resulting model using iPSCs carrying different *APOE* alleles was employed to assess the deposition of amyloid β, a protein known to accumulate in AD progression, and the authors concluded that that the *APOE4* genotype led to increased amyloid- accumulation as a result of pericyte effects [70].

In addition to modeling genetic diseases, stem cell-derived models of the BBB have been used to analyze the mechanism of brain invasion in bacterial meningitis. The application of Group B *Streptococcus*, a known pathogen responsible for meningitis, to a monolayer of hPSC-BMECs resulted in a reduction of protein and transcript levels of occludin, claudin-5, and ZO-1, three critical tight junction associated proteins [48] as well as in P-gp, a major efflux transporter [100]. Another study applied *Neisseria meningitidis,* the pathogen responsible for a subtype of meningococcal meningitis, to hPSC derived BMEC-like cells [49]. *Neisseria* infection resulted in almost total loss of TEER within 48 hours, as well as increased permeability to small

molecules. This impact was directly observed via immunocytochemistry and corresponded to a reduction in TJP1and CLDN5 transcripts. Infection also increased secretion of the cytokines RANTES, IFN-γ, and IL-8 after 24 hours, indicating an inflammatory response of the hPSC derived BMEC-like cells.

1.9 Conclusion

Stem cell models of the human BBB provide advantages compared to other *in vitro* models or *in vivo* animal studies. In particular, human stem cells provide a renewable source of human BMEC-like cells and other cell types in the NVU, enabling a consistent product and scalable models. hPSCs in particular facilitate modeling genetic diseases that influence the BBB.

Human stem cell-derived BBB models have been implemented in various configurations. Transwell models offer ease of use, and high expandability which are useful for screening studies. While these models can capture interactions between BMECs and other NVU cell types mediated by soluble factors, direct contact between cells and flow are difficult to implement in transwells. Fluidic models capture dynamic flow of the *in vivo* microenvironment and enable precise spatial and temporal control over application of soluble factors, however they are not as easily scaled. Brain spheroids and organoids offer the potential to study BBB morphogenesis, however assessing the barrier properties of the BMECs is more complicated than other configurations. To date, proof-of-concept studies of generating vascular networks in neural aggregates indicate promise for these models, but additional work is needed to recapitulate development of bona fide neurovascular organoids containing mesoderm and ectoderm-derived cell types.

hPSC-derived BBB models can advance efforts for accurate, human relevant *in vitro* screening of novel neurotherapeutics. The high passive resistance of these models and polarized

expression of BBB transporters make them especially adept at eliminating prospective candidates that cannot penetrate the human BBB and developing trans-BBB delivery strategies. hPSC-derived BBB models also provide a useful tool for studying molecular and cellular mechanisms of BBB induction and regulation, complementing animal models. Disease models using patient-derived or gene edited iPSCs have thus far focused on genetic diseases impacting BMECs and microbial disease. There is significant potential in expanding these disease models to investigate the roles of different NVU cell types in more complex neurodegenerative diseases.

1.10 Figures

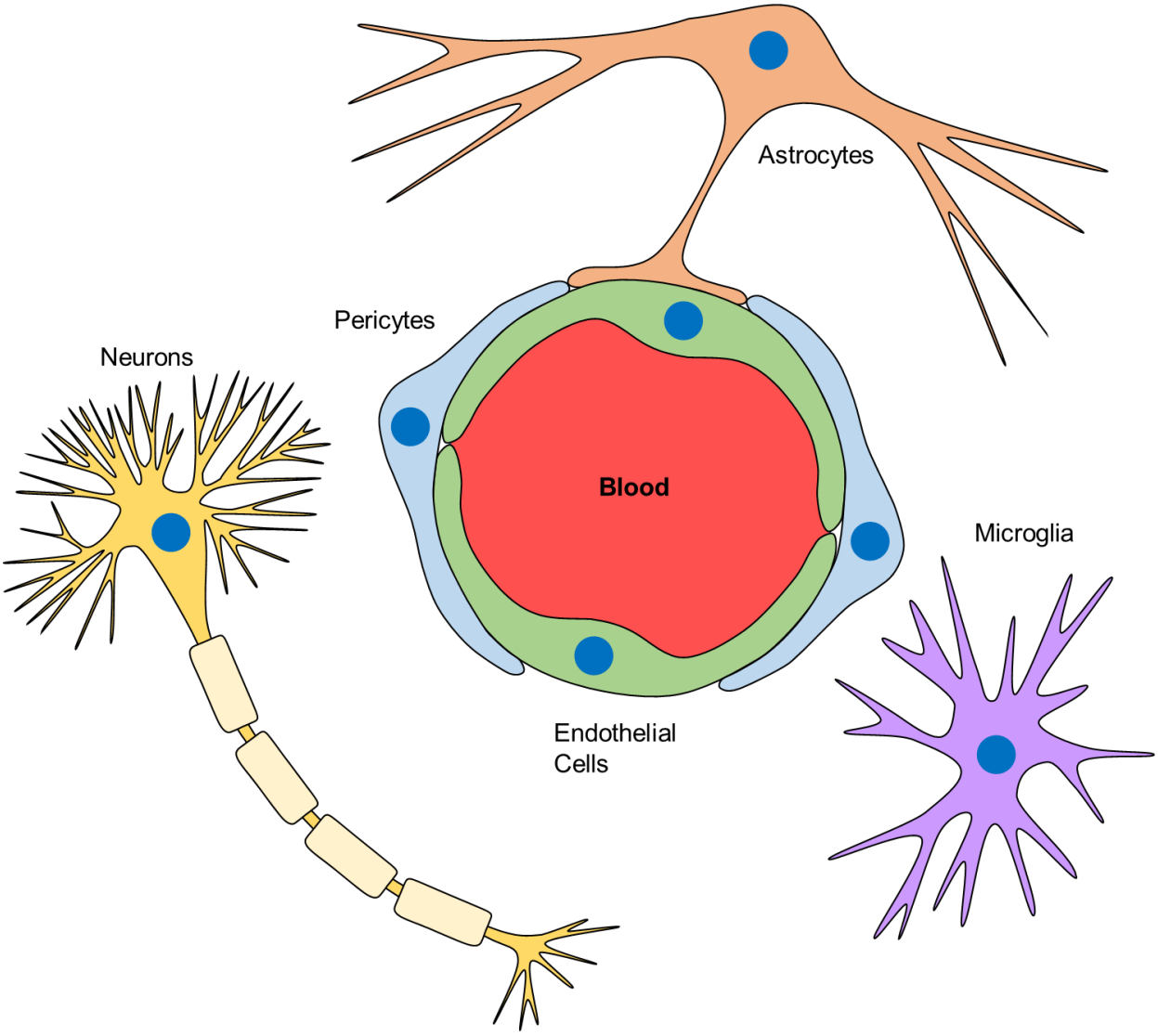

Figure 1.1 NVU diagram. The NVU is composed of BMECs that possess the properties most often associated with BBB function as well as surrounding cells such as pericytes which share a basement membrane with BMECs, astrocytes whose endfeet are intimately associated with microvessels, neurons and microglia which communicate without contact with BMECs.

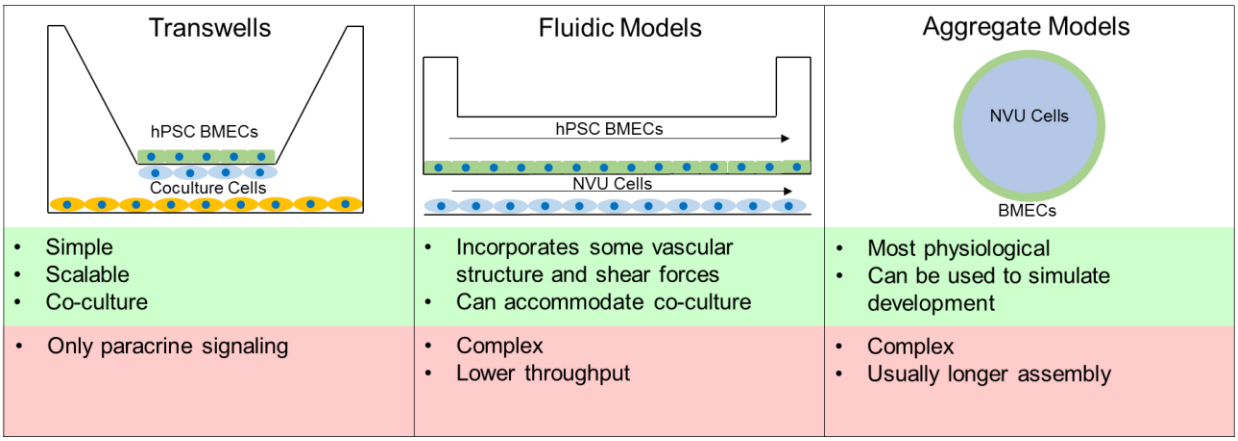

Figure 1.2 Examples of the different architectures of BBB models. Transwells can be utilized in monoculture or co-culture formats, with hPSC-BMECs on the top of the membrane and co-cultured cells on the bottom of the membrane and/or on the bottom of the well. The Fluidic model chip shows a co-culture enabled chip, though single channel chips are also widely employed. The aggregate model gives an example of an aggregated BBB spheroid with a shell of BMECs organized around a core of NVU cells. However, not all aggregates exhibit this localization.

1.11 Tables

Table 1.1 Summary of human stem cell-derived BMEC properties

Refs	Endothelial Proteins	Tight Junction Associated Proteins	Efflux Transporters	Other BBB Proteins	TEER	Efflux Activity Measured	Additional Assays
[21,27]	vWF, VE-cad, PECAM-1	ZO-1, Ocln, Cldn-5	P-gp, BCRP, MRP1	GLUT-1	100-2000 Ω-cm^2 (RA Dependent)	P-gp, BCRP, MRP1	Tube formation, small/large molecule and drug permeability
[39,42]	PECAM-1, VE-cad	Ocln, Cldn-5		GLUT-1	2000-8000 Ω-cm^2	P-gp, MRP	Small molecule permeability, TEER duration,
[43]	PECAM-1, vWF	ZO-1, Ocln, Cldn-5	P-gp	GLUT-1	400-1500 Ω-cm^2		Drug permeability, sucrose permeability
[30]	PECAM-1, VE-cad, Flk-1	ZO-1, Ocln, Cldn-5	P-gp, BCRP, MRP1	GLUT-1	2000-3000 Ω-cm^2	P-gp, BCRP, MRP1	Tube formation, small molecule permeability
[101]	vWF, VE-cad, PECAM-1	ZO-1, Ocln, Cldn-5		GLUT-1	~100 Ω-cm^2	P-gp, BCRP	Drug permeability, small molecule permeability
[44]	vWF, VE-cad, Tie2	ZO-1, Ocln, Cldn-5	P-gp	GLUT-1	~60 Ω-cm^2	P-gp	
[19]	JAM-A	ZO-1, Ocln, Cldn-5	P-gp, BCRP, MRP1, MRP2, MRP4, MRP5	RAGE, LRP1	~60 Ω-cm^2		Small and large molecule and drug permeability
[18]	VE-cad	ZO-1, Ocln, Cldn-5, Cldn-3	P-gp	GLUT-1		P-gp	Small and large molecule permeability, tube formation

Cldn-5 = Claudin-5, Cldn-3 = Claudin-3, Ocln = occludin, VE-cad = VE-cadherin, vWF = von Willebrand factor, RA = retinoic acid

Table 1.2 Summary of hPSC-BMEC and NVU cell co-culture conditions

Reference	NVU Cells	Architecture	Changes Observed
[21]	r A	Transwell	Increased TEER
[33]	h NPC, h P	Transwell	Increased TEER
[39]	h A/P	Transwell	Increased TEER with all cell types, further improvement with both
[42]	hPSC A	Transwell	Increased TEER
[19]	b P	Transwell	Used to drive cord-blood derived cells to BBB phenotypes like decreased permeability and increased efflux transporter activity
[18]	r A	Transwell	Used to drive cord-blood derived cells to BBB phenotypes like decreased permeability
[45]	hPSC Mesoderm P, h A, h N	Transwell	Induction of BBB properties in endothelial progenitors, improvement of TEER, improved resistance to small molecules
[44]	h P	Transwell	Necessary to see efflux transport activity in patterned hPSC-EPC derived BMECs
[56]	hPSC N/A, r A	Transwell	TEER improvements, continuous tight junctions, no improvement of P-gp activity or increase in tight junction protein levels
[54]	hPSC N/A/P	Transwell	As previous, with pericyte induced reduction of non-receptor mediated transcytosis
[64]	hPSC Neural Crest P	Transwell	Improvement in TEER, resistance to small molecule permeability, lowered non-receptor mediated transcytosis
[65]	hPSC-Mesoderm and Neural Crest P, h Neural Crest P	Transwell	Improvements in TEER with mesoderm and neural crest pericytes, tube formation assay
[58]	h A	Transwell	Investigation of the effects of region specific astrocytes on TEER, small molecule permeability, and tight junction continuity
[50]	h T Cells	Transwell	Selective T cell transmigration was observed
[67]	hPSC NSC, h A, h P, h NSC	Transwell	Increased TEER and assessed transcript and protein level changes
[61]	hPSC Mesoderm P	Direct + Fluidic	No TEER change, rescue of TEER under stress
[47]	hPSC A/N	Fluidic	Resistance to blood-to-brain transport in chip
[69]	h P/A	Fluidic	Improved BBB relevant transcripts when applied with hypoxia
[102]	hPSC A	Fluidic	No changes in TEER observed on coculture with astrocytes suspended in 3D hydrogel
[70]	hPSC Mesoderm P, hPSC A,	Direct	Improved TEER compared to monocultured controls

r = rat, h = human, b = bovine, hPSC = human pluripotent stem cell derived, A = astrocyte, P = pericyte, N = neuron, NSC = neural stem cell, NPC = neural progenitor cell

1.12 References

1. Foreman KL, Palecek SP, Shusta EV. Chapter 9: Human in vitro Blood-Brain Barrier Models Derived from Stem Cells. In: De Lange ECM, Hammarlund-Udenaes M, Thorne RG, editors. Drug Delivery to the Brain: Physiological Concepts, Methodologies and Approaches [Internet]. Cham: Springer International Publishing; 2022 [cited 2023 Jul 10]. Available from: https://link.springer.com/10.1007/978-3-030-88773-5

2. Pardridge WM. The Blood-Brain Barrier: Bottleneck in Brain Drug Development. 2005;2:12.

3. Helms HC, Abbott NJ, Burek M, Cecchelli R, Couraud P-O, Deli MA, et al. In vitro models of the blood–brain barrier: An overview of commonly used brain endothelial cell culture models and guidelines for their use. J Cereb Blood Flow Metab. 2016;36:862–90.

4. Weksler BB, Subileau EA, Perrière N, Charneau P, Holloway K, Leveque M, et al. Blood-brain barrier-specific properties of a human adult brain endothelial cell line. The FASEB Journal. 2005;19:1872–4.

5. Butt AM, Jones HC, Abbott NJ. Electrical Resistance Across the Blood-Brain Barrier in Anaesthetized Rats: A Developmental Study. Journal of Physiology. 1990;429:47–62.

6. Srinivasan B, Kolli AR, Esch MB, Abaci HE, Shuler ML, Hickman JJ. TEER Measurement Techniques for In Vitro Barrier Model Systems. J Lab Autom. 2015;20:107–26.

7. Mantle JL, Min L, Lee KH. Minimum Transendothelial Electrical Resistance Thresholds for the Study of Small and Large Molecule Drug Transport in a Human *in Vitro* Blood–Brain Barrier Model. Molecular Pharmaceutics. 2016;13:4191–8.

8. Aday S, Cecchelli R, Hallier-Vanuxeem D, Dehouck MP, Ferreira L. Stem Cell-Based Human Blood–Brain Barrier Models for Drug Discovery and Delivery. Trends in Biotechnology. 2016;34:382–93.

9. Song HW, Foreman KL, Gastfriend BD, Kuo JS, Palecek SP, Shusta EV. Transcriptomic comparison of human and mouse brain microvessels. Sci Rep. 2020;10:12358.

10. Uchida Y, Ohtsuki S, Katsukura Y, Ikeda C, Suzuki T, Kamiie J, et al. Quantitative targeted absolute proteomics of human blood-brain barrier transporters and receptors: Protein levels of transporters at human BBB. Journal of Neurochemistry. 2011;117:333–45.

11. Ohtsuki S, Ikeda C, Uchida Y, Sakamoto Y, Miller F, Glacial F, et al. Quantitative Targeted Absolute Proteomic Analysis of Transporters, Receptors and Junction Proteins for Validation of Human Cerebral Microvascular Endothelial Cell Line hCMEC/D3 as a Human Blood–Brain Barrier Model. Mol Pharmaceutics. 2013;10:289–96.

12. Chagastelles PC, Nardi NB. Biology of stem cells: an overview. Kidney International Supplements. 2011;1:63–7.

13. Nagy A, Gocza E, Diaz EM, Prideaux VR, Ivanyi E, Markkl'La M, et al. Embryonic stem cells alone are able to support fetal development in the mouse. Development. 1990;110:815–21.

14. Thomson JA. Embryonic Stem Cell Lines Derived from Human Blastocysts. Science. 1998;282:1145–7.

15. Takahashi K, Yamanaka S. Induction of Pluripotent Stem Cells from Mouse Embryonic and Adult Fibroblast Cultures by Defined Factors. Cell. 2006;126:663–76.

16. Yu J, Vodyanik MA, Smuga-Otto K, Antosiewicz-Bourget J, Frane JL, Tian S, et al. Induced Pluripotent Stem Cell Lines Derived from Human Somatic Cells. 2007;318:5.

17. Bailey, AS, Jiang S, Afentoulis M, Baumann CI, Schroider DA, Olson SB, et al. Transplanted adult hematopoietic stems cells differentiate into functional endothelial cells. Blood. 2004;103.

18. Boyer-Di Ponio J, El-Ayoubi F, Glacial F, Ganeshamoorthy K, Driancourt C, Godet M, et al. Instruction of Circulating Endothelial Progenitors In Vitro towards Specialized Blood-Brain Barrier and Arterial Phenotypes. Deli MA, editor. PLoS ONE. 2014;9:e84179.

19. Cecchelli R, Aday S, Sevin E, Almeida C, Culot M, Dehouck L, et al. A Stable and Reproducible Human Blood-Brain Barrier Model Derived from Hematopoietic Stem Cells. Klein R, editor. PLoS ONE. 2014;9:e99733.

20. Bauer H-C, Bauer H. Neural Induction of the Blood–Brain Barrier: Still an Enigma. Cellular and Molecular Neurobiology. 1997;20:13–28.

21. Lippmann ES, Azarin SM, Kay JE, Nessler RA, Wilson HK, Al-Ahmad A, et al. Derivation of blood-brain barrier endothelial cells from human pluripotent stem cells. Nature Biotechnology. 2012;30:783–91.

22. Lippmann ES, Al-Ahmad A, Palecek SP, Shusta EV. Modeling the blood–brain barrier using stem cell sources. Fluids and Barriers of the CNS. 2013;10:2.

23. Cho C, Smallwood PM, Nathans J. Reck and Gpr124 Are Essential Receptor Cofactors for Wnt7a/Wnt7b-Specific Signaling in Mammalian CNS Angiogenesis and Blood-Brain Barrier Regulation. Neuron. 2017;95:1056-1073.e5.

24. Daneman R, Agalliu D, Zhou L, Kuhnert F, Kuo CJ, Barres BA. Wnt/ -catenin signaling is required for CNS, but not non-CNS, angiogenesis. Proceedings of the National Academy of Sciences. 2009;106:641–6.

25. Liebner S, Corada M, Bangsow T, Babbage J, Taddei A, Czupalla CJ, et al. Wnt/β-catenin signaling controls development of the blood–brain barrier. J Cell Biol. 2008;183:409–17.

26. Stenman JM, Rajagopal J, Carroll TJ, Ishibashi M, McMahon J, McMahon AP. Canonical Wnt Signaling Regulates Organ-Specific Assembly and Differentiation of CNS Vasculature. Science. 2008;322:1247–50.

27. Stebbins MJ, Wilson HK, Canfield SG, Qian T, Palecek SP, Shusta EV. Differentiation and characterization of human pluripotent stem cell-derived brain microvascular endothelial cells. Methods. 2016;101:93–102.

28. Katt ME, Xu ZS, Gerecht S, Searson PC. Human Brain Microvascular Endothelial Cells Derived from the BC1 iPS Cell Line Exhibit a Blood-Brain Barrier Phenotype. Deli MA, editor. PLOS ONE. 2016;11:e0152105.

29. Wilson HK, Canfield SG, Hjortness MK, Palecek SP, Shusta EV. Exploring the effects of cell seeding density on the differentiation of human pluripotent stem cells to brain microvascular endothelial cells. Fluids and Barriers of the CNS. 2015;12:13.

30. Qian T, Maguire SE, Canfield SG, Bao X, Olson WR, Shusta EV, et al. Directed differentiation of human pluripotent stem cells to blood-brain barrier endothelial cells. Science Advances. 2017;3:e1701679.

31. Wilson HK, Faubion MG, Hjortness MK, Palecek SP, Shusta EV. Cryopreservation of Brain Endothelial Cells Derived from Human Induced Pluripotent Stem Cells Is Enhanced by Rho-Associated Coiled Coil-Containing Kinase Inhibition. Tissue Engineering Part C: Methods. 2016;22:1085–94.

32. Grifno GN, Farrell AM, Linville RM, Arevalo D, Kim JH, Gu L, et al. Tissue-engineered blood-brain barrier models via directed differentiation of human induced pluripotent stem cells. Sci Rep. 2019;9:13957.

33. Lippmann ES, Al-Ahmad A, Azarin SM, Palecek SP, Shusta EV. A retinoic acid-enhanced, multicellular human blood-brain barrier model derived from stem cell sources. Scientific Reports. 2014;4:4160.

34. Schubert M, Holland ND, Laudet V, Holland LZ. A retinoic acid-Hox hierarchy controls both anterior/posterior patterning and neuronal specification in the developing central nervous system of the cephalochordate amphioxus. Developmental Biology. 2006;296:190–202.

35. Bonney S, Harrison-Uy S, Mishra S, MacPherson AM, Choe Y, Li D, et al. Diverse Functions of Retinoic Acid in Brain Vascular Development. Journal of Neuroscience. 2016;36:7786–801.

36. Bonney S, Dennison BJC, Wendlandt M, Siegenthaler JA. Retinoic Acid Regulates Endothelial β-catenin Expression and Pericyte Numbers in the Developing Brain Vasculature. Front Cell Neurosci. 2018;12:476.

37. Mizee MR, Wooldrik D, Lakeman KAM, van het Hof B, Drexhage JAR, Geerts D, et al. Retinoic Acid Induces Blood-Brain Barrier Development. Journal of Neuroscience. 2013;33:1660–71.

38. Obermeier B, Daneman R, Ransohoff RM. Development, maintenance and disruption of the blood-brain barrier. Nat Med. 2013;19:1584–96.

39. Hollmann EK, Bailey AK, Potharazu AV, Neely MD, Bowman AB, Lippmann ES. Accelerated differentiation of human induced pluripotent stem cells to blood–brain barrier endothelial cells. Fluids Barriers CNS. 2017;14:9.

40. Bottenstein JE, Sato GH. Growth of a rat neuroblastoma cell line in serum-free supplemented medium. Proceedings of the National Academy of Sciences. 1979;76:514–7.

41. Brewer GJ, Cotman CW. Survival and growth of hippocampal neurons in defined medium at low density: advantages of a sandwich culture technique or low oxygen. Brain Research. 1989;494:65–74.

42. Neal EH, Marinelli NA, Shi Y, McClatchey PM, Balotin KM, Gullett DR, et al. A Simplified, Fully Defined Differentiation Scheme for Producing Blood-Brain Barrier Endothelial Cells from Human iPSCs. Stem Cell Reports. 2019;12:1380–8.

43. Ribecco-Lutkiewicz M, Sodja C, Haukenfrers J, Haqqani AS, Ly D, Zachar P, et al. A novel human induced pluripotent stem cell blood-brain barrier model: Applicability to study antibody-triggered receptor-mediated transcytosis. Scientific Reports. 2018;8:1873.

44. Praça C, Rosa SC, Sevin E, Cecchelli R, Dehouck M-P, Ferreira LS. Derivation of Brain Capillary-like Endothelial Cells from Human Pluripotent Stem Cell-Derived Endothelial Progenitor Cells. Stem Cell Reports. 2019;13:599–611.

45. Delsing L, Dönnes P, Sánchez J, Clausen M, Voulgaris D, Falk A, et al. Barrier Properties and Transcriptome Expression in Human iPSC-Derived Models of the Blood-Brain Barrier: Barrier Properties and Transcriptome Expression in Human iPSC-Derived Models. Stem Cells. 2018;36:1816–27.

46. Tschugguel W, Zhegu Z, Gajdzik L, Maier M, Binder BR, Graf J. High precision measurement of electrical resistance across endothelial cell monolayers. Pflügers Arch - Eur J Physiol. 1995;430:145–7.

47. Vatine GD, Barrile R, Workman MJ, Sances S, Barriga BK, Rahnama M, et al. Human iPSC-Derived Blood-Brain Barrier Chips Enable Disease Modeling and Personalized Medicine Applications. Cell Stem Cell. 2019;24:995-1005.e6.

48. Kim BJ, Bee OB, McDonagh MA, Stebbins MJ, Palecek SP, Doran KS, et al. Modeling Group B *Streptococcus* and Blood-Brain Barrier Interaction by Using Induced Pluripotent Stem Cell-Derived Brain Endothelial Cells. D'Orazio SEF, editor. mSphere. 2017;2:e00398-17, /msphere/2/6/mSphere0398-17.atom.

49. Martins Gomes SF, Westermann AJ, Sauerwein T, Hertlein T, Förstner KU, Ohlsen K, et al. Induced Pluripotent Stem Cell-Derived Brain Endothelial Cells as a Cellular Model to Study Neisseria meningitidis Infection. Front Microbiol. 2019;10:1181.

50. Nishihara H, Soldati S, Mossu A, Rosito M, Rudolph H, Muller WA, et al. Human CD4+ T cell subsets differ in their abilities to cross endothelial and epithelial brain barriers in vitro. Fluids Barriers CNS. 2020;17:3.

51. Engelhardt B, Liebner S. Novel insights into the development and maintenance of the blood–brain barrier. Cell Tissue Res. 2014;355:687–99.

52. Gastfriend BD, Palecek SP, Shusta EV. Modeling the blood–brain barrier: Beyond the endothelial cells. Current Opinion in Biomedical Engineering. 2018;5:6–12.

53. Hawkins BT, Davis TP. The Blood-Brain Barrier/Neurovascular Unit in Health and Disease. Pharmacol Rev. 2005;57:173–85.

54. Canfield SG, Stebbins MJ, Faubion MG, Gastfriend BD, Palecek SP, Shusta EV. An isogenic neurovascular unit model comprised of human induced pluripotent stem cell-derived brain microvascular endothelial cells, pericytes, astrocytes, and neurons. Fluids Barriers CNS. 2019;16:25.

55. Ebert AD, Shelley BC, Hurley AM, Onorati M, Castiglioni V, Patitucci TN, et al. EZ spheres: A stable and expandable culture system for the generation of pre-rosette multipotent stem cells from human ESCs and iPSCs. Stem Cell Research. 2013;10:417–27.

56. Canfield SG, Stebbins MJ, Morales BS, Asai SW, Vatine GD, Svendsen CN, et al. An isogenic blood-brain barrier model comprising brain endothelial cells, astrocytes, and neurons derived from human induced pluripotent stem cells. Journal of Neurochemistry. 2017;140:874–88.

57. Sareen D, Gowing G, Sahabian A, Staggenborg K, Paradis R, Avalos P, et al. Human induced pluripotent stem cells are a novel source of neural progenitor cells (iNPCs) that migrate and integrate in the rodent spinal cord: Human neural progenitor cells. J Comp Neurol. 2014;522:2707–28.

58. Bradley RA, Shireman J, McFalls C, Choi J, Canfield SG, Dong Y, et al. Regionally specified human pluripotent stem cell-derived astrocytes exhibit different molecular signatures and functional properties. Development. 2019;146:dev170910.

59. Armulik A, Genové G, Mäe M, Nisancioglu MH, Wallgard E, Niaudet C, et al. Pericytes regulate the blood–brain barrier. Nature. 2010;468:557–61.

60. Daneman R, Zhou L, Kebede AA, Barres BA. Pericytes are required for blood–brain barrier integrity during embryogenesis. Nature. 2010;468:562–6.

61. Jamieson JJ, Linville RM, Ding YY, Gerecht S, Searson PC. Role of iPSC-derived pericytes on barrier function of iPSC-derived brain microvascular endothelial cells in 2D and 3D. Fluids Barriers CNS. 2019;16:15.

62. Adams MS, Bronner-Fraser M. Review: The Role of Neural Crest Cells in the Endocrine System. Endocr Pathol. 2009;20:92–100.

63. Leung AW, Murdoch B, Salem AF, Prasad MS, Gomez GA, García-Castro MI. WNT/β-catenin signaling mediates human neural crest induction via a pre-neural border intermediate. Development. 2016;143:398–410.

64. Stebbins MJ, Gastfriend BD, Canfield SG, Lee M-S, Richards D, Faubion MG, et al. Human pluripotent stem cell-derived brain pericyte-like cells induce blood-brain barrier properties. Science Advances. 2019;5.

65. Faal T, Phan DTT, Davtyan H, Scarfone VM, Varady E, Blurton-Jones M, et al. Induction of Mesoderm and Neural Crest-Derived Pericytes from Human Pluripotent Stem Cells to Study Blood-Brain Barrier Interactions. Stem Cell Reports. 2019;12:451–60.

66. Vanlandewijck M, He L, Mäe MA, Andrae J, Ando K, Del Gaudio F, et al. A molecular atlas of cell types and zonation in the brain vasculature. Nature. 2018;554:475–80.

67. Appelt-Menzel A, Cubukova A, Günther K, Edenhofer F, Piontek J, Krause G, et al. Establishment of a Human Blood-Brain Barrier Co-culture Model Mimicking the Neurovascular Unit Using Induced Pluri- and Multipotent Stem Cells. Stem Cell Reports. 2017;8:894–906.

68. Wang YI, Abaci HE, Shuler ML. Microfluidic blood-brain barrier model provides in vivo-like barrier properties for drug permeability screening: Microfluidic BBB Model Mimics In Vivo Properties. Biotechnol Bioeng. 2017;114:184–94.

69. Park T-E, Mustafaoglu N, Herland A, Hasselkus R, Mannix R, FitzGerald EA, et al. Hypoxia-enhanced Blood-Brain Barrier Chip recapitulates human barrier function and shuttling of drugs and antibodies. Nat Commun. 2019;10:2621.

70. Blanchard JW, Bula M, Davila-Velderrain J, Akay LA, Zhu L, Frank A, et al. Reconstruction of the human blood–brain barrier in vitro reveals a pathogenic mechanism of APOE4 in pericytes. Nat Med. 2020;26:952–63.

71. Faley SL, Neal EH, Wang JX, Bosworth AM, Weber CM, Balotin KM, et al. iPSC-Derived Brain Endothelium Exhibits Stable, Long-Term Barrier Function in Perfused Hydrogel Scaffolds. Stem Cell Reports. 2019;12:474–87.

72. Ruano-Salguero JS, Lee KH. Efflux Pump Substrates Shuttled to Cytosolic or Vesicular Compartments Exhibit Different Permeability in a Quantitative Human Blood–Brain Barrier Model. Mol Pharmaceutics. 2018;15:5081–8.

73. Lancaster MA, Knoblich JA. Organogenesis in a dish: Modeling development and disease using organoid technologies. Science. 2014;345:1247125–1247125.

74. Bergmann S, Lawler SE, Qu Y, Fadzen CM, Wolfe JM, Regan MS, et al. Blood–brain-barrier organoids for investigating the permeability of CNS therapeutics. Nat Protoc. 2018;13:2827–43.

75. Cho C-F, Wolfe JM, Fadzen CM, Calligaris D, Hornburg K, Chiocca EA, et al. Blood-brain-barrier spheroids as an in vitro screening platform for brain-penetrating agents. Nat Commun. 2017;8:15623.

76. Urich E, Patsch C, Aigner S, Graf M, Iacone R, Freskgård P-O. Multicellular Self-Assembled Spheroidal Model of the Blood Brain Barrier. Sci Rep. 2013;3:1500.

77. Nzou G, Wicks RT, Wicks EE, Seale SA, Sane CH, Chen A, et al. Human Cortex Spheroid with a Functional Blood Brain Barrier for High-Throughput Neurotoxicity Screening and Disease Modeling. Sci Rep. 2018;8:7413.

78. Song L, Yuan X, Jones Z, Griffin K, Zhou Y, Ma T, et al. Assembly of Human Stem Cell-Derived Cortical Spheroids and Vascular Spheroids to Model 3-D Brain-like Tissues. Sci Rep. 2019;9:5977.

79. Schwartz MP, Hou Z, Propson NE, Zhang J, Engstrom CJ, Costa VS, et al. Human pluripotent stem cell-derived neural constructs for predicting neural toxicity. Proc Natl Acad Sci USA. 2015;112:12516–21.

80. Pham MT, Pollock KM, Rose MD, Cary WA, Stewart HR, Zhou P, et al. Generation of human vascularized brain organoids: NeuroReport. 2018;29:588–93.

81. Lancaster MA, Renner M, Martin C-A, Wenzel D, Bicknell LS, Hurles ME, et al. Cerebral organoids model human brain development and microcephaly. Nature. 2013;501:373–9.

82. McCauley HA, Wells JM. Pluripotent stem cell-derived organoids: using principles of developmental biology to grow human tissues in a dish. Development. 2017;144:958–62.

83. Cakir B, Xiang Y, Tanaka Y, Kural MH, Parent M, Kang Y-J, et al. Engineering of human brain organoids with a functional vascular-like system. Nat Methods. 2019;16:1169–75.

84. Cecchelli R, Berezowski V, Lundquist S, Culot M, Renftel M, Dehouck M-P, et al. Modelling of the blood–brain barrier in drug discovery and development. Nat Rev Drug Discov. 2007;6:650–61.

85. Vatine GD, Al-Ahmad A, Barriga BK, Svendsen S, Salim A, Garcia L, et al. Modeling Psychomotor Retardation using iPSCs from MCT8-Deficient Patients Indicates a Prominent Role for the Blood-Brain Barrier. Cell Stem Cell. 2017;20:831-843.e5.

86. Clark PA, Al-Ahmad AJ, Qian T, Zhang RR, Wilson HK, Weichert JP, et al. Analysis of Cancer-Targeting Alkylphosphocholine Analogue Permeability Characteristics Using a Human Induced Pluripotent Stem Cell Blood–Brain Barrier Model. Mol Pharmaceutics. 2016;13:3341–9.

87. Stebbins MJ, Lippmann ES, Faubion MG, Daneman R, Palecek SP, Shusta EV. Activation of RARα, RARγ, or RXRα Increases Barrier Tightness in Human Induced Pluripotent Stem Cell-Derived Brain Endothelial Cells. Biotechnol J. 2018;13:1700093.

88. Davies PF. Flow-mediated endothelial mechanotransduction. Physiological Reviews. 1995;75:519–60.

89. Iba T, Sumpio BE. Morphological response of human endothelial cells subjected to cyclic strain in vitro. Microvascular Research. 1991;42:245–54.

90. Malek AM, Izumo S. Mechanism of endothelial cell shape change and cytoskeletal remodeling in response to fluid shear stress. J Cell Sci. 1996;109:713–26.

91. Ye M, Sanchez HM, Hultz M, Yang Z, Bogorad M, Wong AD, et al. Brain microvascular endothelial cells resist elongation due to curvature and shear stress. Sci Rep. 2015;4:4681.

92. DeStefano JG, Xu ZS, Williams AJ, Yimam N, Searson PC. Effect of shear stress on iPSC-derived human brain microvascular endothelial cells (dhBMECs). Fluids and Barriers of the CNS. 2017;14:20.

93. Reinitz A, DeStefano J, Ye M, Wong AD, Searson PC. Human brain microvascular endothelial cells resist elongation due to shear stress. Microvascular Research. 2015;99:8–18.

94. Bosworth AM, Faley SL, Bellan LM, Lippmann ES. Modeling Neurovascular Disorders and Therapeutic Outcomes with Human-Induced Pluripotent Stem Cells. Front Bioeng Biotechnol. 2018;5:87.

95. Anık A, Kersseboom S, Demir K, Çatlı G, Yiş U, Böber E, et al. Psychomotor Retardation Caused by a Defective Thyroid Hormone Transporter: Report of Two Families with Different ***MCT8*** Mutations. Horm Res Paediatr. 2014;82:261–71.

96. Katt ME, Mayo LN, Ellis SE, Mahairaki V, Rothstein JD, Cheng L, et al. The role of mutations associated with familial neurodegenerative disorders on blood–brain barrier function in an iPSC model. Fluids Barriers CNS. 2019;16:20.

97. Lim RG, Quan C, Reyes-Ortiz AM, Lutz SE, Kedaigle AJ, Gipson TA, et al. Huntington's Disease iPSC-Derived Brain Microvascular Endothelial Cells Reveal WNT-Mediated Angiogenic and Blood-Brain Barrier Deficits. Cell Reports. 2017;19:1365–77.

98. Lee CAA, Seo HS, Armien AG, Bates FS, Tolar J, Azarin SM. Modeling and rescue of defective blood–brain barrier function of induced brain microvascular endothelial cells from childhood cerebral adrenoleukodystrophy patients. Fluids Barriers CNS. 2018;15:9.

99. Myers RH. Huntington's Disease Genetics. 2004;1:8.

100. Kim BJ, McDonagh MA, Deng L, Gastfriend BD, Schubert-Unkmeir A, Doran KS, et al. Streptococcus agalactiae disrupts P-glycoprotein function in brain endothelial cells. Fluids Barriers CNS. 2019;16:26.

101. Delsing L, Dönnes P, Sánchez J, Clausen M, Voulgaris D, Falk A, et al. Barrier Properties and Transcriptome Expression in Human iPSC-Derived Models of the Blood-Brain Barrier: Barrier Properties and Transcriptome Expression in Human iPSC-Derived Models. Stem Cells. 2018;36:1816–27.

102. Motallebnejad P, Thomas A, Swisher SL, Azarin SM. An isogenic hiPSC-derived BBB-on-a-chip. Biomicrofluidics. 2019;13:064119.

Chapter 2 – Transcriptomic Comparison of Human and Mouse Brain Microvessels[2]

[2] The following chapter is adapted from a co-first authored document [1]:

Song HW, Foreman KL, Gastfriend BD, Kuo JS, Palecek SP, Shusta EV. Transcriptomic comparison of human and mouse brain microvessels. Sci Rep. 2020;10:12358.

Authors' contributions: HWS, KLF and BDG are cofirst authors on this document. HWS performed experiments. KLF and BDG analyzed data. HWS, KLF, BDG, SPP, JSK and EVS wrote the manuscript.

2.1 Summary

The brain vasculature maintains brain homeostasis by tightly regulating ionic, molecular, and cellular transport between the blood and the brain parenchyma. These blood-brain barrier (BBB) properties are impede brain drug delivery, and brain vascular dysfunction accompanies many neurological disorders. The molecular constituents of brain microvascular endothelial cells (BMECs) and pericytes, which share a basement membrane and comprise the microvessel structure, remain incompletely characterized, particularly in humans. To improve the molecular database of these cell types, we performed RNA sequencing on brain microvessel preparations isolated from snap-frozen human and mouse tissues by laser capture microdissection (LCM). The resulting transcriptome datasets from LCM microvessels were enriched in known brain endothelial and pericyte markers, and global comparison identified previously unknown microvessel-enriched genes. We used these datasets to identify mouse-human species differences in microvessel-associated gene expression that may have relevance to BBB regulation and drug delivery. Further, by comparison of human LCM microvessel data with existing human BMEC transcriptomic datasets, we identified novel putative markers of human brain pericytes. Together, these data improve the molecular definition of BMECs and brain pericytes, and are a resource for rational development of new brain-penetrant therapeutics and for advancing understanding of brain vascular function and dysfunction.

2.2 Introduction

The blood-brain barrier (BBB) regulates blood flow, supplies the brain with nutrients, and facilitates clearance of a variety of substances. The BBB is comprised of brain microvascular endothelial cells (BMECs), the principal barrier-forming cell. BMECs are also intimately associated with brain pericytes, mural cells that line the outside of microvessels and are linked to endothelial cells by a shared vascular basement membrane[2]. The BBB is required to maintain brain homeostasis, but also prevents clinically relevant doses of many therapeutics from entering the brain[3,4]. Brain vascular dysfunction plays a role in several neurological disorders, including some with cell-autonomous defects in BMEC or pericyte function[5–8]. Due to its role in neurological disorders and important implications for brain drug delivery, the brain vasculature has been the subject of intense research, often focused on identifying mechanisms underlying its unique behavior. Our understanding of brain vascular development, function, dysfunction, and molecular constituents, however, has been advanced largely by mouse models. The scarcity of human brain tissue and low abundance of brain vascular cells has limited molecular profiling of the human brain vasculature. Improved molecular understanding of human BMECs and pericytes could aid in the development of new BBB-penetrant therapeutics and advance new hypotheses about mechanisms of brain vascular dysfunction in disease.

Mouse brain vascular cells have previously been isolated and transcriptionally profiled[9–13]. For example, fluorescence-activated cell sorting (FACS) has been used to isolate brain endothelial cells from *Tie2*-GFP mice, and microarray analysis identified transcripts that were enriched or depleted in brain endothelial cells compared to lung and liver endothelial cells[9]. Full transcriptomic datasets of mouse brain endothelial cells and pericytes have also been obtained by performing RNA sequencing (RNA-seq) after cell isolation by FACS or

immunopanning methods[12,14]. Similarly, bulk and single cell RNA-seq of endothelial cells in mice have also been used to identify transcription factors and β-catenin-regulated genes related to blood-brain barrier specification during the developmental timecourse[13]. Recently, single cell RNA-seq has also been used to improve the transcriptomic definition of mouse brain pericytes and identify positional variation in mural and endothelial cell gene expression[10,11]. While the mouse data have been instrumental in advancing our understanding of BMECs and pericytes there are numerous species-specific differences that have been identified between mouse and human brain including in solute carrier and efflux transporter expression[15–17]. Gene expression profiling in human brain samples has been much more limited and largely focused on non-vascular cell types, including neurons and astrocytes. For example, single cell RNA-seq of human adult and embryonic cortex samples has been used to identify regional, developmental, and species differences in neuronal and glial gene expression; however, the approaches employed yielded extremely small populations of endothelial cells and pericytes, impeding analysis of human brain microvessel transcriptomes[18–20]. Recently, brain microvessels isolated by centrifugation from two patient samples were subjected to RNA-seq to analyze expression of ATP binding cassette (*ABC*) transporters and solute carriers (*SLC*s)[21], and brain endothelial cells isolated via immunopanning from two patient samples were also transcriptomically profiled[22]. A detailed, transcriptome-wide analysis of human brain microvessels, however, is currently lacking. Furthermore, the limited number of existing human brain vascular datasets motivates transcriptomic characterization of additional patient samples. A more complete understanding of mouse-human species differences may help inform choice of model systems for studying BBB biology or screening for brain penetrant therapeutics.

In this study, we performed RNA-seq on normal mouse and human brain microvessels isolated using laser capture microdissection (LCM). LCM allowed the isolation of brain microvessels from snap-frozen tissue sections, limiting possible transcriptional changes induced by techniques used in previous BBB transcriptomic analyses such as cell homogenization, sorting, immunopanning, or short periods of *in vitro* culture[23–25]. The isolated microvessels contained both BMEC and pericyte components and the transcriptomes were enriched in both BMEC and pericyte transcripts as expected. Data analysis allowed the identification of genes with microvessel-enriched expression despite patient-to-patient variability, identified species differences between mouse and human samples, and suggested putative novel human brain pericyte markers.

2.3 Results

2.3.1 Laser capture microdissection and RNA-sequencing of brain microvessels

Normal brain tissue from three human patients undergoing neurosurgery was obtained and flash frozen immediately to preserve mRNA content. Similarly, brains were removed and flash frozen from three C57/BL6N mice. Tissue sections were first labeled with fluorescent lectins, which bind to the endothelial glycocaylx, to identify microvessels for capture (Fig. 1A). The lectin^{+} microvessels were manually outlined and captured for RNA isolation using an LCM system (Fig. 1B). To enrich samples for microvascular endothelial cells and associated pericytes while limiting the contribution of vascular smooth muscle cells, which vary in phenotype and gene expression from microvascular pericytes[11], only vessels ≤ 10 μm in diameter were isolated. Given the spatial resolving constraints of LCM, it is impossible to isolate solely BMECs, and hence the isolated microvessels also contained microvessel-associated pericytes. Thus, this combination of BMECs and pericytes will be defined as “microvessels” throughout

the manuscript. Microvessel fragments totaling roughly 2.5 mm^2 and an equivalent area of whole brain tissue were isolated from each human and murine brain sample, yielding 0.8–5.5 ng of total RNA per sample (Supplementary Table S1; Supplementary Fig. S1).

RNA sequencing of the resulting LCM microvessel and whole brain RNA samples each yielded approximately 20 million reads, which were then aligned to the human and mouse genomes. The number of reads and alignment percentages for each sample are shown in Supplementary Table S1 and gene count data are provided in Supplementary Table S2. To validate the resulting datasets, we examined expression of a subset of known brain endothelial, pericyte, and neural (astrocyte and neuron) genes in LCM microvessels and whole brain. As expected, mouse LCM microvessels had increased expression of endothelial genes (*Cldn5*, *Cdh5*, *Slc2a1*, *Abcb1a*, *Vwf*, *Mfsd2a*) and pericyte genes (*Anpep*, *Cspg4*, *Rgs5*, *Kcnj8*, *Abcc9*, *Pdgfrb*), and no enrichment of neural genes (*Gabbr1*, *Tubb3*, *Aqp4*) compared to whole brain samples (Fig. 1C). In human LCM microvessels, we observed similar enrichment of endothelial genes (*CLDN5*, *CDH5*, *SLC2A1*, *ABCB1*, *VWF*, *MFSD2A*) and lack of enrichment of neural genes (*GABBR1*, *TUBB3*, *AQP4*). Compared to mouse, the human LCM microvessels had enrichment of *RGS5*, *ABCC9,* and *PDGFRB*, but lacked statistically significant enrichment of other pericyte markers, such as *ANPEP*, *CSPG4*, and *KCNJ8*, which may be a result of increased variability between human patient samples, lower pericyte numbers in human samples compared to mouse, or mouse-human species differences in pericyte gene expression (Fig. 1D).

To further examine the LCM microvessel datasets, we compared expression of all genes in the mouse samples to recent single cell RNA-seq datasets of FACS-purified mouse BMECs and pericytes (Supplementary Table S3)[11]. The Pearson correlation coefficient (r_p) between LCM microvessels (average of three biological replicates) and the reference endothelial dataset

was 0.27 ($P < 0.001$), while the correlation for the reference pericyte dataset was 0.22 ($P < 0.001$), indicating a positive, but poor correlation for both cell types (Fig. 2A). Spearman's correlation coefficient (r_s) between LCM microvessels and the reference endothelial dataset was 0.74, and for the reference pericyte dataset was 0.73, indicating similar ranking of genes despite poor correlation on absolute abundance (Fig. 2A). Since LCM microvessel datasets are derived from a mixture of cell types, largely BMECs and pericytes, these results were not surprising. In an effort to adjust for the presence of multiple cell types, we recalculated Pearson correlation coefficients between the LCM datasets and reference single cell RNA-seq datasets by mathematically combining different ratios of endothelial cell and pericyte datasets (see Methods for details). This analysis revealed an optimal Pearson correlation ($r_p = 0.33$, $P < 0.001$) for a reference dataset comprising approximately 42% pericyte-derived transcripts and 58% BMEC-derived (Fig. 2B, C), while the Spearman's correlation coefficient ($r_s = 0.74$) did not increase over the endothelial-only dataset (Fig. 2C). The low Pearson correlation, and lack of improvement in Spearman's correlation, is likely due to parenchymal cell contamination in the microvessel preparations and technical differences between single cell and bulk RNA-seq methodologies. Nonetheless, the non-monotonic relationship between Pearson correlation and ratio of endothelial cell and pericyte reference datasets supports the presence of both endothelial cells and pericytes in the LCM microvessel samples.

2.3.2 Comparison of LCM and whole brain transcriptomes identifies microvessel-enriched genes

We used hierarchical clustering and principal component analysis (PCA) to make transcriptome-wide, unbiased comparisons of LCM microvessels and whole brain. Mouse microvessel datasets clustered together and were distinct from whole brain datasets (Fig. 3A).

Human datasets did not produce this expected clustering, with one whole brain dataset clustering more closely with a microvessel dataset from a different patient sample than with other whole brain datasets (Fig. 3B). In PCA, mouse microvessel and whole brain datasets also clustered together along principal component 1 (PC1; explaining 73% of the variance) (Fig. 3C), while weaker clustering along principal component 2 (PC2; explaining 26% of the variance) was observed for the human datasets (Fig. 3D). Together, these analyses suggest that patient-derived human datasets have more variability than mouse samples, potentially attributable to differences in genetic background, brain region, or underlying complications that required neurosurgical intervention.

We next identified genes differentially expressed in LCM microvessels compared to whole brain. This analysis revealed 1120 genes enriched and 986 genes depleted in mouse LCM microvessels compared to whole brain (Fig. 3E; Supplementary Table S4). We similarly identified 587 enriched and 861 depleted genes in human LCM microvessels (Fig. 3F; Supplementary Table S4). Mouse microvessel-enriched genes included known pericyte and endothelial markers (*Rgs5*, *Slc2a1*, *Flt1*, *Fn1*, and *Ptprb*) (Fig. 3G). Human microvessel-enriched genes included pericyte and endothelial markers (*TAGLN2*, *RGS5*, *FLT1*, *VWF*, *FN1*, and *EMCN*) (Fig. 3H). Additional microvessel-enriched transcripts include, *ATP10A*, *ADGRL4*, *ITM2A*, *NET1*, and *PODXL*, consistent with a role for podocalyxin in BBB maintenance as recently demonstrated in mouse[26]. Whole brain-enriched (microvessel-depleted) genes included *RIMS4*, encoding a neuronal synaptic regulator[27], *CDH18*, which is also highly expressed in neurons[22], and *SLC12A5* (KCC2), a potassium-chloride transporter involved in synapse inhibition[28]. Thus, while the discrete set of neural genes examined in Figure 1

(*GABBR1*, *TUBB3*, and *AQP4*) were not depleted in LCM microvessels, our global differential expression analysis indicated some depletion of neuronal genes.

Gene ontology (GO) analysis of the 100 highest confidence LCM microvessel-enriched genes in mouse and human samples yielded GO terms such as tube morphogenesis, blood vessel morphogenesis/development, and vasculature development, consistent with a vascular transcriptomic signature (Fig. 3I, J). We additionally performed Gene Set Enrichment Analysis (GSEA) on the complete list of human genes ranked from the highest confidence microvessel-enriched gene to the highest confidence microvessel-depleted gene (Supplementary Table S4). Testing this list against 154 gene sets from the KEGG database revealed 13 gene sets enriched in LCM microvessel samples ($P < 0.05$), including the TGFβ signaling pathway, consistent with known roles for TGFβ signaling in vascular biology, BBB development, and endothelial-pericyte interactions[29,30] (Supplementary Fig. S2). We additionally tested our ranked list against 35 gene sets designed to infer which cell types are present in brain transcriptomic datasets[31]. This analysis confirmed endothelial and mural cell enrichment in microvessel samples, and neuron and astrocyte enrichment in whole brain (Supplementary Fig. S2).

2.3.3 Mouse-human species differences in vasculature-associated gene expression

Because our mouse and human datasets are derived from samples isolated using identical methods for isolation, sequencing, and analysis, they provide a powerful opportunity to detect species differences in brain microvessel gene expression. We performed a transcriptome-wide comparison of homologous gene expression in the human and mouse LCM microvessel datasets, which revealed 1122 human-enriched and 1278 mouse-enriched genes (Fig. 4A; Supplementary Table S5). To identify genes for which microvessel, rather than parenchymal, expression drives

species-specific enrichment, we filtered human- and mouse-enriched genes based on microvessel-enrichment in the respective species (Approach 1; Fig. 4B). 142 mouse-enriched genes were also microvessel-enriched over whole brain in mouse samples, including *Slco1c1* and *Vtn* (Fig 4B,C; Supplementary Table S5). Notably, expression of *VTN*/*Vtn*, which encodes the ECM protein vitronectin and has been identified as a pericyte marker in mouse[11,12], was highly enriched in mouse microvessels (Fig. 4A,C), suggesting human brain pericytes express less *VTN* transcript than mouse pericytes. In fact, we detected no *VTN* transcripts in human microvessels (Supplementary Fig. S3). We confirmed the ability of our pipeline to detect *VTN* transcripts by mapping a human liver RNA-seq dataset[32] (Supplementary Table S3), which had robust *VTN* expression at 1,330 TPM. We also reviewed two independent human single cell RNA-seq datasets[19,20], which confirmed a lack of *VTN* expression in human brain pericytes, although these datasets differ in developmental stage and brain region (Supplementary Fig. S3). 211 human-enriched genes were also microvessel-enriched over whole brain in human samples, including *SLCO2A1*, *GIMAP7*, *A2M*, *CD109*, *FGR*, *VWA2*, *RNASE1*, and *NHEJ1*. (Fig. 4B,D; Supplementary Table S5). We validated a subset of these human-enriched vascular genes using single cell RNA-seq data from the literature[10,11,19,20] and immunohistochemistry from the Human Protein Atlas[33] (Supplementary Fig. S4). For example, the GTPase-encoding transcript *GIMAP7* is not expressed by mouse brain pericytes or endothelial cells, but is expressed by endothelial cells in human embryonic midbrain and neocortex single cell RNA-seq data[19,20], and Human Protein Atlas data supports vascular enrichment of the protein in adult human cortex[33] (Supplementary Fig. S4). Similarly, *A2M*, encoding alpha-2-macroglobulin, is not expressed by mouse brain pericytes or endothelial cells, but single cell RNA-seq and

immunohistochemistry data support its expression in human brain pericytes, endothelial cells, and microglia (Supplementary Fig. S4).

Because Approach 1 eliminates genes of potential interest with expression both in vasculature and parenchyma, we also filtered human-and mouse-enriched gene lists based on the less stringent criterion of no microvessel- or whole brain-enrichment in the respective species (Approach 2; Fig. 4B; Supplementary Table S5). Further, because Approaches 1 and 2 do not consider genes without known mouse-human homology, or genes with similar expression in microvessels in both species but microvessel-enrichment in only one species, we also identified potential species differences by comparing the lists of mouse microvessel-enriched genes (Fig. 3E) and human microvessel-enriched genes (Fig. 3F) (Approach 3; Fig. 4E; Supplementary Table S5).

This transcriptome-wide analysis identified several solute carrier (*SLC*) transcripts with high differential expression and confidence: *Slco1c1* (Oatp1c1) was highly enriched in mouse microvessels (Fig. 4A,C). Expression of this thyroid hormone transporter in mouse, but not human, brain endothelial cells is consistent with previous observations and explains the lack of central nervous system (CNS) hypothyroidism in mouse models of Allan-Herndon-Dudley Syndrome (AHDS) generated by *Slc16a2* (MCT8) knockout[7]. The amino acid transporter *Slc6a20* and organic anion transporter *Slc22a8* were also highly enriched in mouse microvessels (Fig. 4C). *SLCO1A2* (homologous to mouse *Slco1a5*) was expressed in human microvessels and absent in mouse (Fig. 4A,D), consistent with previous observations of *SLCO1A2* expression in human brain microvessels[34] and endothelial cells[22]. Given these discrete validated examples and the importance of *SLC* and ATP-binding cassette (*ABC*) transporters in CNS drug delivery, we compared expression of all *SLC* and *ABC* transcripts (Supplementary Fig. S5; Supplementary

Table S5). We also found that the ratio of *ABCB1* (mouse *Abcb1a*) to *ABCG2* transcripts, which encode the efflux transporters P-glycoprotein (P-gp) and breast cancer resistance protein (BCRP), respectively, was higher in mouse microvessels (Supplementary Fig. S5), consistent with previous reports[15]. Together, this analysis reveals widespread species differences in microvessel-associated gene expression and demonstrates the utility of whole brain datasets in identifying which species differences are attributable to microvessel gene expression.

2.3.4 A putative gene expression profile of human brain pericytes

Pericytes play important roles in brain vascular function and BBB development[35–37]. While recent work has characterized the transcriptional profiles of mouse brain pericytes[11], human brain pericytes after *in vitro* culture[38], and small numbers of human embryonic brain pericytes[19,20], a comprehensive molecular definition of adult human brain pericytes *in vivo* is lacking. We reasoned that because our human LCM microvessel samples contain both endothelial and pericyte-derived transcripts, we could identify genes putatively expressed by human brain pericytes by subtractive comparison of our microvessel datasets to existing transcriptomic data from purified human brain endothelial cells (Supplementary Table S3)[18]. Similar strategies have been used to identify mouse brain pericyte enriched-genes from microvessel and pericyte-depleted microvessel transcriptome datasets[9,39]. We compared expression of the 587 human LCM microvessel-enriched genes identified via paired DESeq2 analysis (Fig. 3F) to expression in an adult human temporal lobe brain endothelial single cell RNA-seq dataset[18] (Fig. 5A). Genes with expression of 1 TPM or greater in this reference endothelial cell dataset were excluded from the list, resulting in 186 putative pericyte-enriched genes (Fig. 5B). This 1 TPM threshold yielded a putative pericyte-enriched gene list that

included known pericyte markers (*PDGFRB*, *NOTCH3*, *S1PR3*, *ABCC9*, *ADGRA2* [GPR124]) and excluded known endothelial genes (*PECAM1*, *A2M*, *SLC2A1*, *MSFD2A*) (Fig. 5A,C; Supplementary Table S6).

To identify potential species differences in pericyte gene expression, we compared this putative pericyte-enriched gene list to the human-enriched gene list (Fig. 4A,B) and found 48 such human-enriched putative pericyte genes (Fig. 5D,E). We evaluated expression of a subset of these genes using and immunohistochemical analysis from the Human Protein Atlas[33] and several independent RNA-seq datasets from the literature: mouse brain vascular single cell RNA-seq[10,11], human embryonic midbrain single cell RNA-seq[19], human embryonic neocortex single cell RNA-seq[20], and adult human cortex single cell/nucleus RNA-seq[40] (Supplementary Fig. S6). These data support expression of *SLC6A12*, *SLC12A7*, *GEM*, *FRZB*, *FOXL1*, *PTGDR2*, *FHL5*, *SMOC2*, and *LPL* in human brain pericytes in at least one validation dataset, and suggest lower or a lack of expression in mouse brain pericytes. For example, the human single cell RNA-seq and immunohistochemistry datasets corroborated our finding of human cortex and midbrain pericyte expression of *SLC12A7* (Supplementary Fig. S6). Notably, mouse single cell RNA-seq data suggests that *Slc12a7* is expressed by a small number of pericytes and endothelial cells[11], in contrast to humans where virtually no endothelial expression is detected (Supplementary Fig. S6). Similarly, *GEM*, encoding a GTP-binding protein, *FRZB*, encoding a Wnt-binding protein, and the transcription factor *FOXL1* are absent or nearly so in mouse brain pericytes but robustly expressed by human brain pericytes (Supplementary Fig. S6). Other genes (*MMP25*, *ANGPT2*) were expressed in both human endothelial cells and pericytes but nearly absent in the corresponding mouse cell types (Supplementary Fig. S6).

This multi-dataset validation also revealed that some genes, including *ZIC1*, *NOTCH3*, *PRELP*, *NDUFA4L2*, *LRRC32*, *COLEC12*, *KIAA0040*, and *C1QTNF1* are expressed by both mouse and human pericytes; our analysis suggests that these genes may be enriched in relative abundance in human microvessels versus mouse (Supplementary Fig. S6). Additionally, *EHD2*, while expressed at similar levels by mouse brain endothelial cells and pericytes, was highly pericyte-enriched in human single cell/nucleus RNA-seq datasets (Supplementary Fig. S6). *PRX* (periaxin), a gene required for myelination by Schwann cells[41], was recently identified as expressed in human brain microvasculature by immunohistochemistry[42], but *PRX* transcripts were nearly absent in mouse microvessels and mouse brain pericytes and endothelial cells (Supplementary Fig. S6). We again used independent, human single cell RNA-seq datasets to corroborate these findings, and found very low *PRX* expression in both endothelial cells and pericytes despite strong vascular localization in the immunohistochemistry dataset (Supplementary Fig. S6). Finally, some genes (*HAPLN3*, *SLC38A5*, *STARD8*) were indeed expressed by endothelial cells in these validation datasets, suggesting an erroneous lack of expression in the initial endothelial reference dataset or potentially reflecting differences in developmental stage or brain region (Supplementary Fig. S6), highlighting the importance of evaluating multiple datasets.

Together, this analysis demonstrates the utility of human LCM microvessel and whole brain datasets in identifying potential human pericyte-derived transcripts, suggests additional mouse-human species differences in endothelial and pericyte gene expression, and motivates the integration of several independent RNA-seq datasets to build confidence in cell type-specific gene expression. Further work will be required to confirm expression, cellular origin, and potential functional roles of genes identified in this analysis in the human adult brain vasculature.

2.4 Discussion

In this study, we isolated human and mouse brain microvessels and used RNA-seq to characterize the transcriptomes of these samples. LCM yielded microvessel samples containing the two cell types sharing the microvascular basement membrane, BMECs and pericytes. We observed some expression of neuronal and glial marker genes in LCM microvessel datasets, consistent with the technically unavoidable capture of some parenchymal cells. The common issue of multiple or contaminating cell types in tissue-derived RNA-seq samples has been largely obviated by single cell RNA-seq; however, single cell RNA-seq presents other challenges such as poor ability to detect very low abundance transcripts and potential transcriptomic alterations induced by cell dissociation and purification[43]. Thus, bulk and single cell RNA-seq are complementary strategies, and LCM has been used previously to isolate human blood-nerve barrier endoneurial microvessels from patient samples for downstream transcriptomic profiling[44]. To further validate our mouse LCM microvessel datasets, we used data from recent single cell RNA-seq of mouse brain endothelial cells and pericytes[10,11]. We found the highest correlation between our data at an approximately 1:1 combination of endothelial cell- and pericyte-derived transcripts, approximately consistent with the ratio of the two cell types in mouse brain microvasculature[45], assuming similar global transcript abundance in BMECs and pericytes. The maximum transcriptome-wide correlation we observed, however, had a Pearson correlation coefficient of only 0.34, consistent with the presence of parenchyma-derived transcripts in our LCM microvessel samples. Thus, the RNA-seq of matched whole brain samples is paramount in identifying endothelial and pericyte genes based on microvessel-enriched expression. Furthermore, while numerical methods to estimate the relative population of different cell types from such datasets are available[46,47], they require reliable reference

datasets for the cell types present. The extremely limited number and depth of human brain endothelial and pericyte RNA-seq datasets currently precludes the application of such techniques to our human LCM microvessel data.

Further analysis of our datasets via PCA and hierarchical clustering demonstrated expected similarity between three biological replicates of mouse microvessels, which clustered distinctly from whole brain. Similar analyses of the human datasets produced no such predictable clustering, demonstrating patient-to-patient variability, differences in sampling location, or different effects of neurological condition. Despite this, results of transcriptome-wide differential expression analysis, GO analysis, and GSEA support depletion of neural-associated genes and enrichment of vasculature-associated genes in both human and mouse LCM microvessel datasets compared to whole brain in a pairwise differential expression analysis. Overall, though there was high variability between human samples, LCM microvessel datasets were enriched in known BMEC and pericyte genes, confirming the utility of both the isolation method and the resulting datasets. The observed variability in human samples and uncertainty of sample location motivates future efforts to characterize additional patient samples. Additional matched samples would be required to understand how brain vascular gene expression varies with factors such as brain region, age, or disease, some of which have recently begun to be explored in mouse[11,39].

To demonstrate the utility of the resulting datasets, we identified species-specific differences in brain vascular gene expression. Species differences in neural progenitor, neuronal, and astrocyte gene expression have been characterized by RNA-seq[19,22], but such differences in vascular gene expression have not been comprehensively analyzed. In addition to a transcriptome wide comparison of homologous gene expression, using whole brain datasets to eliminate those genes with species-specific expression attributable to the brain parenchyma and

not the vasculature, we focused on *SLC* and *ABC* transporters. Given that BBB efflux by *ABC* transporters hinders delivery of many small molecule drugs, and *SLC* transporters may facilitate transport of some pharmaceuticals, it is important to understand differences in expression between human and mouse for drug development[15,16,21,48]. Additionally, recent work demonstrated an enrichment of transporter genes in mouse brain pericytes compared to mouse lung pericytes, suggesting that brain pericytes may be directly involved in molecular transport[11]. Thus, our data permit identification of putative human pericyte-enriched transporters that may be involved in molecular transport across the human BBB, such as the potassium-chloride cotransporter *SLC12A7* and the betaine transporter *SLC6A12* identified in our analysis. Further, improved insight into differences in gene expression between mouse and human brain vasculature is key to assess potential limitations of mouse models of brain vascular and BBB development and disease, as is the case in AHDS[7]. For example, we found that *VTN*, a gene highly and selectively expressed in mouse brain pericytes with a recently-described functional role in neurogenesis[49], was not expressed at a detectable level by human brain pericytes. These results were validated in transcriptomics data collected by other groups, though these datasets vary in developmental stage and brain region[19,20]. Availability of human vascular transcriptomes can aid investigators in identifying potential roles for BMECs and pericytes in the etiology of neurological disorders with known genetic bases. Thus, availability of full transcriptome datasets should allow others to quickly assess expression of molecules with potential relevance to drug delivery (e.g. *SLC*s, *ABC*s, and large molecule receptors) and disease in human brain vasculature.

Finally, we demonstrated how human brain microvessel transcriptome datasets could further be mined by comparison to existing brain endothelial transcriptomes[18]. We identified

several genes enriched in our human LCM microvessel datasets compared to both whole brain and existing human brain endothelial cell datasets, such as *SLC6A12, SLC12A7, PRELP, NDUFA4L2, GEM, FRZB, LRRC32, EHD2, FOXL1, COLEC12, KIAA0040, PTGDR2, C1QTNF1, FHL5, SMOC2,* and *LPL,* suggesting these as possible human pericyte-expressed genes some of which are human-specific. For example, *SLC12A7,* which is weakly expressed in both pericytes and endothelial cells in mouse brain vasculature, was strongly and selectively expressed by human brain pericytes in single-cell RNA-seq datasets, and had vascular localization in immunohistochemistry data from the Human Protein Atlas. These results motivate the use of several independent datasets to account for patient-to-patient variability and technical differences in cell isolation and sequencing methodologies to validate putative human pericyte and BMEC gene expression. Our human LCM microvessel datasets should facilitate hypothesis generation and future validation of hypothesized human pericyte-expressed transcripts with potential roles in vascular function or disease.

2.5 Conclusion

Overall, this work contributes brain microvessel transcriptome datasets enriched in BMEC and pericyte genes from three human patient and three mouse samples. We also contribute matched whole brain datasets to aid in identification and assessment of microvessel-associated genes. Further, our work demonstrates the utility of LCM as a valuable tool for isolation and molecular analysis of brain microvasculature. Finally, we have demonstrated application of our datasets to identify differences between mouse and human brain vasculature with potential implications for drug delivery and disease, and to discover previously unknown human BMEC- and brain pericyte-expressed genes within these relatively unexplored transcriptomes.

2.6 Methods

2.6.1 Human tissue

This analysis was performed on normal human brain tissue that is usually discarded during surgery to access deeper diseased brain regions. Human brain tissue was obtained during three surgeries for other indications under a protocol approved by the University of Wisconsin-Madison's Institutional Review Board. All research was conducted in accordance with the guidelines and supervision of the University of Wisconsin-Madison's Institutional Review Board. The obtained tissue specimens were flash-frozen in liquid nitrogen and stored at –80°C until sectioned.

2.6.2 Mouse tissue

All procedures were performed in compliance with the University of Wisconsin-Madison Animal Care and Use Committee and following National Institutes of Health (NIH) guidelines for care and use of laboratory animals. Mouse brain tissue was obtained from C57/BL6N mice aged 6–7 weeks, and tissue was flash-frozen in liquid nitrogen and stored at –80°C until sectioned.

2.6.3 Laser capture microdissection and RNA extraction

Tissues were sectioned onto RNase-free membrane slides (Molecular Machines & Industries) using RNase-free techniques at a thickness of 8 μm and stored at –80°C until proceeding to laser capture. Tissue sections were used within 1 week of sectioning to prevent RNA degradation.

All subsequent procedures were performed at room temperature using RNase-free techniques. Slides were thawed for 1.5 min, fixed in 100% acetone (Sigma) for 2 min, and air dried for 2 min. Capillaries were labeled for 2 min using a lectin stain: mouse tissue was stained with fluorescein labeled *Rincinus communis* Agglutinin I (RCA-I, 1:20, Vector Labs), and human tissue

was stained with fluorescein labeled *Ulex europaeus* Agglutinin I (UEA-I, 1:10, Vector Labs) diluted in water. Slides were washed 3 times with water and placed in a desiccator for 10 minutes. Slides were then dehydrated via two 30 s incubations in 95% ethanol (Sigma) followed by two 30 s incubations in 100% ethanol and finally a 3 min incubation in 100% isopropyl alcohol (Sigma). Slides were placed in a desiccator for another 3 min before proceeding to capture. The lectin-labeled blood vessels were cut from the sections and captured on an adhesive cap (Molecular Machines and Industries) using the MMI Cell Cut instrument (Molecular Machines and Industries). Only microvessels (≤10 μm in diameter) were selected for capture.

A total of 2.2-3.0 mm^2 of mouse brain microvessels and 2.3-3.0 mm^2 of human brain microvessels were collected per biological replicate, and three biological replicates were obtained. An equivalent area of whole brain tissue was captured onto an adhesive cap from each sample as a control. Captured tissue was lysed with buffer RLT (Qiagen) supplemented with β-mercaptoethanol (Sigma), vortexed for 30 s, and stored at –80°C until RNA extraction.

For RNA isolation, lysed tissue was thawed at room temperature and total RNA was extracted using an RNeasy Micro kit (Qiagen) per the manufacturer's instructions. On-column DNase I digestion was performed to remove genomic DNA. RNA was quantified on an Agilent Bioanalyzer using the RNA 6000 Pico kit, and electropherogram presence of 18S and 28S ribosomal RNA was used to confirm intact RNA prior to library construction and sequencing (Supplementary Fig. S1).

2.6.4 RNA-sequencing and data analysis

Sequencing libraries enriched for non-rRNA sequences were constructed using the NuGEN Ovation Single Cell RNA-Seq High Volume Beta Kit. Libraries were sequenced on an Illumina

HiSeq 2000 sequencer using 100 bp single-end reads. Between 19 and 33 million reads were collected per sample (Supplementary Table S1).

Raw FASTQ files from our sequencing or obtained from NCBI SRA (for reference dataset accession numbers, see Supplementary Table S3) were mapped to the mouse genome (mm10) or human genome (hg38) using STAR[50] (version 2.6.0b-1) implemented in Galaxy[51] on the public server at http://usegalaxy.org. Gene-level transcript abundances were calculated using featureCounts[52] (version 1.6.3) also implemented in Galaxy.

Differential expression analysis was performed using DESeq2[53] (version 3.10), implemented in R (version 3.6.2), using raw counts as input. When comparing LCM microvessel and whole brain samples, sample pairing was included in the DESeq2 design. Elsewhere in the paper, transcript abundances are presented as transcripts per million (TPM). For each gene *i*, TPM_i was calculated as

$$TPM_i = \frac{FPKM_i}{\sum_i FPKM_i} \times 10^6 \quad (1)$$

where fragments per kilobase of transcript per million mapped reads (FPKM) was calculated as

$$FPKM_i = \frac{\text{counts}_i}{L_i \sum_i \text{counts}_i} \times 10^6 \quad (2)$$

where L_i is the length of the transcript, in kilobases, reported by featureCounts, and sums run over all genes in a single sample. Count, FPKM, and TPM data for our datasets and reference datasets are provided in Supplementary Table S2. All P-values presented in the context of differential expression analyses are those adjusted for multiple comparisons by DESeq2 using the Benjamini-Hochberg procedure.

Hierarchical clustering on TPM was performed with GENE-E (version 3.0.215), using the one minus Pearson correlation with average linkage. Principal component analysis on TPM was performed using MATLAB. GO analysis was performed using the PANTHER[54] online tool at http://pantherdb.org. Gene Set Enrichment Analysis (GSEA)[55,56] was performed using a list of genes ranked based on DESeq2 output, using the ranking metric $-\log_{10}(P)\times\text{sign}[\log_2(\text{fold change})]$, which organizes high-confidence microvessel enriched genes at the top of the list, and high-confidence microvessel-depleted genes at the bottom.

2.6.5 Human-mouse gene expression comparison

To compare gene expression in human LCM microvessels and mouse LCM microvessels, a human-mouse gene homology database was obtained from Mouse Genome Informatics (http://www.informatics.jax.org/homology.shtml) and manually curated to match gene symbols to those in featureCounts outputs derived from genome annotation files. Human genes with no mouse homolog and mouse genes with no human homolog were not considered in this analysis. The majority (98%) of genes had 1:1 mouse-human homology. For human genes with multiple mouse homologs, TPM values for the mouse homologs were summed. For mouse genes with multiple human homologs, either (i) the single human homolog with the highest TPM was retained and the human homolog(s) with zero or negligible expression were eliminated, or (ii) if multiple human homologs existed with similar expression, these were each compared individually to the mouse homolog. Supplementary Table S5 contains a complete list of mouse-human homology as used in this analysis. Because mouse and human homologs for a given gene differ in transcript length, raw counts from each dataset do not permit an authentic comparison of expression. Thus, as a DESeq2 input, we used TPM values to reverse-calculate an unnormalized counts metric for each gene in

mouse and human samples using the human gene length. Other comparisons of mouse and human gene expression were performed using TPM values.

2.6.6 Comparison to single cell RNA-seq reference datasets

Raw counts from mouse brain endothelial single-cell RNA-seq datasets[11] (Supplementary Table S3) were averaged across all single cells and normalized using transcript lengths to generate a single vector of TPM values. The same process was used for mouse brain pericyte single-cell RNA-seq datasets (Supplementary Table S3). We mathematically generated new vectors of TPM values by combining these reference datasets in different pericyte-to-endothelial ratios as

$$TPM_a = a\left(TPM_{\text{peri}}\right) + \left(1 - a\right)\left(TPM_{\text{endo}}\right) \quad (3)$$

where α represents the fraction of transcripts derived from pericytes and varies between 0 and 1. To assess global similarity between reference datasets and LCM microvessel data, Pearson and Spearman's correlation coefficients were calculated on TPM values using MATLAB.

2.6.6 Validation of pericyte-enriched transcripts

Human and mouse brain single-cell and single-nucleus RNA-seq datasets[10,11,19,20,40] were used for validation of putative pericyte-enriched transcripts, with cell assignments to clusters as reported by the authors. Seurat (version 3.1.2)[57] implemented in R was used for visualization except where indicated in figure legends. Images from the Human Protein Atlas (http://v19.proteinatlas.org)[33] were also used for validation.

2.6.7 Statistical Analyses

DESeq2 was used for all differential expression analyses as described above, and all P-values reported in the context of differential expression analyses are those generated by DESeq2

using the Wald test and adjusted to control the false discovery rate using the Benjamini-Hochberg procedure, except where otherwise indicated. P-values reported for Pearson correlation coefficients were calculated in MATLAB using Student's *t* distribution. P-values reported for GO and GSEA analyses were those generated by the tools as described above. Student's *t* test was used to compare the ratio of *ABCB1* and *ABCG2* transcripts (Supplementary Fig. S5).

2.6 Figures

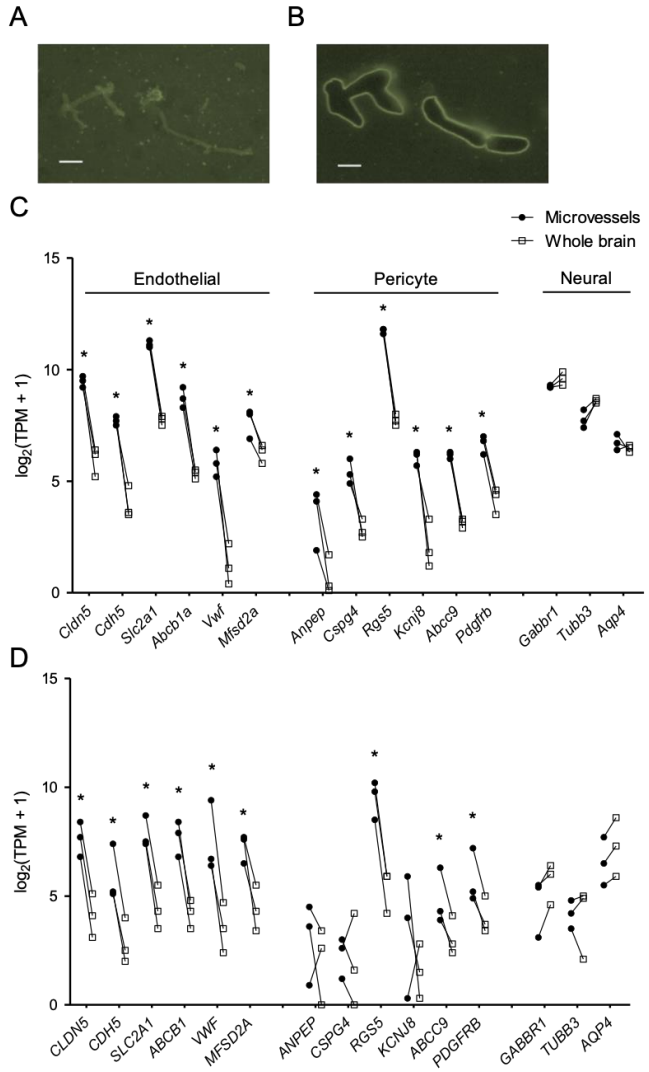

Figure 2.1 LCM of brain microvessels yields transcriptomic datasets enriched in endothelial and pericyte markers. **(A,B)** Representative lectin-stained mouse brain sections before (A) and after (B) LCM. Scale bars: 50 μm. **(C,D)** Transcript abundance [$\log_2$(TPM+1)] of endothelial, pericyte, and neural genes in mouse (C) and human (D) whole brain and LCM microvessel samples. Lines connect datapoints from matched LCM microvessel and whole brain samples. *$P < 0.05$ versus whole brain, DESeq2 Wald test with Benjamini-Hochberg correction. Exact P-values are provided in Supplementary Table S4.

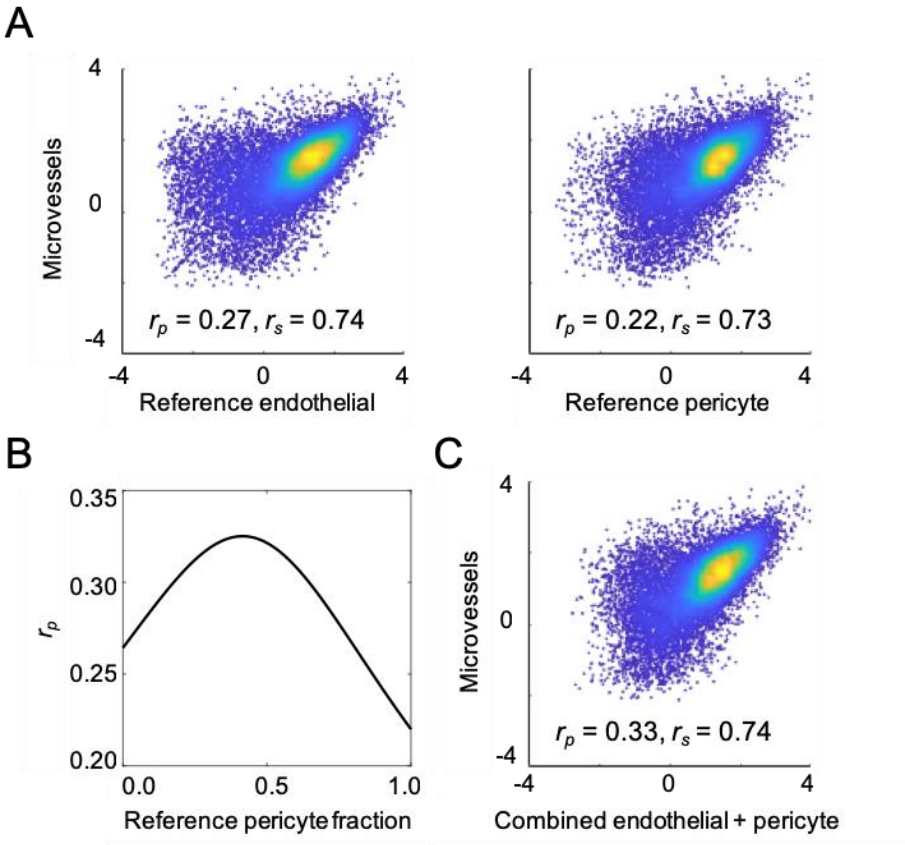

Figure 2.2 Comparison of mouse LCM microvessel with existing mouse BMEC and pericyte transcriptomic datasets. **(A)** Comparison of transcript abundances [$\log_{10}$(TPM)] in mouse LCM microvessels (y-axes; average of three biological replicates) versus the reference BMEC dataset or the reference pericyte dataset [11]. Each point represents one gene with nonzero expression in both LCM microvessel and reference endothelial or pericyte datasets. The Pearson (r_s) and Spearman's (r_p) correlation coefficients are inset and were calculated on raw TPM values prior to removal of undetected transcripts and log-transformation. Pseudocoloring indicates relative population density. **(B)** Pearson correlation coefficient (r_p) for the average of the biological replicates of mouse LCM microvessels calculated against reference datasets generated by combining brain pericyte and endothelial cell transcriptomes in different ratios (x-axis). **(C)** Comparison of transcript abundances [$\log_{10}$(TPM)] in mouse LCM microvessels (y-axis; average

of three biological replicates) versus the optimal combined reference dataset (42% pericyte transcript and 58% BMEC transcript weighting). Each point represents one gene with nonzero expression in both LCM microvessel and the reference dataset. The Pearson (r_s) and Spearman's (r_p) correlation coefficients are inset and were calculated on raw TPM values prior to removal of undetected transcripts and log-transformation. Pseudocoloring indicates relative population density.

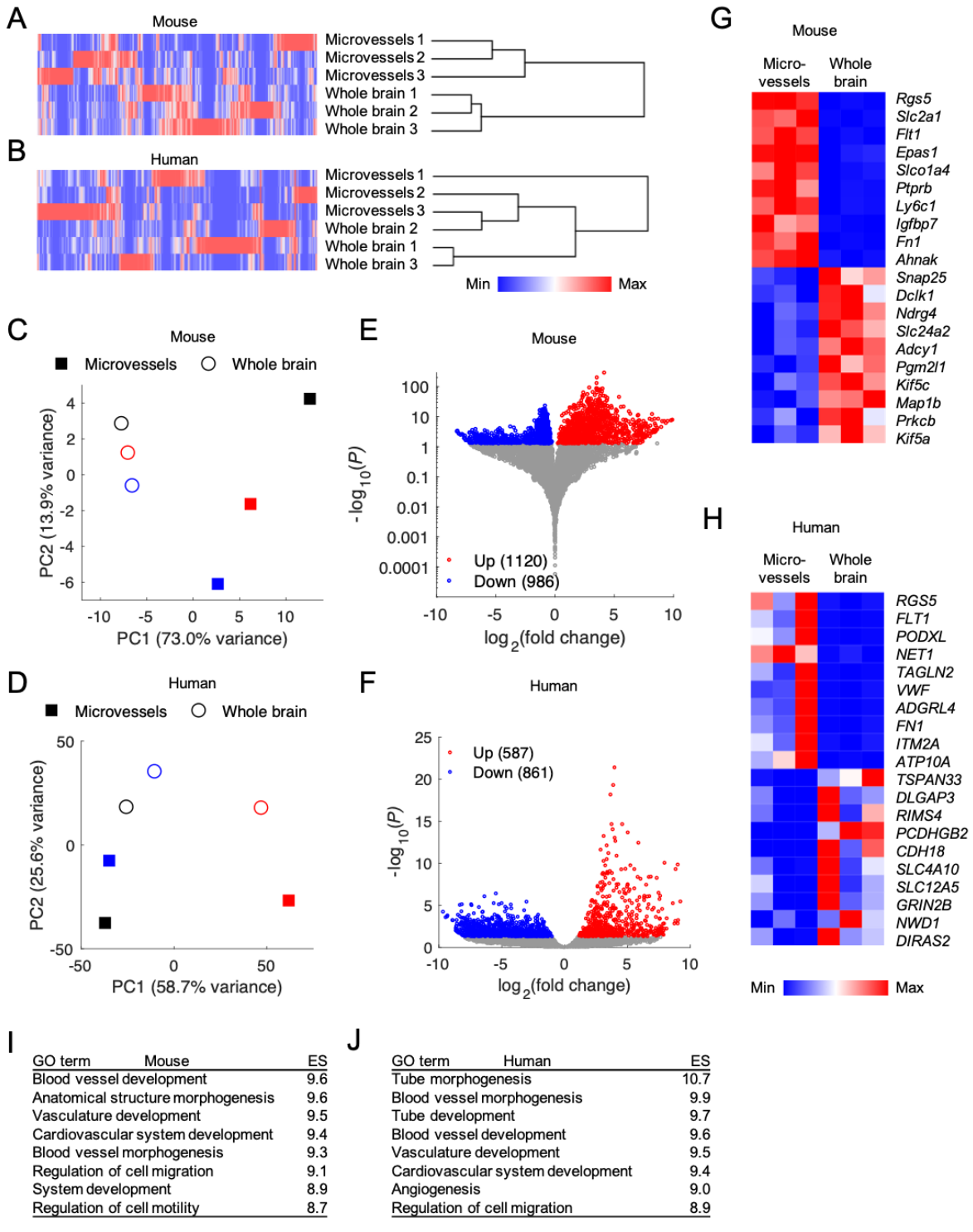

I

GO term	Mouse	ES
Blood vessel development		9.6
Anatomical structure morphogenesis		9.6
Vasculature development		9.5
Cardiovascular system development		9.4
Blood vessel morphogenesis		9.3
Regulation of cell migration		9.1
System development		8.9
Regulation of cell motility		8.7

J

GO term	Human	ES
Tube morphogenesis		10.7
Blood vessel morphogenesis		9.9
Tube development		9.7
Blood vessel development		9.6
Vasculature development		9.5
Cardiovascular system development		9.4
Angiogenesis		9.0
Regulation of cell migration		8.9

Figure 2.3 Differentially expressed genes in mouse and human LCM microvessels compared to whole brain. **(A,B)** Whole-transcriptome hierarchical clustering of mouse (A) and human (B)

LCM microvessels and whole brain datasets. Color indicates expression that has been normalized within each gene (column). **(C,D)** Principal component analysis of mouse (C) and human (D) LCM microvessels and whole brain datasets. Data are plotted in the space of the first two principal components, with the percentage of variance explained by principal component 1 (PC1) and principal component 2 (PC2) shown in axis labels. Microvessel and whole brain datapoints of the same color are derived from matched samples. **(E,F)** Volcano plots illustrating genes differentially expressed between LCM microvessels and whole brain samples from mouse (E) and human (F). The number of LCM microvessel-enriched (Up) and depleted (Down) genes with adjusted P-values < 0.05 (from DESeq2) are shown in the legends. Full results of differential expression analysis are in Supplementary Table S4. **(G,H)** Heat maps illustrating transcript abundance in biological triplicates of LCM microvessels and whole brain for the 10 highest confidence LCM microvessel-enriched and the 10 highest confidence microvessel-depleted genes in mouse (G) and human (H). Color indicates expression that has been normalized within each gene (row). **(I,J)** Gene ontology (GO) terms for biological processes enriched in LCM microvessels compared to whole brain from mouse (I) and human (J). ES: enrichment score [$-\log_{10}(P)$].

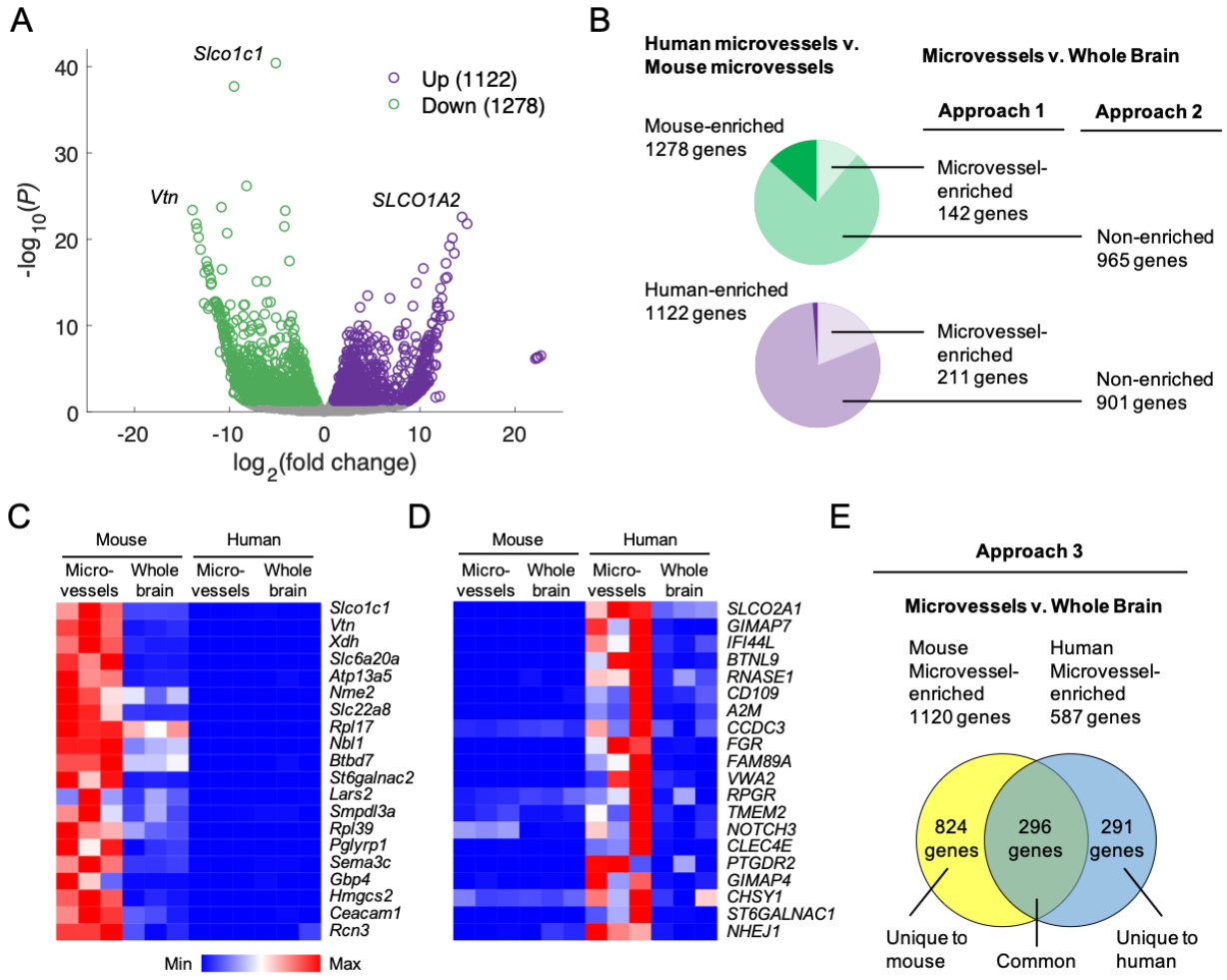

Figure 2.4 Mouse-human species differences in vasculature-associated gene expression. **(A)** Volcano plot illustrating genes differentially expressed between human LCM microvessels and mouse LCM microvessels. The number of human-enriched (Up) and depleted (Down) genes with adjusted P-values < 0.05 (from DESeq2) are shown in the legend. The complete list of mouse-human gene homology as used in this analysis, and full results of differential expression analysis, are in Supplementary Table S5. **(B)** Summary of filtering strategies used to identify human-mouse species differences potentially attributable to vascular gene expression. Of the 1278 mouse-enriched transcripts identified in (A), Approach 1 selects the 142 genes also

enriched in mouse microvessels versus whole brain (Fig. 3E) and Approach 2 selects the 965 genes not enriched in mouse microvessels or whole brain (Fig. 3E). Of the 1122 human-enriched transcripts identified in (A), Approach 1 selects the 211 genes also enriched in human microvessels versus whole brain (Fig. 3F) and Approach 2 selects the 901 genes not enriched in human microvessels or whole brain (Fig. 3F). Complete filtered gene lists are in Supplementary Table S5. **(C,D)** Heat maps illustrating transcript abundance in biological triplicates of mouse and human LCM microvessels and whole brain for the 20 highest confidence mouse-enriched (C) and human-enriched (D) genes from lists filtered by Approach 1 (genes also microvessel-enriched in the respective species). Color indicates expression that has been normalized within each gene (row). **(E)** Summary of Approach 3, a filtering strategy that identifies species-specific microvessel-enriched genes as those not also microvessel-enriched in the other species, or those without known mouse-human homology. Complete filtered gene lists are in Supplementary Table S5.

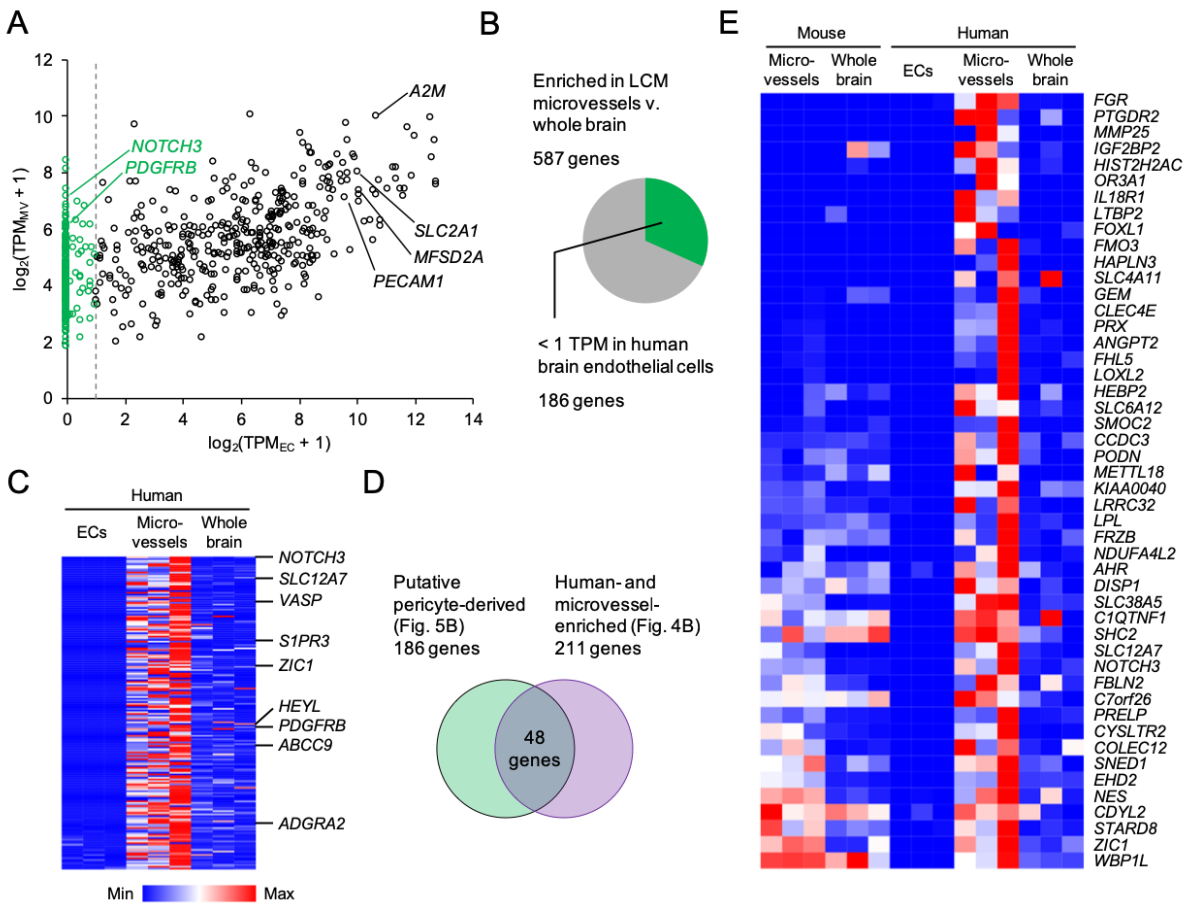

Figure 2.5 Comparison of human LCM microvessel and brain endothelial cell transcriptomes. **(A)** Average transcript abundance of the 587 human microvessel-enriched genes (Fig. 3F) in human LCM microvessels (TPM_{MV}) versus reference human adult brain endothelial cells analyzed by single cell RNA-seq (TPM_{EC})[18]. Vertical line at $\log_2(TPM_{EC} + 1) = 1$ indicates the 1 TPM threshold employed to identify putative pericyte-derived transcripts in the microvessel samples. Endothelial genes (e.g. *PECAM1*, *MFSD2A*, *SLC2A1*, *A2M*) fall to the right of this line and are excluded, while known pericyte genes (e.g. *NOTCH3*, *PDGFRB*) fall to the left. Full results of this analysis are in Supplementary Table S6. **(B)** Summary of results of thresholding analysis described in (A). **(C)** Heat map illustrating transcript abundance in biological triplicates of human brain endothelial cells and LCM microvessels and whole brain for the 186 putative

pericyte genes identified in (A). Known and putative novel pericyte genes are annotated. Color indicates expression that has been normalized within each gene (row). **(D)** Summary of filtering strategy used to identify putative human-specific pericyte genes. Of the 186 putative pericyte genes identified in (A), 48 are also human-enriched (Fig. 4B). **(E)** Heat map illustrating transcript abundance in biological triplicates of mouse LCM microvessels and whole brain, human brain endothelial cells, and human LCM microvessels and whole brain for the 48 putative human-enriched pericyte genes identified in (D). Genes are ranked by fold change in human versus mouse microvessels. Color indicates expression that has been normalized within each gene (row).

2.7 Supplemental

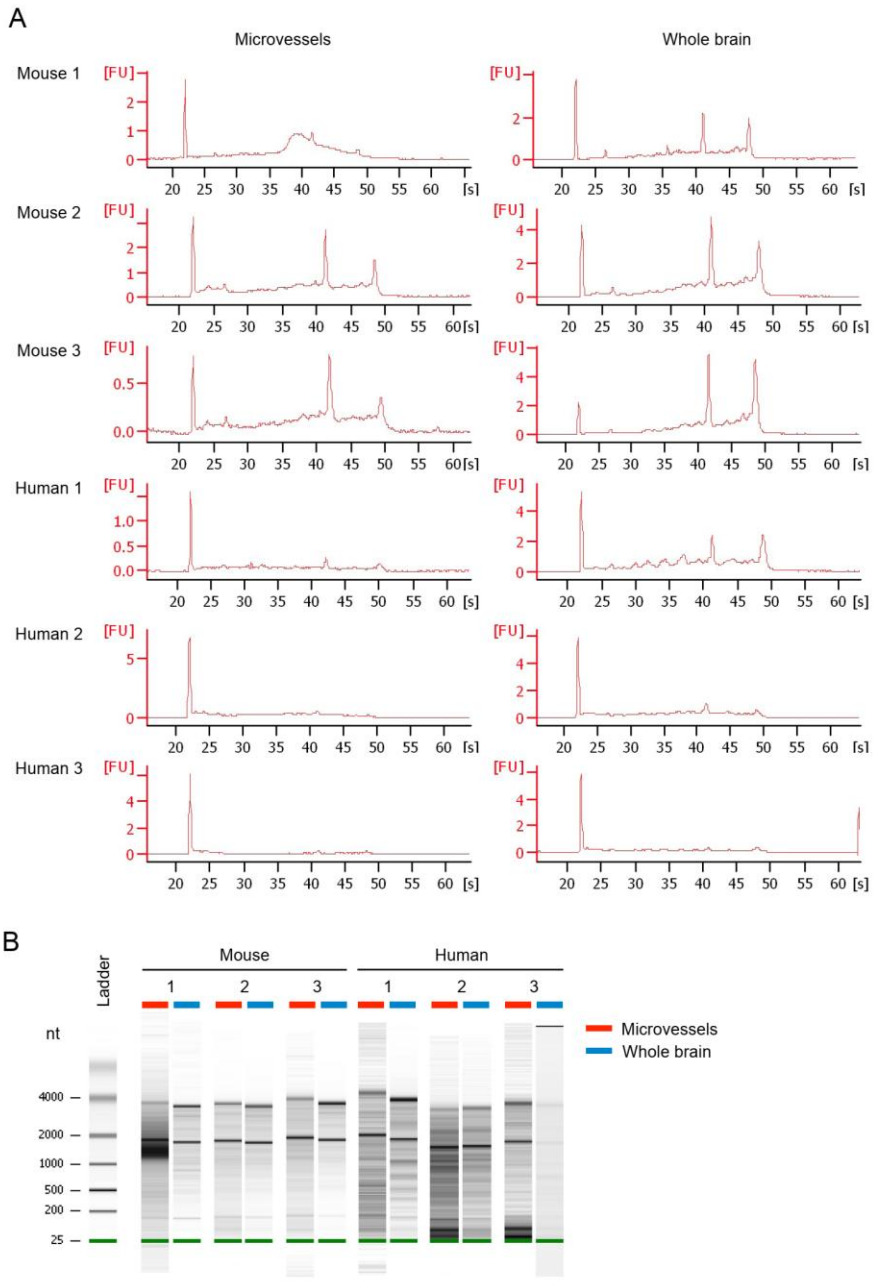

Supplemental Figure 2.1 RNA electropherograms. **(A,B)** Agilent Bioanalyzer analysis of RNA samples from mouse and human LCM microvessel and whole brain samples. Electropherograms (A) and gellike images (B) are shown.

A

Gene sets (KEGG) Microvessel-enriched	NES	*P*	FDR
TGF-beta signaling pathway	1.74	0	0.0040
Focal adhesion	1.74	0	0.0034
Dorso-ventral axis formation	1.63	0	0.062
Cytokine-cytokine receptor interaction	1.62	0	0.065
Complement and coagulation cascades	1.60	0.016	0.075
Selenoamino acid metabolism	1.58	0.011	0.076
Adipocytokine signaling pathway	1.53	0	0.14
Arachidonic acid metabolism	1.50	0.030	0.18
Vascular smooth muscle contraction	1.47	0.022	0.25
ECM-receptor interaction	1.44	0.018	0.30
Arrhythmogenic right ventricular cardiomyopathy	1.40	0.046	0.37
Leukocyte transendothelial migration	1.36	0.046	0.41
Small cell lung cancer	1.35	0.050	0.43

B

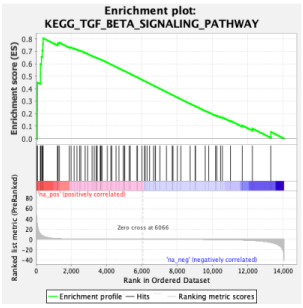

C

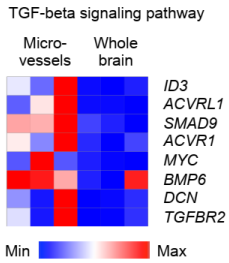

D

Gene sets (Hagenauer *et al.* 2018) Microvessel-enriched	NES	*P*	FDR
Endothelial all, Zeisel Science 2015	2.18	0	0
Endothelial all, Daneman PLoS 2010	1.75	0	0.00069
Endothelial all, Zhang JNeuro 2014	1.75	0	0.00046
Endothelial all, Darmanis PNAS 2015	1.69	0	0.0019
Neuron corticospinal, Doyle Cell 2008	1.59	0.0088	0.0094
Mural pericyte, Zhang JNeuro 2014	1.49	0.053	0.046

Gene sets (Hagenauer *et al.* 2018) Microvessel-depleted	NES	*P*	FDR
Neuron interneuron, Zeisel Science 2015	-1.71	0	0
Neuron all, Darmanis PNAS 2015	-1.45	0.011	0.059
Astrocyte all, Zhang JNeuro 2014	-1.39	0.028	0.12
Neuron all, Cahoy JNeuro 2008	-1.36	0.048	0.15

E

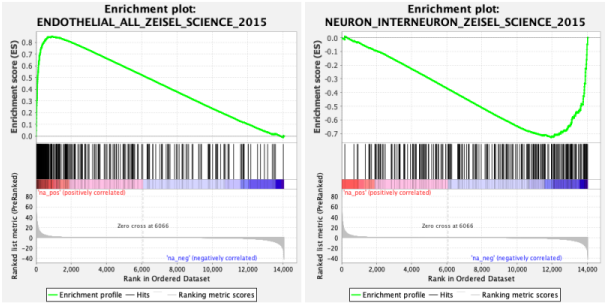

F

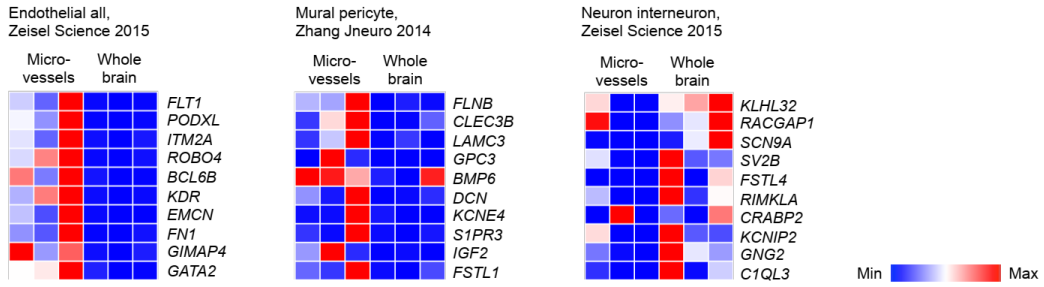

Supplemental Figure 2.2 Gene Set Enrichment Analysis (GSEA) of human LCM microvessel datasets. **(A)** Gene sets from the KEGG database enriched (*P* or FDR < 0.05) in human LCM microvessels compared to whole brain. NES: normalized enrichment score. The GSEA input was

a list of genes ranked from the highest-confidence LCM microvessel-enriched to the highest-confidence LCM microvessel-depleted gene, using the ranking metric $-\log_{10}(P)\times\text{sign}[\log_2(\text{fold change})]$ (Supplementary Table S4). **(B)** GSEA enrichment plots for the KEGG TGF-beta signaling pathway gene sets. **(C)** Heat maps illustrating transcript abundance in biological triplicates of LCM microvessels and whole brain for the highest ranked LCM microvessel-enriched genes in the indicated gene sets. Color indicates expression that has been normalized within each gene (row). **(D)** Gene sets from Hagenauer *et al.* [30] enriched (P or FDR < 0.05) in human LCM microvessels compared to whole brain (top) and enriched (P or FDR < 0.05) in whole brain compared to LCM microvessels (bottom). GSEA input was as described in (A). **(E)** GSEA enrichment plots for endothelial and interneuron gene sets from Hagenauer *et al.* [30]. **(F)** Heat maps illustrating transcript abundance in biological triplicates of LCM microvessels and whole brain for the highest ranked LCM microvessel-enriched genes in the indicated gene sets. Color indicates expression that has been normalized within each gene (row).

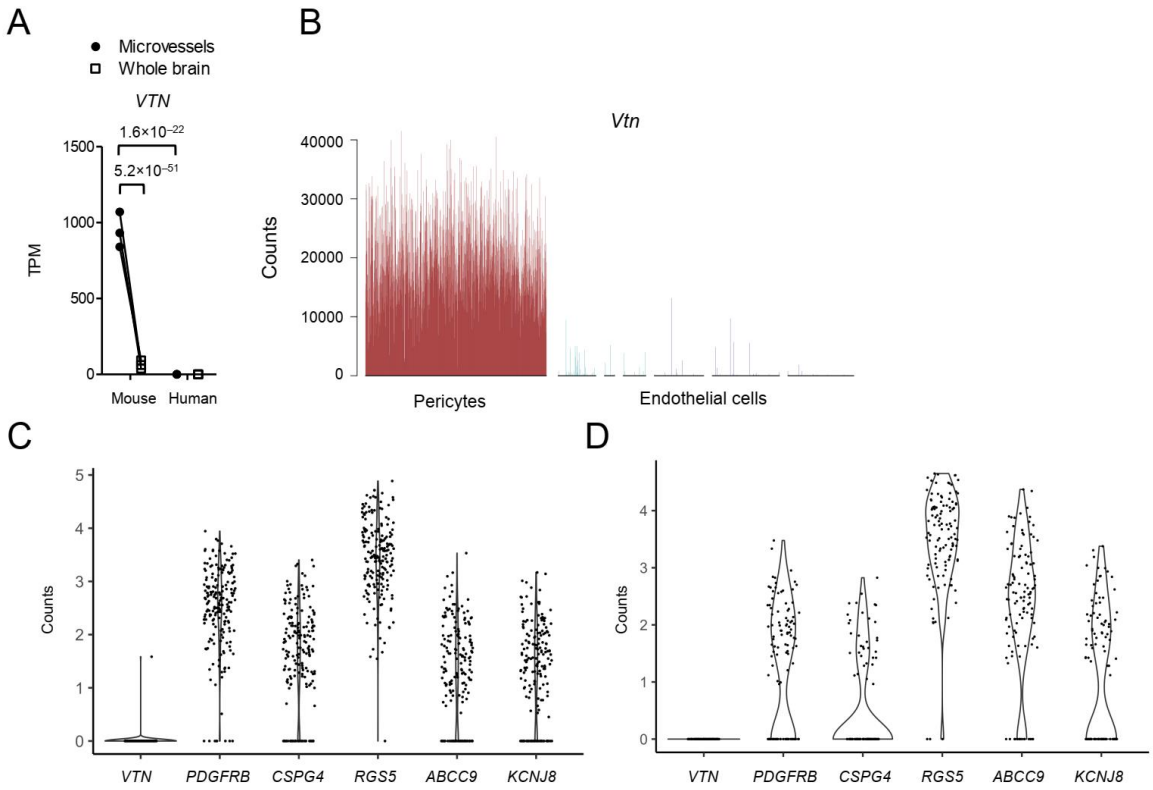

Supplemental Figure 2.3 Lack of VTN expression in human brain pericytes. **(A)** Transcript abundance of *VTN/Vtn* in biological triplicates of LCM microvessels and whole brain from human and mouse. Lines connect datapoints from matched LCM microvessel and whole brain samples. Adjusted Pvalues (from DESeq2) are shown; Wald test with Benjamini-Hochberg correction. **(B)** *Vtn* expression in single cell RNA-seq of mouse brain pericytes and endothelial cells [9,10]. Single cell RNA-seq plot in this panel adapted from http://betsholtzlab.org/VascularSingleCells/database.html. **(C,D)** *VTN* expression in human brain pericytes. Other pericyte genes (*PDGFRB*, *CSPG4*, *RGS5*, *ABCC9*, and *KCNJ8*) are included for comparison. Single cell RNA-seq data from (C) La Manno *et al.* [18] and (D) Polioudakis *et al.* [19].

i. Vanlandewijck *et al.* Mouse brain vascular scRNA-seq

ii. La Manno *et al.* Human embryonic midbrain scRNA-seq

iii. Polioudakis *et al.* Human embryonic neocortex scRNA-seq

iv. Human Protein Atlas cortex immunohistochemisty

GIMAP7

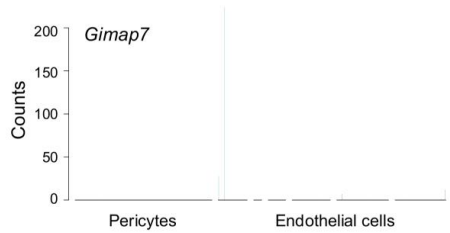

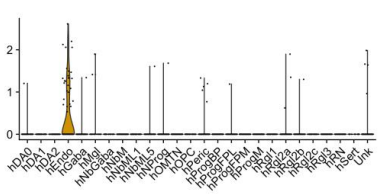

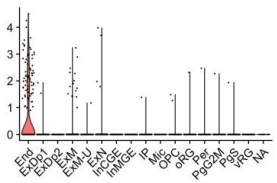

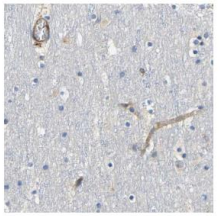

images.proteinatlas.org/20266/46803_B_7_5.jpg

A2M

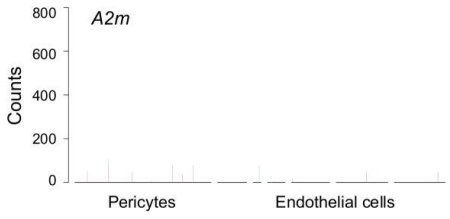

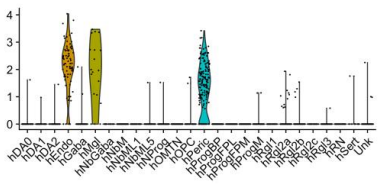

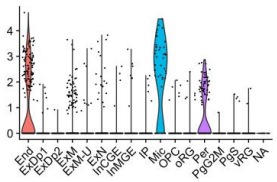

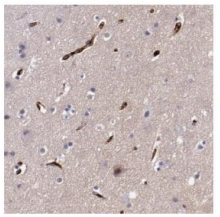

images.proteinatlas.org/2265/7607_B_8_5.jpg

NHEJ1

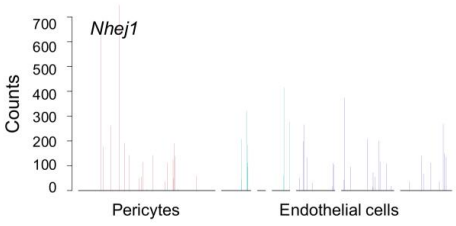

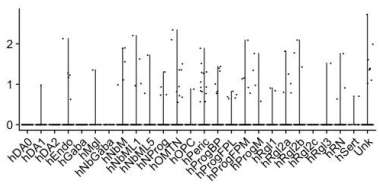

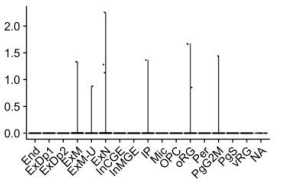

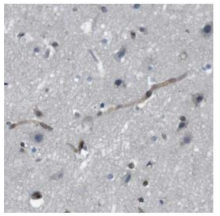

images.proteinatlas.org/12334/32934_B_7_5.jpg

RNASE1

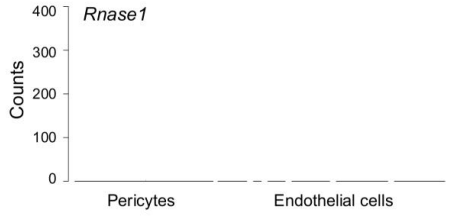

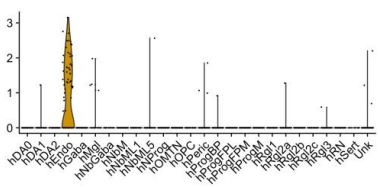

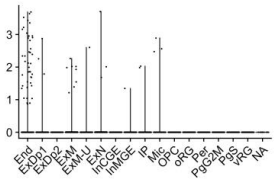

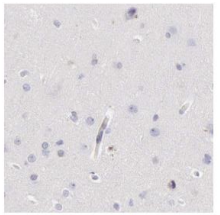

images.proteinatlas.org/1140/2634_B_8_5.jpg

Supplemental Figure 2.4 Validation of putative human-enriched vascular transcripts. Each row shows data from several sources for one transcript/protein of interest. (i) Transcript expression in single cell RNA-seq of mouse brain pericytes and endothelial cells [9,10]. Single cell RNA-seq plots in these panels adapted from http://betsholtzlab.org/VascularSingleCells/database.html. (ii) Transcript abundance (counts) in human embryonic midbrain single cell RNA-seq data [18]. Cell assignment to clusters and cluster names are as reported by La Manno *et al.* [18]. hPeric: human pericytes. hEndo: human endothelial cells. (iii) Transcript abundance (counts) in human embryonic neocortex single cell RNA-seq data [19]. Cell assignment to clusters and cluster names are as reported by Polioudakis *et al.* [19]. Per: pericytes. End: endothelial cells. (iv) Immunohistochemistry on human cortex samples from the Human Protein Atlas (v19.proteinatlas.org) [32]. URLs for each image are provided in the figure.

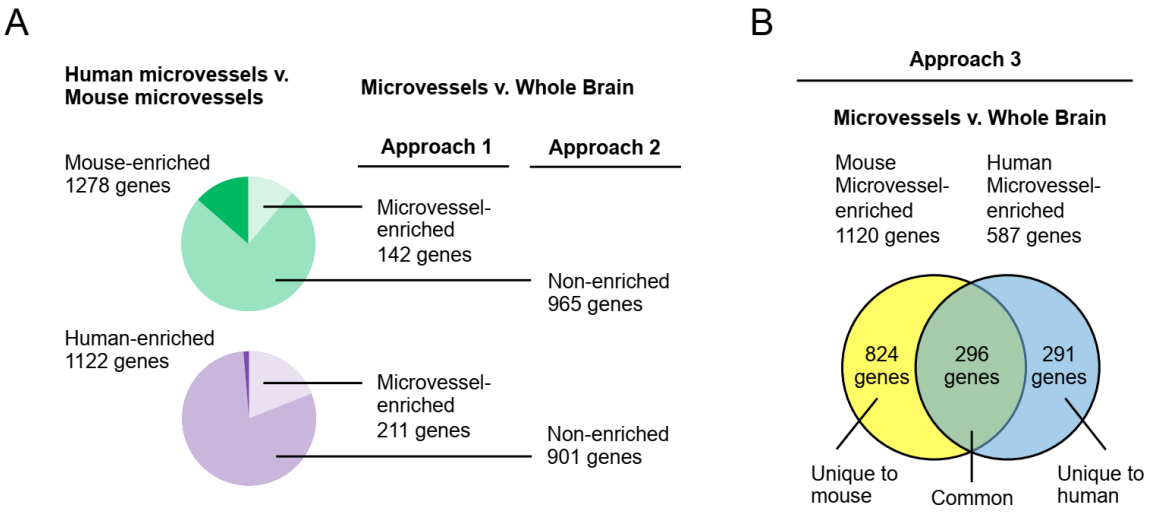

Supplemental Figure 2.5 Mouse-human species differences in SLC and ABC transporter expression. **(A)** Summary of Approaches 1 and 2. Approach 1 is as shown in Figure 4. Of the 1278 mouse-enriched transcripts identified in (A), Approach 2 selects the 965 genes not enriched in mouse microvessels or whole brain (as determined in Fig. 3E). Of the 1122 humanenriched transcripts identified in (A), Approach 2 selects the 901 genes not enriched in human microvessels or whole brain (as determined in Fig. 3F). The small number of genes not selected by Approach 1 or Approach 2 (shaded dark) are whole brain-enriched. Complete filtered gene lists are in Supplementary Table S5. **(B)** Summary of Approach 3, a filtering strategy that identifies species-specific microvessel-enriched genes by comparing the lists of mouse genes with microvessel enrichment versus whole brain (as determined in Fig. 3E) and human genes with microvessel enrichment versus whole brain (as determined in Fig. 3F). 824 genes appear only on the mouse list and 291 genes appear only on the human list. Complete filtered gene lists are in Supplementary Table S5.

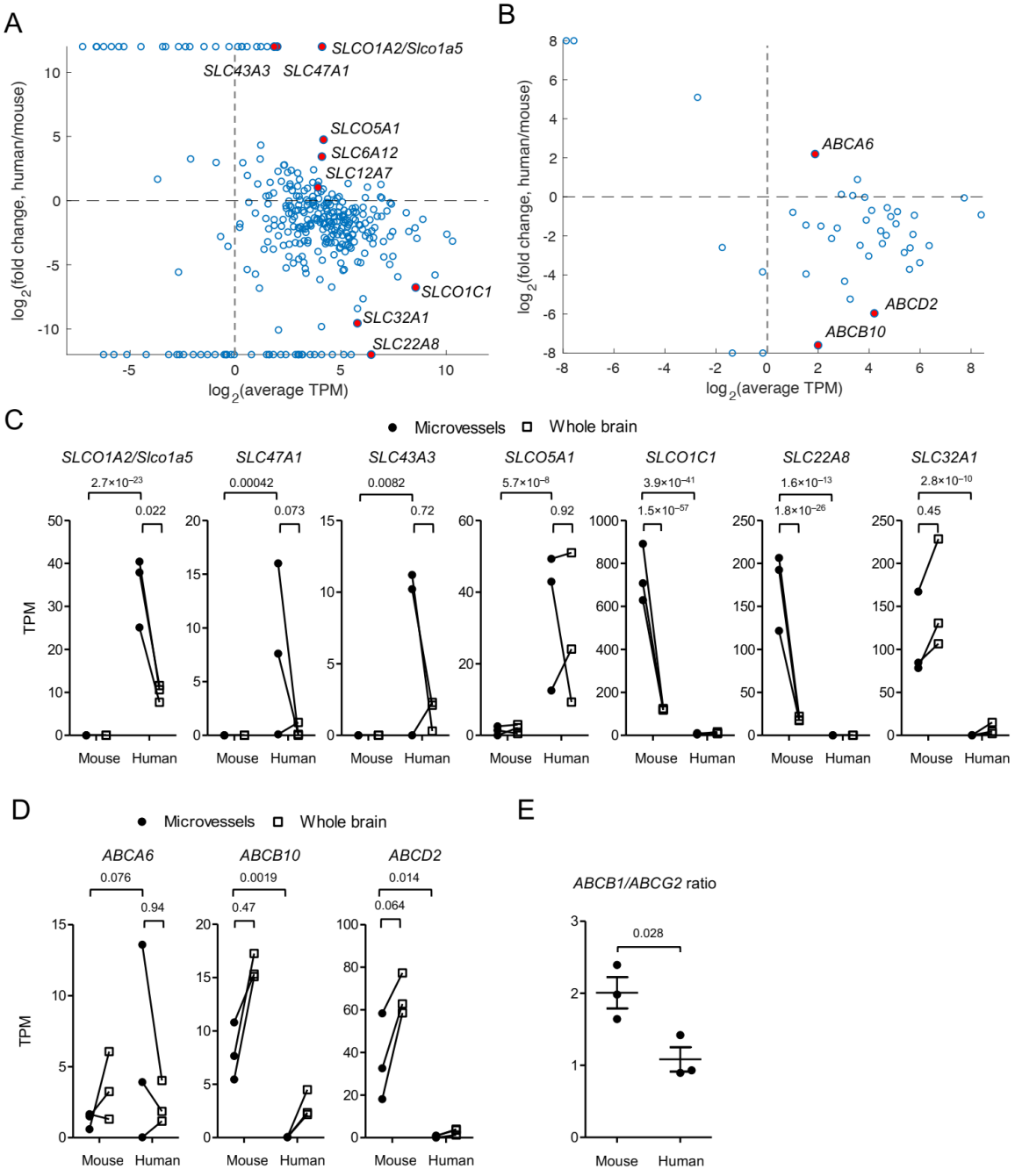

Supplemental Figure 2.6 Validation of putative human brain pericyte-enriched transcripts. Differential expression analysis for human LCM microvessels compared to human brain endothelial cells. **(A)** Comparison of solute carrier (*SLC*) transcript abundance in human and mouse LCM microvessels. The log2(fold change) of human transcript abundance versus the

homologous mouse transcript abundance is plotted against the average abundance in human and mouse. Each point represents one gene with known mouse-human homology. Genes with zero expression in all samples were excluded. Genes to the right of the vertical line at $\log_2$(average TPM) = 0 are moderately or highly expressed in at least one species. A subset of human-enriched *SLC*s (*SLCO1A2*, *SLC47A1*, *SLC43A3*, *SLCO5A1*, *SLC6A12*, and *SLC12A7*) and mouse-enriched *SLC*s (*SLCO1C1*, *SLC22A8*, and *SLC32A1*) are highlighted. Genes with zero expression in one species were visualized with an average $\log_2$(fold change) of ± 12. Complete results of this analysis are in Supplementary Table S5. **(B)** Comparison of ATP binding cassette (*ABC*) transcript abundance in human and mouse LCM microvessels. The $\log_2$(fold change) of human transcript abundance versus the homologous mouse transcript abundance is plotted against the average abundance in human and mouse. Each point represents one gene with known mousehuman homology. Genes with zero expression in all samples were excluded. Genes to the right of the vertical line at $\log_2$(average TPM) = 0 are moderately or highly expressed in at least one species. A subset of human-enriched *ABC*s (*ABCA6*) and mouse-enriched *ABC*s (*ABCB10* and *ABCD2*) are highlighted. Genes with zero expression in one species were visualized with an average $\log_2$(fold change) of ± 8. Complete results of this analysis are in Supplementary Table S5. **(C)** Transcript abundance of selected genes in biological triplicates of LCM microvessels and whole brain from human and mouse. *Slco1a5* is the mouse homolog of human *SLCO1A2*. Lines connect datapoints from matched LCM microvessel and whole brain samples. Adjusted P-values (from DESeq2) are shown; Wald test with Benjamini-Hochberg correction. **(D)** Transcript abundance of genes highlighted in (B) in biological triplicates of LCM microvessels and whole brain from human and mouse. Lines connect datapoints from matched LCM microvessel and whole brain samples. Adjusted P-values (from DESeq2) are shown; Wald test with

BenjaminiHochberg correction. **(E)** Ratio of *ABCB1* (mouse *Abcb1a*) to *ABCG2* transcript abundance (TPM) in human and mouse LCM microvessels. P-value shown from Student's *t* test.

Supplemental files available online [1].

Supplemental File 2.1 Characteristics of RNA samples and associated RNA-seq datasets.

Supplemental File 2.2 Count, FPKM, and TPM values for mouse and human LCM microvessel and whole brain datasets.

Supplemental File 2.3 SRA accession numbers for reference datasets.

Supplemental File 2.4 Differential expression analysis for mouse and human LCM microvessels compared to whole brain.

Supplemental File 2.5 Human-mouse gene homology and differential expression analysis.

Supplemental File 2.6 Putative pericyte transcripts.

2.8 References

1. Song HW, Foreman KL, Gastfriend BD, Kuo JS, Palecek SP, Shusta EV. Transcriptomic comparison of human and mouse brain microvessels. Sci Rep. 2020;10:12358.

2. Engelhardt B, Sorokin L. The blood-brain and the blood-cerebrospinal fluid barriers: Function and dysfunction. Seminars in Immunopathology. 2009;31:497–511.

3. Abbott NJ, Patabendige AAK, Dolman DEM, Yusof SR, Begley DJ. Structure and function of the blood-brain barrier. Neurobiology of Disease. 2010;37:13–25.

4. Pardridge WM. The blood-brain barrier: Bottleneck in brain drug development. NeuroRX. 2005;2:3–14.

5. Zhao Z, Sagare AP, Ma Q, Halliday MR, Kong P, Kisler K, et al. Central role for PICALM in amyloid-β blood-brain barrier transcytosis and clearance. Nature Neuroscience. 2015;18:978–87.

6. Halliday MR, Rege S V, Ma Q, Zhao Z, Miller CA, Winkler EA, et al. Accelerated pericyte degeneration and blood-brain barrier breakdown in apolipoprotein E4 carriers with Alzheimer's disease. Journal of cerebral blood flow and metabolism : official journal of the International Society of Cerebral Blood Flow and Metabolism. 2015;36:1–9.

7. Vatine GD, Al-Ahmad A, Barriga BK, Svendsen S, Salim A, Garcia L, et al. Modeling Psychomotor Retardation using iPSCs from MCT8-Deficient Patients Indicates a Prominent Role for the Blood-Brain Barrier. Cell Stem Cell. 2016;1–13.

8. Lim RG, Quan C, Reyes-Ortiz AM, Lutz SE, Kedaigle AJ, Gipson TA, et al. Huntington's Disease iPSC-Derived Brain Microvascular Endothelial Cells Reveal WNT-Mediated Angiogenic and Blood-Brain Barrier Deficits. Cell Reports. 2017;19:1365–77.

9. Daneman R, Zhou L, Agalliu D, Cahoy JD, Kaushal A, Barres BA. The mouse blood-brain barrier transcriptome: A new resource for understanding the development and function of brain endothelial cells. PLoS ONE. 2010;5:1–16.

10. He L, Vanlandewijck M, Mäe MA, Andrae J, Ando K, Del Gaudio F, et al. Single-cell RNA sequencing of mouse brain and lung vascular and vessel-associated cell types. Scientific data. 2018;5:180160.

11. Vanlandewijck M, He L, Mäe MA, Andrae J, Ando K, Del Gaudio F, et al. A molecular atlas of cell types and zonation in the brain vasculature. Nature. 2018;554:475–80.

12. Zhang Y, Chen K, Sloan SA, Bennett ML, Scholze AR, O'Keeffe S, et al. An RNA-Sequencing Transcriptome and Splicing Database of Glia, Neurons, and Vascular Cells of the Cerebral Cortex. Journal of Neuroscience. 2014;34:11929–47.

13. Hupe M, Li MX, Kneitz S, Davydova D, Yokota C, Kele-Olovsson J, et al. Gene expression profiles of brain endothelial cells during embryonic development at bulk and single-cell levels. Science Signaling. 2017;10:1–13.

14. He L, Vanlandewijck M, Raschperger E, Andaloussi Mäe M, Jung B, Lebouvier T, et al. Analysis of the brain mural cell transcriptome. Scientific Reports. 2016;6:35108.

15. Aday S, Cecchelli R, Hallier-Vanuxeem D, Dehouck MP, Ferreira L. Stem Cell-Based Human Blood-Brain Barrier Models for Drug Discovery and Delivery. Trends in Biotechnology. 2016;34:382–93.

16. Syvänen S, Lindhe Ö, Palner M, Kornum BR, Rahman O, Långström B, et al. Species differences in blood-brain barrier transport of three positron emission tomography radioligands with emphasis on P-glycoprotein transport. Drug Metabolism and Disposition. 2009;37:635–43.

17. Uchida Y, Ohtsuki S, Katsukura Y, Ikeda C, Suzuki T, Kamiie J, et al. Quantitative targeted absolute proteomics of human blood-brain barrier transporters and receptors. Journal of neurochemistry. 2011;117:333–45.

18. Darmanis S, Sloan SA, Zhang Y, Enge M, Caneda C, Shuer LM, et al. A survey of human brain transcriptome diversity at the single cell level. Proceedings of the National Academy of Sciences of the United States of America. 2015;112:7285–90.

19. La Manno G, Gyllborg D, Codeluppi S, Nishimura K, Salto C, Zeisel A, et al. Molecular Diversity of Midbrain Development in Mouse, Human, and Stem Cells. Cell. 2016;167:566-580.e19.

20. Polioudakis D, de la Torre-Ubieta L, Langerman J, Elkins AG, Shi X, Stein JL, et al. A Single-Cell Transcriptomic Atlas of Human Neocortical Development during Mid-gestation. Neuron. 2019;103:785-801.e8.

21. Suhy AM, Webb A, Papp AC, Geier EG, Sadee W. Expression and splicing of ABC and SLC transporters in the human blood-brain barrier measured with RNAseq. European Journal of Pharmaceutical Sciences. 2017;103:47–51.

22. Zhang Y, Sloan SA, Clarke LE, Caneda C, Plaza CA, Blumenthal PD, et al. Purification and Characterization of Progenitor and Mature Human Astrocytes Reveals Transcriptional and Functional Differences with Mouse. Neuron. 2016;89:37–53.

23. van den Brink SC, Sage F, Vértesy Á, Spanjaard B, Peterson-Maduro J, Baron CS, et al. Single-cell sequencing reveals dissociation-induced gene expression in tissue subpopulations. Nature Methods. 2017;14:935–6.

24. Emmert-Buck MR, Bonner RF, Smith PD, Chuaqui RF, Zhuang Z, Goldstein SR, et al. Laser capture microdissection. Science (New York, NY). 1996;274:998–1001.

25. Calabria AR, Shusta E V. A Genomic Comparison of *in vivo* and *in vitro* Brain Microvascular Endothelial Cells. Journal of Cerebral Blood Flow & Metabolism. 2008;28:135–48.

26. Cait J, Hughes MR, Zeglinski MR, Chan AW, Osterhof S, Scott RW, et al. Podocalyxin is required for maintaining blood–brain barrier function during acute inflammation. Proceedings of the National Academy of Sciences. 2019;116:4518–27.

27. Wang Y, Südhof TC. Genomic definition of RIM proteins: Evolutionary amplification of a family of synaptic regulatory proteins. Genomics. 2003;81:126–37.

28. Rivera C, Voipio J, Payne JA, Ruusuvuori E, Lahtinen H, Lamsa K, et al. The K+/Cl- co-transporter KCC2 renders GABA hyperpolarizing during neuronal maturation. Nature. 1999;397:251–5.

29. Li F, Lan Y, Wang Y, Wang J, Yang G, Meng F, et al. Endothelial Smad4 Maintains Cerebrovascular Integrity by Activating N-Cadherin through Cooperation with Notch. Developmental Cell. 2011;20:291–302.

30. Armulik A, Abramsson A, Betsholtz C. Endothelial/pericyte interactions. Circulation Research. 2005;97:512–23.

31. Hagenauer MH, Schulmann A, Li JZ, Vawter MP, Walsh DM, Thompson RC, et al. Inference of cell type content from human brain transcriptomic datasets illuminates the effects of age, manner of death, dissection, and psychiatric diagnosis. Hetman M, editor. PLOS ONE. 2018;13:e0200003.

32. Li J, Li Y, Li W, Luo H, Xi Y, Dong S, et al. Guide Positioning Sequencing identifies aberrant DNA methylation patterns that alter cell identity and tumor-immune surveillance networks. Genome Res. 2019;29:270–80.

33. Uhlén M, Fagerberg L, Hallström BM, Lindskog C, Oksvold P, Mardinoglu A, et al. Proteomics. Tissue-based map of the human proteome. Science (New York, NY). 2015;347:1260419.

34. Geier EG, Chen EC, Webb A, Papp AC, Yee SW, Sadee W, et al. Profiling Solute Carrier Transporters in the Human Blood – Brain Barrier. Clin Pharmacol Ther. 2013;94:636–9.

35. Armulik A, Genové G, Mäe M, Nisancioglu MH, Wallgard E, Niaudet C, et al. Pericytes regulate the blood-brain barrier. Nature. 2010;468:557–61.

36. Daneman R, Zhou L, Kebede AA, Barres BA. Pericytes are required for blood–brain barrier integrity during embryogenesis. Nature. 2010;468:562–6.

37. Hall CN, Reynell C, Gesslein B, Hamilton NB, Mishra A, Sutherland BA, et al. Capillary pericytes regulate cerebral blood flow in health and disease. Nature. 2014;508:55–60.

38. Stebbins MJ, Gastfriend BD, Canfield SG, Lee M-S, Richards D, Faubion MG, et al. Human pluripotent stem cell–derived brain pericyte–like cells induce blood-brain barrier properties. Science Advances. 2019;5:eaau7375.

39. Munji RN, Soung AL, Weiner GA, Sohet F, Semple BD, Trivedi A, et al. Profiling the mouse brain endothelial transcriptome in health and disease models reveals a core blood-brain barrier dysfunction module. Nature neuroscience. 2019;22:1892–902.

40. Tasic B, Yao Z, Graybuck LT, Smith KA, Nguyen TN, Bertagnolli D, et al. Shared and distinct transcriptomic cell types across neocortical areas. Nature. 2018;563:72–8.

41. Boerkoel CF, Takashima H, Stankiewicz P, Garcia CA, Leber SM, Rhee-Morris L, et al. Periaxin Mutations Cause Recessive Dejerine-Sottas Neuropathy. The American Journal of Human Genetics. 2002;68:325–33.

42. Wang MM, Zhang X, Lee SJ, Maripudi S. Expression of periaxin (PRX) specifically in the human cerebrovascular system: PDZ domain-mediated strengthening of endothelial barrier function. Scientific Reports. 2018;8:10042.

43. Haque A, Engel J, Teichmann SA, Lönnberg T. A practical guide to single-cell RNA-sequencing for biomedical research and clinical applications. Genome Medicine. 2017;9:75.

44. Palladino SP, Helton ES, Jain P, Dong C, Crowley MR, Crossman DK, et al. The Human Blood-Nerve Barrier Transcriptome. Scientific Reports. 2017;7:17477.

45. Armulik A, Genové G, Betsholtz C. Pericytes: Developmental, Physiological, and Pathological Perspectives, Problems, and Promises. Developmental Cell. 2011;21:193–215.

46. Shen-Orr SS, Gaujoux R. Computational deconvolution: extracting cell type-specific information from heterogeneous samples. Current Opinion in Immunology. 2013;25:571–8.

47. Gong T, Szustakowski JD. DeconRNASeq: A statistical framework for deconvolution of heterogeneous tissue samples based on mRNA-Seq data. Bioinformatics. 2013;29:1083–5.

48. Warren MS, Zerangue N, Woodford K, Roberts LM, Tate EH, Feng B, et al. Comparative gene expression profiles of ABC transporters in brain microvessel endothelial cells and brain in five species including human. Pharmacological Research. 2009;59:404–13.

49. Jia C, Keasey MP, Malone HM, Lovins C, Sante RR, Razskazovskiy V, et al. Vitronectin from brain pericytes promotes adult forebrain neurogenesis by stimulating CNTF. Experimental Neurology. 2019;312:20–32.

50. Dobin A, Davis CA, Schlesinger F, Drenkow J, Zaleski C, Jha S, et al. STAR: Ultrafast universal RNA-seq aligner. Bioinformatics. 2013;29:15–21.

51. Afgan E, Baker D, van den Beek M, Blankenberg D, Bouvier D, Čech M, et al. The Galaxy platform for accessible, reproducible and collaborative biomedical analyses: 2016 update. Nucleic Acids Research. 2016;44:W3–10.

52. Liao Y, Smyth GK, Shi W. featureCounts: an efficient general purpose program for assigning sequence reads to genomic features. Bioinformatics. 2014;30:923–30.

53. Love MI, Huber W, Anders S. Moderated estimation of fold change and dispersion for RNA-seq data with DESeq2. Genome biology. 2014;15:550.

54. Mi H, Huang X, Muruganujan A, Tang H, Mills C, Kang D, et al. PANTHER version 11: Expanded annotation data from Gene Ontology and Reactome pathways, and data analysis tool enhancements. Nucleic Acids Research. 2017;45:D183–9.

55. Mootha VK, Lindgren CM, Eriksson K-F, Subramanian A, Sihag S, Lehar J, et al. PGC-1alpha-responsive genes involved in oxidative phosphorylation are coordinately downregulated in human diabetes. Nature genetics. 2003;34:267–73.

56. Subramanian A, Tamayo P, Mootha VK, Mukherjee S, Ebert BL, Gillette MA, et al. Gene set enrichment analysis: A knowledge-based approach for interpreting genome-wide expression profiles. Proceedings of the National Academy of Sciences of the United States of America. 2005;102:15545–50.

57. Butler A, Hoffman P, Smibert P, Papalexi E, Satija R. Integrating single-cell transcriptomic data across different conditions, technologies, and species. Nature Biotechnology. 2018;36:411–20.

Chapter 3 – Short-Term Shear Stress and Activation of Piezo1 Causes Reduced Efflux Transport Activity at the Blood-Brain Barrier

3.1 Summary

Background: Recent work has suggested the efflux activity of the blood-brain barrier (BBB) is a dynamic feature controlled by inputs such as the circadian rhythm. Here we test a major component of the endothelial niche, shear stress, to identify if increased shear stress during neuronal activity could reduce efflux transport activity. We further explored if induction of the BBB relevant mechanosensitive channel, Piezo1, through the agonist Yoda1 (Y1) could similarly reduce efflux activity.

Methods: We accomplished this by the direct application of shear stress to cultured rat brain endothelial cells and observed accumulation of Rhodamine123, a substrate for the major efflux transporter, P-glycoprotein (P-gp). We further explored a potential contribution of mechanosensory pathways by activating Piezo1 using the Y1 agonist. By applying Y1 to both a human pluripotent stem cell derived BBB model and to rat brain endothelial cells, we were able to artificially simulate shear and evaluate P-gp activity.

Results: The application of shear stress drove a significant increase in Rhodamine123 accumulation, consistent with reduced efflux transport activity in the BBB model. Further, Yoda1 application similarly caused increased Rhodamine123 accumulation in an acute and reversible manner.

Conclusions: In this work, we have demonstrated that shear stress and activation of Piezo1 can reduce P-gp efflux activity at the *in vitro* BBB. Our work here could suggest an energy conservation mechanism at the endothelium during periods of neuronal activity potentially through Piezo1. However, further experiments directly linking Piezo1 activation to shear stress regulation of P-gp activity will be necessary to confirm this hypothesis.

3.2 Introduction

The central nervous system (CNS) is protected by numerous mechanisms to ensure its continuing function and health. The blood-brain barrier (BBB) allows the selective and restrictive transport between blood and the brain parenchyma [1] which protects from perturbations in blood compounds and nutrients, as well as preventing the passage of foreign compounds including, but not limited to, most small molecule drugs and almost all antibody therapeutics [2]. The BBB is predominantly a result of the unique properties of CNS endothelium. These brain microvascular endothelial cells (BMECs), express substantial tight junctions to restrict hydrophilic compounds and polarized efflux transporters which expel more hydrophobic compounds that can successfully cross the cell membrane and return them to the bloodstream[3,4].

Current work has begun to explore the impact of various components of the neurovascular niche that may impact the behavior of the BBB endothelium. One factor of interest is the mechanical forces caused by changes in blood flow. Shear stress has been linked in generic endothelial cell models to increased transcription factor expression (*KLF2*, *KFL4*, e.g.) [5–7], reduced proliferation [8], and alignment with flow [9,10]. Similarly, for brain endothelium, immortalized and stem cell derived models saw reduced proliferation and apoptosis rates, but no alignment to flow [11,12]. Other work with stem cell derived BBB models have suggested transcriptional increases of BBB relevant genes including P-gp, encoded by *ABCB1* in response to shear stress [13,14]. However, most of these experiments tend to apply shear stress for a minimum of 24 hours. These experiments are particularly helpful in indicating genes regulated or dysregulated by shear stress. They do not, however, describe short term sensing and

response to dynamic changes in shear flow. One of the classic changes brought on by regional neuronal activation is increased blood flow [15,16] which drives a transient increase in shear.

Endothelial cells across the body express numerous mechanisms to detect physical forces and perturbations within their environment [17]. One particular mechanism of interest is mechanosensitive cation channels. These channels open due to physical flow over the surface of the cell or membrane deflection. These channels open and allow cation influx, including calcium. Recent work into mechanosensitive cation channels has identified Piezo1 as a novel and potentially important endothelial transport involved in tip cell invasion into developing tissues [18,19] and in calcium influx in response to pressure at the mouse brain endothelium [20,21].

Additionally, an *in vivo* experiment utilizing mice with regionally expressed engineered neuronal receptors (DREADD) saw regional permeability associated with regional neuronal activation [22]. In this model, neuronal activation led to an increase in brain accumulation of Rhodamine 123, a target of P-gp efflux transport. Conversely, reducing neuronal activity in that region with a modified DREADD decreased accumulation. We therefore hypothesized that short term increases in shear stress from neuronal activation may drive downregulation of efflux activity and tested this hypothesis using *in vitro* BBB models.

3.3 Methods

3.3.*1 Stem Cell Maintenance*

In this study we utilized either the WTC 11 GCaMP or IMR90-4 hPSC lines. Both were maintained on 6 well tissue culture polystyrene plates coated for a minimum of 1 hour with 2.5 mg of Matrigel. Cells were fed E8 stem cell maintenance medium every day. When at 70% confluency, cells were passaged via a 7 minute (IMR90-4) or 5 minute (WTC11 GCaMP)

Versene treatment followed by gentle disassociation and replating. Remaining cells were used to start differentiations as described below.

3.3.2 hBMEC-like Cell Differentiation

These cells were differentiated as described previously [23] and will be briefly described here. On Day -3, cells were lifted via 7 minutes of Accutase, quenched with 4 mL DMEM/F12 per 1 mL of Accutase, then spun down at 200 RCF for 5 minutes. Afterwards cells were resuspended in 2 mL E8 + 10 µM Y-27632 per well to be coated and replated onto Matrigel coated plates as above. Every 24 hours for the next 2 days, medium was replaced with 2 mL E8. On Day 0, medium was replaced with 2 mL DMEM/F12 + 1x Non-Essential Amino Acids + 2x GlutaMAX + 4 µM CHIR99021. After 23 hours, medium was replaced with 2 mL DMEM/F12 + 1x Non-Essential Amino Acids + 2x GlutaMAX + 1x B27 and fed daily until Day 6. On Day 6 cells were fed HESFM + 1x B27 + 10 µM Retinoic Acid + 20 ng/mL FGF2. On Day 7 plates were coated with 20 µg/mL fibronectin and 80 µg/mL collagen IV diluted with water and transwells were coated with 100 µg/mL fibronectin and 400 µg/mL collagen IV diluted with water. On Day 8, cells were detached using 30-45 minutes of Accutase treatment followed by quenching in 4:1 DMEM/F12 as previously. Cells were spun down at 200 RCF for 5 minutes before being replated onto the previously prepared plates and transwells in HESFM + 1x B-27 + 10 µM Retinoic Acid + 20 ng/mL FGF2 at 500,000 cells/cm^2 for transwells and 25,000 cells/cm^2 for plates. On Day 9, medium is replaced with HESFM + 1x B27. All assays are started on Day 10.

3.3.3 MDCK-MDR1 Cell Culture

Cells were maintained on uncoated 6 well tissue culture treated polystyrene plates in 2 mL DMEM + 10% Fetal Bovine Serum. At confluency, cells were passaged 1:6 with Accutase.

For experimental samples, cells were passaged to uncoated tissue culture treated polystyrene 24 well plates.

3.3.4 rBMEC Isolation

Half a rat brain was used to seed each chip as a rough way to control consistency. For tissue culture plates, roughly 1 rat brain per plate was used. 96 wells for ICC were seeded from small volumes of remaining liquid. Each isolation is a pool of 2 rat brains and treated separately from other isolations to ensure sufficient numbers of microvessels. Sprague-Dawley rats between 220-250 g were first anesthetized with 2-5% isoflurane. Once the rats failed both the pinch and righting tests, they were swiftly beheaded using a guillotine and brains extracted. Brain segments were stored in DMEM on ice. Brain hemispheres were rolled on paper to capture meninges, followed by vigorous disassociation into 1 mL DMEM. Solution was diluted with a further 9 mL of DMEM before trituration. Then 0.75 mL of 10 mg/mL collagenase and 150 µL of 1 mg/mL Dnase I were added. Solution was incubated for 1 hour and 15 minutes at 37 °C on a shaker at 250 rpm. Percoll gradient was prepared in a 30 mL Oakridge tube with 10 mL Percoll, 19 mL PBS, 1 mL 10x PBS, 1 mL FBS and centrifuged at 30,000 g for at least 30 minutes. After incubation, brain solution was diluted to 40 mL using DMEM, and then spun down at 1000 RCF for 8 minutes. Supernatant was aspirated and pellet resuspended in 25 mL 20% (m/v) BSA in DMEM, triturated again, and then centrifuged at 1000 RCF and 4 °C for 20 minutes. Neuron/glia layer and supernatant were aspirated before resuspension in 6.75 mL DMEM followed by trituration. 0.5 mL of 10 mg/mL Collagenase-dispase and 50 µL of 1 mg/mL DNase 1 were added and solution was incubated for 1 hour at 37 °C on a shaker at 250 RPM. Fragments were spun down at 700 RCF for 6 minutes and supernatant aspirated. Pellet was resuspended in 1 mL DMEM and added to the top of the prepared Percoll gradient. Percoll was centrifuged at 1000

RCF for 10 minutes at 4 °C. A 5 mL syringe with a blunt 16 gauge 5” needle was used to extract the microvessel containing layer which was diluted with DMEM at roughly 4 mL per mL of microvessel solution. This was spun down at 200 RCF for 10 minutes and then and plated into ibidi 0.8 mm and 0.6 mm microfluidic chips coated 250-300 µL of 0.2 mg/mL collagen IV and 0.2 mg/mL fibronectin for at least 1 hour, in rat primary medium (DMEM + 10% FBS + 1x GlutaMAX + 1x Anti-anti + 4 µg/mL puromycin + 100 ng/mL heparin + 20 ng/mL FGF2) every 8 hours until confluent (usually between 3-4 days). To ensure medium was successfully changed, 200 µL was added to one side and removed from the other two times. Cells were connected to microfluidics devices after visibly confluent.

3.3.5 Immunocytochemistry (ICC)

Cells were plated onto 96 well tissue culture polystyrene plates on the appropriate plating day dependent on cell type. Cells were washed with cold PBS and then 50 µL of methanol was added for 15 minutes to fix. Cells were washed again in PBS before 100 µL of 10% Goat Serum in PBS for 1 hour at room temperature. Primary solutions were prepared with the dilutions in Table 3.1 in 10% Goat Serum in PBS. Cells were incubated with primary solution overnight at 4 °C shaking slowly. Afterwards, cells were washed 3 times with cold PBS before applying secondary solution and shaking at room temperature for 1 hour or overnight at 4 °C protected from light. Cells were then washed twice, treated with Hoechst 33342 solution for 5-10 minutes, switched to PBS and then imaged.

3.3.6 Rhodamine 123 (Rh123) Accumulation Assay

Assay was performed as previously described [24], with modifications as described in the experiment. Cells were plated onto 24 well tissue culture treated polystyrene plates and allowed at least 24 hours to recover. Wells were treated preemptively with 1 hour of various

concentrations of Y1, 10 μM CsA or an appropriate amount of DMSO to serve as a vehicle in 100 μL Hanks' Balanced Salt Solution (HBSS) to ensure that CsA or Y1 had time to take effect before addition of the Rh123. Plates were shaken at 30 RPM in a 37 °C incubator with humidification and 5% CO_2. HBSS was then replaced with HBSS + Y1/CsA/DMSO as previously + 10 μM Rh123 and returned to the incubator and shaker for 1 to 2 hours depending on the experiment. Cells were then thoroughly washed with cold PBS 3 times before being lysed with 100 μL of RIPA. Lysate was then imaged on a TECAN Plate Reader to assess Rh123 accumulation. Samples were frozen and at a later time an BCA Assay Kit was utilized to assess protein concentration in each well used for normalization. A blank well with cells but no Rh123 was used as a background control.

3.3.7 RNA Isolation and qPCR

Cells were plated onto 24 well tissue culture treated polystyrene plates and treated with Y1 or vehicle. RNA was isolated by utilizing the Qiagen Miniprep kit. qPCR was performed using SYBR Green qPCR mix. Primers used are provided in Table 3.2 and normalized to GAPDH.

3.3.8 Microfluidic Device Assembly and Operation

Fluidic devices were assembled from cell culture grade silicone tubing of internal diameter 1/16" or 1/32" with nylon 1/16" hose barb to luer lock or Y-splitter connectors. Lengths of tubing were designed according to ibidi devices. All components were soaped, soaked in bleach, and then soaked in Ethanol to kill contaminants before being autoclaved and assembled prior to use. ibidi Fluid flow was controlled by using tubing of different internal diameters and measured at the start of each run to ensure consistent shear stress.

3.4 Results

3.4.1 BBB Models Used

We chose two BBB models to assess reductions in efflux activity associated with shear stress and Piezo1 activation. We chose these models due to presence of efflux activity, ability to support genetic modifications, and similarity to *in vivo* BMECs [24–26]. The first model was primary cultured rat BMECs (rBMECs). The rBMECs have good efflux transport activity although they are known to suffer from de-differentiation over time in culture [25,27]. To avoid the effects of de-differentiation, we used rBMECs as soon as they were confluent to minimize time in culture. The other model we utilized was hPSC-derived brain microvascular endothelial cell-like (hBMEC-like) cells [23]. This model has high resistance across the tight junctions, and expresses active efflux transporters [23,28] and is therefore applicable to this work, although the model has its shortcomings, transcriptional in particular [29,30]. In addition, hBMEC-like model is more easily scaled up and can be differentiated from genetically modified stem cell lines allowing mechanistic experiments experiments as described below.

For each rBMEC isolation or hBMEC-like cell differentiation, we plated cells or microvessels onto static 96 well tissue culture polystyrene plates. When assays were performed in microfluidic chips, we simultaneously fixed the static cultures and performed validation immunocytochemistry (ICC). For rBMECs, we stained for Cldn5, PECAM-1, and Ocln which showed good endothelial “spindle like” morphology in a monolayer as well as expression of P-gp (Fig 3.1B). For the hPSC derived model, we stained for P-gp, Cldn5, Ocln, and MRP1 (Fig 3.1C). These markers are relevant to critical barrier properties and have previously been shown to be expressed in this model [23]. Tight junctions, as shown by Cldn5 and Ocln, appear continuous with no significant breaks, and transporter expression appears membrane associated

both of which are consistent with previous work [23,28]. Once we were confident that the differentiation and purification protocols were successfully generating the cell types of interest, we proceeded with functional assays.

3.4.2 Shear Stress Drives Increased Accumulation of Rhodamine 123 in rBMECs

As discussed briefly, neuronal activation drives increased blood flow, and a corresponding local increases in shear stress and a coordinate decrease in P-gp activity. We therefore initially hypothesized that application of shear stress would be sufficient to reduce P-gp efflux transport activity in the rBMEC model. To test this hypothesis, we plated microvessels into ibidi microfluidic chips. Chips were fed media containing puromycin every 8 hours for 4-5 days under static conditions until rBMECs expanded and reached confluence [25]. After which, shear stress was applied for 3 hours. We exposed each isolation to either ~0 dyne/cm^2, a minimal shear perfusion control to ensure nutrient delivery and waste removal from the chips, or 16 dyne/cm^2 which is within the physiological range for brain capillary beds [31], and this magnitude had previously been shown to induce effects in BMEC models under longer treatment durations (24+ hours) [11,12]. Flow rate and total reservoir volume were chosen to ensure that the Rh123 efflux substrate solution was thoroughly mixed in each reservoir before being passed over the cells (Fig 3.2A). . We also added cyclosporin A (CsA), a known inhibitor of Pgp, to serve as a maximum accumulation control.

In static culture controls, we observed a statistically significant increase in accumulation on application of our P-gp inhibitor, CsA, indicating that rBMECs exhibit efflux activity in static 96 well plate conditions as expected (Fig 3.2B) [24]. We observed a statistically significant increase in accumulation of Rh123 in CsA conditions versus vehicle in both high and low shear comparisons in the microfluidic device as expected (Fig 3.2C), demonstrating rBMECs in this

geometry are still capable of Rh123 efflux. However, there was no statistically significant difference between low and high shear with CsA which suggests that the total efflux capacity of rBMECs was not impacted by the shear treatment (Fig 3.2C). Most interestingly, the high shear vehicle condition also showed a statistically significant increase in accumulation over the low shear control. This suggests, consistent with our hypothesis, that high shear stress reduces Pgp efflux activity.

3.4.3 Piezo1 Activation Increases Intercellular Calcium in the hPSC Derived Model

Endothelial response to shear stress can activate numerous mechanosensitive pathways [17]. We chose to explore efflux transport inhibition to Piezo1 because it has been implicated in vascular pathfinding throughout the body [18,19] and specifically in the developing neural tube [20,21]. In addition, knock out (KO) experiments in extracted mouse microvessels have suggested that the loss of Piezo1 severely inhibits calcium influx [20]. Further, it has a readily available semi selective agonist, Yoda1 (Y1) [32]. We hypothesized that activation of a singular mechanosensory pathway would be sufficient to inhibit P-gp efflux transport.

We started by confirming successful calcium influx, a known effect of Piezo1 channel opening [32], upon application of Yoda1 to a BBB model. The WTC11 GCaMP hPSC line was differentiated into the hPSC-derived BMEC-like cells as described previously [23]. These cells constitutively express GCaMP, which fluoresces upon binding intercellular calcium. After differentiation, we applied Y1 at 25 μM, and immediately performed live cell imaging for 5 minutes (Sup File 3.1). We observed a sudden spike in calcium influx in the first 2 minutes after Y1 addition (Fig 3.3A). ANOVA analysis further confirmed a statistically significant difference in normalized fluorescence over time due to Y1 treatment (FDR < 0.05) versus a vehicle (DMSO) control (Fig 3.3B), though there was clear well-to-well variability in response time. It

should be noted that there is basal GCaMP fluorescence due to normal levels of intracellular calcium, which drives a clear drop in fluorescence over time consistent with photobleaching. The observed calcium influx is consistent with known effects of Piezo1 activation [18–21], and with studies establishing Y1 as a selective activator of Piezo1 [32]. We next proceeded to investigate the impact of Y1 on efflux activity.

3.4.4 Piezo1 Activation Leads to Reduced Efflux Activity

Once calcium influx upon Piezo1 activation was confirmed, we differentiated IMR90-4 iPSCs into BMEC-like cells plated onto 24 well tissue culture treated polystyrene plates to perform efflux transport assays. Cells were first allowed to reach confluence following differentiation and replating. Y1, vehicle, or CsA were added for 3 hours. Rh123 was applied after 1 hour to ensure that the Y1 and CsA had time to successfully inhibit activity and to match other previously published *in vitro* Rh123 accumulation protocols (Fig 3.4A) [24].

We observed a statistically significant decrease in efflux activity following treatment with Y1 (Fig 3.4B). At the highest concentrations of Y1, we observed comparable inhibition to CsA treatment, suggesting a total loss of efflux transport in this model. In addition, there is a Y1 dose-dependent response. At the lowest concentrations of Y1 there is minimal to no additional accumulation above vehicle with steady increases with increasing concentration before reaching maximum accumulation as demonstrated by CsA. This suggests that Y1 is sufficient to inhibit P-gp activity within our hBMEC-like cell model. Withdrawal of Y1 after 1 hour of treatment, and prior to application of Rh123, led to a complete restoration of accumulation to baseline after 2 hours, efflux activity had returned to normal (Fig 3.4B), suggesting that the effects of Y1 are reversible.

We repeated the experimental with rBMECs (Fig 3.4C). There was again a reduction in efflux transport activity. Due to the higher noise within this dataset, it is difficult to confirm a Y1 dose dependent response. There is a statistically significant increase in accumulation on increasing dosage. The highest concentration of Y1 is not statistically different from the CsA control however, which suggests that Y1 can elicit maximum inhibition of P-gp at this dose.

To ensure that P-gp efflux activity is not reduced by direct interactions with Y1, we repeated the accumulation assay utilizing MDCK-MRP1. These canine cells overexpress human P-gp, but do not express any regulatory mechanisms for human P-gp. On treatment with Y1, we observed no change in accumulation behavior, even going well beyond the concentrations utilized in previous experiments (Fig 3.4D). This shows that Y1 itself is not driving the change in efflux behavior. Taken together, we see that Y1 treatment inhibits P-gp in the *in vitro* BBB models tested here.

3.4.5 Effect of Y1 is Retained for a Short Period After Treatment

We hypothesized that if we were observing a regulatory inhibition of efflux activity, it would last for a short period post Piezo1 activation. However, our previous Y1 withdrawal condition had shown a complete restoration to baseline (Fig 3.4B). We then measured accumulation after 1 hour instead to capture a restoration to baseline on removal of Y1 (Fig 3.4A). At 1 hour of accumulation, we observed partial efflux inhibition relative to CsA. Suggesting that efflux inhibition returns to basal activity levels within 2 hours of Piezo1 activation (Fig 3.4B,E).

3.4.6 Y1 Activation Does Not Drive P-gp Transcriptional Changes

Since we had demonstrated that there were decreases in P-gp activity, we further sought to explore whether these could be linked to transcriptional changes. There have been several

reports suggesting, either an up or downregulation of *ABCB1*, the gene encoding P-gp, under shear stress dependent on model and duration of shear [13,22]. We took both our hPSC-derived BMEC-like cell and rBMEC models and applied Y1 at 25 μM for 3 hours to match the Rh123 accumulation assays. After treatment, cells were immediately lysed and RNA was collected. We performed qPCR for *ABCB1* for the hPSC model and *Abcb1a* and *Abcb1b* in rBMECs (Fig 3.5). Our results indicate that there were no statistically significant changes in *ABCB1*, *Abcb1a*, or *Abcb1b* upon Y1 application. While this runs contrary to some previous work, we have activated only a singular mechanotransduction system as opposed to either neural activation [22] or shear stress (Fig 3.2C). It is likely that we have simply not captured the entirety of the niche with regards to this transcriptional change or that our treatment duration is insufficient compared to shear stress application experiments which typically go for 24+ hours.

3.4.7 Long Term Application of Yoda1 Reduces Barrier Properties in BMEC-like Cells

Therefore, we repeated our initial assays of Y1 treatment utilizing hPSC BMEC-like cells. Cells were plated onto either 24 well plates or transwells before application of Y1 for 24 hours. Afterwards, cells on plates were subjected to the same Rh123 accumulation assay as performed previously, while BMEC-like cell monolayers on transwells were used to measure tight junction integrity via transendothelial electrical resistance (TEER). Interestingly, no increased accumulation was observed at any Y1 concentration versus the no Y1 control (Fig 3.5B). This is in contradiction to clear results from the 3 hour treatments with Y1. There was also retained efflux activity in all samples, as evidenced by increased accumulation upon CsA treatment. Interestingly, you would not expect a change in CsA conditions between samples. We also observed a substantial statistically significant drop in TEER (Fig 3.6A), a loss of roughly 75% at concentrations of 10 μM Y1 or higher. Though the TEER value was high enough to

continue to exclude most small molecules [33], this could be indicative of cell stress. Overall, activation of Piezo1 for 24 hours does not inhibit efflux transport activity, but does lead to a substantial reduction in TEER.

3.5 Discussion

We started by first exploring shear stress as an inhibitor of P-gp efflux transport and observed a reduction in activity on application of shear stress, but no reduction in maximum efflux transport in an rBMEC model. These results are consistent with prior work demonstrating the impact of increased neural activity on Rh123 efflux [22] and suggest that shear alone is able to recreate the *in vivo* phenotype with regards to efflux activity.

We further narrowed our experiments to target a single mechanotransduction pathway that has been linked to calcium influx in BMECs *in vivo* [20]. We found that artificial activation of Piezo1 via Y1 induces calcium influx in our hPSC BBB model. This is consistent with literature regarding cations permeability through Piezo1 and the effects of Y1 and Piezo1 opening [20,32]. In addition, calcium has been strongly linked to both immediate short term shear response [20] in cultured mouse BMECs and P-gp efflux transport has been linked in prior literature to fluctuations of magnesium or calcium [24,34–37]. This is consistent with subsequent experiments where Y1 successfully reduced P-gp activity, possibly through this calcium influx in both rBMECs and the hPSC model.

Of note, numerous studies regarding BBB P-gp activity with regards to magnesium and calcium cycling over the circadian rhythm also observe transcriptional cycling of P-gp [22,36,37]. We observed no changes in P-gp transcripts on Piezo1 induction, but do observe changes in activity. This is possibly because shear at that time scale, is not sufficient to drive transcriptional differences and that the differences observed in other work is due to alternative

signaling from the brain parenchyma, increased duration, additional shear responsive signaling, or through circadian mechanisms, none of which are captured within this experimental design [13,14]. Alternatively, calcium concentrations have been linked previously to P-gp activity and changes in calcium have been linked to the application of force on the brain endothelium [20] and to Piezo1 channel opening [32,34]

Our Y1 removal experiments further cemented the reversibility of this response while simultaneously strongly suggesting that the effect observed was not due to direct P-gp interaction. Fluorescent accumulation returned to baseline in our hBMEC-like model following 2 hours without Y1, which suggested either a direct interaction of P-gp and Y1 or activity was restored. A measurement at 1 hour instead of 2 hours showed some loss of efflux activity, but not as much as positive controls potentially suggesting a reversible effect.

We also attempted longer term experiments with a 24 hour treatment window, more closely mimicking some of the *in vivo* shear stress work. However, we observed a loss in tight junction integrity as measured by TEER, and no change in efflux activity. A drop in tight junction integrity was not observed in short term *in vivo* experiments and we did not observe conclusive reductions in P-gp activity [22]. It is difficult to interpret these results given the changing magnitudes of CsA inhibited controls suggested a change in maximum efflux activity or altered accumulation rates.

Lastly, we sought to demonstrate a conclusive link between shear response and Piezo1 activation in our models. However, siRNA knockdown in rBMECs proved ineffective in the microfluidic devices. We additionally tried to generate an hPSC Piezo1 KO line, however loss of Piezo1 expression appeared to negatively impact proliferation rate, leading to loss of heterozygous knockouts after two or three passages and we were not able to isolate any

homozygous knock outs. Therefore, we are currently unable to definitively conclude that Piezo1 is the cause of the calcium influx or the changes observed under shear.

3.6 Conclusion

Our data here demonstrates that shear plays a role in short term regulation of P-gp activity. In addition, we were able to capture a similar phenotype using a Piezo1 agonist in two BBB models. However, further work is needed to confirm the exact mechanism behind this shift in behavior as well as to confirm if Piezo1 is the shear-responsive agent responsible for the reduction in efflux activity.

3.7 Figures

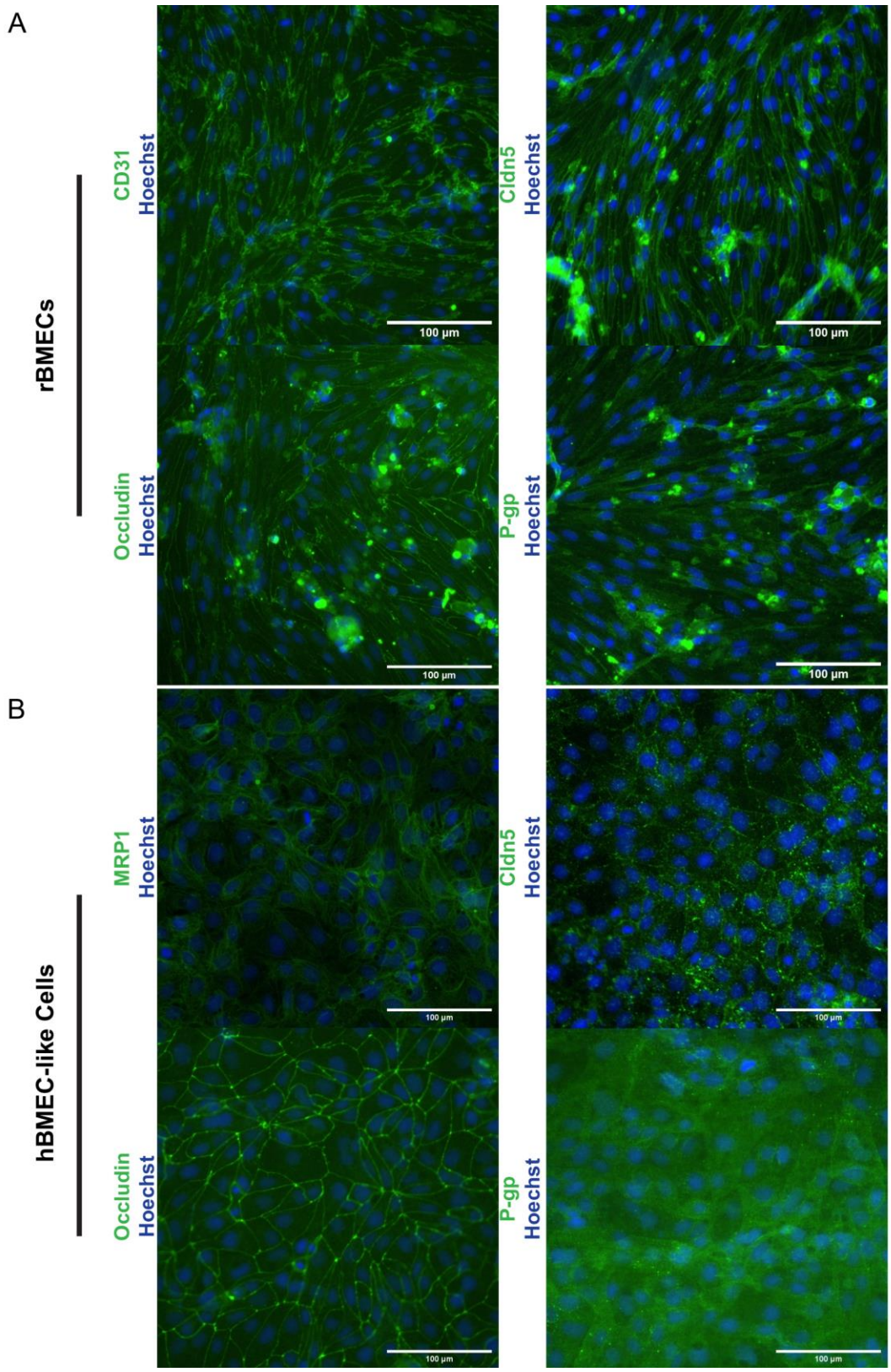
A
rBMECs
CD31
Hoechst
Cldn5
Hoechst
Occludin
Hoechst
P-gp
Hoechst
100 µm
B
hBMEC-like Cells
MRP1
Hoechst
Cldn5
Hoechst
Occludin
Hoechst
P-gp
Hoechst
100 µm

Figure 3.1 ICC of various, previously published, markers of the BBB models utilized in this study. A) rBMECs fixed and imaged at the same time as down stream assays demonstrating tight junction protein expression and localization and efflux transporter expression. B) hBMEC-like cells demonstrating continuous tight junctions and efflux transporter expression.

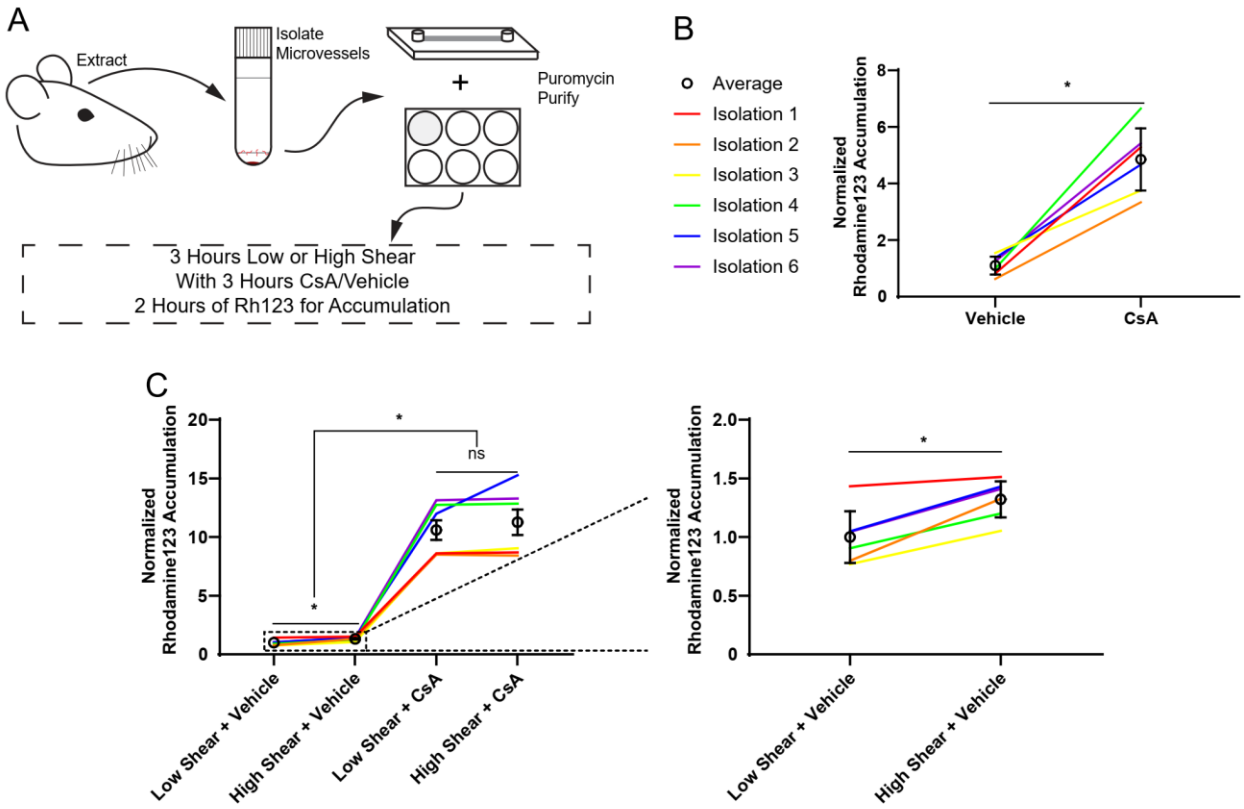

Figure 3.2 Shear stress leads to deactivation of P-gp. A) Visual depiction of experimental design. B) Static plate accumulation assay control. Lines represent paired isolations (N = 6). Black lines are grand means with standard deviation. Statistics via a paired t-test *p<0.05 C) Rh123 accumulation inside microfluidic chips treated with shear stress for 3 hours. Left is all conditions, right is just the vehicle + shear conditions. Lines represent a single isolation (N = 6). Statistics via paired t-test with Sidak's correction * $p < 0.05$

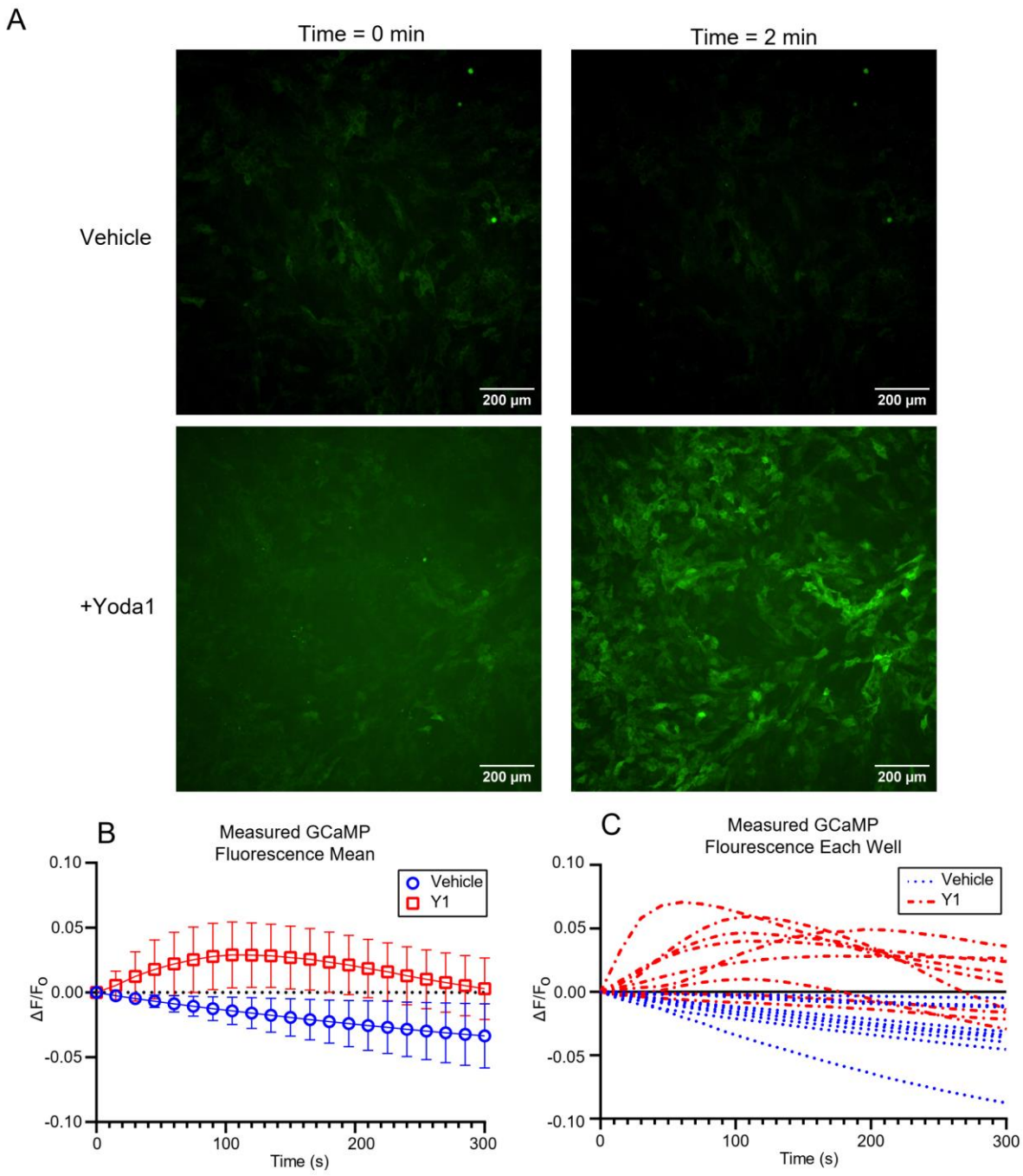

Figure 3.3 Y1 drives calcium influx in hBMEC-like cells. A) Example images of hBMEC-like GCaMP expressing cells treated with either vehicle (DMSO) or 25 µM Y1 and imaged at multiple images. B) Y axis is change in fluorescence from initial fluorescence normalized to initial fluorescence. Mean of n = 3 biological replicates over N = 3 differentiations. Statistically

significant difference with an FDR < 0.05 according to 2 Way ANOVA. C) Same data as in B, but with each individual well used shown to demonstrate variability of Y1 response and the consistency of the vehicle photobleaching response between wells.

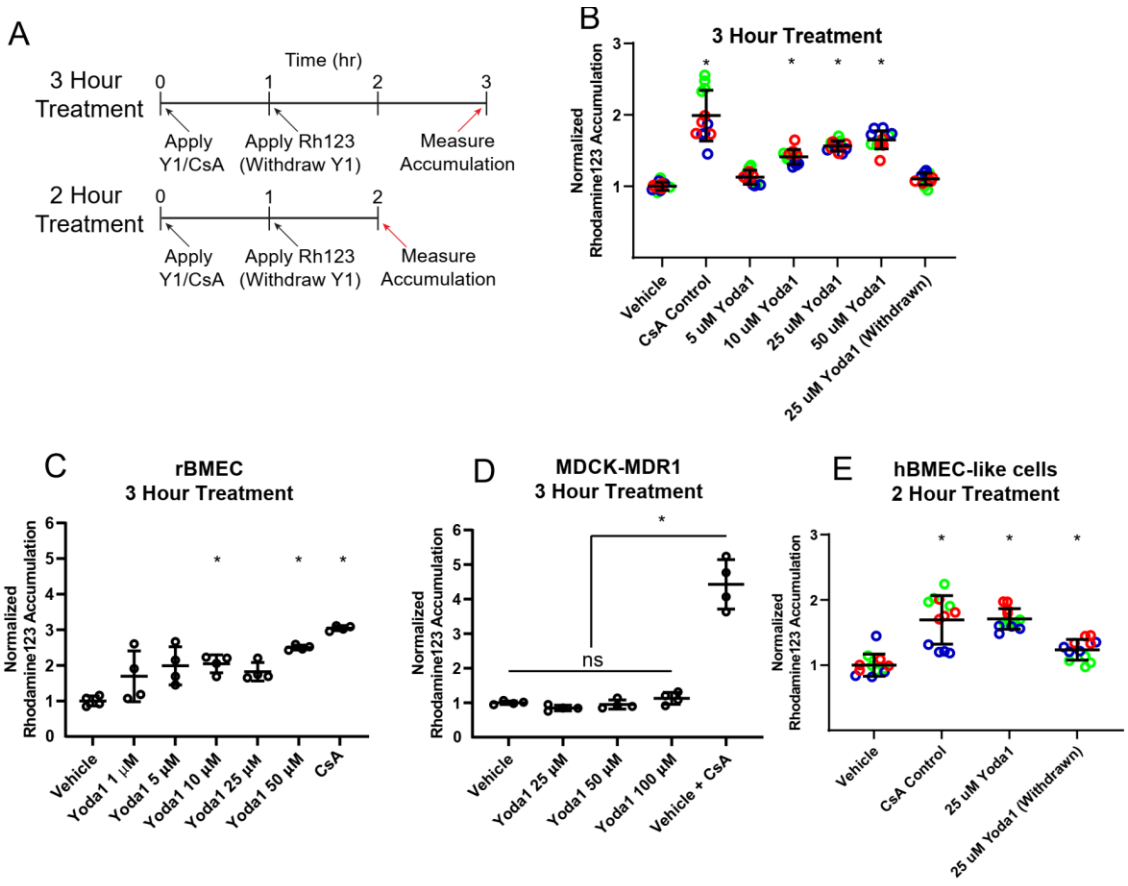

Figure 3.4 Application of Y1 to three different BBB models. A) Visual depiction of treatment design and similarity to shear stress treatment B) Rh123 accumulation on a static Y1 treated IMR90 hPSC-BBB model with CsA positive control. Dots represent n = 4 biological replicates, colors represent N = 3 differentiations. Statistics only shown versus Vehicle for clarity. C) Rh123 accumulation assay in rBMECs treated with Y1. Normalized to average of the vehicle. Dots represent n = 6 biological replicates from 1 isolation. Statistics only shown versus Vehicle. D) Rh123 accumulation in MDCK-MDR1 cells treated with Y1, normalized to the average of the vehicle controls. Dots represent n = 4 biological well replicates. E) Rh123 accumulation in IMR90 hPSC-BBB model cells post treatment with Y1 with only 1 hour for accumulation. Dots represent biological replicates (n = 3), colors represent differentiations (N = 3). All statistics via a Two-way ANOVA with Tukey's post hoc * $p<0.05$

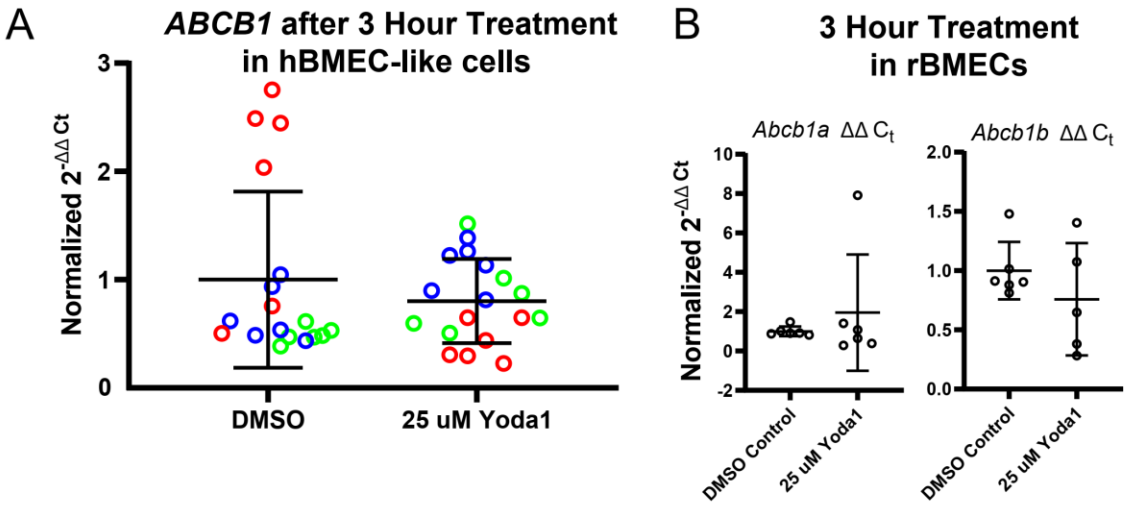

Figure 3.5 Transcriptional changes after 3 hours of treatment with Y1. A) hPSC derived cells in static culture treated with Y1 for 3 hours. Dots represent different biological replicates (n = 6), colors represent differentiations (N = 3). No statistically significant ($p < 0.05$) difference was observed between DMSO control and Y1 treatment by Student's t test. B) rBMECs in static culture treated with Y1 for 3 hours. Dots represent biological replicates (n = 6). No statistically significant ($p < 0.05$) difference was observed between DMSO control and Y1 with either Abcb1a or Abcb1b via Student's t-test.

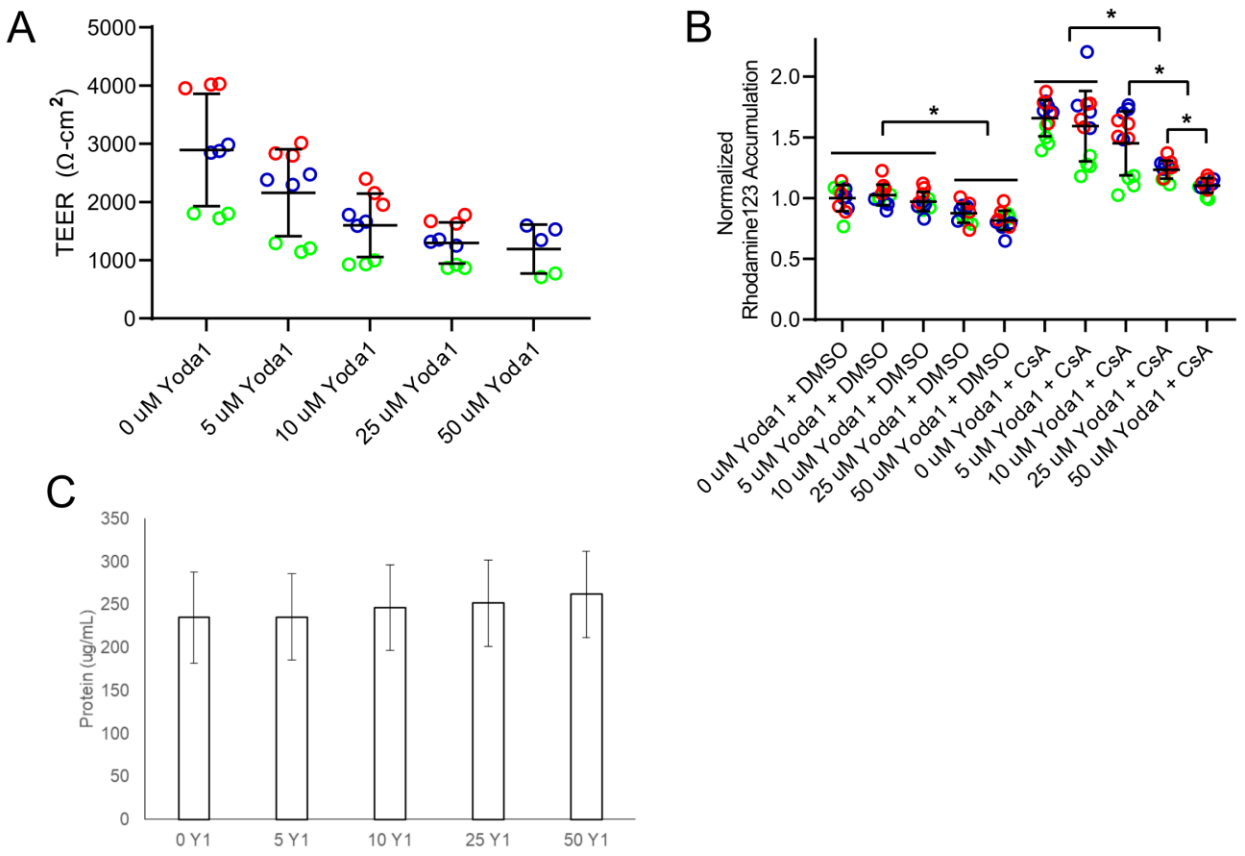

Figure 3.6 24 hour treatment of the IMR90 derived hBMEC-like cells with Y1. A) TEER after 24 hours. Dots represent biological replicates (n = 3), colors represent differentiations (N = 3), black lines represent average and statistical significance. B) Rh123 accumulation performed post 24 hours of Y1 treatment with and without CsA or DMSO (Vehicle) all normalized to the average value of 0 µM Y1 + DMSO. Dots represent replicates (n = 4), colors represent differentiations (N = 3), black lines represent average with standard deviations. C) Total protein concentration per well post lysis for the Rh123 accumulation assay. All samples treated with either CsA or DMSO were aggregated to determine if there was an effect due to Y1 concentration.

3.8 Tables

Table 3.1 Antibody dilutions used for ICC

Target	Manufacturer	Cat. No.	Species	Concentration
PECAM	Thermo Fisher	RB-10333-P1	Rabbit	1:100
Ocln	Invitrogen	33-1500	Mouse	1:50
Pgp	Invitrogen	MA5 13854	Mouse	1:25
Cldn5	Invitrogen	35-2500	Mouse	1:200
MRP1	Sigma-Aldrich	MAB4100	Mouse	1:50
Mouse IgG (H+L) 488	Invitrogen	A-11001	Goat	1:200
Rabbit IgG (H+L) 488	Invitrogen	A-11008	Goat	1:200

Table 3.2 Primers used for rat and human samples

Target	Length (bp)	Forward	Reverse
GAPDH	231	GAAGGTGAAGGTCGGAGTCAACG	TCCTGGAAGATGGTGATGGGAT
ABCB1	110	GAAGAGATTGTGAGGGCAGC	CCACCAGAGAGCTGAGTTCC
PIEZO1	212	ACCAACCTCATCAGCGACTT	AACAGGTATCGGAAGACGGC
Gapdh	89	GGGAAACCCATCACCATCTT	CCAGTAGACTCCACGACATACT
Piezo1	100	GCCGAGAGACAGAGAAGAAATAC	GCAATGAGGAAGAGGATGATGA
Abcb1a	100	TCCCGAATATGCCAACAGCA	CTTGTATGTTGTCGGGTTTGTG
Abcb1b	145	TCTCGCTGCTATCATCCACG	GCTGACGGTCTGTGTACTGT

3.9 Supplemental

Supplemental files available upon request

Supplemental File 3.1 – GCaMP video example

3.10 References

1. Pardridge WM. Drug Transport across the Blood–Brain Barrier. Journal of Cerebral Blood Flow & Metabolism. 2012;32:1959–72.

2. Pardridge WM. The Blood-Brain Barrier: Bottleneck in Brain Drug Development. NeuroRx. 2005;2:12.

3. Abbott NJ, Patabendige AAK, Dolman DEM, Yusof SR, Begley DJ. Structure and function of the blood–brain barrier. Neurobiol Dis. 2010;37:13–25.

4. Aday S, Cecchelli R, Hallier-Vanuxeem D, Dehouck MP, Ferreira L. Stem Cell-Based Human Blood–Brain Barrier Models for Drug Discovery and Delivery. Trends Biotechnol. 2016;34:382–93.

5. Dekker RJ, van Soest S, Fontijn RD, Salamanca S, de Groot PG, VanBavel E, et al. Prolonged fluid shear stress induces a distinct set of endothelial cell genes, most specifically lung Krüppel-like factor (KLF2). Blood. 2002;100:1689–98.

6. Tsaryk R, Yucel N, Leonard EV, Diaz N, Bondareva O, Odenthal-Schnittler M, et al. Shear stress switches the association of endothelial enhancers from ETV/ETS to KLF transcription factor binding sites. Sci Rep. 2022;12:4795.

7. Moonen J-R, Chappell J, Shi M, Shinohara T, Li D, Mumbach MR, et al. KLF4 recruits SWI/SNF to increase chromatin accessibility and reprogram the endothelial enhancer landscape under laminar shear stress. Nat Commun. 2022;13:4941.

8. Dimmeler S, Haendeler J, Rippmann V, Nehls M, Zeiher AM. Shear stress inhibits apoptosis of human endothelial cells. FEBS Letters. 1996;399:71–4.

9. Remuzzi A, Dewey CF, Davies PF, Gimbrone MA. Orientation of endothelial cells in shear fields in vitro. Copley AL, Witte S, editors. BIR. 1984;21:617–30.

10. Levesque MJ, Nerem RM. The Elongation and Orientation of Cultured Endothelial Cells in Response to Shear Stress. Journal of Biomechanical Engineering. 1985;107:341–7.

11. Reinitz A, DeStefano J, Ye M, Wong AD, Searson PC. Human brain microvascular endothelial cells resist elongation due to shear stress. Microvascular Research. 2015;99:8–18.

12. DeStefano JG, Xu ZS, Williams AJ, Yimam N, Searson PC. Effect of shear stress on iPSC-derived human brain microvascular endothelial cells (dhBMECs). Fluids and Barriers of the CNS. 2017;14:20.

13. Cecchelli R, Aday S, Sevin E, Almeida C, Culot M, Dehouck L, et al. A Stable and Reproducible Human Blood-Brain Barrier Model Derived from Hematopoietic Stem Cells. Klein R, editor. PLoS ONE. 2014;9:e99733.

14. Park T-E, Mustafaoglu N, Herland A, Hasselkus R, Mannix R, FitzGerald EA, et al. Hypoxia-enhanced Blood-Brain Barrier Chip recapitulates human barrier function and shuttling of drugs and antibodies. Nat Commun. 2019;10:2621.

15. Lassen NA, Ingvar DH, Skinhøj E. Brain Function and Blood Flow. Scientific American. 1978;239:62–71.

16. Paulson O. Blood–brain barrier, brain metabolism and cerebral blood flow. European Neuropsychopharmacology. 2002;12:495–501.

17. Tiezzi M, Deng H, Baeyens N. Endothelial mechanosensing: A forgotten target to treat vascular remodeling in hypertension? Biochemical Pharmacology. 2022;206:115290.

18. Ranade SS, Qiu Z, Woo S-H, Hur SS, Murthy SE, Cahalan SM, et al. Piezo1, a mechanically activated ion channel, is required for vascular development in mice. PNAS. 2014;111:10347–52.

19. Li J, Hou B, Tumova S, Muraki K, Bruns A, Ludlow MJ, et al. Piezo1 integration of vascular architecture with physiological force. Nature. 2014;515:279–82.

20. Harraz OF, Klug NR, Senatore AJ, Hill-Eubanks DC, Nelson MT. Piezo1 Is a Mechanosensor Channel in Central Nervous System Capillaries. Circ Res. 2022;10.1161/CIRCRESAHA.122.320827.

21. Liu T, Du X, Zhang B, Zi H, Yan Y, Yin J, et al. Piezo1-Mediated Ca2+ Activities Regulate Brain Vascular Pathfinding during Development. Neuron. 2020;108:180-192.e5.

22. Pulido RS, Munji RN, Chan TC, Quirk CR, Weiner GA, Weger BD, et al. Neuronal Activity Regulates Blood-Brain Barrier Efflux Transport through Endothelial Circadian Genes. Neuron. 2020;108:41.

23. Qian T, Maguire SE, Canfield SG, Bao X, Olson WR, Shusta EV, et al. Directed differentiation of human pluripotent stem cells to blood-brain barrier endothelial cells. Sci Adv. 2017;3:e1701679.

24. Stebbins MJ, Wilson HK, Canfield SG, Qian T, Palecek SP, Shusta EV. Differentiation and characterization of human pluripotent stem cell-derived brain microvascular endothelial cells. Methods. 2016;101:93–102.

25. Calabria AR, Shusta EV. A Genomic Comparison of *in vivo* and *in vitro* Brain Microvascular Endothelial Cells. J Cereb Blood Flow Metab. 2008;28:135–48.

26. Canfield SG, Stebbins MJ, Morales BS, Asai SW, Vatine GD, Svendsen CN, et al. An isogenic blood-brain barrier model comprising brain endothelial cells, astrocytes, and neurons derived from human induced pluripotent stem cells. J Neurochem. 2017;140:874–88.

27. Sabbagh MF, Nathans J. A genome-wide view of the de-differentiation of central nervous system endothelial cells in culture. eLife. 2020;9:e51276.

28. Grifno GN, Farrell AM, Linville RM, Arevalo D, Kim JH, Gu L, et al. Tissue-engineered blood-brain barrier models via directed differentiation of human induced pluripotent stem cells. Sci Rep. 2019;9:13957.

29. Delsing L, Dönnes P, Sánchez J, Clausen M, Voulgaris D, Falk A, et al. Barrier Properties and Transcriptome Expression in Human iPSC-Derived Models of the Blood-Brain Barrier: Barrier Properties and Transcriptome Expression in Human iPSC-Derived Models. Stem Cells. 2018;36:1816–27.

30. Lu TM, Houghton S, Magdeldin T, Durán JGB, Minotti AP, Snead A, et al. Pluripotent stem cell-derived epithelium misidentified as brain microvascular endothelium requires ETS factors to acquire vascular fate. Proc Natl Acad Sci USA. 2021;118:e2016950118.

31. Mairey E, Genovesio A, Donnadieu E, Bernard C, Jaubert F, Pinard E, et al. Cerebral microcirculation shear stress levels determine Neisseria meningitidis attachment sites along the blood–brain barrier. Journal of Experimental Medicine. 2006;203:1939–50.

32. Syeda R, Xu J, Dubin AE, Coste B, Mathur J, Huynh T, et al. Chemical activation of the mechanotransduction channel Piezo1. eLife. 2015;4:e07369.

33. Mantle JL, Min L, Lee KH. Minimum Transendothelial Electrical Resistance Thresholds for the Study of Small and Large Molecule Drug Transport in a Human *in Vitro* Blood–Brain Barrier Model. Mol Pharmaceutics. 2016;13:4191–8.

34. Liang X, Huang Y. Intracellular Free Calcium Concentration and Cisplatin Resistance in Human Lung Adenocarcinoma A549 Cells. Bioscience Reports. 2000;20:129–38.

35. Cuddapah VA, Zhang SL, Sehgal A. Regulation of the Blood–Brain Barrier by Circadian Rhythms and Sleep. Trends in Neurosciences. 2019;42:500–10.

36. Zhang SL, Lahens NF, Yue Z, Arnold DM, Pakstis PP, Schwarz JE, et al. A circadian clock regulates efflux by the blood-brain barrier in mice and human cells. Nat Commun. 2021;12:617.

37. Zhang SL, Yue Z, Arnold DM, Artiushin G, Sehgal A. A Circadian Clock in the Blood-Brain Barrier Regulates Xenobiotic Efflux. Cell. 2018;173:130-139.e10.

Chapter 4 – Transcriptional Responses of *in vitro* Blood-Brain Barrier Models to Shear Stress

4.1 Summary

Background: Endothelial cells in vascular beds throughout the body sense blood flow eliciting transcriptional and phenotypic responses. Brain endothelium, known as the blood-brain barrier (BBB), possesses unique barrier and transport properties which are in part regulated by blood flow. Here, we assessed the impact of flow-based shear stress on the transcriptome for multiple *in vitro* BBB models to provide insight into the role of shear in regulating BBB attributes and to potentially improve the predictive capabilities of these *in vitro* models.

Methods: We utilized next generation sequencing to analyze the transcriptome of primary cultured rat brain microvascular endothelial cells (BMECs) as well as three human induced pluripotent stem cell-derived models. We compared the transcriptional responses of these cells to either low (~0.5 dyne/cm^2) or high (12 dyne/cm^2) shear stresses, and subsequent analysis identified genes and pathways that were influenced by shear.

Results: Several key BBB-associated genes including *SLC2A1, LSR,* and *PLVAP* increased in expression at high shear stress in all of the models. We then utilized pathway analysis tools to identify potential BBB relevant signaling cascades and upstream regulators. We observed pathways such as the canonical endothelial shear stress response, *KLF2* and *KLF4*, and BBB associated pathways like Wnt, PPAR, and TGFβ superfamily signaling. We also used the transcriptomics data to explore if shear stress application could reverse the transcriptional de-differentiation induced by *in vitro* culture of primary BMECs. Interestingly, we saw no statistically significant improvement in global transcriptional fit to *in vivo* BMECs suggesting that shear stress does not provide an appreciable maintenance or restoration of BBB characteristics lost under *in vitro* culture.

Conclusions: In this work, we characterized the effects of physiologic shear stress on several *in vitro* BBB models. In addition to identifying shear-responsive genes and pathways, we identified potential upstream regulators of the differential response to shear and show that shear alone is insufficient to rescue de-differentiation caused by *in vitro* primary BMEC culture. Overall, these data sets and analyses provide new insights into the role of shear on BBB models that will aid in model selection and further development.

4.2 Introduction

Despite the prevalence of central nervous system (CNS) diseases, new therapeutic treatments are approved at a much lower rate than therapies targeting other tissues [1,2]. A major challenge to treating disorders within the CNS is the general inaccessibility of circulating drugs to brain tissue, driven in part by the blood-brain barrier (BBB)[1–3]. The brain endothelial cells comprising the BBB mediate selective resistance to molecular transport. Brain microvascular endothelial cells (BMECs), working in conjunction with the surrounding pericytes, astrocytes, and neurons of the neurovascular unit (NVU), help maintain brain homeostasis by facilitating the transport of nutrients like iron and glucose, while simultaneously insulating the brain from changes in blood composition, including brain accumulation of blood-borne drugs [4–6]. While brain-specific properties of BMECs are largely thought to arise from NVU interactions, CNS endothelium also experiences physical cues such as shear stress originating from cerebral blood flow. Blood flow has long been known to impact the behavior of aortic [7,8], capillary [9], and human umbilical vein [10,11] endothelial cells. As a few examples of the effects of flow and fluid shear stress, endothelial cells undergo structural changes and align [7,8,10], have reduced proliferation [12,13], exhibit downregulated p21 signaling [14] and upregulated TGFβ [15,16] and JAK-STAT [17,18] signaling, and possess altered transcriptomes [19,20] that include increased expression of transcription factors like *KLF2* [21] and *KLF4* [22,23].

The transcriptional response of brain endothelium in response to shear has not been studied as extensively, particularly in human cells. However, numerous human BBB models ranging from immortalized BMECs to human hematopoietic and human pluripotent stem cell-derived models have previously been generated [24,25]. Of particular interest to this study are induced human pluripotent stem cell-derived BBB models which can facilitate human disease

modeling [26–28] as well as provide an isogenic source of additional cells of the NVU [29]. Studies using hematopoietic stem cell and iPSC-derived BBB models have noted transcriptional increases in many BBB relevant genes under shear stress [30,31], suggesting a BBB-specific response to shear stress. For example, genes encoding efflux transporters including P-gp (*ABCB1*), tight junction forming proteins like claudin-5 (*CLDN5*), and the canonical BBB glucose transporter, Glut1 (*SLC2A1*), were upregulated by shear in these models. However, other work has suggested that the general shear response phenotype is less pronounced in *in vitro* BBB models compared to endothelial cells cultured from other tissues [10,11,32]. For example, both an iPSC BBB model and immortalized human BMEC model reported a lack of alignment under flow, a well characterized response of endothelial cells to shear stress [10,11], although there was a reduction in both apoptosis and proliferation [11], consistent with non-brain endothelial cells [13]. Unfortunately, direct comparisons between various published datasets can be difficult due to differences in shear magnitude, duration of shear, parenchymal cell types, vascular model, transcriptomic sequencing depth, *in vitro* chip geometry, and data availability.

Here, to partially address this knowledge gap, we employed RNA sequencing to directly compare the shear responses of four endothelial or BBB models: primary rat BMECs (rBMECs), iPSC-derived ECs without BBB character (hECs) [33], Wnt-activated iPSC-derived ECs with CNS-like character (hCECs) [34,35] and iPSC derived brain microvascular endothelial cell-like (hBMEC-like) cells [36]. Each model was subjected to the same magnitudes of low (~0.5 dyne/cm^2) and physiological (~12 dyne/cm^2) shear stress for 72 hours [10,11,37] in identical microfluidic chips to enable direct comparison of their transcriptional responses to shear flow. Subsequent transcriptional analysis and comparison was performed to identify genes and pathways that are shear responsive.

4.3 Results

4.3.1 Endothelial Cell Models Used

Rat brain microvessels (Fig 4.1A) were isolated using standard enzymatic isolation and culture techniques and outgrowing rBMECs contaminant cells removed via puromycin treatment as previously described [38,39]. Importantly, the microvessels were directly plated into the microfluidic device to minimize time *ex vivo* which is known to drive de-differentiation of rBMECs [40]. Rat BMECs cultured in this way express efflux transporters as well as numerous endothelial and BBB markers [38] and rBMECs grown in companion 96-well static tissue culture wells were evaluated PECAM-1 and occludin here (Fig 4.1B).

All iPSC derived models were differentiated from the IMR90-4 iPSC line. For the iPSC derived endothelial like cells (hECs) and Wnt-activated iPSC-derived ECs with CNS-like character (hCECs) models. iPSCs were differentiated according to previously published protocols [33–35]. hECs represent a naïve EC lacking organospecific signatures [34,35] and served as both a generic EC control for shear response and to provide a genetically matched comparison to the hCECs and hBMEC-like cells derived from the same iPSC line. iPSC-derived endothelial progenitor-like cells (hEPCs) were first generated from iPSCs according to previously published protocols [33] before enrichment via magnetic activated cell sorting (MACS). The hEPC population was then either maintained for one passage to yield hECs or treated with CHIR99021, a GSK3 inhibitor, to generate hCECs (Fig 4.1A, Sup Fig 4.1). The hECs and hCECs expressed PECAM-1 and VE-cadherin as expected [33,34] (Fig 4.1B). hCECs also display several hallmarks of *in vivo* BMECs including elevated Glut1 expression, decreased PLVAP expression and increased barrier properties [34]. Here, we demonstrate GLUT-1 and

VE-Cadherin expression in hCECs [34](Fig 4.1B). For the fourth model, iPSC-derived brain microvascular endothelial cell-like (hBMEC-like) cells were differentiated as described previously [36]. The hBMEC-like cells have substantial barrier and transport properties and expression of barrier-related genes (Fig 4.1B), but express epithelial-related genes and significantly lower levels of EC genes than the other three models used here [34,36,41–44] .

4.3.2 Shear Stress Induces a Transcriptomic Shift in Each Model

All models were seeded onto ibidi microfluidic chips (Sup Fig 4.2) and allowed to reach confluence before application of fluid flow (see Methods, Fig 4.1A, Sup Fig 4.1). Flow rates were chosen to generate shear stress at two levels: low shear stress of ~0.5 dyne/cm^2 which allows nutrient supply to the cells in the chip but which is below where shear responses are typically detected [10,11,25], and high shear stress of 12 dyne/cm^2 which is approximately the physiological levels observed in the brain microvasculature [7,45]. Flow was applied for 72 hours before cells were lysed and collected for RNA-sequencing analysis. RNA quality measures are available in Supplemental File 4.1 and all transcript counts are provided in Supplemental File 4.2.

We utilized two forms of unbiased whole transcriptome data dimensionality reduction, hierarchical clustering and principal component analysis (PCA). Both analysis methods showed separation predominantly by model type (Fig 4.2A,C). This suggests that shear accounted for less of the transcriptional variability between the samples than species and model cell type differences. Given known species-specific differences at the BBB [46,47] and the differences in the stem cell-derived models, it is perhaps unsurprising that the largest differences captured were between models and not between high and low shear. To directly assess the effects of shear on

the transcriptome, we performed PCA on each model separately (Fig 4.2B), which showed a clear separation between low and high shear within each model on PC1 and/or PC2, as expected.

Once it was evident that shear treatment drove a transcriptional change, we compared the transcriptional fold changes between low and high shear in each model via the DESeq2 package which analyzes raw counts of transcriptional samples to compare two input conditions, and accounts for the paired nature of our samples. High versus low shear was compared in each model with hECs exhibiting the most differentially-regulated genes (1253 Up, 1329 Down), and rBEMCs (193 Up, 119 Down) exhibiting the fewest differentially-regulated genes (Table 1, Fig 4.2D). Of note, though many of the genes in hBMEC-like cells were regulated by shear, the magnitude of the fold changes were more modest (< 2-fold) compared to other models (Table 1). A complete list of all gene expression TPM data (Sup File 4.3) and DESeq2 results (Sup File 4.4) are available in the supplement.

4.3.3 Shear Response Elements are Upregulated in Each of the Models

We next utilized several tools to relate cellular behavior to shear-induced changes in gene expression. Statistically significantly (padj < 0.05) and positively upregulated genes from DESeq2 were used to perform gene ontology (GO) analysis utilizing the bioprocess collection [48]. Every result is available in supplemental information (Sup File 4.5). We observed terms such as response to fluid shear stress (GO:0034405) or response to laminar fluid shear stress (GO:0071499) in all models except the hBMEC-like cells (Fig 4.3A), suggesting that the hECs, hCECs, and rBMECs respond in a canonical manner to shear flow. We additionally generated a relative heat map of all genes in the response to fluid shear stress (GO:0034405) GO term, where we can see shear responsive elements such as *KLF2/Klf2* and *KLF4/Klf4*, as well as TGFβ signaling inhibitors *SMAD6/Smad6* and *SMAD7/Smad7* (Fig 4.3B). Since we used genes

upregulated by shear in this analysis, genes downregulated by shear (e.g. SMAD6 in hECs) were not included in the GO analysis list. While hBMEC-like cells did not return GO terms directly relevant to shear, they did upregulate several shear-associated transcripts such as *MMP2* and *TFPI2*. Once it was clear that fluid flow was sufficient to induce a shear stress response in the models, we sought to identify signaling pathways that are affected by shear.

4.3.4 Key Signaling Pathways are Transcriptionally Upregulated Under Shear Stress

Further analysis of the GO results identified shear-regulated terms relevant to key endothelial phenotypes and signaling pathways (Fig 4.3A). However, one of the weaknesses of GO is it does not take into account whether a gene is up or downregulated in a given pathway. Therefore, we also utilized Gene Set Enrichment Analysis (GSEA) [49] to compare a list of genes pre-ranked by padj and all fold change (see Methods) against those that would be expected to change in response to cataloged signaling pathways. GSEA terms responsive to shear included DNA replication and cell cycle along with developmental signaling pathways such as TGFβ, Wnt and VEGF signaling (Fig 4.3D). Interestingly, while some pathways were conserved amongst several models, such as PPAR and Wnt signaling, GSEA indicated that different models responded to shear in opposite directions for some pathways, including TGFβ signaling. A complete list of all GSEA results is provided in the supplement (Sup File 4.6).

We next coupled our GO and GSEA analysis to infer shear effects on the different models. We initially compared which GO terms were upregulated in each model (Fig 4.3C). Among those shared between all samples were generic terms such as positive regulation of biological process (GO:0048518). Across all but the rBMECs, we observed GO terms related to either DNA replication or cell proliferation, including positive regulation of cell cycle phase transition (GO1901989), positive regulation of cell population proliferation (GO:0008284), and

regulation of cell cycle G2/M phase transition (GO:1902749) which suggests transcriptional regulation of cell proliferation by shear (Fig 4.3A, Supplemental File 4.4). However, two GSEA gene sets, Cell Proliferation and DNA Replication, moved in opposite directions amongst the models (Fig 4.3D) with rBMECs and hBMEC-like cells both having reduced DNA Replication. By contrast, hECs and hCECs had upregulation of DNA Replication as well as Cell Proliferation for hECs, which suggests that the hECs and hCECs may be more proliferative under high shear.

GO terms associated with various signaling pathways were also identified upon shear flow (Fig 4.3A,D). TGFβ signaling, for example, was observed in all four cell types via GO analysis, with terms such as cellular response to TGFβ (GO:0071560) and regulation of TGFβ production (GO:0071634). Similar to proliferation, GSEA results suggested different directions of TGFβ signaling or that the TGFβ pathway was not identified in the top 20 most enriched pathways. hCECs and rBMECs saw no increase in TGFβ signaling, while hECs exhibited downregulated signaling and hBMEC-like cells exhibited upregulated TGFβ signaling with shear. Some signaling pathways were identified, primarily via GSEA, in only the BBB models (hCECs, rBMECs, hBMEC-like cells) but not the general hECs. In fact, several of these pathways are known to be associated with BBB property acquisition. The GSEA terms for PPAR signaling were increased in all three BBB models, which includes genes which respond to the BBB patterning molecule retinoic acid (RA) [50]. The GSEA term for Wnt signaling, which is well known to be associated with BBB development [6,34,51], was upregulated in both rBMECs and hBMEC-like cells and identified in the GO analysis for the hCEC. Finally, the GSEA term for sonic hedgehog signaling, which has also been associated with BBB development [52], was decreased in both the hECs and hCECs. Overall, GO and GSEA analysis suggested that shear

can affect key signaling cascades involved in both cell proliferation and BBB relevant signaling pathways.

4.3.5 A Subset of BBB Genes are Upregulated Under Increased Shear Stress

On seeing upregulation of BBB relevant signaling pathways via GSEA, we then hypothesized that BBB relevant genes may similarly be upregulated. This led us to directly assess the impact of shear on BBB genes expressed in human BMECs. We assessed the effects of shear on a curated list of genes that was assembled to include key BBB tight junction and transcytosis components and as well as highly expressed solute carriers and efflux transporters as determined from a meta-analysis of human brain scRNAseq data [34,53].

Several of the BBB-associated genes were upregulated by shear, and in general the changes differed between the models. For example, expression of *SLC2A1/Slc2a1*, the gene encoding the GLUT1 glucose transporter highly expressed at the BBB [5], was increased by shear in both the rBMECs and hCECs but not in the hECs [34]. Similarly, *LSR/Lsr* encoding lipolysis stimulated lipoprotein receptor which is typically seen associated at tri-cellular junctions including at the BBB [54], was also increased in rBMECs and hCECs. Lastly, *CAV1/Cav1* encoding caveolin 1, expected to be downregulated at the BBB, was slightly downregulated in hCECs under shear. Conversely, *PLVAP/Plvap*, known to be downregulated in brain endothelium [55] was increased under shear in the hEC, hCEC, and rBMEC models. 15 BBB-associated genes were regulated by shear in hBMEC-like cells with the bulk of these changes occurring in the transporter subset. Only *SLC6A6/Slc6a6,* which encodes a cation dependent transporter, was regulated in a conserved manner across all models. Interestingly, the only model lacking BBB character, hECs, had the most BBB-associated genes that were

decreased by shear. Our analysis suggests that that a subset of BBB-associated genes are regulated by shear stress, and that this response is not conserved within the hEC model.

4.3.6 Transcriptional Machinery is Differentially Regulated Between hECs and BBB Models

We hypothesized that the differential shear responses observed between the hEC and the BBB models could be driven by differential expression of shear-responsive transcription factors or their associated machinery that results from their underlying BBB character. We employed multiple tools that have been developed to predict upstream regulators of transcriptional changes including Chea3 [56] (Fig 4.5A) and BART [57]. Both utilize previously published ChIP-seq datasets and return potential transcription factors that could account for any observed changes. Chea3 and BART analyses were performed with all genes differentially upregulated at high shear according to DESeq2 for each model. To be identified in this analysis the transcription factors themselves do not need to be differentially expressed under high shear since the software can accommodate for transcription factors that are regulated via non-transcriptional mechanisms like phosphorylation. However, we did limit our results to transcription factors that had an average expression of at least 1 TPM (Figs 4.5 A-C). Similar to GO analysis, Chea3 and BART do not account for fold change. Therefore we also utilized Quaternary Prod [58] which takes both fold change and padj from DESeq2 into account while predicting potential upstream regulators. Further, Quaternary Prod can also suggest signaling factors as well as transcription factors as potential upstream regulators. As before, we only kept results with average TPM greater than 1 (Fig 4.5D, Sup File 4.9). We then compared upstream regulators generated by each analysis package and identified those that were differentially regulated between hECs and either hCECs or rBMECs, to identify potential regulators of BBB-selective responses to shear (Fig 4.5D). We attempted to utilize those hits that were conserved between the analysis packages

as well, however there were minimal overlapping upstream transcriptional regulators (Sup Fig 4.4A).

Chea3, BART, and Quaternary Prod together identified upstream transcriptional elements for signaling cascades known to be involved in BBB development. For example, *SMAD4* is involved in TGFβ superfamily signaling transduction while *RXRA* and *RARG* are RA receptors (Sup Fig 4.4B). This is consistent with GSEA results which saw changes in both TGFβ and PPAR signaling in response to shear in some of the models (Fig 4.4D). Quaternary Prod also returned 2 upstream regulators, *ATIC* and *EDN1* that were elevated in hCEC and rBMECs and not identified in hECs (Fig 4.5D,E). *EDN1* encodes a precursor to endothelin-1, is a signaling protein released by the endothelium that is thought to drive vascular contraction, though interestingly this regulator was not predicted to be involved in the hEC response to shear [59]. Next, we identified regulators with different directionality in response to shear in the BBB (hEC and rBMEC) and non-BBB (hEC) models (Fig 4.5E). Of the 5 upstream regulators shared between these three models, 3 were differentially regulated and of the 75 between hECs and either hCECs or rBMECs, 33 were differently regulated (Fig 4.5B, D). Among these differentially upstream regulators were *WNT5A*, a ligand for Wnt signaling involved in BBB patterning, *SMAD4*, and the shear-responsive transcription factors *KLF2* and *KLF4* (Fig 4.5E). Overall, particularly among our Quaternary Prod hits, we see confirmation of BBB pathways identified previously. In addition, we identified potential regulators that could drive this response between the hECs and rBMECs and hCECs.

4.3.7 Application of Shear Stress Does Not Substantially Mitigate In Vitro Dedifferentiation

As a final utilization of this dataset, we assessed if shear stress maintained a more BBB phenotype in rBMECs. It has long been known that BMECs dedifferentiate upon *in vitro* culture.

Previous work [30,31] and some of the data presented above (Fig 4.4), suggest that some aspects of dedifferentiation could be reversed by application of shear stress. A recent detailed transcriptomic analysis of the impact of dedifferentiation in mouse BMECs (mBMECs) identified 164 genes associated with BBB and endothelial phenotypes that are downregulated in mBMECs as a consequence of *in vitro* culturing [40] (Fig 4.6A). To explore whether shear could substantially impact culture induced dedifferentiation, we compared rBMECs under low (RL) and high (RH) shear to the aforementioned previous data set which compared both acutely isolated mBMECs (MV) and cultured mBMECs (MC) [40]. Initially, we assessed whether shear stress rescued expression of any of the 164 BBB genes reportedly lost during long-term *in vitro* culture (Fig 4.6A). The rBMECs have been cultured *in vitro* for a similar length of time to the mBMECs in culture and several genes such as *Acacb, Ccl21a/Ccl21, Notum,* and *Slc7a3* clearly track with cultured mBMECs. We observed that 14 out of 164 genes were improved in our rBMECs under shear. One gene, *St6galnac2,* was downregulated both by shear and extended culture. To more quantitatively determine if the application of shear is driving a more *in vivo*-like transcriptome we calculated the coefficient of determination (R^2), which functionally represents the goodness of fit of each rBMEC sample to the average TPM of acutely isolated mBMECs (Fig 4.6B). However, when looking at the whole transcriptome, there is no statistically significant improvement in R^2 (Fig 4.6C). We then limited the list to only those BBB specific genes in Fig 4.6A and Fig 4.4, which would be a list of BBB expressed barrier and carrier genes and *in vitro* affected BBB genes. There was also no statistically significant improvement in R^2 (Fig 4.6C). Overall this suggests that shear may be positively impacting some of the genes reduced on *in vitro* culture, this component of the neurovascular niche alone is insufficient to reverse the observed dedifferentiation model.

4.4 Methods

4.4.1 iPSC Culture

IMR90-4 human iPSCs were maintained in E8 stem cell maintenance media on Matrigel coated tissue culture treated polystyrene six well plates. At 50-70% confluence, iPSCs were passaged 1:6 using Versene.

4.4.2 iPSC-EPC Differentiation

When iPSCs were ready for passaging, iPSCs were lifted using 1 mL Accutase per well for 7-8 minutes, when cells were mostly visible detached. Accutase and cells were then triturated to break up clumps before addition to 4 mL DMEM/F12 per 1 mL Accutase. Cells were spun down at 200 RCF for 5 minutes and supernatant aspirated. Pellet was resuspended in E8 + 10 µM Y-27632. 12 well Matrigel coated tissue culture treated polystyrene plates were seeded at 70,000 cells/well in 1 mL E8 + 10 µM Y-27632 per well. Cells were fed 1 mL E8 per well for two days. Afterwards cells were fed 2 mL LaSR (500 mL Advanced DMEM/F12, 30 mg ascorbic acid, 6.25 mL GlutaMAX) + 8 µM CHIR99021 per well daily for two days. Cells were then fed 2 mL LaSR per well daily for an additional 3 days. Cells were then lifted and sorted via magnetic activated cell sorting (MACS) via the Stem Cell Technologies EasySep Human FITC Positive Selection Kit II, using either the CD34-FITC (130-113-178) or CD31-FITC (555445). Cells were resuspended in HECSR (HESFM + B-27) + 10% DMSO + 30% FBS at ~5 million cells/cm^2. 1 mL vials were then frozen in a freezing container (UCP1001) following the manufacturers' instructions at -80 °C for at least overnight before being moved to liquid nitrogen for long term storage.

4.4.3 iPSC-EC +/- Wnt Differentiation

This process was adopted from previously published protocols [34,35]. Briefly, to generate iPSC-ECs +/- Wnt, EPCs were thawed into HECSR + 20 ng/mL FGF2 + 10 ng/mL VEGF + 4 µM CHIR99021/DMSO. Media was changed every 48 hours until cells reached confluency. At confluency, cells were passaged 1 confluent well to 2 fluidic chips and maintained at minimum shear stress for 24 hours to ensure confluency was reached before shear application. To note, differentiations of hECs and hCECs can generate contaminant mesenchymal smooth muscle-like cells over time [33], but very few of these cells were observed in this study due to the passaging step as well as the addition of CHIR99021 to the hCEC cultures (Fig 4.1B) [33–35].

4.4.4 hBMEC-like Cell Differentiation

When iPSCs were ready for passaging, cells were seeded at 35,000 cells/cm^2 into Matrigel coated tissue culture treated 6 well plastic plates in 2 mL E8 media + 10 µM Y-27632. Cells are then fed 2 mL E8 for two days before switching to DeSR1 + 4 µM CHIR99021. 23.5-24 hours after application of CHIR99021 to DeSR2 for 5 days. Cells were then fed HECSR + 10 µM retinoic acid + 20 ng/mL FGF2. After 48 hours cells were replated onto collagen IV and fibronectin coated ibidi microfluidic chips at 0.8 and 0.6 mm heights. Cells were given 24 hours at minimal flow rate in HECSR + 10 µM retinoic acid + 20 ng/mL FGF2 + anti-anti before changing to HECSR + anti-anti and applying shear stress.

4.4.5 rBMEC Purification

Half a rat brain was used to seed each chip as a rough way to control consistency. For conditions where multiple rat brains were needed, rats were pooled and treated a singular isolation. Sprague-Dawley rats between 220-250 g were first anesthetized with 2-5% isoflurane until they

failed both the pinch and righting tests. Afterwards they were sacrificed using a guillotine to swiftly remove the head. Surgical scissors were used to remove the back of the skull and extract the brain. Brain segments were stored in DMEM on ice while awaiting processing. Microvessels were initially mechanically separated by rolling brain hemispheres on paper to capture meninges, vigorous chopping, and then mixing into 1 mL DMEM. Brain solution was then transferred to a 50 mL conical and an additional 9 mL of DMEM added. Solution was triturated to mechanically disassociate fragments before the addition of 0.75 mL of 10 mg/mL collagenase and 150 µL of 1 mg/mL Dnase I. Solution was incubated for 1 hour and 15 minutes at 37 °C on a shaker at 250 rpm. During the incubation, Percoll gradient was prepared in a 30 mL Oakridge tube with 10 mL Percoll, 19 mL PBS, 1 mL 10x PBS, 1 mL FBS and centrifuged at 30,000 g for at least 30 minutes. After incubation, solution was diluted to 40 mL using DMEM, and then spun down at 1000 RCF for 8 minutes. Supernatant was aspirated. Solution was resuspended in 25 mL 20% (m/v) BSA in DMEM and triturated to further mechanically separate. Mixture was centrifuged at 1000 g and 4 ℃ for 20 minutes to separate the bulk of the neurons and glia. The neuron/glia layer and supernatant were aspirated before resuspension and triturating in 6.75 mL DMEM. 0.5 mL of 10 mg/mL Collagenase-dispase and 50 µL of 1 mg/mL DNase 1 were added and solution was incubated for 1 hour at 37 ℃ on a shaker at 250 RPM. Fragments were spun down at 700 RCF for 6 minutes and supernatant aspirated. Pellet was resuspended in 1 mL DMEM and added to the prepared Percoll gradient and centrifuged at 1000 RCF for 10 minutes at 4 ℃. After the gradient, a 5 mL syringe with a blunt 16 gauge 5” needle was used to extract the microvessel containing layer which was diluted with DMEM at roughly 4 mL per mL of microvessel solution. This was spun down at 200 RCF for 10 minutes and then and plated into ibidi 0.8 mm and 0.6 mm microfluidic chips coated 250-300 µL of 0.2 mg/mL collagen IV and 0.2 mg/mL

fibronectin for at least 1 hour, in rat primary medium (DMEM + 10% FBS + 1x GlutaMAX + 1x Anti-anti + 4 µg/mL puromycin + 100 ng/mL heparin + 20 ng/mL FGF2) every 8 hours until confluent (usually between 3-4 days) before proceeding with connection to microfluidic devices. To ensure medium was successfully changed, 200 µL was added to one side and removed from the other two times. After connection, medium was replaced every 48 hours.

4.4.6 Preparation of microfluidic devices

Microfluidic devices were assembled from 1/16" and 1/32" internal diameter silicone tubing cut to lengths and connected to nylon components according to Sup Fig 4.2. Prior to assembly, components were washed with water, soap and water, 10% bleach solution, and then ethanol before autoclaving to sterilize. Components were assembled in a sterile laminar flow hood. Tubing was rewashed and reassembled after usage up to 5 times before components were thrown away and fresh devices constructed.

4.4.7 Application of shear stress

For all cells in chips, shear stress was applied after a confluent monolayer was achieved. Due to the design of the ibidi pump system, a uniform pressure can be applied to all microfluidic devices. By changing the size of the tubing and the height of the ibidi µLock chip, we were able to apply different levels of shear to multiple chips simultaneously. Pressure was selected using calibration curves calculated previously and flow rates were recalculated during the ramp up phase to ensure correct shear stress was being applied. Low shear cells received between 0 and 1 dyne/cm^2 to ensure appropriate nutrient and oxygen levels while matching geometry. During the ramp up phase, for the high shear chips, shear was increased by approximately 3 dyne/cm^2 every half an hour until ~12 dyne/cm^2 was reached. Low shear stress chips, changed minimally over the ramp up period. Chips were then maintained for 72 hours before collection for RNA.

4.4.8 RNA Collection and Sequencing

Chips were first disconnected from the microfluidic device, followed by a short DPBS wash. Chips were then assessed under a bright field microscope to ensure cells were still attached before lysing with the cell lysis buffer provided in the Qiagen RNeasy Mini Kit. Samples were then processed using Qiagen Shredder columns and the Qiagen RNeasy Mini Kit. Samples were prepared using poly A enrichment, library preparation, and sequencing were performed by Novagene. Samples were sequenced using paired-end reads. STAR was used for alignment to the hg38 genome, featurecounts was used to generate count tables, and differential expression was analyzed using DeSeq2 on the raw counts.

4.4.9 Immunocytochemistry (ICC)

For plate ICC, cells were initially washed twice with cold PBS, before fixing with either Methanol or 4% PFA in PBS (see Sup Table 1). Afterwards, cells were blocked 10% Goat Serum in PBS at either 4 °C overnight or 1 hour at room temperature. Cells were then incubated overnight with primary (see Sup Table 1) at 4 °C while shaking at 30 rpm. Cells were washed 3 times with PBS and then secondary solution in 10% Goat Serum was applied for either 1 hour at room temperature or overnight at 4 °C. Cells were then rinsed twice with PBS and a solution of 2 µg/mL Hoechst 33342 in PBS was applied for 10-15 minutes. Then aspirated and replaced with PBS. Cells were stored at 4 °C in the dark before imaging.

4.4.10 Statistics and Analysis

Replication was at the differentiation/isolation level. Either with cells differentiated from the same iPSC population at different passages or with isolated microvessels taken from multiple rats. Paired DESeq2 was utilized for comparisons between High and Low shear samples. Statistics reported are those returned by paired DESeq2 analysis. Results for GO were only

considered significant if they had an FDR of less than 0.05. GO was performed via the PANTHER online interface [48,60]. GSEA gene inputs were ranked by negative log base ten of the padj value provided by DESeq2 multiplied by the log two fold change. These lists were input into the GSEA software provided by the Broad institute [49,61]. For any comparison between rat and human, we utilized the Homologene2 dataset which uses gene names updated to 2019 to assign human orthologs for rat genes. Any gene lacking an ortholog was discarded from the analysis. For Chea3 and BART analysis, we again used only genes with a positive fold change and statistical significance according to DESeq2. For Chea3, which offers multiple libraries of the aforementioned ChIP-seq meta analysis we utilized the "literature" library. Statistical significance was set at an FDR/Irwin-Hall pvalue (as reported by Chea3/BART respectively) of less than 0.05. Upstream factors that did not have an average TPM of 1 or greater were discarded as non-expressed. For Quaternary prod analysis, the software package was provided with results from prior DESeq2. All upstream regulators with a padj < 0.05 and average TPM > 1 were considered statistically significant and expressed.

4.5 Discussion

Here we performed bulk RNA sequencing on one generic EC model and three models that have been used to model various properties of the BBB. The BBB models were chosen to capture a broad swath of potential usages. rBMECs are a definitively specified primary cell model with BBB-relevant efflux activity, though previous work has identified a de-specification that occurs over longer term culture [24,38,40]. The recently-reported hCECs express high levels of endothelial markers and some BBB transporters [34,35], however they lack tight barrier properties and efflux transporter expression. Finally, hBMEC-like cells possesses barrier

properties such as efflux transport and tight junctions enabling modeling of barrier, but express low levels of endothelial-specific genes and proteins limiting utility for studies regarding endothelial function. This model in particular has been utilized numerous times in BBB microfluidic constructs [26,31,44,62–65]. Our analysis contributes to better understanding the transcriptional impact of adding shear to these typically static *in vitro* models.

To ensure that geometry of cell culture did not impact analysis of the effects of shear stress, we utilized low, but non-zero, shear stress applied to cells in the microfluidic chips as a control. A low level of fluid flow ensured that the low shear conditions did not suffer nutrient or oxygen depletion over the 72 hour treatment [32,66]. Consequently, the cells in the low condition experienced between 0 and 1 dyne/cm^2. While this low value of flow is below that required to induce shear-responsive gene expression and phenotypes in ECs [10,11,67], the culture conditions differ from a typical static plate culture.

Our analysis revealed hundreds of differentially regulated genes between high and low shear across the four models. hBMEC-like cells demonstrated the fewest genes that changed more than 2-fold in either direction, consistent with low endothelial nature of these cells (Table 1). rBMECs demonstrated the fewest differentially expressed genes overall, and this may be partially explained by previous shear exposure, or could suggest a limited responsiveness consistent with previous work.

Our results demonstrated that shear-regulated genes in hECs, hCECs, and rBMECs were associated with GO terms relevant to shear stress (Fig 4.3A), individual shear responsive transcripts (Fig 4.3B), and pathways involved in shear response via GSEA (Fig 4.3D). The hBMEC-like cells saw minor increases in a few shear response elements, but did not return any statistically significant terms relevant to shear response. Cell proliferation terms, shown to be

reduced in endothelial cells under shear stress and in some BMEC models [8,10,11,68,69], were predicted upregulated in our hEC and hCEC GSEA results, and down in our rBMECs (Fig 4.3D). Some of these differences may stem from duration of shear treatment, which is typically much higher than these other studies. Prior work, which demonstrated that immortalized BMECs and hBMEC-like cells do not align under shear did observe, via video analysis, an increase in proliferation at 40 hours, roughly half of our treatment duration [11]. It is also possible that GSEA did not accurately assess the transcriptional readout, given that we took the 20 terms with the highest and lowest enrichment factors, which emphasizes the importance of utilizing multiple analysis packages as well as follow up experiments [10,11]. Similarly, TGFβ signaling is known to increase in ECs under short term (< 24 hour) shear application [15,16,70]. We observed GO terms relevant to TGFβ signaling in all four models, and GSEA suggested downregulation of TGFβ signaling in the hECs, while Quaternary prod analysis suggested that *SMAD4* and *BMP4*, both components of TGFβ superfamily signaling were differentially regulated, between the hECs and BBB models as well as matching the direction predicted by GSEA for hECs. It is possible that compared to a 24-hour shear duration, long term application has led to feedback inhibition in our hECs. This is consistent with some of our signaling results, as well as Quaternary Prod results for *KLF2* and *KLF4* which were both listed as downregulated upstream regulators in hECs (Fig 4.5C) despite being upregulated at a transcriptional level (Fig 4.3C) and well known to drive endothelial shear response in literature [21–23].

Up and down regulated signaling cascades from GSEA also suggested a few BBB relevant pathways regulated by shear, though only PPAR signaling was conserved in multiple models. The ligand for that pathway, RA, is associated with BBB character acquisition during the endothelial invasion of the developing neural tube [50,71]. Similarly, Wnt signaling has also

been associated with BBB development and maintenance, however it was only upregulated in the GSEA for rBMECs (Fig 4.3D) and as an upregulated upstream regulator in hCECs through Quaternary Prod (Fig 4.5D) [5,34,51]. Though the hCECs did not experience upregulated Wnt signaling upon shear, sonic hedgehog signaling, thought to be a principal part of astrocyte communication with BMECs in the NVU, was transcriptionally downregulated by shear according to just GSEA [52]. It is possible that Sonic Hedgehog signaling in BMECs is driven by another component in the NVU rather than shear stress.

Interestingly, expression of some BBB-associated genes increased under shear, including *LSR* and *SLC2A1*. This suggests some potential reversal of the loss of BBB relevant transcription under *in vitro* culture at a transcriptional level (Fig 4.4). However, at both a whole transcriptome and BBB only gene level we did not see improvement in transcriptional alignment to acutely isolated, *in vivo*-like, mBMEC transcriptomes (Fig 4.6). This suggests that shear alone is insufficient to restore loss of phenotype due to *in vitro* culture conditions.

By assessing the effects of shear on various BMEC and EC models after 72 hours, we identified genes and pathways chronically regulated by shear. However, this time frame also limits conclusions we can make regarding acute, transient responses to shear. It is possible that over the short term, a different transcriptional regime may occur [72].

4.6 Conclusion

Our data provides a valuable resource to inform model use as well as impacts of longer term shear on these cell types that have previously been characterized under static conditions [34,36,40]. Researchers seeking to deploy these models should consider the expression of genes of interest and the corresponding effect of shear when assessing model use. We have also identified several BBB patterning signals that are impacted by the activation of shear flow and

found that shear stress alone is unable to rescue the loss of BBB transcriptional specification caused by long term culture. Future work should include protein level validation of potential changes of interest, particularly those involved with BBB properties as well as potential phenotype and pathway assessments such as measuring proliferation via video analysis and phosphorylation of downstream intermediates of Wnt or TGFβ superfamily signaling.

4.7 Figures

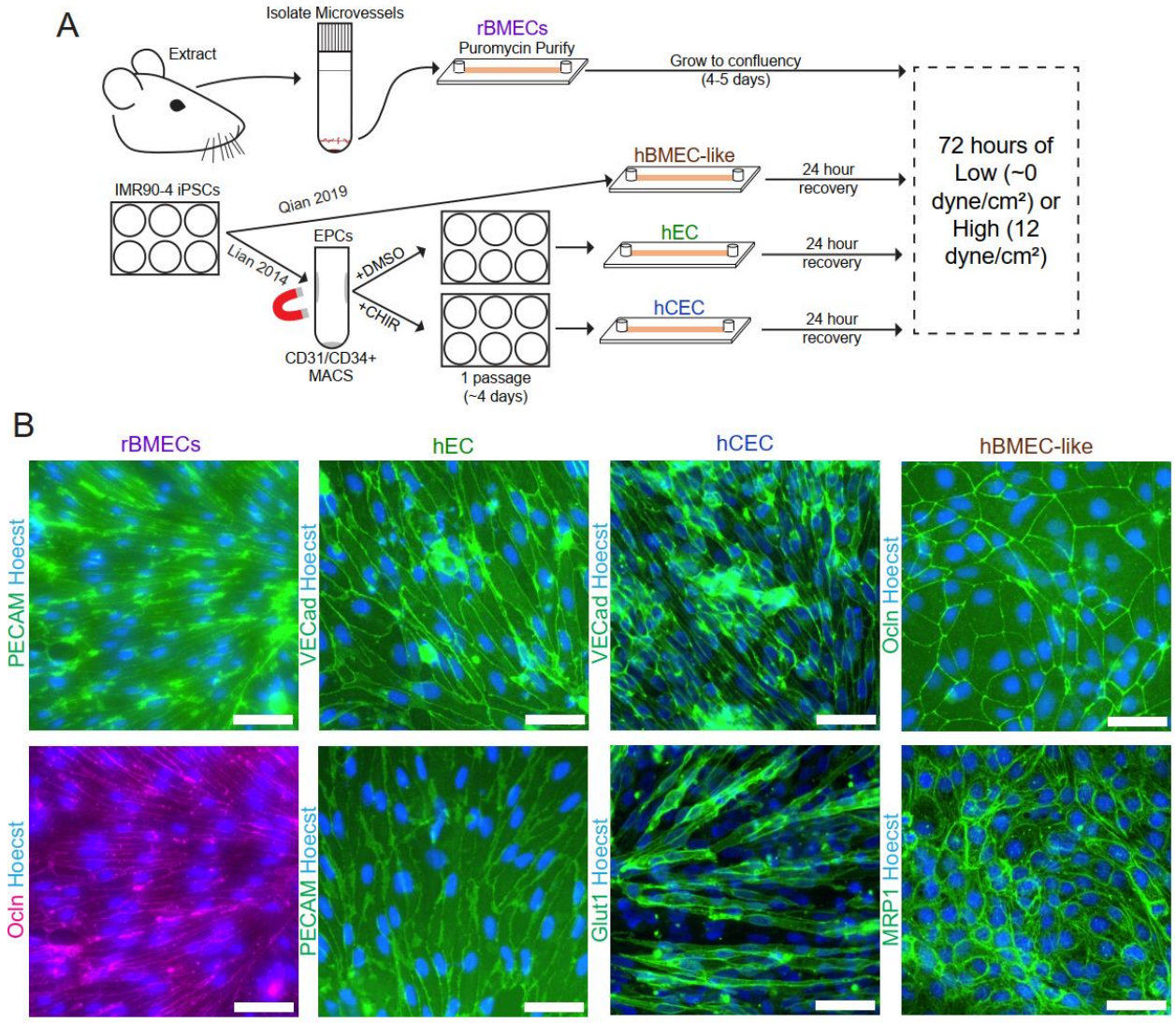

Figure 4.1 Model establishment and validation. A) Schematic of model isolation/differentiation methods before application of shear stress. B) Immunocytochemical analysis of cell fate markers demonstrating cell morphology in rBMECs, hECs, and hCECs and protein expression consistent with previously published literature for these models. Scale bars = 50 μm

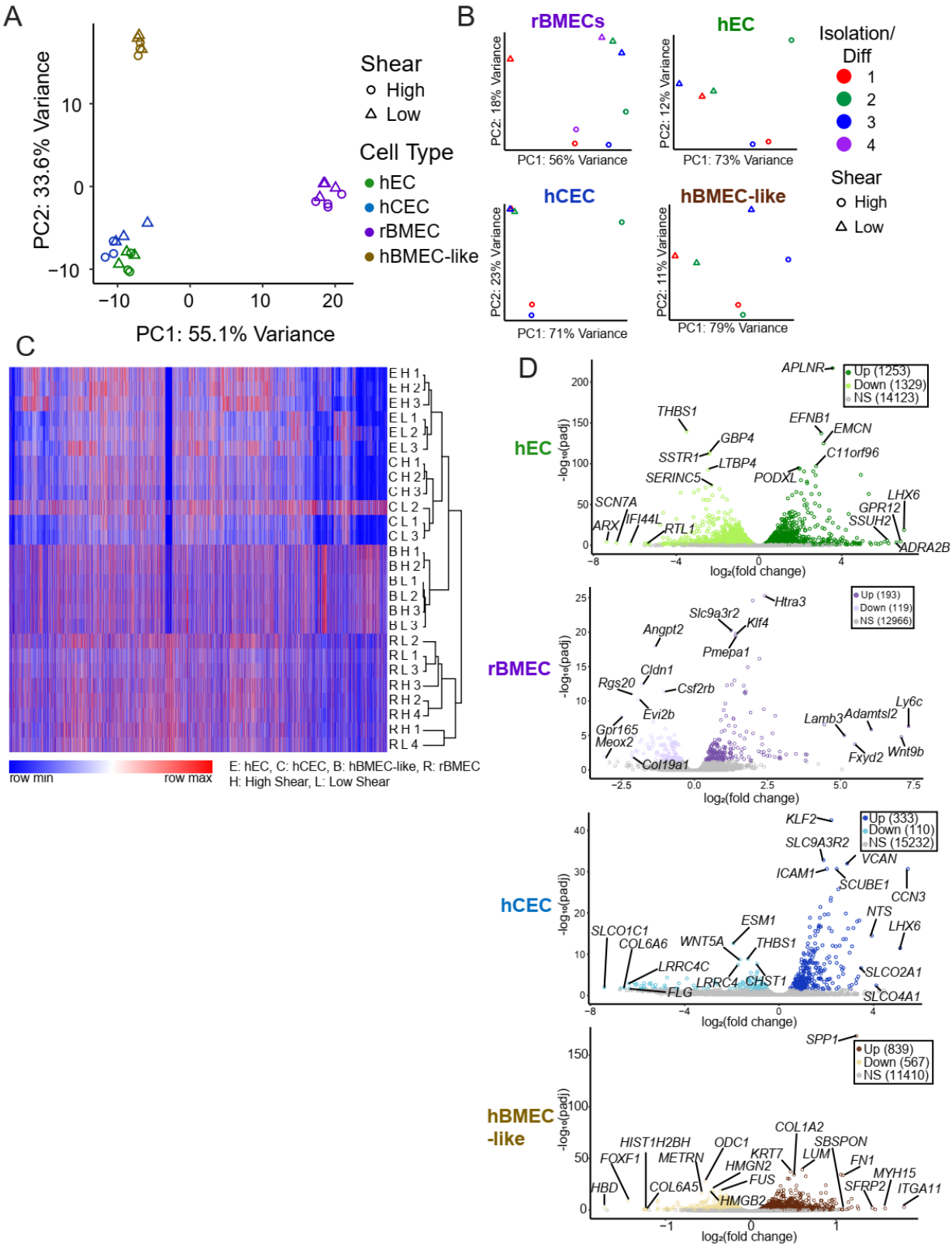
A
PC2: 33.6% Variance
PC1: 55.1% Variance
Shear
High
Low
Cell Type
hEC
hCEC
rBMEC
hBMEC-like
B
rBMECs
hEC
hCEC
hBMEC-like
PC2: 18% Variance
PC1: 56% Variance
PC2: 12% Variance
PC1: 73% Variance
PC2: 23% Variance
PC1: 71%
PC2: 11% Variance
PC1: 79% Variance
Isolation/ Diff
1
2
3
4
Shear
High
Low
C
E H 1
E H 2
E H 3
E L 1
E L 2
E L 3
C H 1
C H 2
C H 3
C L 2
C L 1
C L 3
B H 1
B H 2
B L 1
B L 2
B H 3
B L 3
R L 2
R L 1
R L 3
R H 3
R H 2
R H 4
R H 1
R L 4
row min
row max
E: hEC, C: hCEC, B: hBMEC-like, R: rBMEC
H: High Shear, L: Low Shear
D
hEC
Up (1253)
Down (1329)
NS (14123)
APLNR
THBS1
EFNB1
EMCN
GBP4
SSTR1
C11orf96
LTBP4
SERINC5
PODXL
LHX6
SCN7A
GPR12
ARX
IFI44L
SSUH2
RTL1
ADRA2B
-log10(padj)
log2(fold change)
rBMEC
Up (193)
Down (119)
NS (12966)
Htra3
Slc9a3r2
Klf4
Angpt2
Pmepa1
Cldn1
Rgs20
Csf2rb
Ly6c
Evi2b
Lamb3
Adamtsl2
Gpr165
Meox2
Fxyd2
Wnt9b
Col19a1
hCEC
Up (333)
Down (110)
NS (15232)
KLF2
SLC9A3R2
VCAN
ICAM1
SCUBE1
CCN3
NTS
ESM1
LHX6
SLCO1C1
COL6A6
WNT5A
THBS1
LRRC4C
SLCO2A1
FLG
LRRC4
CHST1
SLCO4A1
hBMEC-like
Up (839)
Down (567)
NS (11410)
SPP1
COL1A2
HIST1H2BH
ODC1
SBSPON
FOXF1
METRN
KRT7
LUM
FN1
HMGN2
MYH15
HBD
COL6A5
FUS
SFRP2
ITGA11
HMGB2

Figure 4.2 Unbiased whole transcriptomic analysis. A) Principal component analysis utilizing TPM for each model under low and high shear with only genes that have an established rat orthologue. B) PCA of each model individually utilizing variance stabilized counts according to DESeq2. C) Overall heat map of hierarchical clustering of $\log_{10}$(TPM+1) from all models. Any genes without an established ortholog or with an average TPM across all samples of less than 1 were excluded. Gene clustering is from hECs and copied to all other samples. Color indicates row normalized minimum or maximum per gene. Heat map and hierarchical clustering performed via the Morpheus tool. D) Volcano plots for each model with the top 5 genes with the highest fold change or lowest padj marked. Grey indicates statistically insignificant fold changes (padj > 0.05 via DESeq2).

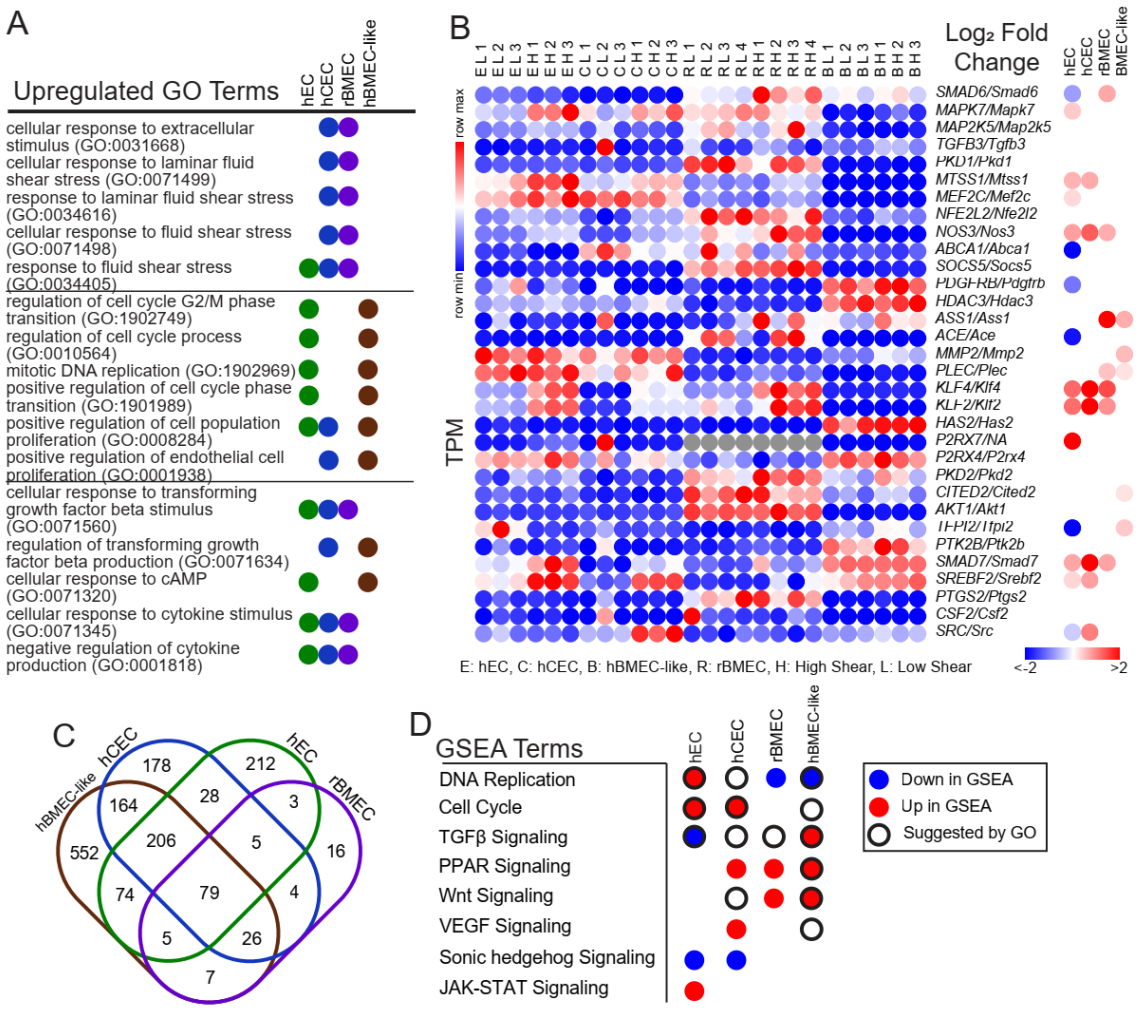

Figure 4.3 Pathway analysis and comparison between models. A) Selected GO terms with an FDR < 0.05 returned from all differentially expressed genes in each model with a positive $\log_2$(fold change) > 0 and padj < 0.05. Remaining GO terms are provided in Supplemental File 4.5. B) Individual genes within the response to fluid shear stress (GO:0034405). Left is TPM in each model with relative expression. Right is Log_2(fold change high versus low) as reported by DESeq2. All nonsignificant results are colorless (padj > 0.05 via DESeq2). C) Venn diagram of overlapping GO results between models. Numbers are total GO terms. D) Direction of pathways in the top twenty most enriched pathways according to GSEA analysis. Colors indicate direction. Black rings indicate that GO terms related to this pathway were also enriched.

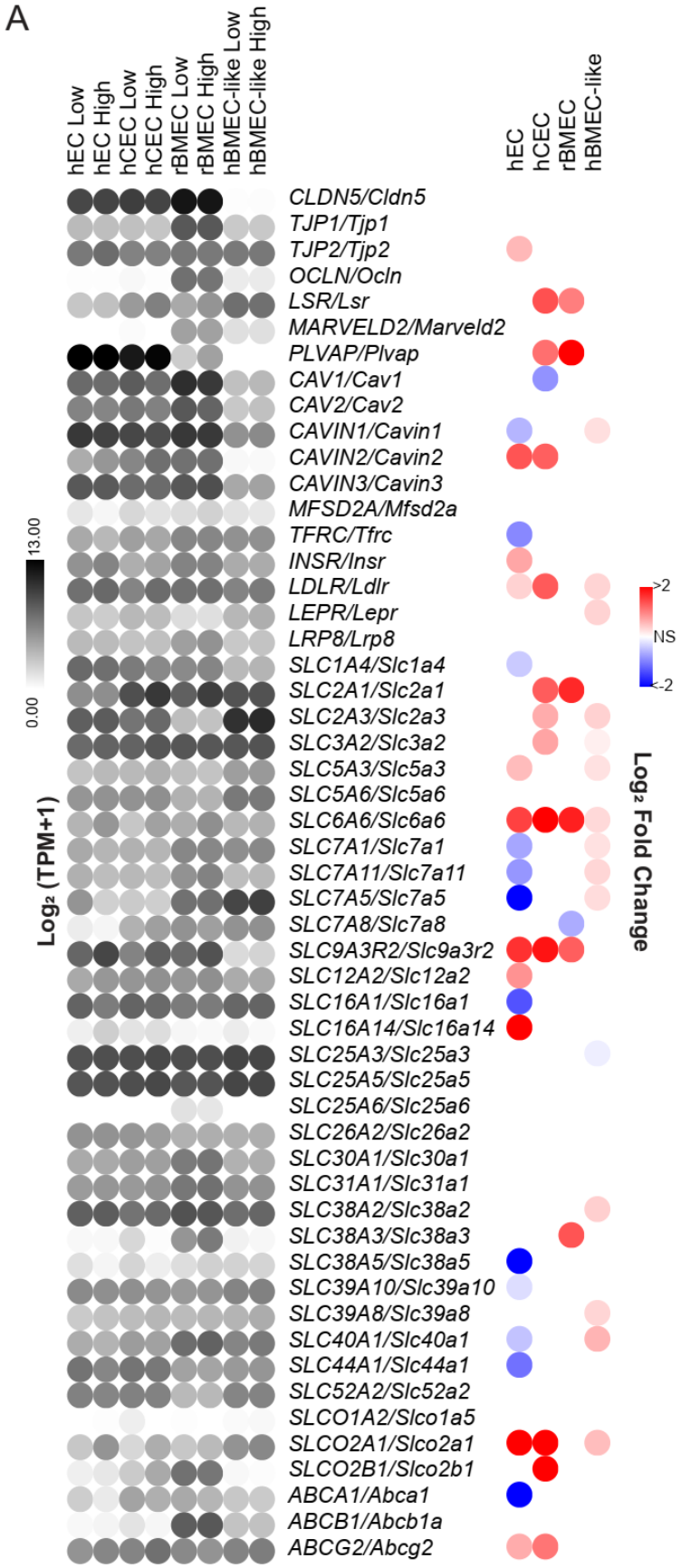
A
hEC Low
hEC High
hCEC Low
hCEC High
rBMEC Low
rBMEC High
hBMEC-like Low
hBMEC-like High
hEC
hCEC
rBMEC
hBMEC-like
CLDN5/Cldn5
TJP1/Tjp1
TJP2/Tjp2
OCLN/Ocln
LSR/Lsr
MARVELD2/Marveld2
PLVAP/Plvap
CAV1/Cav1
CAV2/Cav2
CAVIN1/Cavin1
CAVIN2/Cavin2
CAVIN3/Cavin3
MFSD2A/Mfsd2a
TFRC/Tfrc
INSR/Insr
LDLR/Ldlr
LEPR/Lepr
LRP8/Lrp8
SLC1A4/Slc1a4
SLC2A1/Slc2a1
SLC2A3/Slc2a3
SLC3A2/Slc3a2
SLC5A3/Slc5a3
SLC5A6/Slc5a6
SLC6A6/Slc6a6
SLC7A1/Slc7a1
SLC7A11/Slc7a11
SLC7A5/Slc7a5
SLC7A8/Slc7a8
SLC9A3R2/Slc9a3r2
SLC12A2/Slc12a2
SLC16A1/Slc16a1
SLC16A14/Slc16a14
SLC25A3/Slc25a3
SLC25A5/Slc25a5
SLC25A6/Slc25a6
SLC26A2/Slc26a2
SLC30A1/Slc30a1
SLC31A1/Slc31a1
SLC38A2/Slc38a2
SLC38A3/Slc38a3
SLC38A5/Slc38a5
SLC39A10/Slc39a10
SLC39A8/Slc39a8
SLC40A1/Slc40a1
SLC44A1/Slc44a1
SLC52A2/Slc52a2
SLCO1A2/Slco1a5
SLCO2A1/Slco2a1
SLCO2B1/Slco2b1
ABCA1/Abca1
ABCB1/Abcb1a
ABCG2/Abcg2
13.00
0.00
Log₂ (TPM+1)
>2
NS
<-2
Log₂ Fold Change

Figure 4.4 Shear regulation of BBB-associated genes. The gene list includes tight junction and vesicular transport according to literature and enriched *SLC, ABC,* genes identified as highly expressed in BMECs identified in compiled brain single cell sequencing analysis. Since this list was compiled with respect to human BBB gene expression, rat gene names were converted utilizing the Homologene2 list. Left is $\log_2$(TPM + 1) of the average expression in each model under low or high shear. Right is $\log_2$(fold change) as reported by DESeq2. All nonsignificant results are colorless.

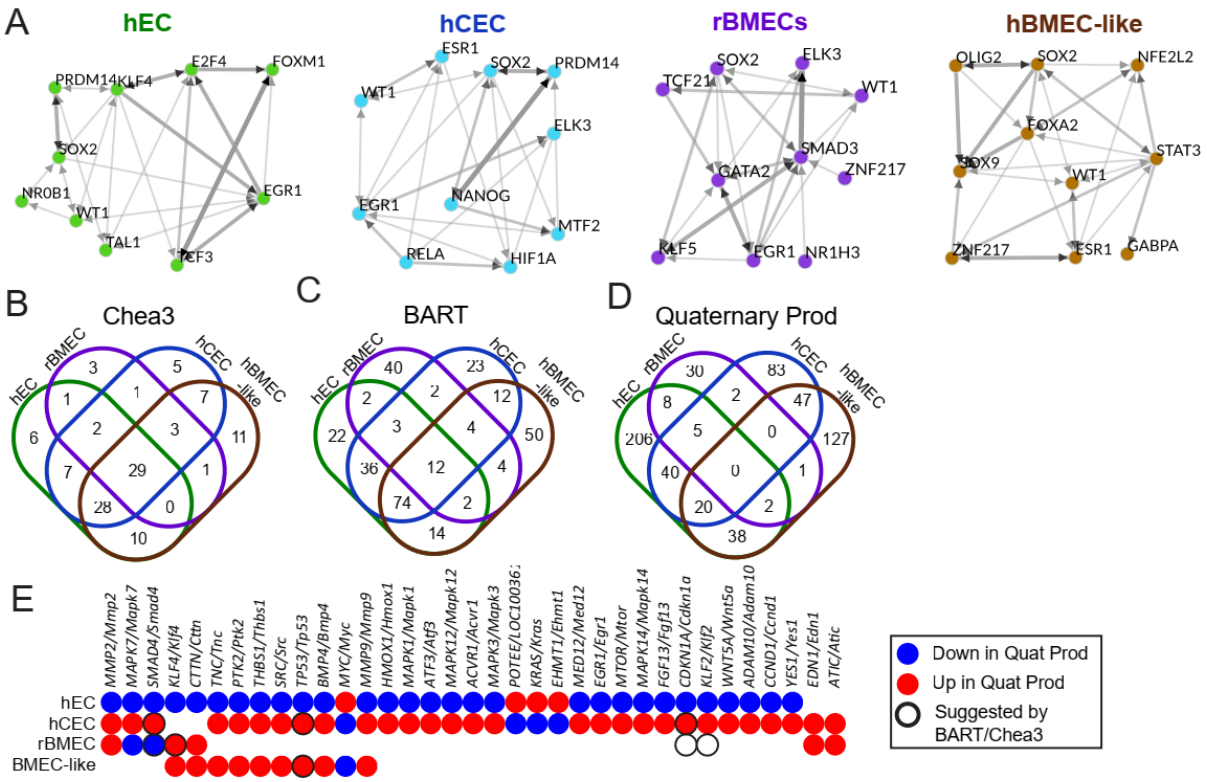

Figure 4.5 Upstream regulator analysis. A) Top 10 enriched transcription factors from Chea3 derived from a meta ChIP-seq in the "literature" library suggested from Chea3 to account for upregulated genes between high and low shear in each model (with an FDR < 0.05). Graphs were generated via Chea3 and represent top 10 most statistically significant transcription factors that may account for differences between high and low shear in each model. Thickness and color of arrow represents number of overlapping downstream targets. B) Venn diagrams demonstrating total number of suggested upstream transcriptional regulators and overlaps between them. Results were generated using the "literature" library and any transcription factor with an average TPM < 1 or FDR > 0.05 was removed. C) BART ChIP-seq analysis results compared between the models. Any transcription factor with an average TPM < 1 or Irwin-Hall p value > 0.05 was removed. D) Quaternary Prod analysis results compared between the models. Any potential

upstream regulator with an average TPM < 1 or padj > 0.05 was removed. E) Chart highlighting upstream regulators that were differentially regulated between hECs and either rBMECs or hCECs. Colors indicate direction, black rings represent transcription factors suggested by BART or Chea3.

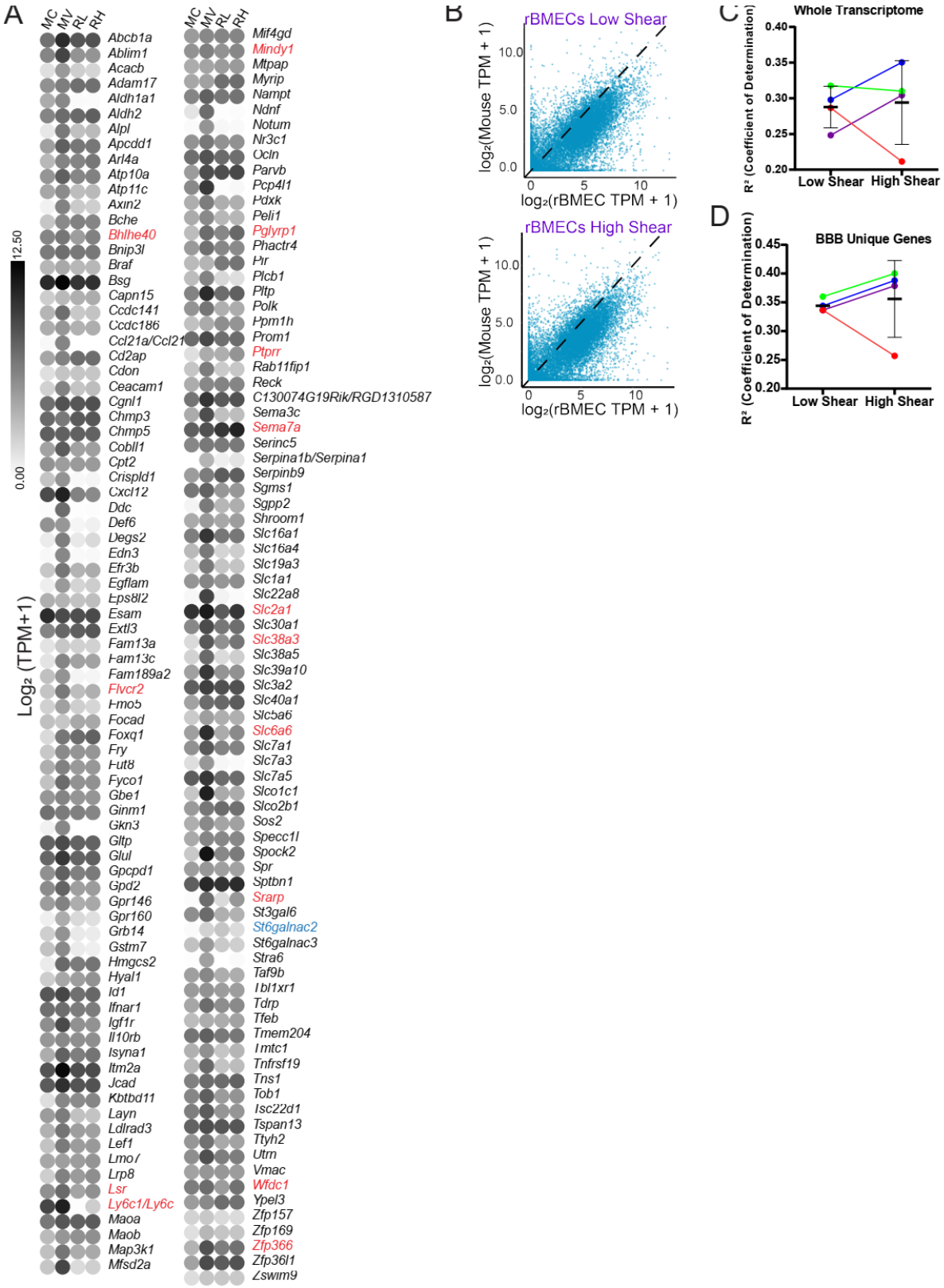
A
MC
MV
RL
RH
Log₂ (TPM+1)
12.50
0.00
Abcb1a
Ablim1
Acacb
Adam17
Aldh1a1
Aldh2
Alpl
Apcdd1
Arl4a
Atp10a
Atp11c
Axin2
Bche
Bhlhe40
Bnip3l
Braf
Bsg
Capn15
Ccdc141
Ccdc186
Ccl21a/Ccl21
Cd2ap
Cdon
Ceacam1
Cgnl1
Chmp3
Chmp5
Cobll1
Cpt2
Crispld1
Cxcl12
Ddc
Def6
Degs2
Edn3
Efr3b
Egflam
Eps8l2
Esam
Extl3
Fam13a
Fam13c
Fam189a2
Flvcr2
Fmo5
Focad
Foxq1
Fry
Fut8
Fyco1
Gbe1
Ginm1
Gkn3
Gltp
Glul
Gpcpd1
Gpd2
Gpr146
Gpr160
Grb14
Gstm7
Hmgcs2
Hyal1
Id1
Ifnar1
Igf1r
Il10rb
Isyna1
Itm2a
Jcad
Kbtbd11
Layn
Ldlrad3
Lef1
Lmo7
Lrp8
Lsr
Ly6c1/Ly6c
Maoa
Maob
Map3k1
Mfsd2a
Mif4gd
Mindy1
Mtpap
Myrip
Nampt
Ndnf
Notum
Nr3c1
Ocln
Parvb
Pcp4l1
Pdxk
Peli1
Pglyrp1
Phactr4
Pir
Plcb1
Pltp
Polk
Ppm1h
Prom1
Ptprr
Rab11fip1
Reck
C130074G19Rik/RGD1310587
Sema3c
Sema7a
Serinc5
Serpina1b/Serpina1
Serpinb9
Sgms1
Sgpp2
Shroom1
Slc16a1
Slc16a4
Slc19a3
Slc1a1
Slc22a8
Slc2a1
Slc30a1
Slc38a3
Slc38a5
Slc39a10
Slc3a2
Slc40a1
Slc5a6
Slc6a6
Slc7a1
Slc7a3
Slc7a5
Slco1c1
Slco2b1
Sos2
Specc1l
Spock2
Spr
Sptbn1
Srarp
St3gal6
St6galnac2
St6galnac3
Stra6
Taf9b
Tbl1xr1
Tdrp
Tfeb
Tmem204
Tmtc1
Tnfrsf19
Tns1
Tob1
Tsc22d1
Tspan13
Ttyh2
Utrn
Vmac
Wfdc1
Ypel3
Zfp157
Zfp169
Zfp366
Zfp36l1
Zswim9
B
rBMECs Low Shear
log₂(Mouse TPM + 1)
log₂(rBMEC TPM + 1)
rBMECs High Shear
log₂(Mouse TPM + 1)
log₂(rBMEC TPM + 1)
C
Whole Transcriptome
R² (Coefficient of Determination)
Low Shear
High Shear
D
BBB Unique Genes
R² (Coefficient of Determination)
Low Shear
High Shear

Figure 4.6 Comparing rBMECs with and without shear post culturing to acutely isolated mBMECs. A) A list of BBB relevant genes lost under long term *in vitro* culture conditions [40] in mBMECs. Color of the dot represents $\log_2$(Average TPM + 1) from either our dataset or Sabbagh 2020. Gene names that are not consistent between mouse and rat are written mouse gene/rat gene. Cultured mBMECs (MC), acutely isolated mBMECs (MV), rBMECs under low shear (RL), and rBMECs under high shear (RH). Genes from this list that showed a statistically significant change via DESeq2 are in red font if upregulated and blue font if downregulated by shear. B) Example alignment plots with average TPM from rBMECs versus acutely isolated mBMECs. Black lines represent theoretical perfect alignment. C) Results of alignment utilizing the whole transcriptome and comparing to acutely isolated mBMECs as measured by coefficient of determination (R^2). Colors represent separate rBMEC isolations and lines connect paired datapoints. No statistical significance was observed via a paired Student's t-test. D) Identical analysis to C, except instead of assessing whole transcriptome alignment, a list comprised of all genes in Fig 4.6A and Fig 4.4 was used instead as as "BBB Gene Specific" alignment. No statistical significance was was observed via a paired Student's t-test.

4.8 Tables

Table 4.1 Summarized of results of different analysis techniques performed

Model	hEC	hCEC	rBMEC	hBMEC-like
Upregulated	1253	333	193	839
Downregulated	1329	110	119	567
Upregulated (> 2 fold)	480	187	92	18
Downregulated (>2 fold)	558	81	42	11
GO Hits (Up)	611	689	144	1112
GO Hits (Down)	66	67	0	275
Chea3 Hits	83	82	40	90
BART Hits	165	166	65	172
Quaternary Prod	331	208	49	241

Supplemental Table 4.1 Antibodies Utilized

Target	Manufacturer	Cat. No.	Concentration
Glut1	Invitrogen	MA1-37783	1:100 (ICC)
PECAM/CD31	Lab Vision	RB-10333 - P	1:100 (ICC)
Occludin	Invitrogen	33-1500	1:50 (ICC)
VE Cadherin/CD144	Santa Cruz	sc-52751	1:25 (ICC)
MRP1	Sigma Aldrich	MAB4100	1:50 (ICC)
Goat Anti-Mouse IgG (H+L) 488	Invitrogen	A11001	1:200 (ICC)
Goat Anti-Mouse IgG (H+L) 647	Invitrogen	A32728	1:200 (ICC)
Goat Anti-Rabbit IgG (H+L) 488	Invitrogen	A11008	1:200 (ICC)

4.9 Supplemental

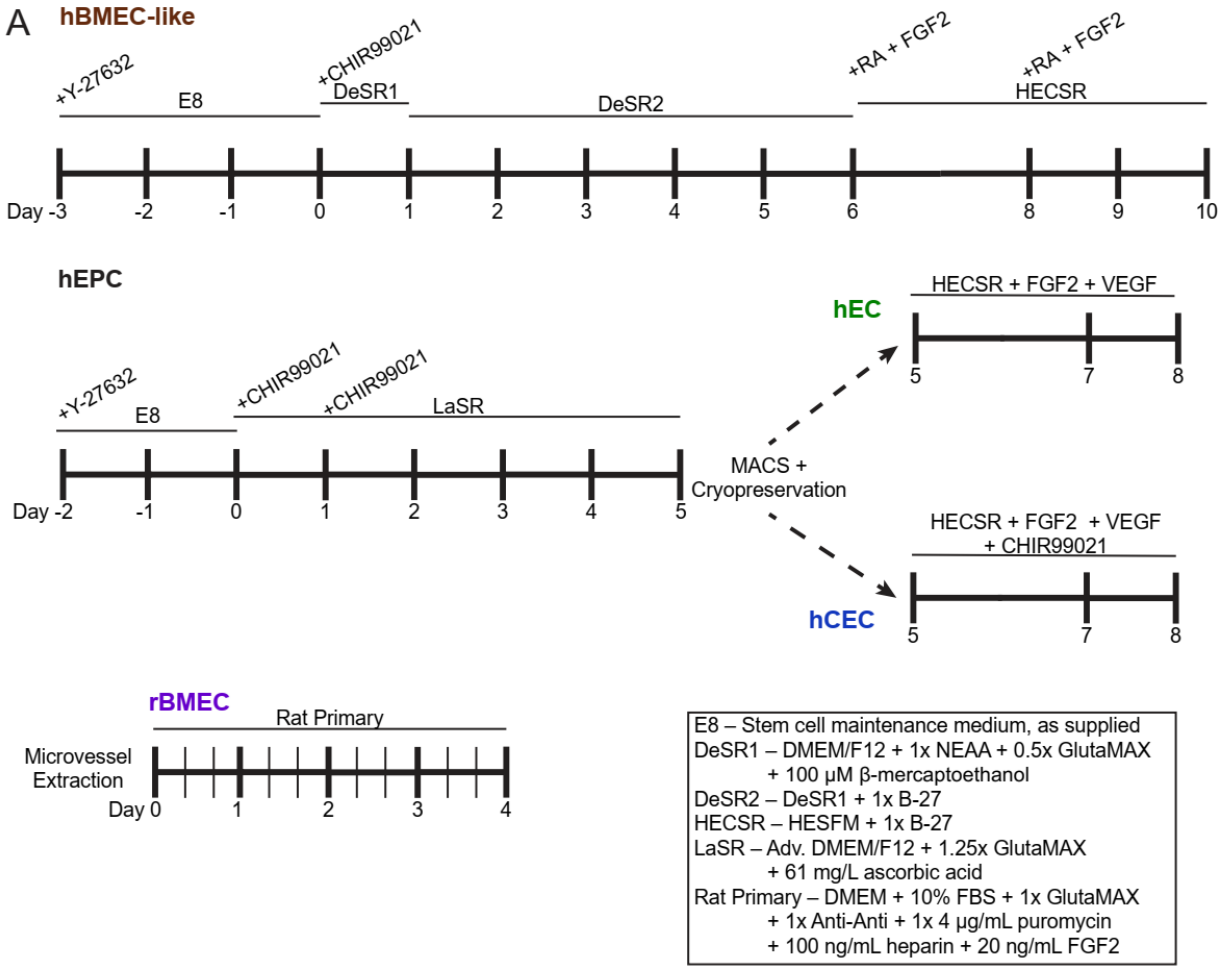

Supplemental Figure 4.1 Overall differentiation schemes for each differentiation used and for the rBMEC isolation. Heavy vertical lines represent daily media changes, thinner vertical lines represent 8 hour media changes. Any day without a feeding does not have a line. Medium and any additional small molecules is provided above the timeline. Differentiations on the final day

are replated to the microfluidic chips. rBMECs are always in the chip due to passaging constraints.

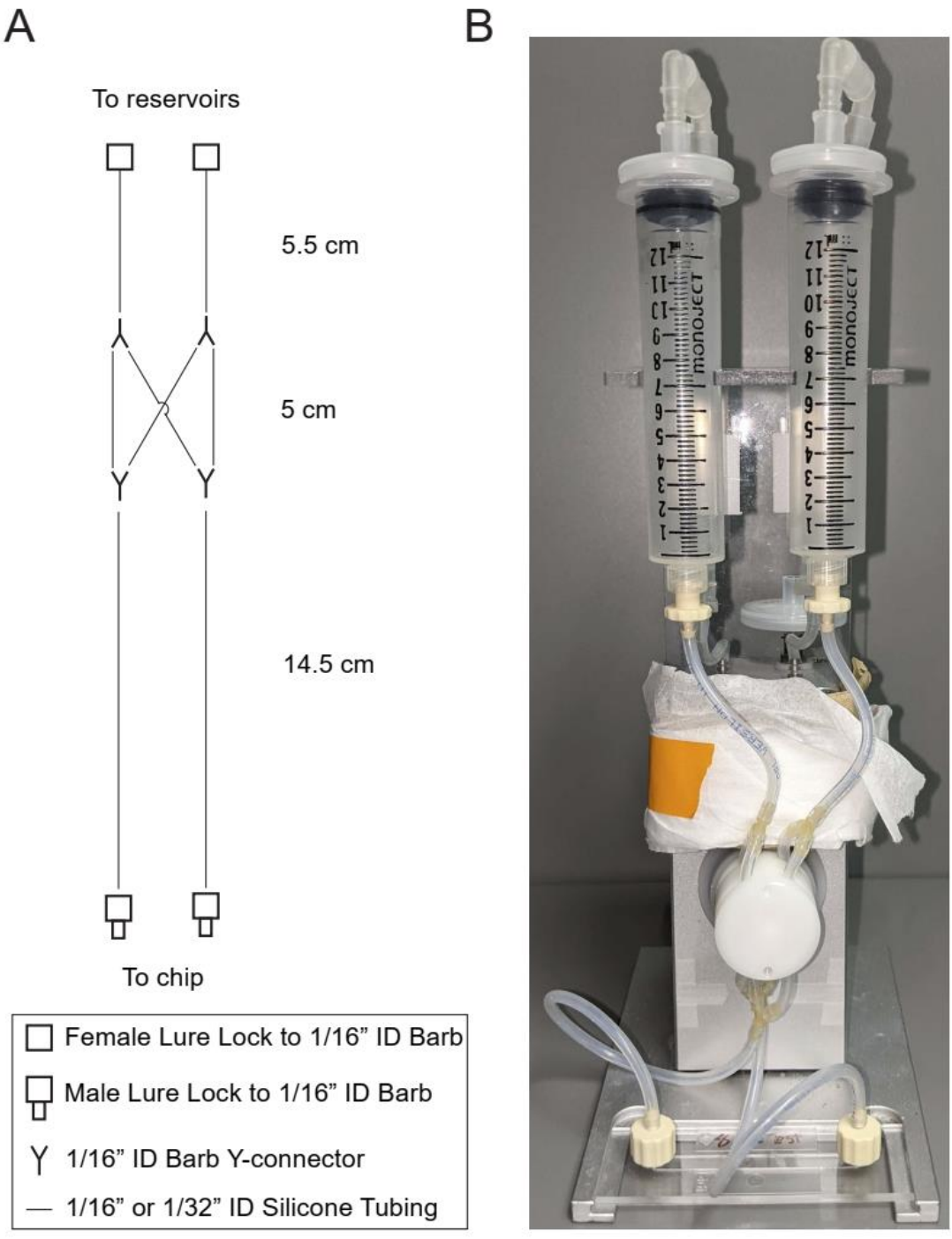

Supplemental Figure 4.2 Microfluidic device. A) Diagram of tubing lengths and components utilized to operate the pump. B) Picture of a fully assembled pump with chip and reservoirs.

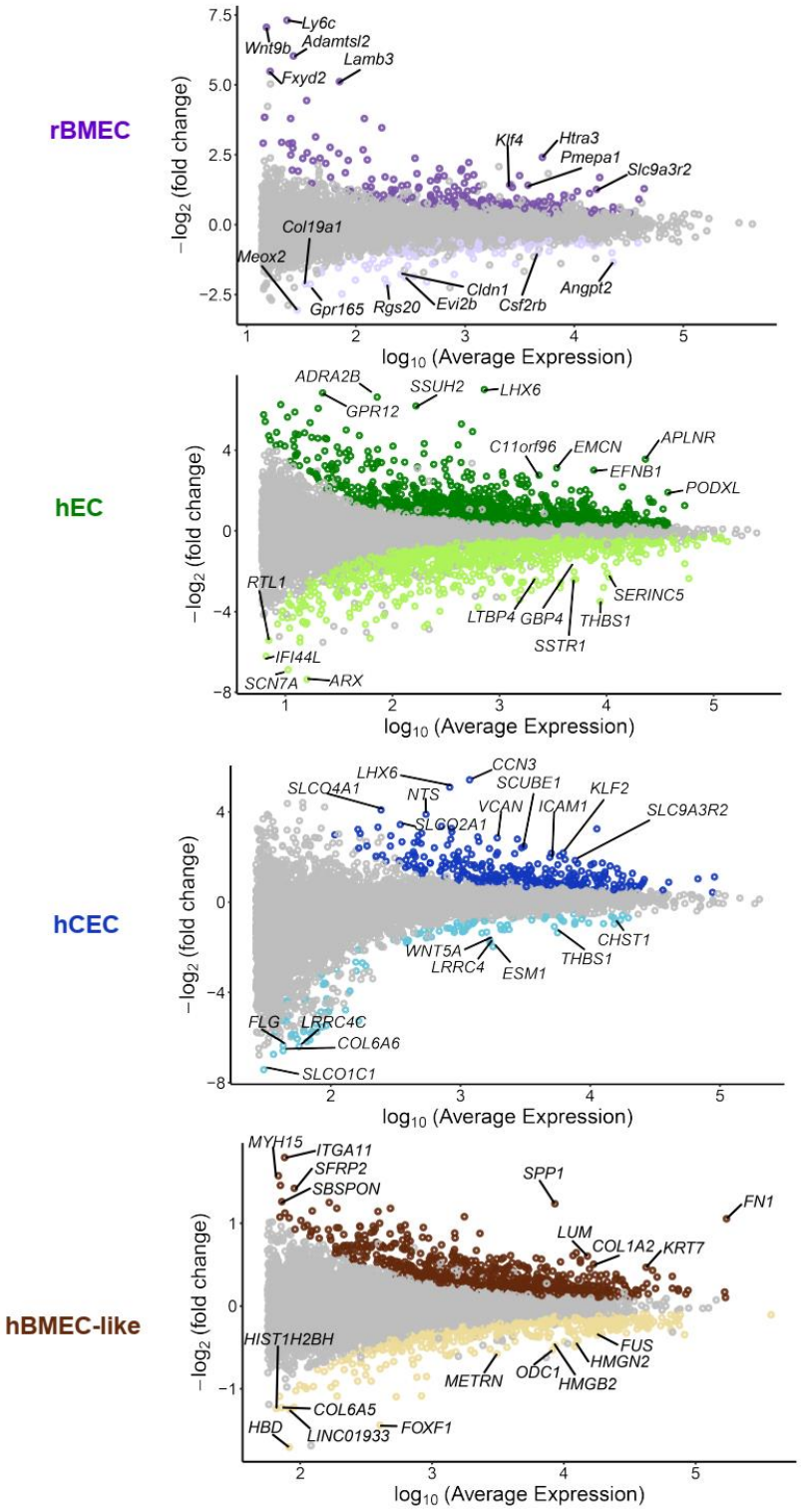

Supplemental Figure 4.3 MA plots for each of the models. Marked genes are those marked on the volcano plots in Figure 2D and are the top 5 smallest padj and highest fold changes.

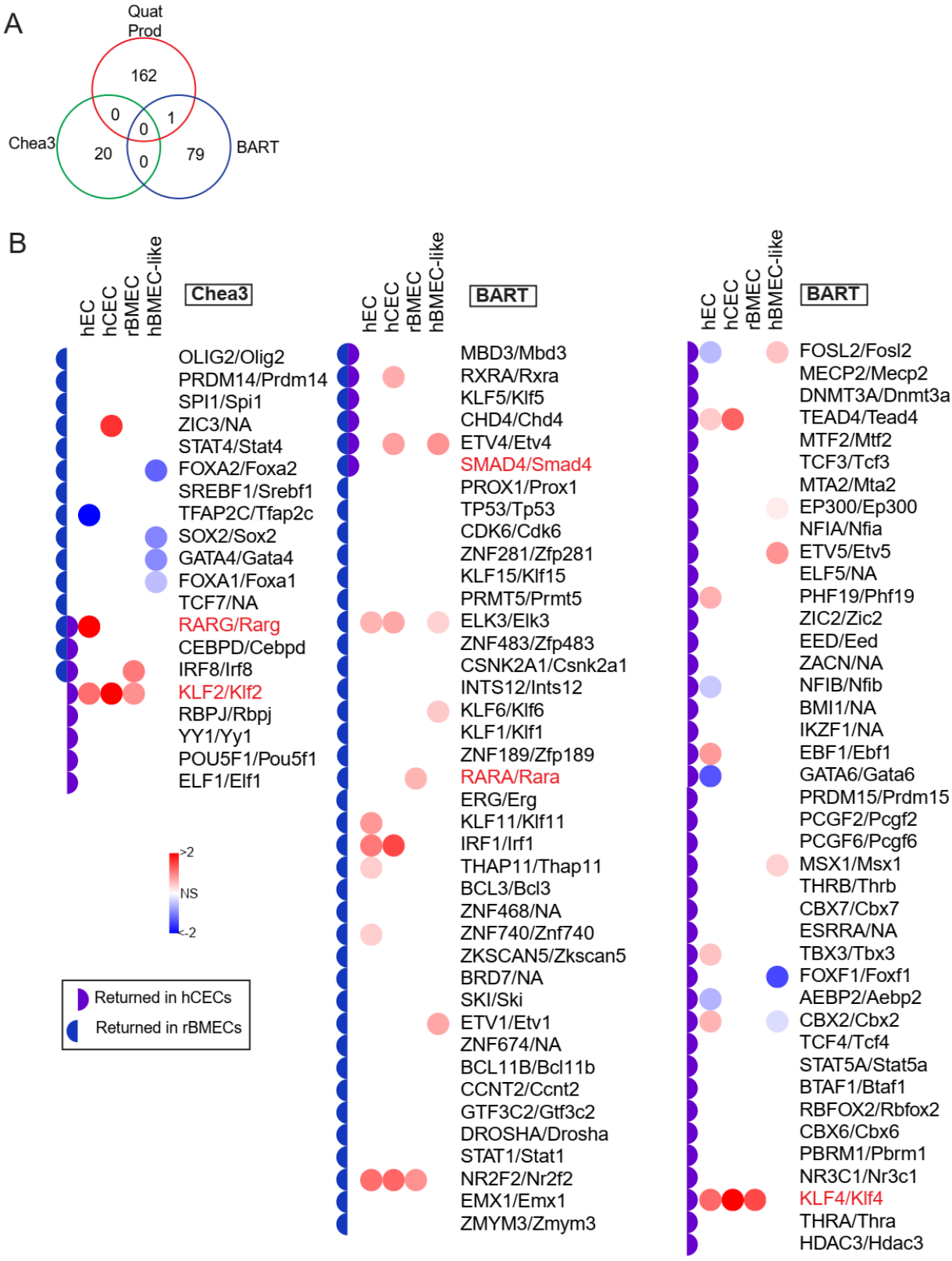
A
Quat
Prod
162
0
0
1
Chea3
20
0
79
BART
B
hEC
hCEC
rBMEC
hBMEC-like
Chea3
OLIG2/Olig2
PRDM14/Prdm14
SPI1/Spi1
ZIC3/NA
STAT4/Stat4
FOXA2/Foxa2
SREBF1/Srebf1
TFAP2C/Tfap2c
SOX2/Sox2
GATA4/Gata4
FOXA1/Foxa1
TCF7/NA
RARG/Rarg
CEBPD/Cebpd
IRF8/Irf8
KLF2/Klf2
RBPJ/Rbpj
YY1/Yy1
POU5F1/Pou5f1
ELF1/Elf1
>2
NS
<-2
Returned in hCECs
Returned in rBMECs
hEC
hCEC
rBMEC
hBMEC-like
BART
MBD3/Mbd3
RXRA/Rxra
KLF5/Klf5
CHD4/Chd4
ETV4/Etv4
SMAD4/Smad4
PROX1/Prox1
TP53/Tp53
CDK6/Cdk6
ZNF281/Zfp281
KLF15/Klf15
PRMT5/Prmt5
ELK3/Elk3
ZNF483/Zfp483
CSNK2A1/Csnk2a1
INTS12/Ints12
KLF6/Klf6
KLF1/Klf1
ZNF189/Zfp189
RARA/Rara
ERG/Erg
KLF11/Klf11
IRF1/Irf1
THAP11/Thap11
BCL3/Bcl3
ZNF468/NA
ZNF740/Znf740
ZKSCAN5/Zkscan5
BRD7/NA
SKI/Ski
ETV1/Etv1
ZNF674/NA
BCL11B/Bcl11b
CCNT2/Ccnt2
GTF3C2/Gtf3c2
DROSHA/Drosha
STAT1/Stat1
NR2F2/Nr2f2
EMX1/Emx1
ZMYM3/Zmym3
hEC
hCEC
rBMEC
hBMEC-like
BART
FOSL2/Fosl2
MECP2/Mecp2
DNMT3A/Dnmt3a
TEAD4/Tead4
MTF2/Mtf2
TCF3/Tcf3
MTA2/Mta2
EP300/Ep300
NFIA/Nfia
ETV5/Etv5
ELF5/NA
PHF19/Phf19
ZIC2/Zic2
EED/Eed
ZACN/NA
NFIB/Nfib
BMI1/NA
IKZF1/NA
EBF1/Ebf1
GATA6/Gata6
PRDM15/Prdm15
PCGF2/Pcgf2
PCGF6/Pcgf6
MSX1/Msx1
THRB/Thrb
CBX7/Cbx7
ESRRA/NA
TBX3/Tbx3
FOXF1/Foxf1
AEBP2/Aebp2
CBX2/Cbx2
TCF4/Tcf4
STAT5A/Stat5a
BTAF1/Btaf1
RBFOX2/Rbfox2
CBX6/Cbx6
PBRM1/Pbrm1
NR3C1/Nr3c1
KLF4/Klf4
THRA/Thra
HDAC3/Hdac3

Supplemental Figure 4.4 Transcription factor analysis hits shared between hCECs and rBMECs. A) Venn diagram comparing suggested upstream transcriptional regulators returned by the three methods utilized. Only includes those hits with TPM > 1, statistical significance, and that are present in either hCECs or rBMECs, but not hECs. B) Lists of all suggested upstream transcriptional regulators by either Chea3 or BART with an average TPM > 1 and FDR/Irwin-Hall p value < 0.05. All hits shown were selected due to presence in either rBMECs or hCECs. Red to blue colored dots represent $\log_2$(fold change) as reported by DESeq2. Non-statistically significant results were colored white.

Supplemental Files available on request.

Supplemental File 4.1 RNA QC Metrics

Supplemental File 4.2 Counts

Supplemental File 4.3 TPMs

Supplemental File 4.4 DESeq2

Supplemental File 4.5 GO Results

Supplemental File 4.6 GSEA Results

Supplemental File 4.7 Chea3 Results

Supplemental File 4.8 BART Results

Supplemental File 4.9 Quaternary Prod Results

4.10 References

1. Gribkoff VK, Kaczmarek LK. The need for new approaches in CNS drug discovery: Why drugs have failed, and what can be done to improve outcomes. Neuropharmacology. 2017;120:11–9.

2. Miller G. Is Pharma Running Out of Brainy Ideas? Science. 2010;329:502–4.

3. Pardridge WM. The Blood-Brain Barrier: Bottleneck in Brain Drug Development. NeuroRx. 2005;2:12.

4. Gastfriend BD, Palecek SP, Shusta EV. Modeling the blood–brain barrier: Beyond the endothelial cells. Current Opinion in Biomedical Engineering. 2018;5:6–12.

5. Abbott NJ, Patabendige AAK, Dolman DEM, Yusof SR, Begley DJ. Structure and function of the blood–brain barrier. Neurobiol Dis. 2010;37:13–25.

6. Obermeier B, Daneman R, Ransohoff RM. Development, maintenance and disruption of the blood-brain barrier. Nat Med. 2013;19:1584–96.

7. Remuzzi A, Dewey CF, Davies PF, Gimbrone MA. Orientation of endothelial cells in shear fields in vitro. Copley AL, Witte S, editors. BIR. 1984;21:617–30.

8. Levesque MJ, Nerem RM. The Elongation and Orientation of Cultured Endothelial Cells in Response to Shear Stress. Journal of Biomechanical Engineering. 1985;107:341–7.

9. Ostrowski MA, Huang NF, Walker TW, Verwijlen T, Poplawski C, Khoo AS, et al. Microvascular Endothelial Cells Migrate Upstream and Align Against the Shear Stress Field Created by Impinging Flow. Biophysical Journal. 2014;106:366–74.

10. Reinitz A, DeStefano J, Ye M, Wong AD, Searson PC. Human brain microvascular endothelial cells resist elongation due to shear stress. Microvascular Research. 2015;99:8–18.

11. DeStefano JG, Xu ZS, Williams AJ, Yimam N, Searson PC. Effect of shear stress on iPSC-derived human brain microvascular endothelial cells (dhBMECs). Fluids and Barriers of the CNS. 2017;14:20.

12. Ando J, Nomura H, Kamiya A. The effect of fluid shear stress on the migration and proliferation of cultured endothelial cells. Microvascular Research. 1987;33:62–70.

13. Dimmeler S, Haendeler J, Rippmann V, Nehls M, Zeiher AM. Shear stress inhibits apoptosis of human endothelial cells. FEBS Letters. 1996;399:71–4.

14. Akimoto S, Mitsumata M, Sasaguri T, Yoshida Y. Laminar Shear Stress Inhibits Vascular Endothelial Cell Proliferation by Inducing Cyclin-Dependent Kinase Inhibitor p21 $^{Sdi1/Cip1/Waf1}$. Circulation Research. 2000;86:185–90.

15. Ohno M, Cooke JP, Dzau VJ, Gibbons GH. Fluid shear stress induces endothelial transforming growth factor beta-1 transcription and production. Modulation by potassium channel blockade. J Clin Invest. 1995;95:1363–9.

16. Walshe TE, dela Paz NG, D'Amore PA. The Role of Shear-Induced Transforming Growth Factor-β Signaling in the Endothelium. ATVB. 2013;33:2608–17.

17. Ni C-W, Hsieh H-J, Chao Y-J, Wang DL. Interleukin-6-induced JAK2/STAT3 signaling pathway in endothelial cells is suppressed by hemodynamic flow. American Journal of Physiology-Cell Physiology. 2004;287:C771–80.

18. Grote K, Luctefeld M, Shieffer B. JANUS under stress—Role of JAK/STAT signaling pathway. Vascular Pharmacology. 2005;43:357–63.

19. White SJ, Hayes EM, Lehoux S, Jeremy JY, Horrevoets AJG, Newby AC. Characterization of the differential response of endothelial cells exposed to normal and elevated laminar shear stress. Journal of Cellular Physiology. 2011;226:2841–8.

20. Qiao C, Meng F, Jang I, Jo H, Chen YE, Zhang J. Deep transcriptomic profiling reveals the similarity between endothelial cells cultured under static and oscillatory shear stress conditions. Physiological Genomics. 2016;48:660–6.

21. Dekker RJ, van Soest S, Fontijn RD, Salamanca S, de Groot PG, VanBavel E, et al. Prolonged fluid shear stress induces a distinct set of endothelial cell genes, most specifically lung Krüppel-like factor (KLF2). Blood. 2002;100:1689–98.

22. Tsaryk R, Yucel N, Leonard EV, Diaz N, Bondareva O, Odenthal-Schnittler M, et al. Shear stress switches the association of endothelial enhancers from ETV/ETS to KLF transcription factor binding sites. Sci Rep. 2022;12:4795.

23. Moonen J-R, Chappell J, Shi M, Shinohara T, Li D, Mumbach MR, et al. KLF4 recruits SWI/SNF to increase chromatin accessibility and reprogram the endothelial enhancer landscape under laminar shear stress. Nat Commun. 2022;13:4941.

24. Helms HC, Abbott NJ, Burek M, Cecchelli R, Couraud P-O, Deli MA, et al. In vitro models of the blood–brain barrier: An overview of commonly used brain endothelial cell culture models and guidelines for their use. J Cereb Blood Flow Metab. 2016;36:862–90.

25. Jamieson JJ, Searson PC, Gerecht S. Engineering the human blood-brain barrier in vitro. J Biol Eng. 2017;11:37.

26. Vatine GD, Barrile R, Workman MJ, Sances S, Barriga BK, Rahnama M, et al. Human iPSC-Derived Blood-Brain Barrier Chips Enable Disease Modeling and Personalized Medicine Applications. Cell Stem Cell. 2019;24:995-1005.e6.

27. Katt ME, Mayo LN, Ellis SE, Mahairaki V, Rothstein JD, Cheng L, et al. The role of mutations associated with familial neurodegenerative disorders on blood–brain barrier function in an iPSC model. Fluids Barriers CNS. 2019;16:20.

28. Katt ME, Xu ZS, Gerecht S, Searson PC. Human Brain Microvascular Endothelial Cells Derived from the BC1 iPS Cell Line Exhibit a Blood-Brain Barrier Phenotype. Deli MA, editor. PLOS ONE. 2016;11:e0152105.

29. Canfield SG, Stebbins MJ, Morales BS, Asai SW, Vatine GD, Svendsen CN, et al. An isogenic blood-brain barrier model comprising brain endothelial cells, astrocytes, and neurons derived from human induced pluripotent stem cells. J Neurochem. 2017;140:874–88.

30. Cucullo L, Hossain M, Puvenna V, Marchi N, Janigro D. The role of shear stress in Blood-Brain Barrier endothelial physiology. BMC Neuroscience. 2011;12:40.

31. Park T-E, Mustafaoglu N, Herland A, Hasselkus R, Mannix R, FitzGerald EA, et al. Hypoxia-enhanced Blood-Brain Barrier Chip recapitulates human barrier function and shuttling of drugs and antibodies. Nat Commun. 2019;10:2621.

32. Ye M, Sanchez HM, Hultz M, Yang Z, Bogorad M, Wong AD, et al. Brain microvascular endothelial cells resist elongation due to curvature and shear stress. Sci Rep. 2015;4:4681.

33. Lian X, Bao X, Al-Ahmad A, Liu J, Wu Y, Dong W, et al. Efficient Differentiation of Human Pluripotent Stem Cells to Endothelial Progenitors via Small-Molecule Activation of WNT Signaling. Stem Cell Rep. 2014;3:804–16.

34. Gastfriend BD, Nishihara H, Canfield SG, Foreman KL, Engelhardt B, Palecek SP, et al. Wnt signaling mediates acquisition of blood–brain barrier properties in naïve endothelium derived from human pluripotent stem cells. eLife. 2021;10:e70992.

35. Nishihara H, Soldati S, Mossu A, Rosito M, Rudolph H, Muller WA, et al. Human CD4+ T cell subsets differ in their abilities to cross endothelial and epithelial brain barriers in vitro. Fluids Barriers CNS. 2020;17:3.

36. Qian T, Maguire SE, Canfield SG, Bao X, Olson WR, Shusta EV, et al. Directed differentiation of human pluripotent stem cells to blood-brain barrier endothelial cells. Sci Adv. 2017;3:e1701679.

37. Mairey E, Genovesio A, Donnadieu E, Bernard C, Jaubert F, Pinard E, et al. Cerebral microcirculation shear stress levels determine Neisseria meningitidis attachment sites along the blood–brain barrier. Journal of Experimental Medicine. 2006;203:1939–50.

38. Calabria AR, Shusta EV. A Genomic Comparison of *in vivo* and *in vitro* Brain Microvascular Endothelial Cells. J Cereb Blood Flow Metab. 2008;28:135–48.

39. Calabria AR, Weidenfeller C, Jones AR, De Vries HE, Shusta EV. Puromycin-purified rat brain microvascular endothelial cell cultures exhibit improved barrier properties in response to glucocorticoid induction. J Neurochem. 2006;97:922–33.

40. Sabbagh MF, Nathans J. A genome-wide view of the de-differentiation of central nervous system endothelial cells in culture. eLife. 2020;9:e51276.

41. Lippmann ES, Azarin SM, Palecek SP, Shusta EV. Commentary on human pluripotent stem cell-based blood–brain barrier models. Fluids Barriers CNS. 2020;17:64, s12987-020-00222–3.

42. Lu TM, Houghton S, Magdeldin T, Durán JGB, Minotti AP, Snead A, et al. Pluripotent stem cell-derived epithelium misidentified as brain microvascular endothelium requires ETS factors to acquire vascular fate. Proc Natl Acad Sci USA. 2021;118:e2016950118.

43. Delsing L, Dönnes P, Sánchez J, Clausen M, Voulgaris D, Falk A, et al. Barrier Properties and Transcriptome Expression in Human iPSC-Derived Models of the Blood-Brain Barrier: Barrier Properties and Transcriptome Expression in Human iPSC-Derived Models. Stem Cells. 2018;36:1816–27.

44. Grifno GN, Farrell AM, Linville RM, Arevalo D, Kim JH, Gu L, et al. Tissue-engineered blood-brain barrier models via directed differentiation of human induced pluripotent stem cells. Sci Rep. 2019;9:13957.

45. Ballermann BJ, Dardik A, Eng E, Liu A. Shear stress and the endothelium. Kidney International. 1998;54:S100–8.

46. Aday S, Cecchelli R, Hallier-Vanuxeem D, Dehouck MP, Ferreira L. Stem Cell-Based Human Blood–Brain Barrier Models for Drug Discovery and Delivery. Trends Biotechnol. 2016;34:382–93.

47. Song HW, Foreman KL, Gastfriend BD, Kuo JS, Palecek SP, Shusta EV. Transcriptomic comparison of human and mouse brain microvessels. Sci Rep. 2020;10:12358.

48. Ashburner M, Ball CA, Blake JA, Botstein D, Butler H, Cherry JM, et al. Gene Ontology: tool for the unification of biology. Nat Genet. 2000;25:25–9.

49. Subramanian A, Tamayo P, Mootha VK, Mukherjee S, Ebert BL, Gillette MA, et al. Gene set enrichment analysis: A knowledge-based approach for interpreting genome-wide expression profiles. Proceedings of the National Academy of Sciences. 2005;102:15545–50.

50. Mizee MR, Wooldrik D, Lakeman KAM, van het Hof B, Drexhage JAR, Geerts D, et al. Retinoic Acid Induces Blood-Brain Barrier Development. Journal of Neuroscience. 2013;33:1660–71.

51. Daneman R, Agalliu D, Zhou L, Kuhnert F, Kuo CJ, Barres BA. Wnt/ -catenin signaling is required for CNS, but not non-CNS, angiogenesis. Proceedings of the National Academy of Sciences. 2009;106:641–6.

52. Alvarez JI, Dodelet-Devillers A, Kebir H, Ifergan I, Fabre PJ, Terouz S, et al. The Hedgehog Pathway Promotes Blood-Brain Barrier Integrity and CNS Immune Quiescence. Science. 2011;334:1727–31.

53. Gastfriend BD, Foreman KL, Katt ME, Palecek SP, Shusta EV. Integrative analysis of the human brain mural cell transcriptome. J Cereb Blood Flow Metab. 2021;41:3052–68.

54. Masuda S, Oda Y, Sasaki H, Ikenouchi J, Higashi T, Akashi M, et al. LSR defines cell corners for tricellular tight junction formation in epithelial cells. Journal of Cell Science. 2011;124:548–55.

55. Bosma EK, Van Noorden CJF, Schlingemann RO, Klaassen I. The role of plasmalemma vesicle-associated protein in pathological breakdown of blood–brain and blood–retinal barriers: potential novel therapeutic target for cerebral edema and diabetic macular edema. Fluids Barriers CNS. 2018;15:24.

56. Keenan AB, Torre D, Lachmann A, Leong AK, Wojciechowicz ML, Utti V, et al. ChEA3: transcription factor enrichment analysis by orthogonal omics integration. Nucleic Acids Research. 2019;47:W212–24.

57. Ma W, Wang Z, Zhang Y, Magee NE, Feng Y, Shi R, et al. BARTweb: a web server for transcriptional regulator association analysis. NAR Genomics and Bioinformatics. 2021;3:lqab022.

58. Fakhry CT, Choudhary P, Gutteridge A, Sidders B, Chen P, Ziemek D, et al. Interpreting transcriptional changes using causal graphs: new methods and their practical utility on public networks. BMC Bioinformatics. 2016;17.

59. Kowalczyk A, Kleniewska P, Kolodziejczyk M, Skibska B, Goraca A. The Role of Endothelin-1 and Endothelin Receptor Antagonists in Inflammatory Response and Sepsis. Arch Immunol Ther Exp. 2015;63:41–52.

60. The Gene Ontology Consortium, Carbon S, Douglass E, Good BM, Unni DR, Harris NL, et al. The Gene Ontology resource: enriching a GOld mine. Nucleic Acids Research. 2021;49:D325–34.

61. Mootha VK, Lindgren CM, Eriksson K-F, Subramanian A, Sihag S, Lehar J, et al. PGC-1α-responsive genes involved in oxidative phosphorylation are coordinately downregulated in human diabetes. Nat Genet. 2003;34:267–73.

62. Motallebnejad P, Thomas A, Swisher SL, Azarin SM. An isogenic hiPSC-derived BBB-on-a-chip. Biomicrofluidics. 2019;13:064119.

63. Jamieson JJ, Linville RM, Ding YY, Gerecht S, Searson PC. Role of iPSC-derived pericytes on barrier function of iPSC-derived brain microvascular endothelial cells in 2D and 3D. Fluids Barriers CNS. 2019;16:15.

64. Faley SL, Neal EH, Wang JX, Bosworth AM, Weber CM, Balotin KM, et al. iPSC-Derived Brain Endothelium Exhibits Stable, Long-Term Barrier Function in Perfused Hydrogel Scaffolds. Stem Cell Rep. 2019;12:474–87.

65. Booth R, Kim H. Characterization of a microfluidic in vitro model of the blood-brain barrier (μBBB). Lab on a Chip. 2012;12:1784.

66. Vanlandewijck M, He L, Mäe MA, Andrae J, Ando K, Del Gaudio F, et al. A molecular atlas of cell types and zonation in the brain vasculature. Nature. 2018;554:475–80.

67. Yang Y, Xu X. Bioinformatic identification of hub genes and related transcription factors in low shear stress treated endothelial cells. BMC Med Genomics. 2021;14:120.

68. Lin K, Hsu P-P, Chen BP, Yuan S, Usami S, Shyy JY-J, et al. Molecular mechanism of endothelial growth arrest by laminar shear stress. Proc Natl Acad Sci USA. 2000;97:9385–9.

69. Tardy Y, Resnick N, Nagel T, Gimbrone MA, Dewey CF. Shear Stress Gradients Remodel Endothelial Monolayers in Vitro via a Cell Proliferation-Migration-Loss Cycle. ATVB. 1997;17:3102–6.

70. Egorova AD, Van der Heiden K, Van de Pas S, Vennemann P, Poelma C, DeRuiter MC, et al. Tgfβ/Alk5 signaling is required for shear stress induced klf2 expression in embryonic endothelial cells. Dev Dyn. 2011;240:1670–80.

71. Stebbins MJ, Lippmann ES, Faubion MG, Daneman R, Palecek SP, Shusta EV. Activation of RARα, RARγ, or RXRα Increases Barrier Tightness in Human Induced Pluripotent Stem Cell-Derived Brain Endothelial Cells. Biotechnol J. 2018;13:1700093.

72. Maurya MR, Gupta S, Li JY-S, Ajami NE, Chen ZB, Shyy JY-J, et al. Longitudinal shear stress response in human endothelial cells to atheroprone and atheroprotective conditions. Proc Natl Acad Sci USA. 2021;118:e2023236118.

Chapter 5 – Defined Differentiation of Human Pluripotent Stem Cells to a Model of the Blood-Brain Barrier[3]

[3] The following chapter is adapted from [1]:

Foreman KL, Shusta EV, Palecek SP. Chapter 10: Defined Differentiation of Human Pluripotent Stem Cells to a Model of the Blood-Brain Barrier. In: Huang Y-WA, Pak C, editors. Methods in Molecular Biology: Stem Cell Based Neural Model Systems for Brain Disorders. Springer International Publishing; 2023.

5.1 Summary

The blood-brain barrier (BBB) comprises brain microvascular endothelial cells (BMECs) that form a high resistance cellular interface that separates the blood compartment from the brain parenchyma. An intact BBB is pivotal to maintaining brain homeostasis, but also impedes the entry of neurotherapeutics. There are limited options for human-specific BBB permeability testing, however. Human pluripotent stem cell models offer a powerful tool for dissecting components of this barrier *in vitro*, including understanding mechanisms of BBB function, and developing strategies to improve the permeability of molecular and cellular therapeutics targeting the brain. Here, we provide a detailed, step-by-step protocol for differentiation of human pluripotent stem cells (hPSCs) to cells exhibiting several key characteristics of BMECs, including paracellular and transcellular transport resistance and transporter function.

5.2 Introduction

Diseases of the central nervous system (CNS) can be devastating for patients, both in terms of prognosis and quality of life [2]. However, novel CNS therapeutics, are much less likely to make it to the clinic than those drugs developed for other indications due to a host of factors that include the presence of the blood-brain barrier (BBB)[2–4]. Delivering therapeutic doses across the BBB is thought to hamper over 98% of all new small molecules, and most current antibody therapies [4]. For instance, BMECs express polarized efflux transporters that semi-selectively pump lipophilic compounds back into the bloodstream, thereby restricting transcellular transport across the BBB[5,6]. BMECs also express transmembrane proteins that mediate tight junctions between the cells which resist paracellular transport[5,7]. A better understanding of this BMEC transport interface is vital to designing approaches to deliver neurotherapeutics across the BBB.

Researchers have developed several cell-based systems to model the BBB. The most direct method is to study molecular penetration and BBB behavior in a live animal [8–11]. Animal models capture the physiological aspects of the BBB, but there are known differences in BBB molecular and functional phenotypes, including differential expression of efflux transporters [12,13], between humans and experimental animals. Animal models are rather low throughput, limiting their applications. By contrast, *in vitro* models consisting of primary brain BMECs can offer a more controlled and scalable platform for evaluating compound transport through the BBB, with human cells offering human relevance. However, these models suffer from BMEC dedifferentiation and poor paracellular permeability after culture *ex vivo* [8,11]. Immortalized human BMECs provide a highly scalable model for BBB research with some

barrier and efflux protein expression, but do not typically form substantial barriers amenable to drug permeability screening [11].

The discovery of human pluripotent stem cells (hPSCs) [14] has opened the possibility of developing a human BBB model for drug screening and permeability studies. Several BBB models that demonstrate high paracellular and functional transcellular resistance have been reported [15–23]. They have been shown to have continuous junctional staining for various tight junction related proteins, and expression and activity of several common efflux transporters such as P glycoprotein (P-gp) and Breast Cancer Resistance Protein (BCRP). Hence, these models have been used to predict permeability of various small molecules and blood borne components [20,24,25].

In addition to predicting molecular permeability, *in vitro* BBB models can be used to study the effects of disease on BBB structure and function. Induced PSCs (iPSCs) reprogrammed from differentiated cell types in adults can be used to study the impact of genetic modifications in some diseases. For example, researchers have explored the effects of genetic defects known to cause neurodegenerative diseases such as Allan Herndon Dudley Synrome, Alzheimer's disease and Huntington's diseases on BBB properties using patient-derived iPSC sources [20,26,27].

Below, we detail a defined protocol for differentiation of hPSC-BBB model published previously [28](Fig. 1A). The differentiation process applies CHIR99021, a GSK-3 inhibitor used to drive Wnt signaling, as well as supplements and signaling factors like B-27, retinoic acid, and FGF2 to further drive the observed BBB phenotypes. Importantly, like any hPSC differentiation, some parameters, such as induction factor concentration, initial seeding density, subculture seeding density and line-to-line variability [28–32] can impact the differentiation process. The sensitivity to these variables can be observed in the attached sample data.

5.3 Materials

Prepare all materials, unless stated otherwise, using cell culture grade sterile water and reagents in a sterile laminar flow hood with proper aseptic technique. Differentiations will require a suitable hPSC line. This method has previously been used in our lab with IMR90-4 iPSCs from WiCell and H9 human embryonic stem cells (hESCs).

5.3.1 Small Molecule and Protein Aliquots

1. Y-27632 Aliquots – Y-27632 is typically provided as a sterile powder. Add water to dilute to produce a 10 mM solution. Y-27632 should solubilize quickly in solution. This is 1000x the needed concentration in the application used here. Aliquots should be 50-100 µL, dependent on rate of use. Store at -20 °C, with one working aliquot kept at 4 °C for up to 2 weeks.
2. CHIR99021 Aliquots – CHIR99021 is provided as a powder. Suspend in dimethyl sulfoxide (DMSO) to 10 mM in aliquots of 20-50 µL, dependent on use. Store aliquots at -80 °C and one working stock at 4 °C for up to 1 week.
3. Retinoic Acid Aliquots – Retinoic acid (RA) is provided as a powder. Suspend in DMSO to 10 mM and aliquots to between 50-200 µL, dependent on use. Store aliquots away from light at -20 °C and one working stock at 4 °C away from light for up to 1 week.
4. FGF2 Aliquots – FGF2 solution should be diluted according to manufacturer's instructions to 100 mg/mL in aliquots of about 20-50 µL, dependent on use. Store aliquots at -80 °C, avoiding freeze thaw cycles, with one working stock at 4 °C for up to 1 week.

5.3.2 ECM Components and Plates

1. Tissue culture treated polystyrene 6-well plates.

2. Matrigel Aliquots – Thaw Matrigel overnight at 4 °C. Chill 1.5 mL tubes. Do not thaw at room temperature. Since Matrigel has batch to batch variability in protein concentration, add sufficient thawed Matrigel solution to reach 2.5 mg per aliquot, which is sufficient to coat 5 6-well plates or about 290 cm^2 of surface area. The concentration of solution will be provided by the manufacturer and the volume is typically close to 250 µL. Once thawed, place the Matrigel on ice, and each aliquot should be stored on ice until transferred to -80 °C storage. Do not store at 4 °C.
3. Acetic Acid Solution (5 mg/mL) – Acetic acid is typically not provided sterile, so the solution should be sterile filtered. Add approximately 100 mL water to the upper chamber of a 0.4 µm sterile filter. Add 1.25 g glacial acetic acid, swirling to mix. Fill with water to the 250 mL line. Store at 4 °C.
4. Collagen Type IV Solution – Cell culture certified collagen type IV is provided as a lyophilized powder. Add sufficient preprepared acetic acid solution to reach 1 mg/mL. Collagen type IV will solubilize slowly, so prepare at least a day in advance and allow to resolubilize overnight at 4 °C. Store at 4 °C when not in use. 5 mg would require 5 mL of acetic acid solution for example. Store at 4 °C for up to 2 weeks.
5. Fibronectin Solution– Purchase at 1 mg/mL or dilute to 1 mg/mL in appropriate solution according to manufacturer's instructions. Store at 4 °C for up to 2 weeks.

5.3.3 Media and Differentiation Materials

1. Accutase
2. Dulbecco's Phosphate Buffered Saline (DPBS) – Purchase without calcium or magnesium. Should be sterile and cell culture grade.
3. Dimethyl sulfoxide (DMSO)

4. Fetal Bovine Serum (FBS) – Purchase at 500 mL. Thaw overnight at 4 °C. Prepare ~40 mL aliquots in 50 mL conical tubes. Store at -20 °C. Keep one working stock at 4 °C for up to 2 weeks. If not using 40 mL of FBS in 2 weeks, create smaller 10 mL aliquots in 15 mL conical tubes and store as above.
5. Human Pluripotent Stem Cell Culture Medium– both E8 and mTeSR have been used successfully.
6. DMEM/F12 – Either purchase directly or mix 1:1 of Dulbecco's Modified Eagle's Media and F12.
7. DeSR1 – Add ~100 mL of DMEM/F12 to the top of a sterile 0.2 µm pore size 500 mL filter. Add 5 mL of MEM Non-Essential Amino Acids (NEAA), 2.5 mL of GlutaMAX, and 3.5 µL of β-mercaptoethanol. Swirl and then fill to 500 mL with DMEM/F12 and filter through a 0.2 µm filter. Store at 4 °C for up to a month.
8. DeSR2 – Add ~100 mL of DeSR1 to the top of a sterile 0.2 µm pore size 250 mL filter. Add 5 mL B-27 media supplement. Swirl and fill to 250 mL with DeSR1 and filter. Store at 4 °C for up to 2 weeks.
9. HECSR - Add ~100 mL of HESFM to the top of a sterile 0.2 µm pore size 250 mL filter. Add 5 mL B-27 media supplement. Swirl and fill to 250 mL with HESFM and filter. Store at 4 °C for up to 2 weeks.
10. HECSR + 10 µM RA + 20 ng/mL FGF2 – Should be made day of use. Do not store. If using aliquot concentrations as described in 2.2, then add 1 µL RA per 1 mL of HECSR and 0.2 µL FGF2 per 1 mL of HECSR.

5.3.4 Immunocytochemistry

1. PBS – Add 20 L of ultrapure water (~18 MΩ) to a 20+ L container. Add a stir bar, 4 g KCl, 4 g KH_2PO_4, 160 g NaCl, and 43.2 g Na_2HPO_4-$7H_2O$. Stir overnight to dissolve. Aliquot into 1-2 L containers for longer term storage. Keeps indefinitely.
2. Methanol
3. 16% Paraformaldehyde solution
4. 4% Paraformaldehyde solution (PFA) – Mix 12.5 µL 16% paraformaldehyde with 37.5 µL PBS. Make fresh as needed.
5. 10% Goat Serum – Dilute 1 mL goat serum in 9 mL PBS. Store at 4 °C for up to a week.
6. Hoechst 33342 – Purchase at or dilute with water to 10 mg/mL.
7. Dilute Hoechst Solution – Add 10 µL of Hoechst 33342 to 50 mL of PBS. Store protected from light at 4 °C for up to a month.
8. Fluorescent microscope capable of exciting at 488 nm and 352 nm.

5.3.5 Accumulation Assay

1. Hank's Balanced Saline Solution – Sterile
2. Ethanol
3. Rhodamine 123 (Rh123) Aliquots – Purchase powder, resuspend to 10 mM in ethanol. Aliquots should be 500-1000 µL and stored at -20 °C protected from light
4. DPBS –As 2.3
5. Cyclosporine A (CsA) - CsA is provided as a powder. Suspend in DMSO to 10 mM in aliquots of 20-50 µL, dependent on use. Store aliquots at -20 °C.
6. RIPA Buffer
7. Plate Reader capable of exciting at 485 nm and measuring fluorescence at 530 nm

5.3.6 Trans Endothelial Electrical Resistance (TEER)

1. Transwells – Corning 3640 or equivalent with 0.4 µm pore size
2. EVOM2 or equivalent
3. Chopstick electrodes
4. DPBS – cell culture and sterile without calcium and magnesium.
5. 70% Ethanol – Mix 7 mL of ethanol with 3 mL of cell culture grade sterile water
6. 70% ethanol in a spray bottle for sterilizing – mix 70% by volume ethanol and fill to 100% volume with deionized water.

5.4 Methods

Unless stated otherwise, all steps should be performed in a sterile laminar flow hood with proper aseptic technique. All media should be warmed at room temperature at least 30 minutes before application.

5.4.1 Differentiation of hPSCs

Differentiation of hPSCs to the previously published BBB model [28]. Equations are provided for ease of scaling.

1. Human pluripotent stem cells should be maintained according to previous established methods with culture at 37 °C and 5% CO_2. We suggest protocols such as Stebbins et al. [18] and maintaining cells on Matrigel-coated tissue culture treated polystyrene 6 well plates, passaging cells between 50-70% confluency. Before starting a differentiation, cells should not be stressed by poor passaging, changes in feeding schedule, exposure to room temperature for prolonged periods, or storage in a non-humidified incubator. Cells should also be at least 2-3 passages post thawing before initiating a differentiation.

2. A minimum of 1 hour before, but up to a week before starting differentiation: Prepare a 50 mL conical tube with ~32 mL of DMEM/F12 (if using the Matrigel aliquot sizes provided in Materials).
3. Remove Matrigel aliquot from freezer and quickly suspend by pipetting 1 mL from the prepared aliquot of DMEM/F12 into the Matrigel aliquot. Pipette up and down until Matrigel is dissolved. Return DMEM/F12 + Matrigel to the DMEM/F12 aliquot.
4. Add 1 mL of DMEM/F12 and Matrigel solution per well of a tissue culture treated polystyrene 6 well plate using a 5 mL stripette. Work quickly.
5. Day -3: When hPSCs are 50-70% confluent, aspirate stem cell culture medium (see Note 1), then add 1 mL of Accutase per well. Typically, for each plate to be seeded, harvest 1 well; there will be excess cell solution (Fig 1A).
6. Return the plate to the 37 °C incubator for 5-7 minutes.
7. While the cells are being incubated with Accutase, prepare a 50 mL conical containing 4 mL of DMEM/F12 per 1 mL of Accutase used to detach the cells.
8. Swirl plate gently by hand. If the cells are not detached, return to the incubator for another 2 minutes.
9. Once ~70% of the cells are detached, use a 1000 uL pipette to wash the well 1-5 times until cells are completely detached and singularized. Any cells still attached to the plate should have been rinsed off during this process. There should be no visible clumps of cells within the Accutase when done. See Note 2. Add cell solution to 50 mL conical containing pre-prepared DMEM/F12. Invert 3-4 times to mix before reserving 50-100 µL of cell solution to count.

10. Centrifuge cells at 200 g for 5 minutes. While doing this, count reserved cell concentration and calculate total cell number according to manufacturer's cell counting protocol.
11. Aspirate supernatant. There should be a visible pellet. Resuspend pellet to 2 million cells/mL in stem cell culture medium by gently pipetting up and down using a 5 or 10 mL stripette to generate concentrated cell solution.
12. Calculate cells needed per well. See Note 3
    a. $\frac{Cells}{Well} = Optimal\ Seeding\ Density\ \left(\frac{cells}{cm^2}\right) * Surface\ Area\ of\ Well\ (cm^2)$
13. Prepare a volume of stem cell medium + 10 μM Y-27632 sufficient for one plus the number of wells to be seeded (see Table 1). Remember to account for required volume of the cell solution.
14. Add cell solution to provide enough cells for total number of wells to be seeded plus one to the prepared stem cell medium plus Y-27632. Invert three times to mix.
15. Quickly fill 3 wells with appropriate volume of the cell suspension. Invert tube to ensure the solution remains well mixed. Repeat until all wells are seeded. See Note 4.
16. Place plates into 37 °C incubator with 5% CO_2.
17. Shake plates 3 times forward and backwards, then 3 times left to right to ensure even distribution of cells. Note 5.
18. Day -2: After 24 hours, aspirate spent medium, add 2 mL stem cell culture medium without Y-27632 to each well (Fig 1A).
19. Day -1: Aspirate spent medium, add 2 mL stem cell culture medium to each well.
20. Day 0: Prepare 2 mL for each well of a 6-well plate of DeSR1 containing the optimal concentration of CHIR99021 determined via an optimization assay (Fig 2B).

21. Aspirate medium, add 2 mL of DeSR1 + CHIR99021 to each well. See Notes 6 and 7.
22. Day 1: After 22.5-24 hours from Step 21, aspirate spent medium and add 2 mL DeSR2 to each well. See Notes 8 and 9.
23. Day 2: Aspirate medium, add 2 mL DeSR2 to each well.
24. Day 3: Aspirate medium, add 2 mL DeSR2 to each well.
25. Day 4: Aspirate medium, add 2 mL DeSR2 to each well.
26. Day 5: Aspirate medium, add 2 mL DeSR2 to each well.
27. Day 6: Prepare a conical with sufficient HECSR + 10 µM RA + 20 ng/mL FGF2.
28. Day 6: Aspirate spent medium, add 2 mL prepared HECSR + 10 µM RA + 20 ng/mL FGF2 to each well. See Note 10.
29. Day 7: Prepare collagen IV and fibronectin-coated wells or Transwells. For Transwells use 100 µg/mL fibronectin and 400 µg/mL collagen IV diluted with water. For flat plates use a solution of 20 µg/mL fibronectin and 80 µg/mL collagen IV. See Table 1 for volumes. Incubate overnight at 37 °C and 5% CO_2. Cell medium does not need to be changed on Day 7.
30. Day 8: Aspirate medium and gently wash cells with DPBS.
31. Add 1 mL Accutase per well, incubate for 20-60 minutes. Check every 10-15 minutes by gently swirling; if cells do not detach continue incubation. See Note 11.
32. During the incubation, prepare 4 mL DMEM/F12 per 1 mL of Accutase used to quench the Accutase.
33. Prepare HECSR + 10 µM retinoic acid + 20 ng/mL FGF2 sufficient for all wells in the experiment, and to resuspend the cells. Typical yield is close to 2-4 million cells per 10 cm^2. Prepare more than needed.

34. Once 60 minutes of Accutase treatment have elapsed or cells are visibly detaching from the well, whichever comes first, rinse cells from each well using a 1000 µL pipette tip, triturating to singularize the cells. Filter solution through a 40 µm sterile filter to remove cell clumps into the prepared DMEM/F12 quench. Collect ~100 µL of cell solution to count
35. Centrifuge at 200 g for 5 minutes. While doing this, count reserved cell concentration and calculate total number of cells according to manufacturer's cell counting protocol.
36. Aspirate supernatant, being careful not to aspirate the cell pellet. Resuspend cells to 2 million cells/mL.
37. Aspirate the remaining collagen and fibronectin solution from prepared plates. Seed Transwells at 500,000 cells/cm^2 (see Note 12) and plates at 100,000 cells/cm^2.
38. Place plates or Transwells into 37 °C incubator with 5% CO_2.
39. Shake plates or Transwells 3 times forward and backwards, then 3 times left to right. Repeat 3 times to ensure even distribution of cells.
40. Day 9: Aspirate medium, add appropriate volume of HECSR per well. This is generally the last medium change; cells can be maintained for up to at least six days afterwards (Fig 3)
41. Day 10: Most cell function assays are performed on this day. A small number of 96 well seeded cells should be fixed and prepared for immunocytochemistry at this time point to ensure appropriate expression of proteins relevant to the properties being assessed. Examples of efflux transporters and tight junction associated proteins have been provided (Fig 1B). See Note 13.

5.4.2 Immunocytochemical Analysis

Unless stated otherwise, all steps should be performed in a sterile laminar flow hood with proper aseptic technique. Staining protocols adapted from Stebbins et al. and Qian et al. [18,28] and example images are provided in Fig 1B. Typically, once a differentiation protocol is optimized, proper expression and localization of proteins of interest are assessed as quality control to ensure appropriate marker expression. For example, if assessing permeability of a hydrophilic molecule, continuous tight junction protein expression is important to validate. Table 1 lists several proteins suggested as potential quality controls along with the antibodies we have used previously.

1. Perform differentiation as described in Method 3.1. On Day 8, cells should be seeded at 100,000 cells/cm^2 or higher to ensure a monolayer into a wells of a collagen IV and fibronectin-coated 96 well plate. See Note 14.
2. Store 100% methanol at -20 °C or allow to chill for at least 1 hour at -20 °C.
3. Day 10: Aspirate medium from each well, then wash 3 times with ~200 µL of DPBS per well.
4. Aspirate DPBS, add 50 µL methanol or 4% PFA (antibody-dependent, see Table 1) per well to fix the cells
5. Incubate for 15 minutes at room temperature.
6. Aspirate methanol or PFA, then wash each well once with ~200 µL PBS (can switch to non-sterile PBS at this stage). Cells no longer need to be kept sterile and the remaining steps can be performed on a bench top.
7. Aspirate PBS. Add 100 µL 10% goat serum per well to block.
8. Incubate 1 hour at room temperature or overnight at 4 °C.

9. During goat serum incubation, prepare primary antibody solutions (See Table 2 for concentrations and solutions) with 50 µL per well.
10. Aspirate blocking goat serum. Add 50 µL primary antibody solution to each well.
11. Incubate overnight at 4 °C.
12. Prepare 50 µL per well of species appropriate secondary antibody solution in 10% goat serum. Protect from light. See Table 2 for concentrations.
13. Aspirate primary antibody solution. Wash 3 times with ~200 µL PBS per well. See Note 15.
14. Add 50 µL per well of appropriate secondary solution.
15. Incubate, protected from light, for 1 hour at room temperature or overnight at 4 °C.
16. Aspirate secondary antibody solution. Wash 2 times with ~200 µL PBS per well.
17. Aspirate PBS. Add 50 µL per well of dilute Hoechst solution. Cover and incubate for 10-20 minutes at room temperature.
18. Aspirate dilute Hoechst solution. Add 200 µL PBS to each well.
19. Image on a fluorescence microscope with appropriate excitation and emission filters according to secondary antibodies used.

5.4.3 Rhodamine 123 Accumulation Assay

Unless stated otherwise, all steps should be performed in a sterile laminar flow hood with proper aseptic technique. This protocol is adapted from Stebbins et al. [18]. This assay can be used to assess the relative activity of P-gp in the model cells by comparing accumulation of a fluorescent substrate of P-gp, Rh123, in normal cells and in cells with P-gp inhibition. The fold change represents both the activity and the maximum accumulation. Typically, fold increases of 1.5 to 2.0 of CsA treated cells over control have been observed [15,18,28,29].

1. Perform differentiation as described in Method 3.1. On Day 8, cells should be seeded at 100,000 cells/cm^2 or higher onto a Collagen IV and Fibronectin coated 24 well plate to obtain a confluent monolayer. Experiment should be performed at n = 4-6. The assay should include a vehicle control (DMSO), an inhibited P-gp condition (CsA), and a single blank well.
2. On Day 10-15 (See Fig 4): Add 0.5 mL of HBSS per well of vehicle control + 1 for the blank to a 15 mL conical. Add 1 µL DMSO per mL of HBSS. Invert 3 times to mix.
3. In another 15 mL conical tube, add 0.5 mL of HBSS per well to be treated with CsA. Add 1 µL CsA per mL of HBSS. Invert 3 times to mix. A white particulate may be visible initially, but should dissolve.
4. Aspirate medium and wash each well twice with 1 mL HBSS. Add 0.5 mL of HBSS + DMSO to half the wells and HBSS + CsA to the remainder.
5. Incubate at 37 °C and 5% CO_2 for 1 hour on an orbital shaker at 30 rpm.
6. While incubating, prepare HBSS + 10 µM Rh123 at 0.5 mL per well. Dilution should be 1 µL of Rh123 solution per mL of HBSS if using the aliquot concentrations in Materials.
7. Split HBSS + Rh123 into two 15 mL conical tubes. One for DMSO, the other for CsA
8. Add 1 µL per mL DMSO or CsA to the conical tubes containing HBSS + Rh123
9. After 1 hour, aspirate HBSS + DMSO/CsA, add 0.5 mL of HBSS + Rh123 + DMSO/CsA and return to shaker and incubator. Do not aspirate or change the contents of the blank control well.
10. Incubate at 37 °C and 5% CO_2 for 2 hours on an orbital shaker at 30 rpm.
11. Place DPBS at 4 °C to chill.

12. After 2 hours, aspirate Rh123 containing HBSS carefully. Be sure to not leave small droplets on the sides of the wells.
13. Wash each well 3 times with 1 mL chilled DPBS.
14. Aspirate DPBS. Add 200 µL RIPA Buffer to each well.
15. Shake at 30 rpm for 10 minutes to completely lyse cells.
16. Scan each well on a plate reader with 485 excitation and 530 emission filters.
17. Freeze cell lysates at -20 °C this stage by placing the entire plate in the freezer. Alternatively, proceed to BCA assay.
18. Perform BCA assay according to manufacturer's instructions on lysate to allow proper normalization.
19. Normalize each well (i) according to the following equation:

$$F = \frac{(Rh_i - Rh_{Blank})}{P_i}$$

Where Rh_i is Rhodamine fluorescence from well i, P is protein concentration according to the standard curve according to the manufacturer's instructions in the BCA kit in well i, Rh_{Blank} is Rhodamine fluorescence from the blank well.

20. Normalize results to the average of all fluorescent values for the control (DMSO) wells. This will provide the fold changes typically reported.

5.4.4 Trans Endothelial Electrical Resistance (TEER)

All steps should be performed in a sterile laminar flow hood with proper aseptic technique. This protocol is adapted from Stebbins et al. [18]. This assay measures the resistance across a cell monolayer and provides an assessment of the paracellular resistance of the model. TEER measurement is nondestructive, and is an important quality control assay prior to measuring

molecular permeability or when interested in passage of hydrophilic molecules. Typically the cell monolayer should have a barrier above 1000 Ω-cm^2 [24].

1. On Day 7 of the differentiation, as described in Methods 3.1: Coat Transwells with collagen IV and fibronectin. Prepare an additional unseeded well to determine baseline resistance of the Transwell membrane. Note 16.
2. On Day 8 of the differentiation: Seed Transwells at 500,000-1,000,000 cells/cm^2 as described in Methods 3.1. Do not seed the unseeded control well.
3. Day 9+: Add ~10 mL of 70% ethanol to a 15 mL conical tube.
4. Place the chopstick probe in 70% ethanol for 5 minutes. Note 17.
5. Prepare a second 15 mL conical containing ~15 mL DPBS
6. Immediately before measuring TEER, remove Transwell plates from the incubator. Minimize duration that the cells are outside the incubator. Lower temperatures can cause erroneously high resistances.
7. Grasp the probe firmly with index finger and thumb.
8. Wrap remaining wire around middle and ring fingers (to avoid loose cable dragging over or touching the wells).
9. Spray 70% ethanol onto the wire.
10. Gently dip the tip of the probe into the DPBS until the TEER reading drops and stabilizes.
11. Insert probe into Transwell being careful to insert the long side into the basolateral chamber. Do not touch the cell monolayer with the probe. Contact with the monolayer will disrupt the barrier.

12. Wait until the TEER measurement is approximately steady for 30 seconds. There is always some volatility in the reading.
13. Record TEER.
14. Remove the probe from the well, taking care to not touch the cell monolayer.
15. Dip the probe gently in the conical containing 70% ethanol for 5 seconds.
16. Repeat Steps 9-12 until all wells are measured. The ethanol dips help to prevent contamination. The DPBS dips prevent ethanol from contacting the cells.
17. When all wells are measured, dip the probe in DPBS and then then submerge in the 70% ethanol for 2 minutes.
18. Allow the probe to air dry completely before returning to storage.

5.4.5 Cell Cryopreservation

Adapted from methods in Grifno et al. and Wilson et al. [25,30]. Unless stated otherwise, all steps should be performed in a sterile laminar flow hood with proper aseptic technique.

1. Differentiate cells as described in Methods 3.1 up through Step 29 (Day 7). Do not coat plates on Day 7.
2. Ensure freezing container is at room temperature and has sufficient isopropanol in the lower chamber, according to manufacturer's instructions.
3. Day 8: Aspirate medium and wash each well with 2 mL DPBS.
4. Add 1 mL Accutase per well, then incubate for 20-60 minutes at 37 °C at 5% CO_2. Check every 10-15 minutes by gently swirling. If cells do not start to detach, continue incubation. See Note 11.
5. During the incubation, prepare 4 mL DMEM/F12 quench solution per 1 mL of Accutase used to detach the cells.

6. Prepare freezing medium consisting of 10% DMSO + 30% FBS + 60% HECSR volumetrically. Typically 10-20 mL is sufficient for a differentiation. Volume required will vary depending on final cell concentration. Typically, prepare enough to resuspend to the chosen concentration for approximately 4 million cells per 6-well plate.
7. Once 60 minutes of Accutase treatment have elapsed or cells are visibly detaching from the well, whichever comes first, rinse cells from each well using a 1000 µL pipette tip, triturating to singularize the cells. Filter the cell solution through a 40 µm sterile filter to remove cell clumps into the prepared DMEM/F12 quench. Reserve ~100 µL of cell solution to count.
8. Centrifuge at 200 g for 5 minutes. While doing this, count reserved cell concentration and calculate total cell number according to manufacturer's cell counting protocol.
9. Label an appropriate number of cryotubes. Typically differentiation number, hPSC line, technician, number of cells per tube, and freezing date are recorded.
10. Aspirate supernatant, being careful not to aspirate the cell pellet.
11. Resuspend to 1-10 million cells/mL, dependent on planned application of the cells. Pipette 1 mL into each labelled tube. Lower concentrations are more useful for plate assays, while higher concentrations are more convenient for seeding Transwells and other high cell concentration applications.
12. Place tubes into a room temperature freezing container.
13. Place freezing container into -80 °C overnight.
14. Transfer tubes to liquid nitrogen tank for long term storage.

5.4.6 Cell Thawing

Adapted from methods in Grifno et al. and Wilson et al. [25,30]. Unless stated otherwise, all steps should be performed in a sterile laminar flow hood with proper aseptic technique. Cells can be expected to have similar barrier and protein expression properties following thaw as if they had not been frozen.

1. One day before thawing, prepare collagen IV and fibronectin coated plates and Transwells as though it was Step 29 of Method 3.1 (Day 7). Seed transwells at 500,000 cells/cm^2 (see Note 12) and plates at 100,000 cells/cm^2.
2. Prepare sufficient HECSR + 10 µM Retinoic Acid + 20 ng/mL FGF2 for plates to be seeded. Volume is dependent on planned downstream experiments. Then add 10 µM Y-27632.
3. Retrieve vials of frozen cells from liquid nitrogen storage.
4. Thaw rapidly by holding or floating in a 37 °C water bath. Do not allow the cap to touch the water.
5. When only a small amount of ice remains in the tube, transfer the 1 mL of cell solution in the vial to a 15 mL conical tube with a 1000 µL pipetter.
6. Add 4 mL of DMEM/F12 to the conical containing the cell solution at a rate of about 2-4 mL/min.
7. Centrifuge 200 g for 5 minutes.
8. Aspirate the supernatant, being careful to not disrupt the cell pellet.
9. Resuspend the cell pellet in prepared HECSR + 10 µM Retanoic Acid + 20 ng/mL FGF2 + 10 µM Y-27632 to 2 million cells/mL.

10. Add cell suspension to collagen and fibronectin coated plates at 100,000 cells/cm^2. Seed Transwells at 500,000 cells/cm^2 (see Note 12) and plates at 100,000 cells/cm^2.
11. Place plates or Transwells into 37 °C incubator with 5% CO_2.
12. Shake plates or Transwells 3 times forward and backwards, then 3 times left to right. Repeat 3 times to ensure even distribution of cells.
13. One day later, resume Method 3.1 at Step 40.

5.5 Notes

1. Our lab has used both mTeSR and E8 hPSC culture media to expand hPSCs prior to differentiation.

2. Do not pipette too vigorously. Excess shear stress can damage the cells. Do not allow bubbles to form while triturating. This can reduce cell viability.

3. Optimal seeding density must be determined for each hPSC line via a screen. Typically a range of around 20,000-60,000 cells per cm^2 with increments of 10,000 cells/cm^2 will identify the optimal density. Typically TEER (Fig 3) is used to screen for barrier properties. Once the optimal density is found, further experiments can be performed at the optimal seeding density to further ensure properties of interest (experiment dependent), such as protein expression or efflux activity, are present. See Fig 2A for an example seeding screen focusing on TEER.

4. Cells will settle over time, so it is important to work quickly and mix frequently to ensure consistent seeding across wells.

5. Shaking is necessary to ensure an even distribution of cells across the plate. After cells are in the incubator, it is best to disturb the plate as little as possible. Heterogenous cell density can result in poor or failed differentiations and high batch-to-batch variability.

6. CHIR99021 concentration at Day 0 should be optimized for each hPSC used. Values typically fall around 3-6 µM. We suggest testing a range from 3-9 µM CHIR99021 at increments of 3 µM. TEER is used to screen barrier integrity in the cells after differentiation (Fig 3B). Once an optimal CHIR99021 concentration is identified, subsequent experiments can be performed at the optimal CHIR99021 concentration. See Fig 2B for an example of CHIR99021 concentration optimization.

7. Extended CHIR99021 exposure can result in toxicity. Do not expose the cells to medium containing CHIR99021 for longer than 24 hours. If cells are not confluent by day 2-3, the differentiation will not produce cells with appreciable barrier properties.

8. Typically a medium change during the differentiation is performed every 24 hours (plus or minus 1 hour).

9. On Day 1, substantial cell death is to be expected. If noticeable cell death is visible on or after day 3, the differentiation will likely fail to produce cells with appreciable barrier properties.

10. HECSR can be made in advance, but RA and FGF2 should be added at the time of use.

11. If detachment takes less than 15 minutes, the resulting cells typically have poor barrier properties. After detachment, cell yield above 2-4 million cells per well also suggests a poor quality differentiation.

12. Previously published protocols have typically used 1 million cells/cm^2 to ensure successful formation of a confluent monolayer [16–18,28]. Testing has demonstrated that as low as 250,000 cells/cm^2 may be sufficient for confluent monolayer formation (Fig 4).

13. A similar model [21] has been shown previously to maintain tight junction integrity for a week. Similarly, this model retains TEER above 1000 Ω*cm^2 for approximately one week without changing medium (Fig 3B), and efflux transport similarly appears unaffected (Fig 3A).

14. If cells are not confluent by Day 10, tight junction visualization and localization will be especially difficult to assess.

15. This wash step is critical. If secondary antibodies are applied without appropriate washing, a low signal or nonspecific background signal could result.

16. TEER can be measured starting from Day 9 onward if the cells form a confluent monolayer.

17. Electrodes are vulnerable to ethanol and prolonged exposure decreases the probe longevity. Do not exceed 15 minutes of treatment with ethanol.

18. This data is from a cell line which was found to contain a paracentric inversion in the short arm of chromosome 11.

5.6 Figures

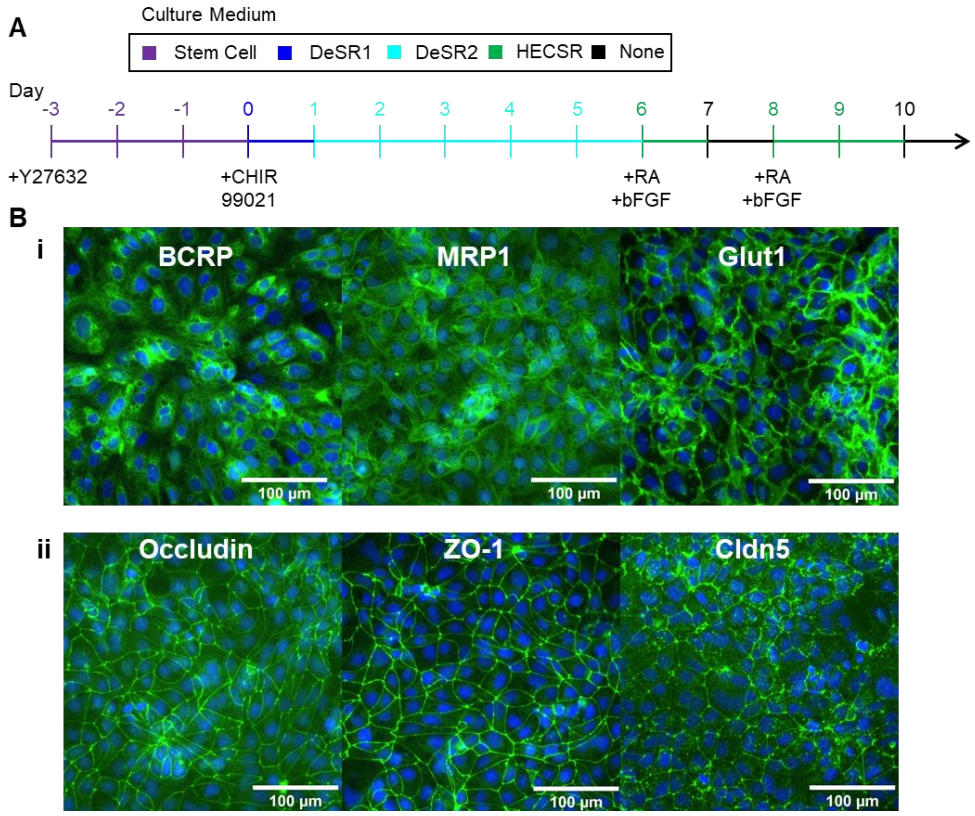

Figure 5.1 Differentiation scheme and BBB marker expression. A) Schematic of differentiation process, color coded by medium composition.Timing and small molecule supplements are provided underneath. B) Example immunofluorescence images stained on day 10 of a differentiation using IMR90-4 iPSCs. i) Sample transporters ii) Sample tight junction associated proteins. Target proteins are pseudocolored green and cell nuclei are blue (Hoescht)

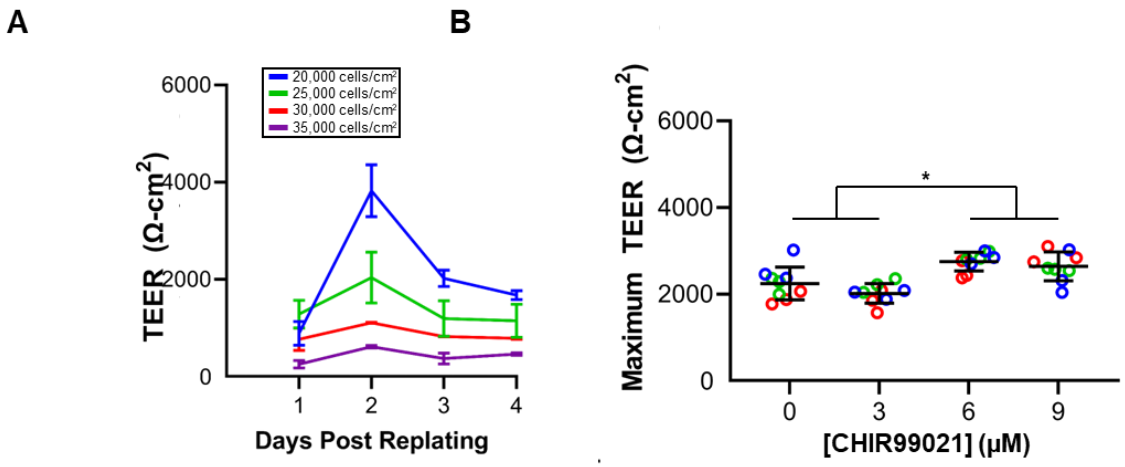

Figure 5.2 Effects of culture time and CHIR concentration on barrier properties. A) An example Day -3 seeding density optimization of TEER. Performed with IMR90-4 iPSCs with n=3 biological replicates. B) Maximum TEER between Day 9 and Day 11 from 3 differentiations of IMR90-C4 iPSCs treated with 0-9 uM CHIR99021 at day 0 for 24 hours. Black line is mean with standard deviation. Circles represent biological replicates (n = 3), colors represent independent differentiations (n = 3). *$p < 0.05$ via 2 Way ANOVA with Tukey's post hoc test.

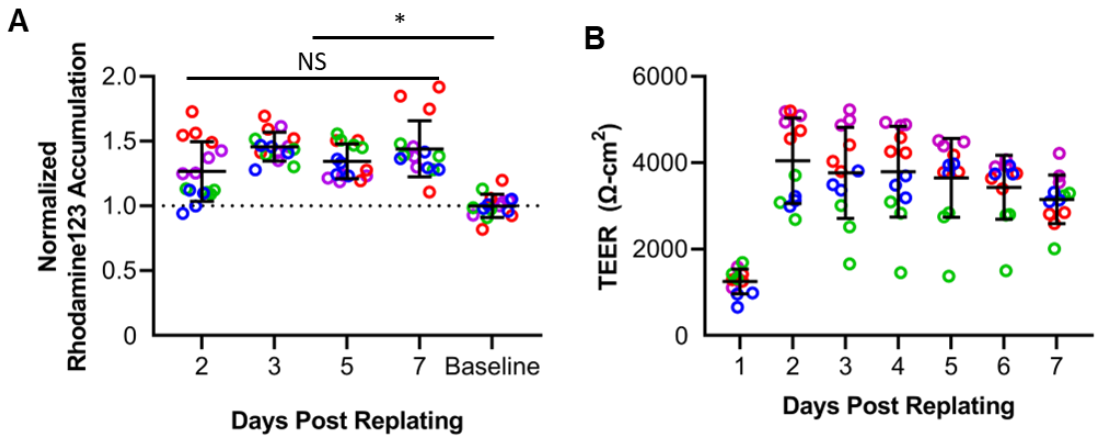

Figure 5.3 P-gp activity and TEER as a function of duration post replating. H9 hESCs were differentiated to BMEC-like cells., See Note 18. A) Cells were replated onto collagen IV and fibronectin coated 24-well plates (Rh123 Accumulation Assay) or Transwells (TEER) on Day 8 and Pgp efflux transport activity measured by Rh123 accumulation. Statistically significant increases above baseline of accumulation under CsA inhibition demonstrate continued activity through 7 days post replating (Day 15 after initiation of differentiation). B) BMEC-like cells were replated onto Transwell membranes on Day 8 and TEER monitored daily. TEER measurements show maintained tight junction integrity through 7 days post replating (Day 15 after initiation of differentiation). Black line is mean with standard deviation. Circles represent biological replicates (n = 3), colors represent independent differentiations (n = 3). *$p < 0.05$ via 2 Way ANOVA with Tukey's post hoc test.

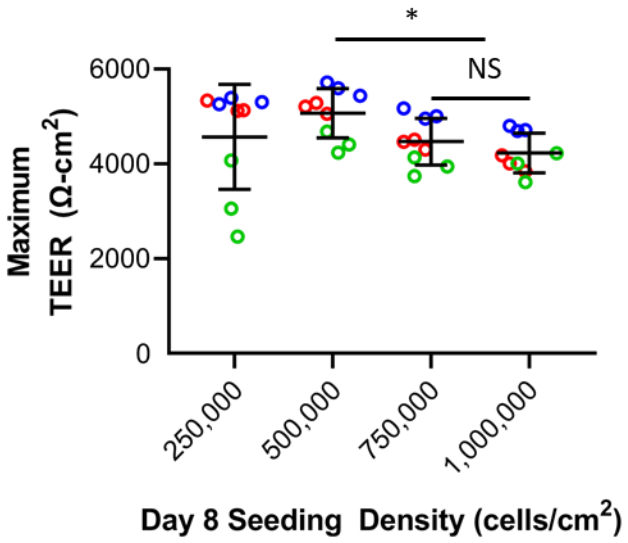

Figure 5.4 Impact of Transwell seeding density on TEER. Performed in H9 hESCs, see Note 18. On Day 8, cells were seeded onto collagen IV and fibronectin-coated Transwells at the indicated cell density, and TEER measured every day for 4 days. Black line is mean with standard deviation. Circles represent biological replicates (n = 3), colors represent independent differentiations (n = 3). *$p < 0.05$ via 2 Way ANOVA with Tukey's post hoc test.

5.7 Tables

Table 5.1 Working media volumes and coating solution volumes for wells by approximate size

Plate	*Volume (mL/well)*	*Coating Solution Volume (uL/well)*
6 Well Plate	2	1000
12 Well Plate	1	500
24 Well Plate	0.5	250
48 Well Plate	0.25	125
96 Well Plate	0.2	50
12 Well with Transwell	0.5 Apical, 1.5 Basolateral	200 (Concentrated)

Table 5.2 Antibody Information

Protein Target	Catalog	Manufacturer	Fixative	Concentration	Species
BCRP	MAB4155	Sigma-Aldrich	4% PFA	1:50	Mouse
MRP1	MAB4100	Sigma-Aldrich	Methanol	1:50	Mouse
Glut1	MA1-37783	Invitrogen	Methanol	1:100	Mouse
Occludin	33-1500	Invitrogen	Methanol	1:50	Mouse
Claudin5	35-2500	Invitrogen	Methanol	1:200	Mouse
ZO1	33-9100	Invitrogen	Methanol	1:200	Mouse
Mouse IgG(H+L) 488	A11001	Invitrogen	N/A	1:200	Goat

5.8 References

1. Foreman KL, Shusta EV, Palecek SP. Chapter 10: Defined Differentiation of Human Pluripotent Stem Cells to a Model of the Blood-Brain Barrier. In: Huang Y-WA, Pak C, editors. Methods in Molecular Biology: Stem Cell Based Neural Model Systems for Brain Disorders. Springer International Publishing; 2023.

2. Miller G. Is Pharma Running Out of Brainy Ideas? Science. 2010;329:502–4.

3. Gribkoff VK, Kaczmarek LK. The need for new approaches in CNS drug discovery: Why drugs have failed, and what can be done to improve outcomes. Neuropharmacology. 2017;120:11–9.

4. Pardridge WM. The Blood-Brain Barrier: Bottleneck in Brain Drug Development. NeuroRx. 2005;2:12.

5. Abbott NJ, Patabendige AAK, Dolman DEM, Yusof SR, Begley DJ. Structure and function of the blood–brain barrier. Neurobiol Dis. 2010;37:13–25.

6. de Boer AG, van der Sandt ICJ, Gaillard PJ. The Role of Drug Transporters at the Blood-Brain Barrier. Annu Rev Pharmacol Toxicol. 2003;43:629–56.

7. Jamieson JJ, Searson PC, Gerecht S. Engineering the human blood-brain barrier in vitro. J Biol Eng. 2017;11:37.

8. Sabbagh MF, Nathans J. A genome-wide view of the de-differentiation of central nervous system endothelial cells in culture. eLife. 2020;9:e51276.

9. Vanlandewijck M, He L, Mäe MA, Andrae J, Ando K, Del Gaudio F, et al. A molecular atlas of cell types and zonation in the brain vasculature. Nature. 2018;554:475–80.

10. Nitta T, Hata M, Gotoh S, Seo Y, Sasaki H, Hashimoto N, et al. Size-selective loosening of the blood-brain barrier in claudin-5–deficient mice. The Journal of Cell Biology. 2003;161:653–60.

11. Helms HC, Abbott NJ, Burek M, Cecchelli R, Couraud P-O, Deli MA, et al. In vitro models of the blood–brain barrier: An overview of commonly used brain endothelial cell culture models and guidelines for their use. J Cereb Blood Flow Metab. 2016;36:862–90.

12. Aday S, Cecchelli R, Hallier-Vanuxeem D, Dehouck MP, Ferreira L. Stem Cell-Based Human Blood–Brain Barrier Models for Drug Discovery and Delivery. Trends Biotechnol. 2016;34:382–93.

13. Song HW, Foreman KL, Gastfriend BD, Kuo JS, Palecek SP, Shusta EV. Transcriptomic comparison of human and mouse brain microvessels. Sci Rep. 2020;10:12358.

14. Chagastelles PC, Nardi NB. Biology of stem cells: an overview. Kidney Int Suppl. 2011;1:63–7.

15. Lippmann ES, Al-Ahmad A, Azarin SM, Palecek SP, Shusta EV. A retinoic acid-enhanced, multicellular human blood-brain barrier model derived from stem cell sources. Sci Rep. 2014;4:4160.

16. Lippmann ES, Azarin SM, Kay JE, Nessler RA, Wilson HK, Al-Ahmad A, et al. Derivation of blood-brain barrier endothelial cells from human pluripotent stem cells. Nat Biotechnol. 2012;30:783–91.

17. Lippmann ES, Al-Ahmad A, Palecek SP, Shusta EV. Modeling the blood–brain barrier using stem cell sources. Fluids Barriers CNS. 2013;10:2.

18. Stebbins MJ, Wilson HK, Canfield SG, Qian T, Palecek SP, Shusta EV. Differentiation and characterization of human pluripotent stem cell-derived brain microvascular endothelial cells. Methods. 2016;101:93–102.

19. Canfield SG, Stebbins MJ, Morales BS, Asai SW, Vatine GD, Svendsen CN, et al. An isogenic blood-brain barrier model comprising brain endothelial cells, astrocytes, and neurons derived from human induced pluripotent stem cells. J Neurochem. 2017;140:874–88.

20. Vatine GD, Barrile R, Workman MJ, Sances S, Barriga BK, Rahnama M, et al. Human iPSC-Derived Blood-Brain Barrier Chips Enable Disease Modeling and Personalized Medicine Applications. Cell Stem Cell. 2019;24:995-1005.e6.

21. Neal EH, Marinelli NA, Shi Y, McClatchey PM, Balotin KM, Gullett DR, et al. A Simplified, Fully Defined Differentiation Scheme for Producing Blood-Brain Barrier Endothelial Cells from Human iPSCs. Stem Cell Rep. 2019;12:1380–8.

22. Faley SL, Neal EH, Wang JX, Bosworth AM, Weber CM, Balotin KM, et al. iPSC-Derived Brain Endothelium Exhibits Stable, Long-Term Barrier Function in Perfused Hydrogel Scaffolds. Stem Cell Rep. 2019;12:474–87.

23. Hollmann EK, Bailey AK, Potharazu AV, Neely MD, Bowman AB, Lippmann ES. Accelerated differentiation of human induced pluripotent stem cells to blood–brain barrier endothelial cells. Fluids Barriers CNS. 2017;14:9.

24. Mantle JL, Min L, Lee KH. Minimum Transendothelial Electrical Resistance Thresholds for the Study of Small and Large Molecule Drug Transport in a Human *in Vitro* Blood–Brain Barrier Model. Mol Pharmaceutics. 2016;13:4191–8.

25. Grifno GN, Farrell AM, Linville RM, Arevalo D, Kim JH, Gu L, et al. Tissue-engineered blood-brain barrier models via directed differentiation of human induced pluripotent stem cells. Sci Rep. 2019;9:13957.

26. Katt ME, Mayo LN, Ellis SE, Mahairaki V, Rothstein JD, Cheng L, et al. The role of mutations associated with familial neurodegenerative disorders on blood–brain barrier function in an iPSC model. Fluids Barriers CNS. 2019;16:20.

27. Vatine GD, Al-Ahmad A, Barriga BK, Svendsen S, Salim A, Garcia L, et al. Modeling Psychomotor Retardation using iPSCs from MCT8-Deficient Patients Indicates a Prominent Role for the Blood-Brain Barrier. Cell Stem Cell. 2017;20:831-843.e5.

28. Qian T, Maguire SE, Canfield SG, Bao X, Olson WR, Shusta EV, et al. Directed differentiation of human pluripotent stem cells to blood-brain barrier endothelial cells. Sci Adv. 2017;3:e1701679.

29. Wilson HK, Canfield SG, Hjortness MK, Palecek SP, Shusta EV. Exploring the effects of cell seeding density on the differentiation of human pluripotent stem cells to brain microvascular endothelial cells. Fluids Barriers CNS. 2015;12:13.

30. Wilson HK, Faubion MG, Hjortness MK, Palecek SP, Shusta EV. Cryopreservation of Brain Endothelial Cells Derived from Human Induced Pluripotent Stem Cells Is Enhanced by Rho-Associated Coiled Coil-Containing Kinase Inhibition. Tissue Eng Part C Methods. 2016;22:1085–94.

31. Katt ME, Xu ZS, Gerecht S, Searson PC. Human Brain Microvascular Endothelial Cells Derived from the BC1 iPS Cell Line Exhibit a Blood-Brain Barrier Phenotype. Deli MA, editor. PLOS ONE. 2016;11:e0152105.

32. Lian X, Bao X, Al-Ahmad A, Liu J, Wu Y, Dong W, et al. Efficient Differentiation of Human Pluripotent Stem Cells to Endothelial Progenitors via Small-Molecule Activation of WNT Signaling. Stem Cell Rep. 2014;3:804–16.

Chapter 6 – Conclusions and Future Directions

6.1 Summary

In this work we generated multiple datasets to assist in development of future blood-brain barrier (BBB) models as well as exploring the phenotypes and transcriptional profiles of both the mouse and human BBB *in vitro*. Our work with laser captured brain microvessels (Chapter 2), provides a tool for downstream drug development, suggesting exceptions between the mouse and human endothelium and pericytes which can impact targeted drug delivery strategies [1,2]. Further, it suggests areas of improvement with regards to BBB models and supplements current single cell brain endothelial and pericyte transcriptomes with greater depth. Phenotypic analysis of multiple *in vitro* BBB models yielded insight into a potential regulatory mechanism driven by shear stress. We also observed that activation of Piezo1, a mechanosensitive cation channel, induced a similar phenotype (Chapter 3). Finally, our analysis of the transcriptional responses of multiple BBB models under long term shear stress suggests some BBB genes are positively upregulated by the application of shear, but this is insufficient to prevent de-specification due to *in vitro* culture (Chapter 4). This aids the field by demonstrating what genes may be impacted by the application of shear across BBB models while simultaneously providing a uniform baseline to compare shear responsiveness thereby informing development of BBB microfluidic models [3–6].

6.2 Future Directions

6.2.1 Further development of an in vivo blood-brain barrier transcriptome

Though our work in Chapter 2 created a brain pericyte and endothelial bulk transcriptome, the ideal scenario would be an isolated transcriptome for both pericytes and endothelial cells. This exists in some part thanks to brain single sequencing experiments already [7–10], however these still suffer from low sensitivity compared to bulk sequencing [11]. One potential future direction would be to work on expanding the understanding of the human *in vivo* brain microvascular transcriptome. This could be accomplished by similarly sourcing human brain samples, singularizing and utilizing fluorescent activated cell sorting (FACS) for an endothelial marker such as CD31. This has been done with mice expressing a fluorescent endothelial reporter [12–14], which can reduce pericyte contamination while also retaining the depth of bulk sequencing. Similarly, to ensure optimal usage of rare human samples, pericytes could also be collected using a pericyte marker as well allowing further expansion of both transcriptomes. Alternatively, instead of seeking to deepen the data, we could instead improve the comparison between species. Previous experiments including our own work have utilized poly A enrichment for RNA preparation, this removes regulatory RNAs such as miRNAs and lncRNAs [15]. The importance of these types of RNA including with regards to the BBB [16] is just beginning to be understood. To better explore this at the BBB, as well as uncover other potential species differences, this same experiment could be conducted as before with human and mouse samples. Alternatively this could be combined with the above isolation method to enable a more pure cell population in addition to uncovering these less studied cell types.

6.2.2 Connecting short term shear response to Piezo1

Our work on the short term response of *in vitro* brain microvascular endothelial cell (BMEC) models to shear stress demonstrated that shear stress alone was sufficient to drive an appreciable reduction in efflux transport activity over 3 hours in the rat BMEC (rBMEC) model. The work with the Piezo1 agonist, Yoda1, demonstrated a single mechanosensory pathway was sufficient to drive a similar reduction in efflux activity. The final connection this project requires is a link between Piezo1 activation and shear stress. By confirming that Piezo1 is indeed the chief driving component of BMEC response to shear, it would suggest calcium, the cation impacted heavily by Piezo1 activation as a potential regulatory mechanism in line with previous studies of P-gp activity in alternate cell and model types [17,18]. Previous attempts to simply knock out Piezo1 in stem cells resulted in heterozygous populations that eventually were outgrown by the homozygous Piezo1 expressing cells suggesting that loss of Piezo1 negatively impacts cell expansion and proliferation. Alternate work utilizing rBMECs treated with lipofectamine loaded with siRNA targeting *Piezo1* showed reduced transcript (Fig 6.1A). However, when the same dosage of lipofectamine and siRNA was loaded into medium in the constrained geometry of the microfluidic chips, we did not observe a similar reduction (Fig 6.1B). Finally, attempts were made to reduce all calcium influx utilizing the pan-calcium channel inhibitor gadolinium chloride ($GdCl_3$). Preventing inhibition of efflux activity with gadolinium chloride under shear stress would suggest whether mechanosensitive cation channels as a whole, not specifically Piezo1, were involved in the reduction in efflux transport observed. However, a preliminary assay in static culture showed a statistically significant reduction in efflux activity with just gadolinium chloride (Fig 6.1C). This inherent efflux transport inhibition is a confounding factor making follow-up experiments pointless. Therefore, to confirm a link

between shear induced efflux transport inhibition and Piezo1 activation induced efflux transport inhibition an alternate strategy is required. One option is an inducible knock out, allowing removal of Piezo1 without the risk of negatively impacting proliferation or embryonic lethality [19–21]. This could be accomplished through direct editing of stem cells as previously, but instead introducing an endothelial marker specific Cre recombinase followed by floxxing of *Piezo1* as has been done to many other genes previously or by purchasing dox inducible *Piezo1* knock out mice and performing a microvessel extraction as previously done with rat BMECs followed by dox induction *in vitro* similar to other experiments [22]. In either case, the BBB model, once exposed to shear stress with and without Piezo1 would demonstrate the importance, or lack thereof, of Piezo1 on inhibition of efflux transport activity under shear. Given our data with Yoda1 and other work suggesting an abolishment of cation influx in mouse BMECs without Piezo1 [22] it seems likely that we would observe retention of efflux activity.

In addition to more thoroughly connecting Piezo1 to shear stress response, it would be reasonable to explore alternative hypotheses. As mentioned in Chapter 3, we hypothesized that shear stress increases driven by neuronal activity reduced efflux activity. However, increased shear stress is one of several components within the neuroactivation niche. For example, release of neurotransmitters such as acetylecholine and dopamine are thought to drive responses in brain endothelium [23,24]. This subset would further characterize potential responsiveness of the BBB to the needs of the surrounding brain parenchyma as well as potentially highlight a downstream influx, like in our Piezo1 experiments calcium influx has been suggested as the intermediate signal for downstream endothelial response [24].

This can accomplished by direct application of neurotransmitters, followed by assessments of efflux activity as before. Many neurotransmitters are available in recombinant

forms from different vendors. We could also more wholly capture the neuroactivation niche utilizing genetically engineered neurons. In this case, to simulate the neural activation niche we would utilize a designer receptor exclusively activated by designer drug (DREADD) expressing neuron model, either by isolating these from a mouse model or by differentiating neurons from genetically engineered human pluripotent stem cells that have previously been generated [22,25,26]. In either case, this would explore an additional component that was not described in our current experiments and opens new avenues for potential modeling applications in microfluidic two chamber devices that accommodate both shear stress and alternative cell types as well as the potential to model diseases with disruptions at both the BBB and in neuronal and parenchymal behavior such as in epilepsy [27].

6.2.3 Validation of potential hits from long term shear exposure

Our assessment of the effects of long term shear on blood-brain barrier models demonstrated some small transcriptional changes as well as confirming a lack of responsiveness in the stem cell derived hBMEC-like cells known from literature to be less responsive than endothelial models [28]. Further, this suggests that shear stress alone is not the critical component of the blood-brain barrier niche whose loss drives de-specification of the brain endothelium.

The most obvious question, for the blood-brain barrier relevant genes, is if the transcriptional changes are recapitulated at the protein level. First *SLC2A1*, *LSR*, *CAV1* and *PLVAP* are all prime options for downstream protein validation via standard protein collection followed by western blotting. β-actin is the typical loading control, however as a cytoskeletal protein, is most likely impacted by shear stress. An alternative control like HPRT1 which is not associated with the cytoskeleton would be a better option. Ideally this analysis would be

performed utilizing rat primary brain microvascular endothelial cells (rBMECs) as well as at least one additional BBB model such as the central nervous system-like endothelial cells (hCECs) utilized previously. If a phosphatase and protease inhibitor was utilized at time of collection, this same sample set could be assessed for activation of phosphorylated intermediates of the signaling cascades identified via Quaternary Prod and GSEA analysis (Chapter 4) further validating the results. Alternatively, assessments of changes in functional activity such as a radioactive glucose uptake would demonstrate phenotypical changes, but should most likely be assessed after a protein level change is observed and would depend on which proteins are statistically up or down regulated under shear.

6.2.4 Further characterization of blood-brain barrier specific transcriptional changes

One of the benefits to our dataset in Chapter 4 is that it is a set of endothelial and BBB models, utilized in microfluidics in literature, that are treated with identical magnitudes of shear stress, in identical culture geometries for identical durations allowing easy comparisons compared to the somewhat divergent literature. We can expand the utility of this dataset by simply adding more models. Though we chose the most common, accurate, or easily expanded models for our current work, future work could include alternate models still utilized by the field including immortalized BMECs and cryopreserved commercially available human primary BMECs. Further, our work intentionally treated cells with 72 hours of shear, this was chosen from among literature in an attempt to identify changes in the overall transcriptome. However, this would not capture any potential attenuation period after short term shear exposure, only what genes are maintained under different shear magnitudes. By assessing the transcriptional behavior at multiple time points, we could demonstrate how endothelial cells immediately respond to shear and what genes change dynamically within this duration. We could perform this on generic

stem cell derived endothelial cells as well as potentially central nervous system like endothelial cells as utilized previously. These would be the ideal models because they both demonstrated substantial changes in gene expression under shear, encompass both endothelial and brain endothelial like characteristics, and are easily expanded. Shear exposure should probably range somewhere between 3 hours and 24 hours to capture the transient transcriptomic changes. This would provide insight into the mechanism behind shear attenuation *in vivo* and could provide insight into diseases like high blood pressure than can alter the baseline shear endothelial cells experience.

6.2.5 Exploration of the impact of cilia at the BBB

Primary cilia, a single larger projection from the surface of many cell types [29], have been linked to both localization of sonic hedgehog signaling [29,30] and mechanosensitivity [31]. Some of our work has sought to characterize this response and better characterize models to explore the impact of cilia at the BBB. By generating a protocol to successfully remove cilia from a BBB model we sought to demonstrate the impact of cilia on BBB properties. We chose to utilize the human stem cell derived brain endothelial like cell like cells (hBMEC-like cells), mainly because of prolific expression of cilia markers, and modest para and transcellular resistance to transport.

hPSC-BMECs were differentiated from the IMR90 hPSC line and on day 10 treated for up to 72 hours with four concentrations of four different compounds thought to chemically deciliate cells according to literature (Figure 6.2A) [32–35]. Due to the cytoskeletal disrupting nature of these compounds, some toxicity and deformation of cells was expected. Deciliation was defined as a loss of Arl13b and acetylated tubulin bright puncta on the cells (Figure 6.2B). these puncta clearly appear at a rate of one per nucleus primarily [36] and the loss of the

distinctive puncta patterning is what we define as deciliation, particularly the disappearance of the small Arl13b positive puncta (Fig 6.2B). Since treatment begins on day 10 of the hBMEC-like differentiation where a monolayer has already formed, loss of a monolayer was taken as indication of toxicity, and those results were discarded regardless of loss of cilia. We found that most common deciliating agents were ineffective, with the exception of the controlled substance chloral hydrate (CH) (Fig 6.2A). This compound appeared effective after 72 hours on the hBMEC-like cells at a dosage between 4 mM and 8 mM. For follow up experiments including barrier property assays, we proceeded with a much tighter concentration screen between these two dosages. This was to ensure that small perturbations between experiments would not prevent successful deciliation.

To assess the impact of deciliation of BBB cells, we observed two common metrics of BBB resistance. Specifically efflux transport assays discussed in depth in Chapters 3 and 5, which provide an understanding of transcellular transport resistance, particularly with regards to the highly expressed P-gp efflux transporter. Paracellular resistance was measured via transepithelial electrical resistance (TEER), which is commonly utilized in the BBB field to approximate resistance at the tight junctions [37,38]. hBMEC-like cells were seeded onto either transwells (for TEER), 24 well plates (for efflux assays), or 96 wells (for ICC) and on day 10 of the differentiation were treated with CH. TEER, as a non-destructive assay, could be measured daily, while efflux assays were performed after 72 hours. In all cases, medium was replaced every 24 hours to ensure that CH dosage did not drop over time.

TEER was measured daily for four days (Figure 6.3A, B), and by 48-72 hours a clear trend developed. Compared to baseline controls we observed a statistically significant increase in TEER at concentrations of CH that drive deciliation which would correspond with increased

resistance. The greatest change was around 4-6 mM, at the same point we would expect deciliation. As of right now, we do not have an explanation for this phenomenon. In addition, it is important to note that this change, though substantial in terms of TEER, does not lead to functional changes with regards to small molecule paracellular transport. The only condition where TEER change would suggest a corresponding functional change is at 8 mM, where a clear loss of barrier can be observed, most likely caused by the loss of a monolayer as seen by ICC in paired 96 well plates. Efflux assays showed a loss in P-gp activity as evidenced by the lack of statistical differences between vehicle and maximal accumulation (CsA) controls at concentrations that also drove deciliation and TEER magnitude changes (Fig 6.3C). Overall, we observe a change in barrier properties on application of CH at deciliating dosages, some non-functional improvement in tight junctions and a decrease in efflux activity.

Future experiments should work to deciliate in a less toxic manner. Given the incredibly narrow margin of error when applying CH, it would be wise to deciliate this model in a manner that is more consistent and less toxic, as the cytotoxicity could be driving some of these barrier changes. Potentially, a cilia knock out line in hPSCs could be generating targeting cilia critical genes like ARL13B or IFT88. Once a less toxic alternative to CH can be identified, there are numerous follow up experiments possible. The most obvious would be repetition of the above barrier experiments with and without cilia in the hBMEC-like cell model. Additional experiments could expand on the mechanosensatory capabilities of cilia by performing similar analysis to above such as repeating the efflux transport assays under 3 hour shear (Chapter 3) with and without cilia or the 72 hour shear treatment experiments (Chapter 4).

6.3 Figures

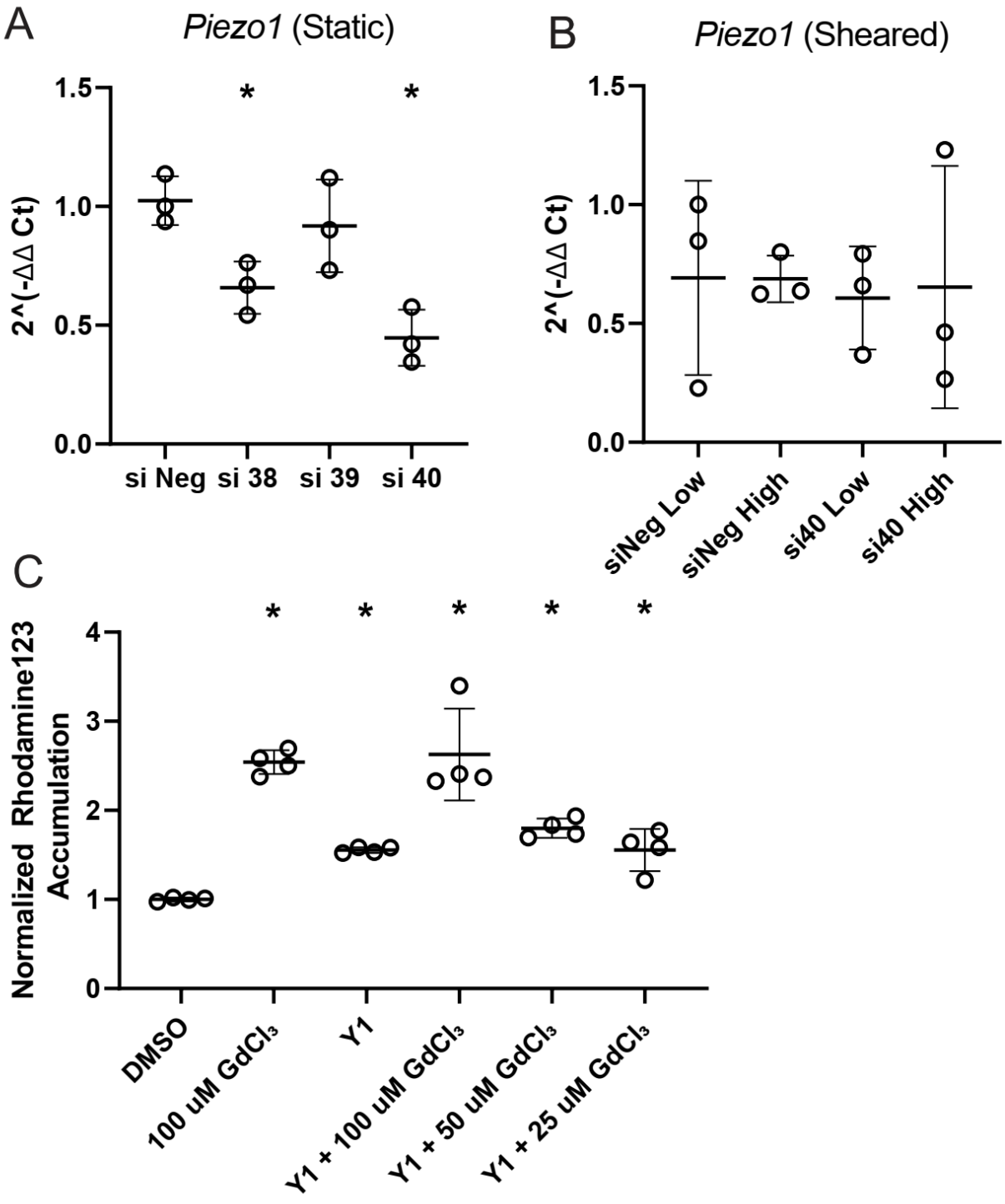
A
Piezo1 (Static)
2^(-ΔΔ Ct)
1.5
1.0
0.5
0.0
*
*
si Neg
si 38
si 39
si 40
B
Piezo1 (Sheared)
2^(-ΔΔ Ct)
1.5
1.0
0.5
0.0
siNeg Low
siNeg High
si40 Low
si40 High
C
Normalized Rhodamine123 Accumulation
4
3
2
1
0
* * * * *
DMSO
100 uM GdCl3
Y1
Y1 + 100 uM GdCl3
Y1 + 50 uM GdCl3
Y1 + 25 uM GdCl3

Figure 6.1 Strategies attempted to link Piezo1 activation induced efflux activity to shear stress. A) 24-well tissue culture polystyrene wells seeded with rBMECs. At seeding, microvessels were treated with 30 pmol of siRNA according to manufacturer's protocol for Lipofectamine RNAiMAX treatment every 24 hours for 72 hours. Cells were lysed, RNA collected and qPCR performed for *Piezo1* with a *Gapdh* control. n = 3 biological replicates, * $p < 0.05$ via One Way ANOVA followed by Dunnet's multiple comparisons to siNeg. (siNeg = Silencer Select Negative Control No. 2, si 38 = Thermo Fisher Silencer Select s167338, si 39 = Thermo Fisher Silencer Select s167339 , si 40 = Thermo Fisher Silencer Select s167340) B) Same dosages were applied to exfiltrating rBMECs in microfluidic devices as described in Chapters 4 and 5. rBMECs were treated every 24 hours with siRNA and lipofectamine according to manufacturers protocol. The most effective siRNA was chosen. n = 3 biological replicates. No statistically differences were detected via 2 way ANOVA. C) hPSC-BMEC-like cells treated with various compounds during a Rhodamine123 accumulation assay performed over 3 hours similar to those utilized in Chapter 3. hPSC line used was an H9 line with a karyotype mutation, however we suspect that this mutation does not impact the conclusion of this preliminary assay. $GdCl_3$ was applied at the given concentrations. Statistical significance versus control shown only for clarity. n = 4 biological replicates from one differentiation with analysis via One Way ANOVA followed by Tukey's multiple comparisons test.

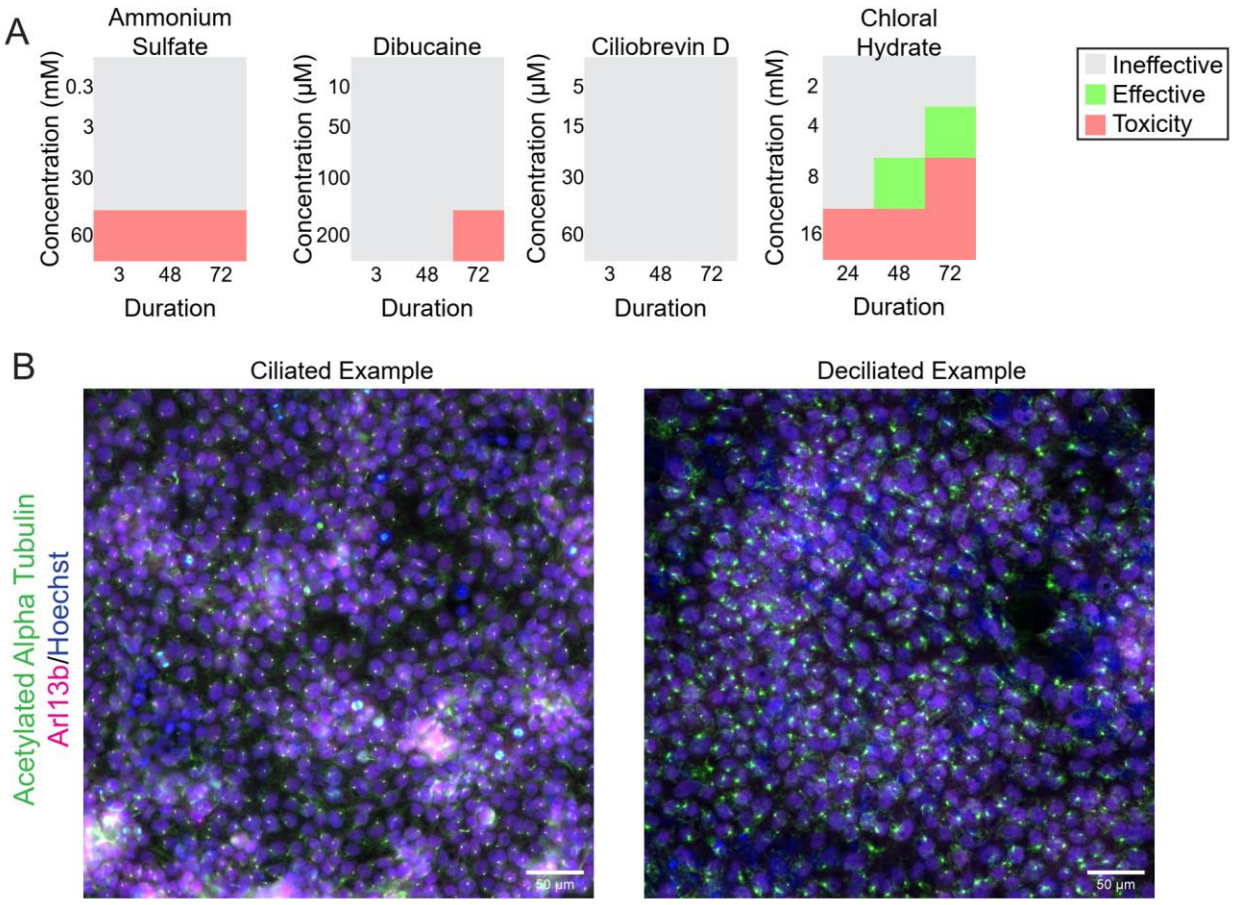

Figure 6.2 Deciliation compounds had varying degrees of efficacy. A) Charts demonstrating if hPSC derived hBMEC-like cells underwent deciliation on treatment for various durations at different concentrations with four different compounds. All dosages, durations, and compounds were taken from literature and manufacturer's suggested values. Deciliation was assessed by dual positive staining of Arl13b and Acetylated tubulin in 3 biological replicates per concentration and compound. B) Example images of a healthy and deciliated population of cells. Note the lack of dual acetylated alpha tubulin and Arl13b positive puncta in the second image.

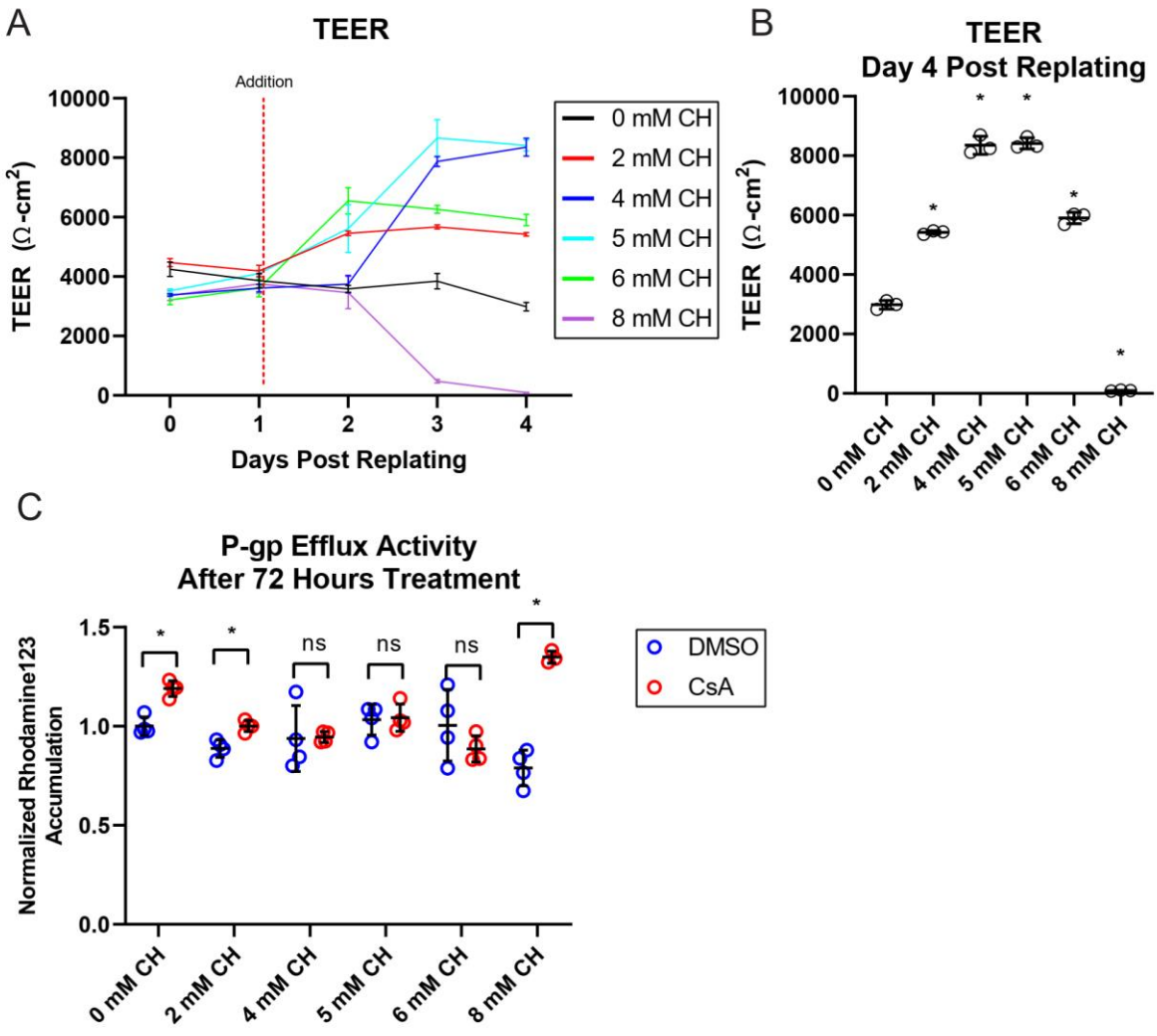
A
TEER
Addition
TEER (Ω-cm²)
Days Post Replating
0 mM CH
2 mM CH
4 mM CH
5 mM CH
6 mM CH
8 mM CH
B
TEER
Day 4 Post Replating
TEER (Ω-cm²)
C
P-gp Efflux Activity
After 72 Hours Treatment
Normalized Rhodamine123 Accumulation
DMSO
CsA
ns

Figure 6.3 Impact of chloral hydrate induced deciliation on barrier properties in hBMEC-like cells. A) TEER measured daily from CH fed wells. Lines represent averages with standard deviation at each time point. Statistical differences assessed via 2 Way ANOVA. Red dashed line represents addition of CH post monolayer formation. n = 3 transwells from 1 differentiation. B) TEER on Day Post Replating 4 from Figure 6.3A. Dots are biological replicates from 1 differentiation. Lines represent mean with standard deviation. * $p < 0.05$ via Two Way ANOVA with Dunnett's multiple comparisons versus 0 mM CH. C) P-gp efflux activity (Chapter 5) performed after different concentrations of CH were applied for 72 hours before cells. Vehicle and CsA for each CH concentration were compared via Student's t-test * $p < 0.05$.

6.4 References

1. Song HW, Foreman KL, Gastfriend BD, Kuo JS, Palecek SP, Shusta EV. Transcriptomic comparison of human and mouse brain microvessels. Sci Rep. 2020;10:12358.

2. Aday S, Cecchelli R, Hallier-Vanuxeem D, Dehouck MP, Ferreira L. Stem Cell-Based Human Blood–Brain Barrier Models for Drug Discovery and Delivery. Trends Biotechnol. 2016;34:382–93.

3. Jamieson JJ, Searson PC, Gerecht S. Engineering the human blood-brain barrier in vitro. J Biol Eng. 2017;11:37.

4. Vatine GD, Barrile R, Workman MJ, Sances S, Barriga BK, Rahnama M, et al. Human iPSC-Derived Blood-Brain Barrier Chips Enable Disease Modeling and Personalized Medicine Applications. Cell Stem Cell. 2019;24:995-1005.e6.

5. Park T-E, Mustafaoglu N, Herland A, Hasselkus R, Mannix R, FitzGerald EA, et al. Hypoxia-enhanced Blood-Brain Barrier Chip recapitulates human barrier function and shuttling of drugs and antibodies. Nat Commun. 2019;10:2621.

6. Cucullo L, Hossain M, Puvenna V, Marchi N, Janigro D. The role of shear stress in Blood-Brain Barrier endothelial physiology. BMC Neuroscience. 2011;12:40.

7. Gastfriend BD, Foreman KL, Katt ME, Palecek SP, Shusta EV. Integrative analysis of the human brain mural cell transcriptome. J Cereb Blood Flow Metab. 2021;41:3052–68.

8. La Manno G, Gyllborg D, Codeluppi S, Nishimura K, Salto C, Zeisel A, et al. Molecular Diversity of Midbrain Development in Mouse, Human, and Stem Cells. Cell. 2016;167:566-580.e19.

9. Darmanis S, Sloan SA, Zhang Y, Enge M, Caneda C, Shuer LM, et al. A survey of human brain transcriptome diversity at the single cell level. Proc Natl Acad Sci USA. 2015;112:7285–90.

10. Polioudakis D, de la Torre-Ubieta L, Langerman J, Elkins AG, Shi X, Stein JL, et al. A Single-Cell Transcriptomic Atlas of Human Neocortical Development during Mid-gestation. Neuron. 2019;S0896627319305616.

11. Vallejo AF. Resolving cellular systems by ultra-sensitive and economical single-cell transcriptome filtering. OPEN ACCESS.

12. Vanlandewijck M, He L, Mäe MA, Andrae J, Ando K, Del Gaudio F, et al. A molecular atlas of cell types and zonation in the brain vasculature. Nature. 2018;554:475–80.

13. He L, Vanlandewijck M, Raschperger E, Mae MA, Jung B, Lebouvier T, et al. He - Analysis of the brain mural cell transcriptome.pdf. Sci Rep. 2016;6.

14. Liu Z, Ruter DL, Quigley K, Tanke NT, Jiang Y, Bautch VL. Single-Cell RNA Sequencing Reveals Endothelial Cell Transcriptome Heterogeneity Under Homeostatic Laminar Flow. ATVB. 2021;41:2575–84.

15. Zhao W, He X, Hoadley KA, Parker JS, Hayes DN, Perou CM. Comparison of RNA-Seq by poly (A) capture, ribosomal RNA depletion, and DNA microarray for expression profiling. 2014;

16. Tominaga N, Kosaka N, Ono M, Katsuda T, Yoshioka Y, Tamura K, et al. Brain metastatic cancer cells release microRNA- 181c-containing extracellular vesicles capable of destructing blood–brain barrier. NATURE COMMUNICATIONS. 2015;

17. Zhang SL, Yue Z, Arnold DM, Artiushin G, Sehgal A. A Circadian Clock in the Blood-Brain Barrier Regulates Xenobiotic Efflux. Cell. 2018;173:130-139.e10.

18. Zhang SL, Lahens NF, Yue Z, Arnold DM, Pakstis PP, Schwarz JE, et al. A circadian clock regulates efflux by the blood-brain barrier in mice and human cells. Nat Commun. 2021;12:617.

19. Li J, Hou B, Tumova S, Muraki K, Bruns A, Ludlow MJ, et al. Piezo1 integration of vascular architecture with physiological force. Nature. 2014;515:279–82.

20. Liu T, Du X, Zhang B, Zi H, Yan Y, Yin J, et al. Piezo1-Mediated Ca2+ Activities Regulate Brain Vascular Pathfinding during Development. Neuron. 2020;108:180-192.e5.

21. Nonomura K, Lukacs V, Sweet DT, Goddard LM, Kanie A, Whitwam T, et al. Mechanically activated ion channel PIEZO1 is required for lymphatic valve formation. Proc Natl Acad Sci USA. 2018;115:12817–22.

22. Harraz OF, Klug NR, Senatore AJ, Hill-Eubanks DC, Nelson MT. Piezo1 Is a Mechanosensor Channel in Central Nervous System Capillaries. Circ Res. 2022;10.1161/CIRCRESAHA.122.320827.

23. Bhattacharya R, Sinha S, Yang S-P, Patra C, Dutta S, Wang E, et al. The neurotransmitter dopamine modulates vascular permeability in the endothelium. JMS. 2008;3:14.

24. Zuccolo E, Lim D, Kheder DA, Perna A, Catarsi P, Botta L, et al. Acetylcholine induces intracellular Ca2+ oscillations and nitric oxide release in mouse brain endothelial cells. Cell Calcium. 2017;66:33–47.

25. Upadhya D, Attaluri S, Liu Y, Hattiangady B, Castro OW, Shuai B, et al. Grafted hPSC-derived GABA-ergic interneurons regulate seizures and specific cognitive function in temporal lobe epilepsy. npj Regen Med. 2022;7:38.

26. Chen Y, Xiong M, Dong Y, Haberman A, Cao J, Liu H, et al. Chemical Control of Grafted Human PSC-Derived Neurons in a Mouse Model of Parkinson's Disease. Cell Stem Cell. 2016;18:817–26.

27. Parfenova H, Leffler CW, Tcheranova D, Basuroy S, Zimmermann A. Epileptic seizures increase circulating endothelial cells in peripheral blood as early indicators of cerebral vascular damage. American Journal of Physiology-Heart and Circulatory Physiology. 2010;298:H1687–98.

28. DeStefano JG, Xu ZS, Williams AJ, Yimam N, Searson PC. Effect of shear stress on iPSC-derived human brain microvascular endothelial cells (dhBMECs). Fluids and Barriers of the CNS. 2017;14:20.

29. Wheway G, Nazlamova L, Hancock JT. Signaling through the Primary Cilium. Front Cell Dev Biol. 2018;6:8.

30. Fu W, Asp P, Canter B, Dynlacht BD. Primary cilia control hedgehog signaling during muscle differentiation and are deregulated in rhabdomyosarcoma. Proceedings of the National Academy of Sciences. 2014;111:9151–6.

31. Bodle J, Hamouda MS, Cai S, Williams RB, Bernacki SH, Loboa EG. Primary Cilia Exhibit Mechanosensitivity to Cyclic Tensile Strain and Lineage-Dependent Expression in Adipose-Derived Stem Cells. Sci Rep. 2019;9:8009.

32. Overgaard CE, Sanzone KM, Spiczka KS, Sheff DR, Sandra A, Yeaman C. Deciliation Is Associated with Dramatic Remodeling of Epithelial Cell Junctions and Surface Domains. Nusrat A, editor. MBoC. 2009;20:102–13.

33. Kunnen SJ, Malas TB, Semeins CM, Bakker AD, Peters DJM. Comprehensive transcriptome analysis of fluid shear stress altered gene expression in renal epithelial cells. J Cell Physiol. 2018;233:3615–28.

34. Sainath R, Gallo G. The dynein inhibitor Ciliobrevin D inhibits the bidirectional transport of organelles along sensory axons and impairs NGF-mediated regulation of growth cones and axon branches: Ciliobrevin D Inhibits Axon Transport. Devel Neurobio. 2015;75:757–77.

35. Deren M, Yang X, Guan Y, Chen Q. Biological and Chemical Removal of Primary Cilia Affects Mechanical Activation of Chondrogenesis Markers in Chondroprogenitors and Hypertrophic Chondrocytes. IJMS. 2016;17:188.

36. Thirugnanam K, Prabhudesai S, Van Why E, Pan A, Gupta A, Foreman K, et al. Ciliogenesis mechanisms mediated by PAK2-ARL13B signaling in brain endothelial cells is responsible for vascular stability. Biochemical Pharmacology. 2022;202:115143.

37. Helms HC, Abbott NJ, Burek M, Cecchelli R, Couraud P-O, Deli MA, et al. In vitro models of the blood–brain barrier: An overview of commonly used brain endothelial cell culture models and guidelines for their use. J Cereb Blood Flow Metab. 2016;36:862–90.

38. Mantle JL, Min L, Lee KH. Minimum Transendothelial Electrical Resistance Thresholds for the Study of Small and Large Molecule Drug Transport in a Human *in Vitro* Blood–Brain Barrier Model. Mol Pharmaceutics. 2016;13:4191–8.